On The Reactivity of Graphene and MoS_2 and the Preparation of Their Heterostructures

Ciara McGlynn

Supervisor: Dr. Aidan R. McDonald

School of Chemistry

University of Dublin, Trinity College

This dissertation is submitted for the degree of

Doctor of Philosophy

University of Dublin Trinity College April 2019

Declaration

I declare that this thesis has not been submitted as an exercise for a degree at this or any other university and it is entirely my own work. I agree to deposit this thesis in the University's open access institutional repository or allow the Library to do so on my behalf, subject to Irish Copyright Legislation and Trinity College Library conditions of use and acknowledgement.

Signature _____

Ciara McGlynn
April 2019

Acknowledgements

I would like to extend my gratitude to Dr Aidan McDonald for the allowing me to undertake this project and for his enduring patience and sound advice. I am eternally grateful to all of my labmates over the last four years; Dr. Adriana Magherusan, Dr. Andy Ure, Dr. Ankita Das, Dr. Bertrand Gerey, Daniel Nelis, Dr Duenpen Unjaroen, Giuseppe "Peppe" Spedalotto, Marta Lovisari, Dr. Paolo Pirovano, Philipp Heim, Dr. Prasenjit Mondal and in particular, my fellow materials chemistry black sheep, Dr. Xin Chen. Thank you all for all the pats, high-fives, baked goods, hugs, casual and serious chats, pints and karaoke nights.

I would also like to thank Dr John O'Brien and Dr Manuel Ruether for their help in running NMR spectra and training me in the use of TGA and TGA-IR, respectively. As much as you two like to joke about it, I like to think I fixed the TGA almost as much as I broke it. Dr Gary Hessman and Dr Martin Feeney deserve mentions for their assistance in running ESI and MALDI-TOF mass spectrometry, and I must also mention Dr Brendan Twamley for his instruction in running pXRD, and remind him that on Wednesdays, we have baked goods in the office. Lastly, from CRANN and the AML, I would like to thank Dr Nina Berner, for producing XPS spectra of some of the samples presented herein and assisting me in the analysis, Mr Owen Brazil, for providing the AFM images, Dr Keith Paton, for his Raman spectroscopy training, Dr. Clodagh Dooley for her SEM training and Dr David McAteer for all his help and suggestions re electrochemistry.

I could not have completed this thesis without the support of my family; my sister for being a role model and occasional life-coach, my mother for her saintly patience when listening to my despairing, general feelings of stress, and not being too polite to snap me out of it, my brother for good-naturedly putting up with my irritability when it was undeservingly directed at him, my father for providing relief through his music suggestions and his own blended brand of comedy, my aunts Anne and Din for never failing to check up on me, and even Gonzo the budgie, for always whistling back to me whenever I was writing from home.

I am extremely grateful to my endlessly supportive boyfriend Rob, who has never known me outside of my PhD and will hopefully be pleasantly surprised, and to Dermot, for providing many, many cups of tea, a fellow PhD student's sympathetic ear and many continuing years of friendship. I must also mention all my friends from DU Karate club, for giving me an outlet for my stress through punches and kicks, not to mention parties, and the Stoneybanter group, in particular Dónal and Árann, for being the best roommates and friends when all of our futures faced varying degrees of uncertainty. My thoughts also go to my close friends, Jo Jo, a *real* doctor, with whom I can go without seeing for several months

and pick up a conversation again as if we'd parted yesterday, and Sarah, an excellent life teacher as well as an undoubtedly scary school teacher, for maintaining a closeness lost to many of our school friends, despite her significant increase in physical distance.

Summary

Graphene and MoS_2 are two of the most researched materials in nanoscience, and are expected to be used for a range of applications in the future. This thesis sets out to deepen the understanding of their chemistry, by studying the possible reactivity of a series of powerful oxidants towards graphene, the chemical interaction of graphene and MoS_2 during heterostructure synthesis, and the functionalisation of these materials for novel, covalently-joined heterostructures. The reaction of graphene with hydrogen peroxide, *tert*-butyl alcohol, peracetic acid, *meta*-chloroperbenzoic acid, iodosobenzene and diacetoxy iodobenzene, found that these inorganic and organic oxidants have little to no ability to oxidise graphene. Comparing this to the reactivity studies performed using Fenton's reagent, some oxidation of the edges of few-layer graphene was observed. The use of the highly reactive $[Fe^{V}(BPMEN)(O)(OH)]$ and $[Fe^{V}(TPA)(O)(OH)]$ species also yielded edge-oxidised graphene, but full degradation was not observed. In conclusion, Fenton's reagent and the metalloenzymes employed by soil bacteria to degrade aromatic detritus may increase in the bioavailability of graphene rather than degrading, increasing its nanotoxicity.

The formation and study of a series of heterostructures of chemically exfoliated-1T-MoS_2/graphene and 2H-MoS_2/graphene revealed an often overlooked but recently postulated donation of electron density from graphene to MoS_2. This was observed spectroscopically as the increase of sp^3-hybridised carbon in graphene after sonication in the presence of either ce-1T-MoS_2 or 2H-MoS_2, with the 1T-phase showing greater reactivity towards graphene. This saturation of graphene was found to be concentration-dependent on MoS_2. Evidence for this was also demonstrated by the effect that saturation had on the HER activity of the heterostructures, from high to low graphene content, compared to ce-1T- or 2H-MoS_2 alone.

A covalently-linked heterostructure of graphene and ce-1T-MoS_2 was prepared by functionalising graphene with benzoyl chloride and ce-1T-MoS_2 with ethanol, and allowing the functionalised materials to undergo esterification. Graphene was also functionalised with benzoic acid and iodoethyl benzoate, demonstrating the versatility of functionalised graphene. The heterostructure was spectroscopically characterised and showed a decrease in resistance compared to functionalised $MoS_,$ remaining similar to pristine ce-1T-MoS_2.

Table of contents

List of figures

List of tables

Abbreviations

AFM Atomic Force Microscopy

ATR-IR Attenuated Total Reflectance Infrared (Spectroscopy)

BPMEN N,N'-dimethyl-N,N'-bis-(2-pyridin-2-ylmethyl)-1,2-ethanediamine

ce-1T-MoS_2 Chemically exfoliated 1T-MoS_2

CNTs Carbon nanotubes

CVD Chemical Vapour Deposition

DAIB Diacetoxy iodobenzene

DI Deionised water

DMF *N,N*-dimethylformamide

DRIFT Diffuse Reflectance Infrared Fourier Transform (Spectroscopy)

FT-IR Fourier Transform infrared spectroscopy

GIC Graphite Intercalated Compound

GO Graphene oxide

HER Hydrogen Evolution Reaction

HOPG Highly Ordered Pyrolytic Graphite

I_D:I_G the ratio of intensity of the D and G peaks of the Raman spectrum

IPA 2-propanol

LPE Liquid Phase Exfoliation

m-CPBA *meta*-chloroperbenzoic acid

n-BuLi n-butyllithium

NMP *N*-methyl-pyrrolidinone

o-DCB *o*-dichlorobenzene

OER Oxygen Evolution Reaction

PABA *para*-aminobenzoic acid

PhIO Iodosobenzene

pXRD Powder X-Ray Diffraction

rGO Reduced graphene oxide

SEM Scanning Electron Microscopy

tBu-OOH Tert-butyl hydroperoxide

TGA Thermogravimetric Analysis

TGA-IR Coupled Thermogravimetric Analysis/Infrared Spectroscopy

TGA-MS Coupled Thermogravimetric Analysis/Mass Spectroscopy

TMDs Transition Metal Dichalcogenides

TPA Tris(2-pyridylmethyl)amine

UV-vis Ultraviolet and Visible Spectroscopy/Spectrophotometry

XPS X-ray photoelectron spectroscopy

Chapter 1

Introduction

1.1 Overview

In the 14 years following the isolation of a single layer of graphite, graphene, by Novoselov and Geim[1], the research field of 'two-dimensional' (2D) materials has exploded to include many different kinds of nanosheets of single or multiple atomic species. Two-dimensional counterparts of bulk materials often display distinct or augmented properties from the parent materials—for example, graphene displays remarkable thermal and electronic conductivity compared to its insulating parent material graphite.[1] As the unique properties of 2D materials become more evident, the study of these novel materials, their isolation and mass production have dominated the field of materials science.[2–4] In time, the industrial use of 2D materials, taking graphene as an example, is expected to rise exponentially. Applications requiring lower quality graphene, developed using scalable and cheap preparation methods (such as chemical exfoliation to graphene oxide (GO) and reduction to reduced GO (rGO) for conductive inks) should appear first in the market, with applications dependent on higher quality graphene, such as graphene sheets currently produced by chemical vapour deposition (CVD) for electronic devices taking decades or more to reach consumers.[5]

Introduction

Although much research has been conducted on how to produce graphene (and other 2D materials) for industrial use, the toxicity or bioremediation of large amounts of graphene or functionalised graphene is still an underdeveloped area.[6] As we are currently seeing with plastics, and microplastics in particular, uncontrolled mass production and subsequent disposal can lead to environmental problems down the road.[7, 8] To this end, this thesis will expose graphene to a series of oxidants, oxygenating reagents, and metal-based oxidants in an effort to learn more about the possible waste treatment methods or bioremediation pathways for graphene once its use has become widespread.

Aside from isolating new materials, the idea of combining nanomaterials in order to harness useful characteristics of both is also a growing field of research in its own right. In preparation for a post-fossil fuel world, the search for alternative, clean sources of fuel have centred on solar energy and the production of hydrogen, an energy-dense fuel that gives only water as the product of its combustion.[9] This in turn leads to the search for cheap, abundant materials that are capable of reducing the energy cost of producing hydrogen—*i.e.*, materials that catalyse the hydrogen evolution reaction (HER) step of water splitting. In this case, transition metal dichalcogenides (TMDs) such as molybdenum disulfide (MoS_2) and tungsten disulfide (WSe_2) have been identified as suitable HER catalysts with their 2D forms showing increased HER activity.[10–12] Combining 2D MoS_2 with graphene has been proposed as a method to increase the efficiency of the HER reaction by coupling the conductivity of graphene with the catalytic activity of MoS_2.[13] This thesis will test this, identifying the best ratio of MoS_2 to graphene to use for potentially improved catalysis, as well as the effect graphene produces in heterostructures composed of either phase of 2D MoS_2. The interaction of the two materials together in the heterostructures will be investigated in chemical terms along with the potential effect graphene has on the HER activity of MoS_2.

Re-stacking is one of the main problems encountered in the production of 2D materials. Monolayers are fundamentally less stable than their bulk counterparts due to the extremely

large surface area generated by the exfoliation of layered materials to single or few-layer components.[14] The use of non-covalently binding surfactants or intercalants, as well as covalent functionalisation with organic or inorganic groups, are two of the most promising ways to prevent re-stacking and prolong the life of 2D materials.[15, 16] The functionalisation of graphene is well-documented,[17–19] with the field of MoS_2 functionalisation still developing.[20] The formation of heterostructures using covalent means is in its infancy, and in order to expand this, this thesis will deliver a method to covalently bind graphene and MoS_2 for use in further applications. This will also be compared with the previously prepared van der Waals heterostructures, *i.e.*, heterostructures formed by the physical stacking of different materials together.[21, 22] The effect the covalent bonding has on the HER activity of the heterostructure will also be investigated.

In preparation for these discussions, this chapter will detail the characteristics, preparation, reactivity and possible applications of two of these 2D materials: graphene and MoS_2. It will also touch on the insight expected to be gained over the studies presented in this thesis: the reactivity of graphene towards highly reactive oxidants, the combination of graphene with 1T-MoS_2 and with 2H-MoS_2 forming heterostructures, and the novel linking of graphene to 1T-MoS_2 *via* functionalisation, with a view to producing efficient catalysts for the hydrogen evolution reaction.

1.2 2D Materials: Introduction to Graphene

Graphene, first isolated in 2004 by Novoselov *et al*,[1] is a single sheet of graphite or sp^2-hybridised carbon, and is an allotrope of carbon. This unassuming material possesses the highest electron mobility of any reported material and demonstrates metallic behaviour due to its lack of a band gap, unlike its parent material graphite, which is well known as a soft, insulating material.[2] Graphene originally attracted notice due to the peculiar properties of its

electron cloud—the highly delocalised π electrons have extremely high mobility, in the range of 250,000 cm^2/ V s. Beyond this, graphene has the highest Young's modulus measured to date, 1 TPa, and extremely high thermal conductivity (5000 W m^{-1} K^{-1}). As a result of the degenerate electrons and holes present in pristine graphene, electrons can behave as massless particles and travel without resistance within the graphene structure.[2] Shortly after it was discovered, the properties of graphene attracted great interest for a range of applications; its remarkable conductivity, the ballistic nature of electrons within its structure attracted research into its use in transistors and conductive inks.[23, 24] Its transparency and its high mechanical strength drew interest as a base for flexible electronics and displays[25, 26] and its excellent chemical and thermal stability also predispose it for use as a protective coating for reactive metal surfaces.[27]

The structure of graphene is well known—a single layer of graphite in the thermodynamically favoured hexagonal crystal system. Due to its two-dimensional form, the simple stacking order of the graphite crystal—ABABAB, etc., where A and B are carbon atoms of one layer fixed in space, can be largely ignored (Figure 1.1).[2] Monolayer graphene can be understood as comprising only of surface and possessing no bulk. This is partially responsible for its increased reactivity compared to graphite. Few-layer graphene, or graphite approaching graphene thinness, has intermediate properties between that of graphite and graphene. Reports have shown the reactivity of bilayer, trilayer and multilayer graphene decrease with layer number, so much so that above 11 layers, the properties of few-layer graphene resemble that of bulk graphite.[28] The edges of a sheet of graphene, possessing non-aromatic double bonds or bonds to heteroatoms, have in turn been shown to be more reactive than the basal plane.[28] Two types of edges have been recognised in graphene: armchair edges, which are aromatic, according to the rules of Clar's aromatic sextet,[29] and zig-zag edges, which have more instances of double bond character rather than aromaticity according to Clar's aromatic sextet theory.[30] Dangling bonds are normally satisfied by

oxygen or hydrogen. Armchair edges have been shown conclusively to react more readily than zig-zag edges,[31, 32] and both are more reactive than the basal planes of graphene, introducing an element of uncertainty into efforts to functionalise or modify graphene for further use. Aside from the dangling bonds of its edges, the presence of 'π clouds' above and below the basal plane also allow modification or functionalisation to occur on either side of graphene. The electron density of graphene precludes its reactivity as nucleophilic, and indeed, many of the methods of modifying graphene rely on aromatic chemistry. In this way, monolayer graphene can be seen as infinitely large polyaromatic molecule.[33]

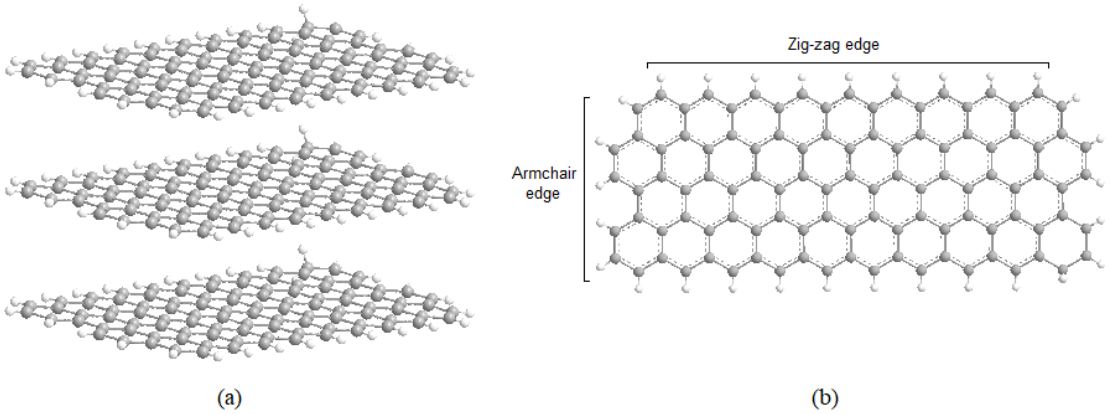

Fig. 1.1 Ball-and-stick models of (a) graphite and (b) graphene. Grey = carbon, white = hydrogen-terminated edges.

1.3 2D Materials: Introduction to Transition Metal Dichalcogenides

The isolation of graphene led to a materials version of a gold rush, as the search for other minerals or atomic species that could be delaminated to form 2D nanosheets began in earnest. In the years succeeding 2004, other 2D crystals were isolated and added to the growing family of 2D materials: hexagonal boron nitride, isoelectronic to graphene,[34] other group 14 elements such as germanene, silicene, stannene, and most recently, phosphorene in 2014[35]

and bismuthene in 2017[36] from Group 15. 2D crystals based on the transition metals were also isolated, including various transition metal dichalcogenides such as MoS_2 in its 2H phase in 2005,[37] quickly followed by others like WSe_2.[38] These were joined in 2011 by transition metal hydroxides such as $Ni(OH)_2$[39] and MXenes, Ti_3AlC_2 being an example of this 60+ strong family.[40, 4] Each of these show distinct properties or enhanced abilities that set them apart from the bulk material. One branch of this family that has attracted in depth research are the various transition metal dichalcogenides as mentioned above. This is any material that contains both a transition metal (most commonly from Group 6, but also from Groups 4-7) and an element from Group 16, the chalcogens, in the empirical formula MX_2, where M is the metal and X is the chalcogen.[41] This introduction will concentrate on the TMDs from Group 6 and 16, specifically MoS_2.

Like graphite, TMDs are naturally abundant and so, inexpensive and readily available. Unlike graphene and graphite, Group 6 TMDs are generally semi-conducting and possess an indirect band gap. Upon delamination, this becomes a direct bandgap.[41] As with graphite, weak van der Waals forces are all that bind each sheet of the material to the bulk along the Z axis of the crystal. For MoS_2, the TMD employed in this thesis, the material crystallises in one of three different phases—1T (trigonal), 2H (hexagonal), and 3R (rhombohedral), with two outer layers of S atoms and one inner layer of Mo atoms making one sheet three atoms thick. Group 6 TMDs such as MoS_2 and WS_2 are found in nature in the 2H phase, in which the chalcogens and metals of the material stack as AbA BaB. The 3R phase stacks as AbA CaC BcB, where A, B and C are sulfur atoms, and a, b and c are molybdenum atoms, with a and A, *etc.* overlapping on different planes. Once the material has been delaminated, both 2H and 3R possess the same structure and will be henceforth referred to as 2H, regardless of the original bulk phase. The coordination environment of the Mo atom in the sheet is trigonal prismatic in the 2H phase. The 1T phase is more common in Group 4 TMDs and has a stacking sequence of AbC AbC, with an octahedral environment around the central metal

ion (Figure 1.2). Group 6 TMDs can be 'forced' into this metastable phase by introducing intercalants, commonly Li^+, into the material.[42, 43] By changing the phase of MoS_2 from thermodynamically stable 2H to metastable 1T, the reactivity can be greatly enhanced.[44] This has proven to be extremely useful for functionalisation[45] and further applications of MoS_2 nanosheets, such as the increased activity of 1T-MoS_2 as an electrocatalyst for the hydrogen evolution reaction.[12]

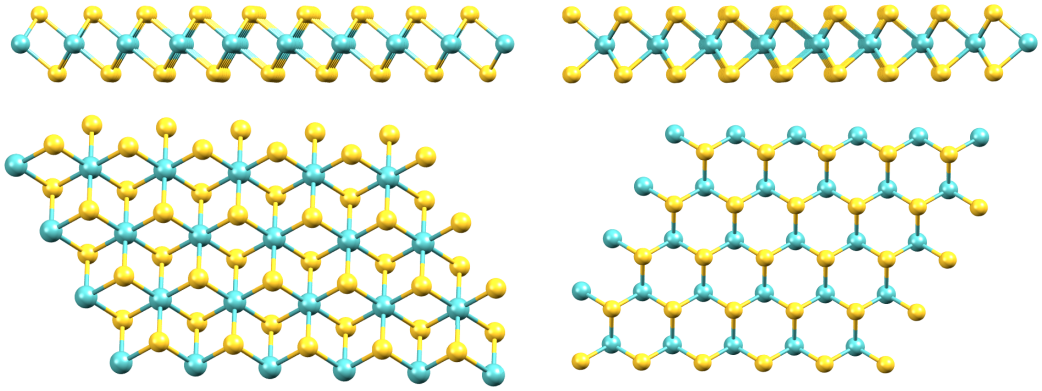

(a) (b)

Fig. 1.2 Ball-and-stick models of monolayer (a) 1T-MoS_2 and (b) 2H-MoS_2, showing side on view and basal plane. Yellow = sulfur, cyan = molybdenum.

1.4 Synthesis and Application of 2D Materials

Graphene was initially produced *via* mechanical exfoliation, also known as micromechanical cleavage—the 'Scotch tape' method,[1, 46] but several other techniques have been developed to synthesise graphene from graphite, SiC or hydrocarbons. Shear or solvent exfoliation,[47, 48] chemical or electrochemical exfoliation,[49] epitaxial growth by thermolysis of SiC on a Cu/Ni substrate,[50] and chemical vapour deposition (CVD) of CH_4 onto a metal substrate[51] are the most common methods.

As mentioned, the first method by which graphene was obtained was *via* mechanical exfoliation of graphite, in which thin flakes of graphite are removed from the parent graphite using sticky tape and are deposited on a suitable substrate. This process is then repeated until the thickness approaches that of a few nm, but this is a slow and low-yielding process.[52] Other problems occur in ensuring the complete removal of tape residue from the graphene, a problem similarly encountered in surfactant stabilised exfoliation—this residue can compromise the otherwise pristine nature of the graphene.[1] CVD and its related process, epitaxial growth, give the highest quality monolayer graphene, through the deposition of carbon onto Cu or Ni. These metals act as catalysts for the thermolysis of the carbon source, usually a hydrocarbon, as well as a support. However, CVD is time-consuming, expensive and although the graphene is pristine, it is low yielding. In reactivity studies concerning the effect of reactants or substrates on a single sheet of graphene, CVD graphene or epitaxial graphene grown on Si is frequently used.[53, 51]

Liquid phase exfoliation, by sonic or shear methods, were used to prepare graphene in this project (Figure 1.3). Initially, liquid phase or solvent exfoliation involved only ultrasonication, in which the sheets are blasted apart by sound energy, of the graphite source for long periods in stabilising solvents.[48] Later, a second form of liquid phase exfoliation was developed that uses high shear forces to overcome the attractive forces between sheets, generated by rapid mixing.[47] For ultrasonic and shear exfoliation, larger, unexfoliated graphite particles are then removed from the dispersion by centrifugation. A suitable solvent, which possesses a surface energy similar to that of the graphene sheets is also required to impede re-aggregation for ultrasonic and shear exfoliated graphene.[54] Aside from production problems, in dispersion, graphene readily re-aggregates to graphite without the presence of a support, intercalant or surfactant, and its hydrophobicity renders chemistry in water or other polar organic solvents difficult. Only a handful of solvents have been shown to produce dispersions of graphene that are stable for practical amounts of

time—N-methyl-pyrrolidone, (NMP) dimethylformamide, (DMF) and o-dichlorobenzene (o-DCB) to name the most common.[48] These solvents are potentially toxic and the former two are suspected of reproductive toxicity in mammalian females.[55] It is possible to prepare graphene in different solvents through the use of surfactants such as sodium cholate and sodium dodecyl sulfate, or other intercalants which cover the graphene sheets or intercalate into the graphite lattice to aid exfoliation or limit re-aggregation. However, for the deposition of films or further reaction of the graphene dispersion, the surfactants must be removed entirely. This presents a new challenge as many surfactants adsorb strongly on the graphene surface and can be difficult to remove by washing alone.[56] Graphene has also been prepared *via* ball milling, in which the shear forces necessary for exfoliation come from the impact and attrition of the steel balls in a rotating grinder on bulk graphite. These exfoliate the graphite to smaller and thinner sheets, though some damage is introduced as monitored by the growth of the ratio of intensity of the D and G peaks (I_D:I_G) in the Raman spectrum. To minimise this, smaller aromatic molecules are included in the milling process as buffering materials.[57]

By far the most common form of chemical exfoliation involves the oxidation of graphite to GO *via* Hummer's method,[58] which involves excessive oxidation of graphite and subsequent exfoliation to GO. This is achieved by reaction of bulk graphite with $KMnO_4$ in the presence of H_2SO_4, refluxing in water, with treatment of the filtrate with H_2O_2 giving graphite oxide. Sonication of this in water yields graphene oxide (GO). GO can then be mostly reduced by reductants such as hydrazine to rGO. This procedure gives good synthetic yields and dispersions of GO/rGO contain a high percentage of mono- and bilayer sheets, as well as being dispersible in hydrophilic solvents. However, GO production can also be seen as an extreme version of graphite functionalisation; excessive oxidation greatly reduces the intrinsic properties of graphene that make it so desirable, and reduction cannot remove 100% of all oxygen-containing groups or repair permanent defects and holes in the basal plane.[2, 59]

The intercalation of graphite by Na/K, accomplished by stirring graphite and Na/K alloy in 1,2-dimethoxyethane under an argon atmosphere for several days, has been extensively employed by the Hirsch group in the production of functionalised graphene from graphite without the need for prior exfoliation. The addition of further reactants to this negatively charged 'graphenide', such as diazonium salts[60] or iodoalkyl species[18] facilitates and sustains exfoliation of the individual graphene sheets by functionalising either side of the basal plane and preventing re-aggregation *via* steric hindrance. The graphene produced by this method is very reactive, and therefore is used for immediate functionalisation—it would be unsuitable for applications that require pristine, inert graphene.

Potential applications for graphene, once it can be exfoliated cheaply and in good yield, are numerous. The most popular of the applications currently being developed include the use of graphene as a sensor or drug delivery agent in biomedicine,[6] as the major component of conductive inks for printing small devices,[61, 23] as a replacement for indium tin oxide in flexible displays and touchscreens,[62] in organic light-emitting diodes (OLEDs),[63] and other devices previously dominated by silicon.[5] However, major drawbacks to the widespread use of graphene lie in its hydrophobic nature and tendency to re-aggregate to graphite, which makes it difficult to mass-produce and tune its properties to specific applications.[3] Despite these drawbacks, research into graphene continues to grow and many believe it is only a matter of time before graphene use becomes widespread. This raises its own concerns about the possible effects of graphene or more reactive functionalised graphene on organisms and the environment, were they to be produced and released into the environment on an industrial scale. This concern forms the basis of one of the studies described in this thesis—the effect of the Fenton reagent, used in water treatment,[64] and two biomimetic catalysts, based on enzymes in soil bacteria, on graphene.

MoS_2 has been produced *via* many of the same methods as graphene. The first dispersion of what is now known as monolayer MoS_2 was produced much earlier than graphene—

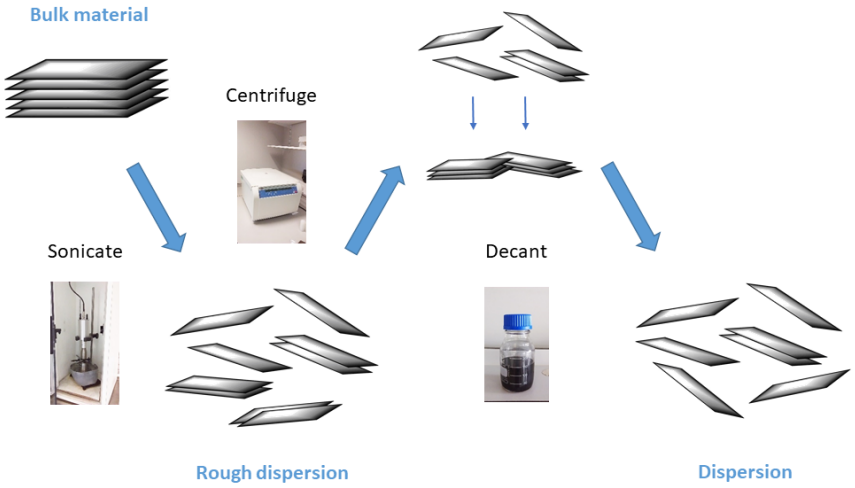

Fig. 1.3 The liquid phase exfoliation of graphite or 2H-MoS_2 by sonication to a dispersion of few-layer nanosheets.

Morrison *et al*[43] chemically exfoliated MoS_2 to single layers by intercalation with lithium in 1986, 18 years before the isolation of monolayer graphene. This method is now widely used to produce aqueous monolayer dispersions of MoS_2, up to 70% of which is in the 1T-phase (Figure 1.4). The source of the lithium is normally n-BuLi, and bulk MoS_2 is stirred in a solution of n-BuLi in n-hexane for several days under an inert atmosphere at room temperature. The intercalated powder is then isolated by filtration and exfoliated by sonication in water. The product of this is known as chemically exfoliated 1T-MoS_2 (ce-1T-MoS_2). Modifications to this method have included electrochemically intercalating Li ions under ambient conditions, using a lithium salt in non-aqueous media and a MoS_2 cathode,[65] and heating the combination of n-BuLi and MoS_2 to reflux for 6–48 h.[66, 67] Liquid phase exfoliation methods have also been shown to work for the preparation of dispersions of 2H-MoS_2. The inclusion of a preliminary sonication and centrifuging step at high rpm is included to remove residual inorganic salts. Because of its lower surface energy, MoS_2 can be dispersed in alcohols such as 2-propanol (IPA) for long periods of time. Dispersibility in common laboratory solvents that are easier to work with than the high boiling point solvent

such as NMP and DMF gives the production of two-dimensional MoS_2 *via* liquid phase exfoliation some advantage over graphene.[48, 68]

Two-dimensional MoS_2 or MoS_2 nanoparticles can also be produced from ammonium molybdenite salts ($(NH_4)_2.MoS_4$ for example) subjected to high pressure and temperature (200–450 °C) in an autoclave. The ammonium salt is exposed to air at high temperature and converted to MoO_3, which is in turn treated with thiourea in similar hydrothermal conditions to form MoS_2.[69] This produces very small flakes or clusters of MoS_2, and is also used for growing MoS_2 on other nanomaterials or supports, and to produce defect-rich MoS_2 for improved catalytic activity.[70] Molybdenum oxides (mostly MoO_3) are also used when producing sheets of MoS_2 for chemical vapour deposition. MoO_3 is treated with a flow of sulfur gas, forming large, low-defect structures known as MoS_2 triangles. The thickness, monolayer to bi- or trilayer, *etc*., can be controlled by the gas flow.[71–73]

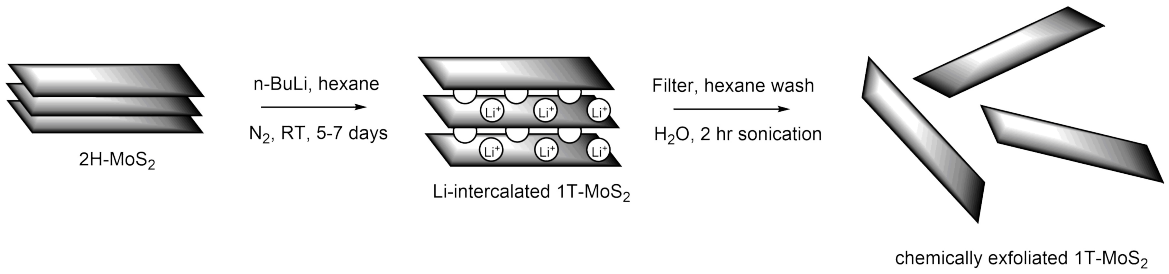

Fig. 1.4 n-BuLi mediated chemical exfoliation of bulk 2H-MoS_2 to monolayer 1T-MoS_2.

For MoS_2, application development centres on its capacity for lithium ion storage for lithium-ion batteries, particularly when combined with conductive graphene.[74] Its direct bandgap gives it an advantage over graphene in electronic applications such as small devices and transistors, and the photoluminescence associated with this bandgap holds great potential for the development of solar cells, LEDs, and other optoelectronic devices.[75–77] Its well-documented HER activity would be incredibly useful in a future hydrogen-powered economy.[12, 78]

1.5 Application: Hydrogen Evolution Reaction

Hydrogen has long been touted as a fuel for a greener future.[9] The hydrogen evolution reaction is a half reaction of water splitting, the other half of which is oxygen evolution.[10] The half-equations for hydrogen and oxygen production, (1.1) and (1.2) respectively, as well as the full equation (1.3) are shown below:

$$2\,H^+ + 2\,e^- \longrightarrow H_2 \tag{1.1}$$

$$O^{2-} \longrightarrow \frac{1}{2}\,O_2 + 2\,e^- \tag{1.2}$$

$$H_2O \longrightarrow H_2 + \frac{1}{2}\,O_2 \tag{1.3}$$

However, the energy required to produce hydrogen from its most abundant source, water, is extremely high and must first be overcome before hydrogen can seriously be considered for widespread use. The electrolysis of water requires at least 237 kJ per mole, which would only produce 2 g of H_2.[79] Years of research and investigation have been dedicated to developing electrocatalysts for both hydrogen evolution and oxygen evolution, in an effort to bypass this large activation energy. By far the best HER catalyst known to date is the noble metal Pt, which possesses a Gibbs free energy change of ≈ 0 eV for the adsorption of hydrogen atoms to its surface.[11] This characteristic has since become a prerequisite for a good HER catalyst—in order to form a hydrogen molecule, protons must be able to adsorb to the surface and stay there long enough to come in contact with either other adsorbed protons or protons in solution. They must also be able to overcome the energy barrier to desorption easily. The small change in Gibbs' energy afford by Pt facilitates both of these steps, by adsorbing hydrogen strongly enough to allow it come in contact with other hydrogen atoms and to be reduced at the anode, and weakly enough that once the hydrogen molecule has been formed,

it can quickly desorb, freeing the Pt surface sites for more hydrogen to adsorb. To use a Goldilocks analogy, hydrogen atoms are neither adsorbed too weakly or too strongly, but 'just right' for hydrogen evolution to occur.[80]

The hydrogen evolution half-equation can be expanded into two steps, adsorption of protons on the surface and the desorption of hydrogen from the catalyst. Either of these steps can be rate-limiting depending on the ΔG_H. The former is known as the Volmer step (equation 1.4 or 1.5 below) and the latter as the Heyrovsky or Tafel step (equation 1.6).

$$H^+(aq) + e^-(m) \longrightarrow H^\bullet(ads) \tag{1.4}$$

$$H^\bullet(ads) + H^+(aq) + e^-(m) \longrightarrow H_2(g) \tag{1.5}$$

$$H^\bullet(ads) + H^\bullet(ads) \longrightarrow H_2(g) \tag{1.6}$$

It was demonstrated by Nørskov *et al*,[81] using DFT calculations, that the exchange current density of a material is directly related to Gibbs free energy for the adsorbed hydrogen atom. The Gibbs free energy for hydrogen adsorption on Pt is $\Delta G_H \approx 0$, and hence, it is an excellent electrocatalyst for HER, with a negligible overpotential compared to RHE and a Tafel slope of 60 mV/dec in 0.1 M $HClO_4$.[82] However, industrial level usage of Pt for hydrogen production is prohibitively expensive, and so, the search continues for a cheaper catalyst. Other materials that have demonstrated HER activity have ΔG_H either greater or less than zero (*i.e.*, the energy of the products and of the reagents are not similar), and this has different effects on the rate of the reaction. Nørskov *et al*[81] also demonstrated that the edges, defects, and steps of MoS_2 were active for HER catalysis due to the concentration of unsaturated bonds in these environments. If the bond between the hydrogen atom and the catalyst is too weak (*i.e.*, $\Delta G_H > 0$), the Volmer step is rate limiting. This is observed when using chemically exfoliated MoS_2 as a HER catalyst (giving an overpotential of -200 mV and

a Tafel slope of 40 mV/dec in 0.5 M H_2SO_4).[83] The Heyrovsky step becomes rate-limiting if the bond between the catalyst and the adsorbed hydrogen is too strong ($\Delta G_H < 0$), leading to overpotentials of -620 mV and Tafel slopes of 152 mV/dec for example,[84] in bulk MoS_2 catalysts.[11]

The Group 6 TMDs have attracted a lot of attention since Jaramillo *et al*[78] discovered the HER activity at the edges of bulk MoS_2. $MoSe_2$, WS_2, and WSe_2 have since been investigated, with $MoSe_2$ purported to be the most active. Most of this research however has centred on MoS_2 as the most abundant of these naturally occurring, cheap alternative catalysts.[80] The active sites and mechanism of HER on MoS_2 took several years to elucidate. From the results of a detailed report on edge passivation, the edges of bulk MoS_2 was discovered to be active towards HER, with the basal plane not showing any noticeable activity.[85] However, it was discovered by Jin *et al*[12] and Chhwalla *et al*[83] independently in 2013 that the octahedral 1T phase of MoS_2 showed greatly increased activity towards HER, with both edges and basal plane active towards hydrogen. This then became a hot area of research, with much of HER research on MoS_2 concentrating on the 1T-phase.[12, 10]

1.6 Combining 2D Materials: Heterostructures

One of the drawbacks of using MoS_2 as a catalyst for HER, particularly the 2H phase, is its lack of conductivity.[78] Attempts to address this have included combining both MoS_2 and graphene into composites or heterostructures.[21, 22] However, there are many other reasons why TMDs such as MoS_2 have been employed together with graphene as composites or heterostructures—they have been tested for applications such as components in lithium/sodium batteries, sensors and hydrogen storage as detailed below.[74, 86, 9] These are usually prepared *via* hydrothermal or solution based syntheses,[87–89] derivatives of chemical vapour deposition,[53, 90] or more rarely, from the formation of films of liquid

exfoliated materials.[56] Most commonly, these heterostructures, as 2D films, 3D foams or particles[91, 92] are used in applications where not only conductivity, but strength and catalytic activity are required: employing MoS_2-graphene hybrids can yield materials with the catalytic activity of MoS_2 towards hydrogen evolution,[93, 13] and its semiconducting nature for transistors and information storage,[94] coupled with the robust, inert, and conductive nature of graphene.[2] Aside from these, they have found applications as anode materials for lithium or sodium ion batteries[86, 74] and as sensors for small organics.[88]

The field of MoS_2/graphene heterostructures has been dominated by Van der Waals or other non-covalent interactions in the preparation of heterostructures. The most common of these methods involve chemical vapour co-deposition of graphene on MoS_2 or *vice versa*,[95, 96] hydrothermal/solvothermal synthesis of GO together with precursor salts such as MoO_3/NaS_2 or $(NH_4)_2MoS_4$[13, 22] and the use of GO or rGO in the place of pristine graphene. Interactions between TMDs such as MoS_2 and graphene, while noted,[56, 97–100] have been addressed in purely physical terms in the literature. In-depth chemical analysis is lacking, despite the significant volume of published research combining the two materials as devices, supports, and catalysts for a wide range of applications as mentioned. Much of the research approached from a chemistry viewpoint is limited to GO or rGO as a conducting base for MoS_2 in applications such as HER.[101] This greatly aids heterostructure formation as GO and its corresponding reduced product, rGO, are easily dispersed in water and other accessible solvents that can also disperse MoS_2 successfully.[102] However, GO and rGO can be poor quality substitutes for pristine graphene. Significant defects are formed during oxidation, and reduction often cannot heal holes or remove all oxygenated groups in the structure of rGO.[101, 103] Therefore, this thesis aims to further the understanding of the interaction of both 2H-MoS_2 and 1T-MoS_2 with graphene during the preparation and use of heterostructures in applications.

Aside from this, reports detailing the covalent linking of graphene and MoS_2 are few. As described above, most heterostructures are prepared by mixing layers of different materials, or the concerted hydrothermal synthesis of both materials together to facilitate close interaction.[97, 13] The formation of a covalently linked heterostructure was published by Rao *et al*[21] in 2016 and utilised Sonogashira coupling (using a Pd(0) catalyst, CuI cocatalyst and triethyl amine (TEA) in 140°C DMF) between sheets of iodobenzene functionalised MoS_2 and iodobenzene functionalised rGO.The heterostructure formed displayed high CO_2 adsorption properties, and they used the same chemistry to create 3D assemblies of MoS_2 which showed enhanced HER activity. The assemblies were then characterised by XPS, Raman spectroscopy, ATR-IR, solid state C^{13}-MAS NMR, pXRD and HR-TEM. Other studies into the covalent linking of graphene or other main group 2D materials and TMDs are mostly computational, as in Kaxiras' 2017 study of 'lateral heterojunctions' of these materials *i.e.*, where materials are covalently joined together at the edges.[104] Therefore this thesis will unveil further possibilities for forming covalently linked structures by functionalising both pristine graphene and ce-1T-MoS_2, and creating a link between the materials based on the reaction of these functional groups. Functionalisation in this way will not only help to prevent re-stacking of the materials but could also increase the hydrophobicity of the materials (particularly graphene) through the use of oxygen-containing groups, allowing them to interact more easily.

1.7 Functionalisation of Graphene and TMDs

As demonstrated earlier, well exfoliated, pristine graphene is notoriously hard to produce en masse, and its lack of dispersibility in polar solvents limits its potential for industry-scale production and applications. The use of toxic solvents and energy-intensive processes such as ultrasonication, CVD and epitaxial growth also generate environmental concerns about the

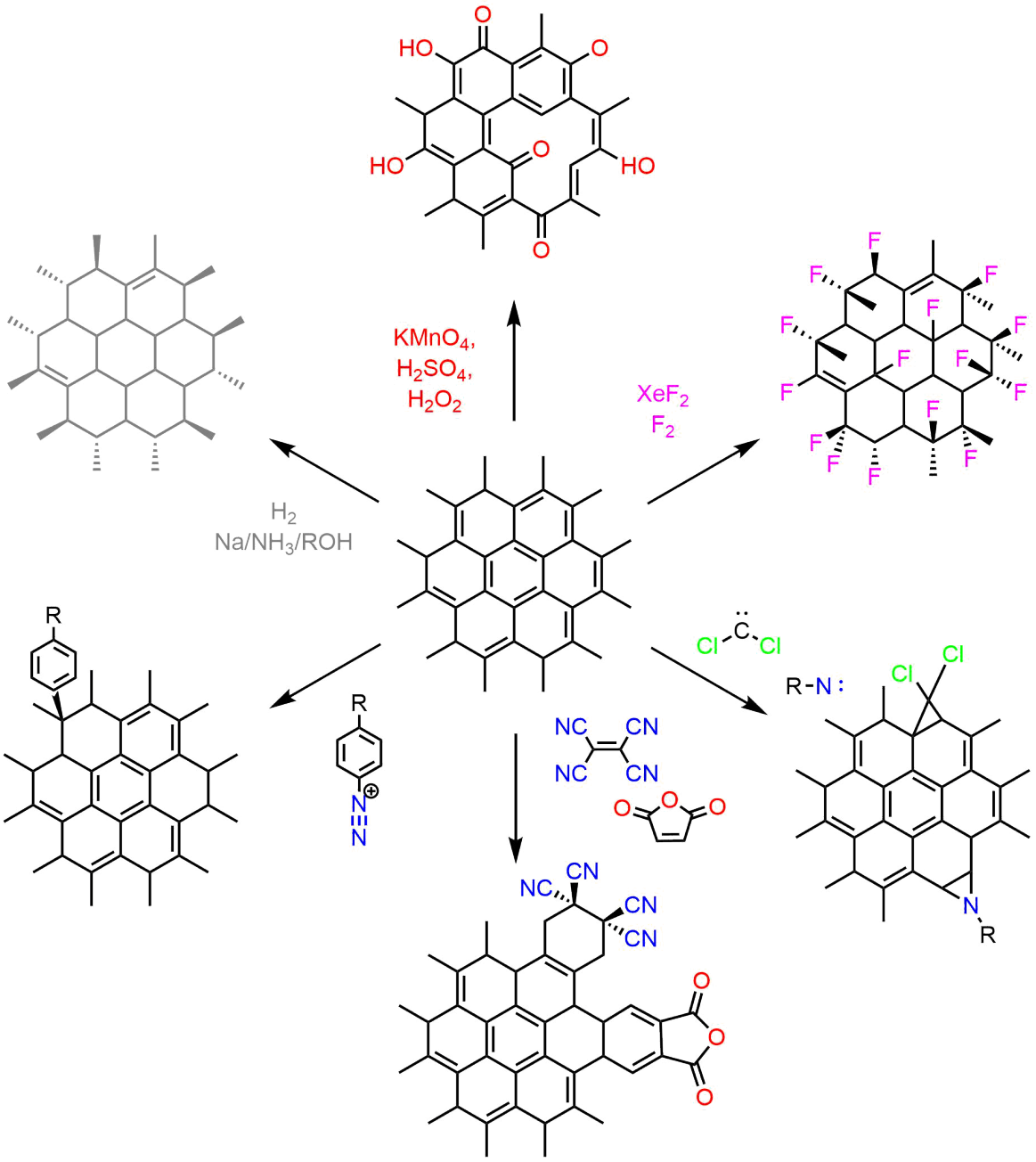

Fig. 1.5 Summary of the main functionalisation pathways of graphene.

production of graphene. The most common way to aid the dispersibility of graphene in polar solvents such as water is through functionalisation of the graphene surface. This involves the introduction of functional groups onto the graphene basal plane and the edges. Hydrophilic groups such as hydroxy, epoxy, amino, and carbonyl groups facilitate the dispersibility of graphene in water by forming hydrogen bonds with the solvent. Their presence also disrupts the π network of graphene, opening a band gap in the structure, and prevents reaggregation, thereby countering the main problems holding back mass graphene production.[17] Figure 1.5 shows a summary of the main pathways of graphene functionalisation.

The widespread use of GO as a graphene base in the literature because of its ease of production and dispersibility in polar solvents is a testament to this. However, GO itself has severely reduced thermal and electronic conductivity, as well as a larger band gap compared to pristine graphene, and the loss of these properties precludes GO from becoming the basis of industrial-level production of graphene.[105] Because of this, much research has been dedicated to developing milder or more selective forms of functionalising graphene. Aside from increasing the dispersibility and impeding or preventing the re-aggregation of exfoliated graphene, selective graphene functionalisation can also tune the properties of graphene to suit various applications such as in field-effect transistors, supports for biosensors, inkjet printing, and graphene/carbon papers and coatings. For these reasons, graphene reactivity has been studied in depth and several reactivity methods have come to light in the last 14 years.[106, 17]

Though the parent material graphite is known to be quite inert, graphene, particularly monolayer graphene, has been shown to undergo attack by sufficiently reactive species.[105] Graphite treated with $KMnO_4$, H_2SO_4, $NaNO_3$ and H_2O_2 produces graphite oxide, a yellowish powder that is easily dispersed in water or other polar solvents to form GO, as mentioned above. Although the exact nature of the functional groups on GO is still debated, it is believed to be composed of mostly hydroxyl and carboxyl functionalities with lower concentrations of

epoxides.[59] Hole formation has also been reported on the basal plane, and the combination of physical holes and high concentration of functionalities, while rendering GO much easier to produce and store in dispersion than graphene, takes a large toll on the very properties that aroused interest in graphene originally.[59, 2] To combat this, GO can also be reduced *via* hydrazine, hydrogen iodide, ascorbic acid or strong heating to rGO, that somewhat reinstates the semimetallic nature and excellent mobility of graphene. However, while regaining a lot of its original structure, reduction is not perfect and cannot heal holes in the basal plane, the main cause of damage to the electron cloud network.[107]

Milder forms of functionalisation have been rigorously investigated and graphene has been found to react with radicals, undergo cycloadditions, take part in Friedel-Crafts reactions (similar to other aromatic systems) and facilitate reduction/oxidation cycles, either as a catalyst or a substrate itself.[105, 106] In these types of reactions, graphene can be seen almost as an extended polyaromatic or conjugated system that readily undergoes aromatic reactions. Also interesting is the redox activity of graphene, as it easily gains or loses electrons to substances such as alkali metals and diazonium salts, and has been reported to aid the redox activity of catalytic nanoparticles.[108]

The hydrogenation of graphene, as a form of functionalisation, stems from an attempt to convert graphene into 'graphane', *i.e.* fully hydrogenated graphene. Over a decade, several methods of hydrogenation have been employed with varying degrees of success and therefore, differing levels of hydrogen functionalisation of graphene.[109] A popular form of hydrogenation is exposing graphene from a variety of sources to a hydrogen atmosphere at either very low pressures (2 mbar) to very high (100 bar) for at least 2 hr. Annealing at temperatures above 450°C converted hydrogenated graphene back to pristine graphene.[110] Another method of hydrogenation employed is Birch reduction, a radical-based technique used for reducing aromatic species such as benzene to an unconjugated cyclohexadiene.[111] It requires the use of strong reagents—Na metal in liquid NH_3 in the presence of an alcohol.

The best results have been obtained using graphite rather than graphene, Na, and liquid NH_3 with tBu-OH.[112] Another method for producing hydrogenated graphene includes plasma-assisted chemical vapour deposition using a plasma beam of methyl radicals and atomic hydrogen. However, none of these techniques have generated graphane, with the highest weight % of hydrogen measured in hydrogenated graphene at 5% compared to a theoretical total of 7.7% for graphane.[113]

The use of radical chemistry on graphene has also been employed for the creation of C-C bonds and incorporating fluorine and hydroxyl groups into graphene. Graphene monofluoride or fluorinated graphene, has received almost as much attention as graphane for its potential in applications—unlike graphene and graphane, it is an insulator with a much greater band gap (3.0 eV) than its other carbon-based cousins.[114] The complete fluorination of graphene has already been reported and the chemistry of fluorinating carbon species is not new, pathways to fluorinated graphite, fullerenes, and CNTs have been known for decades.[115] Fluorinated graphene had been attempted previously by treating graphite with F_2 gas at high T (400–600°C) or with F-based plasma.[116] These harsh conditions can etch graphene, so a milder route through treatment of graphene with XeF_2 was established by Robinson *et al*.[115] A Si etchant, XeF_2 had been shown to functionalise CNTs, and was successfully used to functionalise graphene to C_4F or 25% fluorine coverage. Stoichiometric fluorographene has been produced from carbon monofluoride, the product of the reaction of graphite to F_2 gas at high temperatures, with subsequent liquid phase exfoliation in solvents such as IPA[117] and sulfolane[118] giving the corresponding 2D material.

Aside from the introduction of heteroatoms into the graphene structure *via* the formation of GO, hydrogenation or fluorination of graphene, many other methods of functionalisation result in the formation of new C-C bonds to graphene. Radical chemistry has been mentioned previously in the case of Birch reduction of graphene, which proceeds *via* the generation of solvated electrons from Na in liquid NH_3. Other methods of graphene functionalisation that

rely on radical chemistry include the use of carbenes, nitrenes, phenyl and alkyl iodides, and diazonium salts on graphene.[105, 106, 17]

In particular, Hirsch's group has developed a method of exfoliation of graphene that also facilitates extensive functionalisation by a variety of substrates *via* a radical mechanism. The functionalisation of graphene with diazonium salts has been known since 2009, with Tour's group showing the functionalisation of graphene nanoribbons from CNTs in 2009[119, 120] using nitro-substituted benzenediazonium salts, but the most comprehensive report is from Hirsch's group, which details the diazonium functionalisation of graphene by combining diazonium salts with 'graphenide'—negatively charged graphite produced from graphite treated with NaK alloy in 1,2-dimethoxyethane under Ar.[60] The reduction of the graphite sheets by solvated electrons and the intercalation of potassium cations facilitated exfoliation and the repulsion generated by the reduction ensured that the dispersed sheets were prevented from re-aggregating. To this, they added excess 4-*tert*-butylphenyldiazonium chloride or 4-sulfonylphenyldiazonium chloride and characterised the resultant graphene with a host of spectroscopy techniques. This was then adopted by several other groups and later reports expanded this method of functionalisation of graphene to include epitaxial graphene,[121] rGO,[122] and liquid exfoliated graphene.[123] Graphenide was also used as an intermediate towards graphene functionalised with a series of electrophilic phenyl and alkyl iodides and hypervalent iodine-containing compounds such as bis(4-(tert-butyl)phenyl)-iodonium hexafluorophosphate.[124] Negatively charged graphenide was generated from natural graphite, synthetic graphite and from CVD graphene, all of which showed evidence of functionalisation by statistical Raman spectroscopy and coupled thermogravimetric analysis-mass spectroscopy when exposed to the chosen electrophiles, showcasing the versatility of this functionalisation method.[125]

Functionalisation methods, similarly to Birch reduction, can also come from established aromatic substitution chemistry. The ability of diazonium salts to functionalise graphene *via*

single electron transfer chemistry has been known since 2009, with Tour's group showing the functionalisation of graphene nanoribbons from CNTs in 2009[119, 120] and Strano's group publishing a study on the differing reactivity of the edges and surface of epitaxial graphene towards diazonium salt solutions.[28] Methods such as Diels Alder chemistry work well on graphene—in fact, graphene can be either the diene or the dienophile in the reaction due to its lack of a band gap meaning its HOMO and LUMO are both accessible. This flexibility has been demonstrated numerous times in the literature: Haddon *et al*[126] successfully reacted graphene and highly ordered pyrolytic graphite (HOPG) with dienophiles tetracyanoethylene and maleic anhydride, and dienes 9-methylanthracene and 2,3-dimethoxy-1,3-butadiene at elevated temperatures and demonstrated that cycloaddition could be used to functionalise graphene. Aside from [4+2] cycloaddition in Diels Alder reactions, graphene has been shown to react in [1+2] cycloadditions with both nitrenes and carbenes. This was demonstrated in a report by Pumera's group in which the simplest carbene, dichlorocarbene, was capable of functionalising rGO.[127] Strom *et al*[128] generated azido-phenylalanine in the presence of exfoliated graphene and succeeded in producing highly functionalised graphene *via* nitrene addition. This was later built on by Liu *et al*[129] using nitrenes generated from a series of perfluorophenyl azides on liquid exfoliated graphene. Arynes have also been successfully employed to functionalise graphene *via* [2+2] cycloaddition reactions using arynes generated from 2-(trimethylsilyl)aryl triflates.[130] Prato's group also discovered that *in situ*-generated 1,2,3-triazoles could undergo [1+3] cycloaddition with liquid exfoliated graphene to form amine functionalised graphene. The extent of functionalisation could be easily tracked by the use of both the Kaiser test[131] and the coordination of Au nanoparticles to the amine groups present on the functionalised graphene, as well as identifying any preferences towards edge or basal plane functionalisation.[132]

Work on the functionalisation of 2D materials has not been confined to graphene—both phases of 2D MoS_2 have been functionalised, with the majority of studies concentrating on

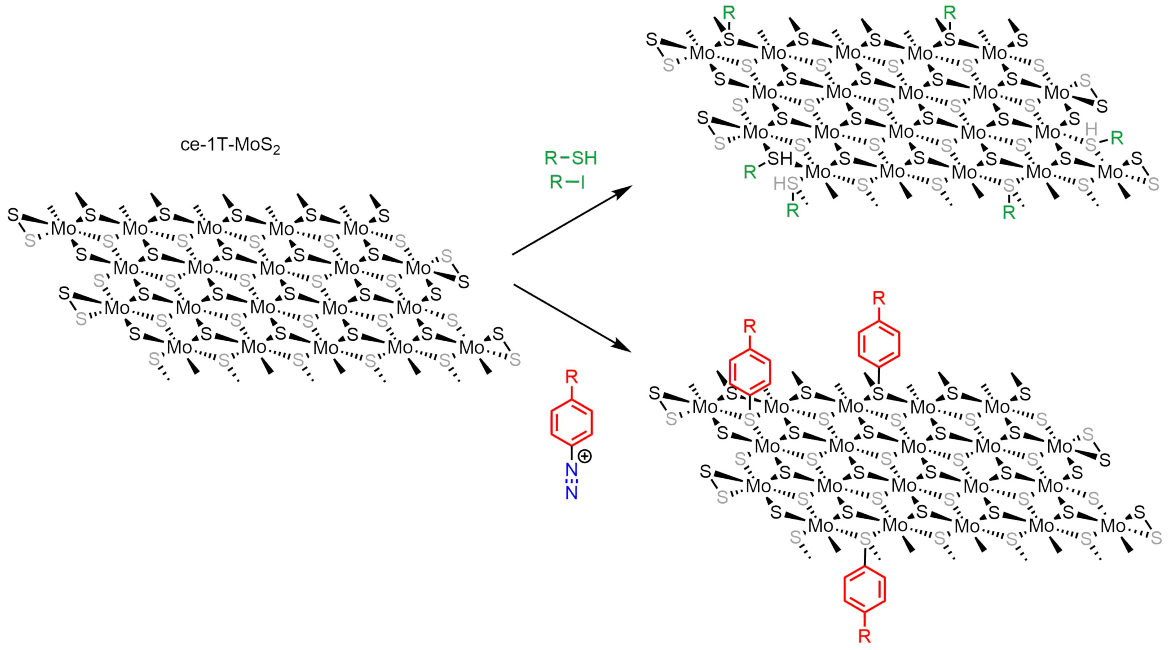

Fig. 1.6 Summary of the two main methods of covalent functionalisation of ce-1T-MoS_2.

ce-1T-MoS_2 due to its increased reactivity. Unlike graphene's accessible π-cloud, the basal plane atoms of MoS_2 are saturated and therefore inert, and it requires chemical exfoliation or the presence of sulfur vacancies or defects to activate 2H-MoS_2.[133, 44, 20] The chemical exfoliation of MoS_2 pioneered by Morrison *et al*[43]—using n-BuLi in hexane to generate lithium-intercalated MoS_2 which is then exfoliated by sonication in water, described above—generates negatively charged, metastable nanosheets that possess areas of 1T phase MoS_2 as well as thermodynamically stable 2H-MoS_2. This excess of negative charge brought about by the intercalation of lithium ions into the crystal lattice of MoS_2 in what is known as a topotactic reaction—intercalation of Li causes a change in the structure of MoS_2 while retaining some of the orientational properties of the original crystal structure.[134] This leads to similar methods of functionalisation to that shown to work on graphenide, the negatively charged graphene used by Hirsch's group (Figure 1.6). Indeed, diazonium salts and alkyl iodides have been reported by Knirsch *et al*[135] and Chhowalla's group[136] respectively to functionalise chemically exfoliated MoS_2. This is accomplished by the nucleophilic attack of

the nanosheets on the substrates, and with diazonium and alkyl functionalisation proceeding *via* homolytic cleavage and radical attack on MoS_2. In this way, 4-methoxybenzene, 4-bromobenzene, acetimide and methane functionalised MoS_2 were prepared successfully, as shown by XPS, changes in zeta potential, FT-IR and TGA-MS.

Lithium intercalated MoS_2, the unexfoliated intercalation compound of bulk MoS_2 and n-BuLi, upon sonication in the presence of mercaptopropionic acid, cysteine or thioglycerol also produced functionalised MoS_2, again highlighting the reactivity of this form of MoS_2. The functional groups present on these substrates could then be further modified—in this report, three further modifications were introduced: Ag nanoparticles were bound to MoS_2 *via* the reaction of $AgNO_3$ and $NaBH_4$ with the acid group of mercaptopropionic acid and polymerisation reactions were carried out on both thioglycerol and mercaptopropionic acid functionalised MoS_2.[137] It was also demonstrated that concomitant functionalisation and exfoliation of lithium intercalated MoS_2 in this way leads to a change in phase of MoS_2 from 1T to the thermodynamically stable 2H phase.[138] These reports were among the first to covalently functionalise MoS_2 with organic groups, highlighting the considerable contribution to functionalisation attributed to the chemical exfoliation of MoS_2.

The routes to functionalisation become more limited when liquid exfoliated 2H-MoS_2 is employed, as the nucleophilic reactivity that dominates the chemistry of ce-1T-MoS_2 is noticeably absent. Non-covalent methods are similar to those used for ce-1T-MoS_2—treatment with auric acid to form gold nanoparticles on the surface, using metal acetates to coordinate to Mo centres,[139] and the use of dithiolane and a carboxylic acid to obtain carboxylic acid-functionalised MoS_2. For several years, the most promising method of 2H-MoS_2 functionalisation was the use of thiols to bind to S vacancies. This was explored in detail, under different conditions, with treatment of 2H-MoS_2 with thiols resulting in the coordination of thiols to S vacancies (particularly at the edges),[140, 141] the conversion of thiols to disulfides or hydrodisulfides,[142] or defect healing[143, 144] according to several

conflicting reports. The mechanism by which thiol functionalisation could occur has also been the subject of debate. Homolytic cleavage of the S-H bond, producing free radicals that then attack MoS_2 has been proposed, but radicals have not been detected in the studies using 2H-MoS_2. Deprotonation of the thiol and coordination of the charged sulfur atom to a S vacancy is more likely. In these cases, the lost hydrogen atom or proton is adsorbed on MoS_2. From here, it reacts with the alkyl group of the thiol, leaving the sulfur atom to fill the S vacancy, or it reacts with another adsorbed hydrogen to be released as a molecule of hydrogen, as MoS_is a well-known HER catalyst.[78, 145, 146] A DFT study by Förster *et al*[147] illustrated these different mechanisms and calculated activation energies and energy losses for each route.

1.8 Graphene in Biology and its Attempted Biomediation

The many types of functionalised graphene generally have slightly different properties to pristine graphene—the presence of functional groups, especially bulky groups prevent reaggregation and can also interact favourably with more solvents, most notably water. Of the many applications that have been proposed for graphene and related carbon nanomaterials, its use in medicine, as a biosensor[148, 149] or drug delivery agent or support[150, 151] is an area in which copious testing and trialling of various factors must be conducted before a product can reach a patient due to the sensitivity of cells to foreign substances. The appeal of graphene stems from its small size, large surface area and its ability to interact with cells and tissue.[152] For example, the interaction of antigens with adsorbed biomolecules on graphene can change the resistivity of biomolecule-laden graphene, which when measured this gives an incredibly sensitive quantitative measurement.[148] GO, being a highly oxidised form of graphene, and its reduced form, rGO, are used in particular as hydrophilic supports for biosensors as well as nanoparticles. The oxidised and disordered surfaces facilitate further

functionalisation with linkers and substrate specific molecules, while the chemical stability of the support can protect adsorbed sensors[153, 149]. However, this raises concerns over the increased environmental impact of such materials. The literature regarding this is ongoing and conflicted.[154, 155]

As the most widely studied graphene derivative in the field of biomedicine,[156] the toxicity of GO has been comprehensively studied. Several cell lines have been tested with varying concentrations of GO and compared with graphene, rGO or CNTs and demonstrated that in general, GO is more cytotoxic, *i.e.*, induces apoptosis or necrosis more than other materials. The mechanisms for GO cytotoxicity were inferred to be the induction of oxidative stress, as a result of the free radicals and oxygen groups present on GO[157] and interference with the cell membrane or cell membrane potential by adsorbing on the cell membrane.[158] The latter was also implicated in the bactericidal behaviour of GO,[159] though the efficacy of GO as an antibacterial agent is still in question. The use of Ag nanoparticles on GO has been reported to act as a more effective antibacterial than Ag nanoparticles alone.[160] The cytotoxicity of rGO and graphene is less clear, and conflicting reports have rGO and graphene showing increased toxicity compared to GO and *vice versa*. rGO has been found to be less cytotoxic than CNTs, but display size-dependent toxicity in that smaller rGO platelets were more toxic, and all induced some amount of oxidative stress. Smaller nanoplatelets that could be taken up by cells (<100 nm) could also induce some genotoxicity.[161–163] Studies on the toxicity of graphene have shown both higher and lower cytotoxicity than CNTs but like its oxidative derivatives, an increase in reactive oxygen species (ROS) and a change in the cell membrane potential point to the mechanisms of graphene interference in cells resembling that of GO and rGO.[164, 165] Because of this potential biotoxicity, especially in the cases of bactericidal agents and functionalised graphene not intended for medical use, methods of waste control and bioremediation for graphene, intentionally or accidentally exposed to the environment, is required.

Degradation of graphene has previously been attempted in the preparation of graphite oxide,[58] but this only provides highly functionalised graphene that still presents toxicity and environmental problems. There have been conflicting reports about the ability of H_2O_2 to degrade graphene—the most successful reports a large excess of constantly replenished oxidant left over 72 h on CVD graphene,[166] whereas others show little to no effect at physiological concentrations on other types of graphene, such as few-layer and epitaxial graphene.[167] Previous reports on the efficacy of high valent Fe species on graphene are described in the discussion on Fenton's reagent—the use of Fenton's reagent on defective graphene and GO has been explored, but reports on the degradation of graphite or graphene by Fe- or other metal-containing complexes or enzymes are scarce.[168, 169]

Reports into the degradation of graphene/graphite and production of GO by a K_2FeO_4, referred to as potassium ferrate(VI), as a replacement for $KMnO_4$ were reported by Chen *et al*[170] and Peng *et al*,[171] with another paper by Hu *et al*[172] using a mixture of $KMnO_4$ and K_2FeO_4. All three papers claim an improved yield of GO with a focus on less toxic by-products from the use of the Fe-based oxidant instead of that based on Mn. This new method was subsequently called into question by Sofer *et al*,[173] citing that the instability of the ferrate ion in acidic media meant it would not survive long enough to oxidise graphite. They also tested this production of GO in neutral and alkaline media, using synthesised and commercial K_2FeO_4 for comparison, all of which yielded graphite with a negligible amount of oxygen groups present by a variety of spectroscopic techniques. Aside from this, a report by Yang and He demonstrated the ability of ferric perchlorate to catalytically functionalise graphene by activating a series of substituted benzonitriles, which then attacked and functionalised the graphene surface, but did not report the ferric salt reacting with the graphene itself.[174]

Metalloenzymes have also been employed in towards the bioremediation of graphene. The attempted oxidation of GO and rGO by horse radish peroxide (HRP), a heme-containing

metalloenzyme, was reported by Star *et al*.[175] GO oxidation was successful, resulting in large holes in its basal plane seen by TEM and supported by Raman spectroscopy. However, the enzyme seemed to have no effect on its reduced counterpart, which is more similar to that of pristine graphene. Another heme-containing enzyme, lignin peroxidase, has also been reported for GO and rGO nanoribbons (thin flakes of graphene prepared by the longitudinal unzipping of multi-walled carbon nanotubes and subsequent reduction, respectively). Treatment with lignin peroxide in the presence of H_2O_2 and veratyl alcohol (a cofactor of the enzyme) fully degraded GO nanoribbons but only partially degraded rGO nanoribbons, again highlighting the difficulty of degrading unfunctionalised graphene.[176] The use of non-heme enzymes or biomimetics has not yet been attempted on pristine graphene, and hence will be explored in this thesis through the use of Rieske dioxygenase mimics discussed below. Use of the Fenton's reagent on graphene will also be explored in more detail.

1.9 Fenton Chemistry

To understand the exploration of Fenton's reagent as an oxidant that may degrade graphene, an explanation of its nature and reactivity is needed. Fenton's reagent, a particularly potent Fe-based oxidant, was discovered in the 1890s,[177] and exploited since the 1960s as an industrial oxidising agent—typically it is used to remove potentially harmful organic compounds from industrial waste water, particularly polychlorophenyls, dyes, and pesticides.[178] Consisting only of an Fe^{II} salt and H_2O_2, it is cheap and effective. It is widely accepted that Fenton chemistry involves the catalytic disproportion of H_2O_2 to oxygen and water *via* highly active hydroxyl radicals, which attack and completely degrade normally persistent organic molecules, particularly aromatic molecules such as dyes, over several hours. The accepted mechanism, known as the Haber-Weiss cycle, is outlined below. (1.7) shows the reduction

of H_2O_2 to the hydroxyl radical and hydroxide, (1.8) oxidation of Fe^{II} to Fe^{III}, (1.9) attack of the hydroxyl radical on the organic substrate (R) and (1.10) reduction of Fe^{III} *via* the organic radical ($R^{\cdot}$). There are many additional reactions to the four outlined, including the possibility of reduction of the organic radical by Fe^{II} and subsequent dimerisation of the charged organic fragments. These processes can also compete and hamper yields, for example, (1.9) competes with (1.10).

$$Fe^{2+} + H_2O_2 \longrightarrow Fe^{3+} + OH^- + OH^{\bullet} \tag{1.7}$$

$$OH^{\bullet} + Fe^{2+} \longrightarrow OH^- + Fe^{3+} \tag{1.8}$$

$$RH + OH^{\bullet} \longrightarrow H_2O + R^{\bullet} \tag{1.9}$$

$$R^{\bullet} + Fe^{3+} \longrightarrow R^+ + Fe^{2+} \tag{1.10}$$

The Fenton reaction has been studied for decades and optimum conditions have been established—a pH of 3 has been shown to optimise the reaction by providing protons for the disproportionation of H_2O_2 into water and to aid the addition of hydroxyl radicals to aromatic and alkyl substrates. The correct ratio of [Fe^{II}] to [H_2O_2] also limits the effect of competing processes. Yoon[179] has published a detailed discussion of the effects of an excess of [Fe^{II}], equivalent [Fe^{II}]/[H_2O_2], and excess of [H_2O_2], but only the latter, which are the optimum concentrations for oxidation, will be discussed here. In this system, the decomposition of the radicals can occur *via* the oxidation of organics, limiting non-productive decomposition *via* the Fe^{III} system. The organic substrates also compete with the decomposition of H_2O_2 by the hydroxyl radical.

However, debates have started again over the exact method of oxidation—some research groups believe that instead of acting only as a catalyst for the production of radicals, H_2O_2

interacts with the Fe^{II} salt to produce the Fe^{IV} species as the active oxidant.[180, 178] Evidence for this is seen when conducting the Fenton reaction at higher pH, *i.e.* pH 7 or above.[178] The Fe^{IV} and hydroxyl radical mechanisms both involve the subsequent generation of highly reactive organic radicals, which lead to further degradation of organic materials, ultimately to carbon dioxide, water and inorganic salts.[181]

As well as its use in waste water treatment, Fenton chemistry is also important in biology; H_2O_2 is a side product of many enzymatic processes, particularly oxidising metalloenzymes.[182] Modified Fenton processes occur in some species of brown rot fungi in soil that degrade lignin and other woody debris.[183] Should graphene end up in the soil, studying the effect of the Fenton reagent on it and other carbon nanomaterials will shed light on how these fungi could deal with environmental CNMs. Use of Fenton's reagent enables the generation of free, high valent Fe^{IV} species in the presence of graphene, and will establish a standard against which the biomimetic catalysts discussed below can be compared. If degradation is seen in these studies, it can give insight into the interaction of free Fe^{II} or metalloenzymes in the presence of O_2/H_2O_2 with graphene in fungal or bacterial cells. Fenton's reagent has already been reported to be very effective in degrading aromatic species (phenol, 4-chlorophenol,2-chloroaniline and hydroquinone) within a matter of hours, in contrast to its inability to degrade alkyl cyclic substrates (cyclohexanol and cyclohexanone) as studied by Ruppert and Bauer *et al*.[184]

As yet, a comprehensive study into the reactivity and possible degradation of pristine graphene by Fenton's reagent is lacking. A review of the literature affords one such study, detailing the degradation of ^{14}C enriched few-layer graphene by Fenton's reagent, using large excesses of the iron salt and H_2O_2.[185] However, all of these reported degradations have relied on long reaction times of up to 6 days, and excessive amounts of Fenton's reagent, which are not ideal conditions for the industrial treatment of waste or waste water, nor are they biologically relevant concentrations. Aside from degradation of the graphene structure,

it is also important to study the interaction of graphene with Fenton's reagent to understand how this might change the structure of graphene to a more hydrophilic and bioavailable form, if Fenton's reagent cannot degrade the structure entirely. Fenton chemistry has already been shown to photocatalytically degrade GO recently, in a paper by Zhang *et al*,[168] which was then expanded on by Star *et al*.[186] GO has also been seen to take a sacrificial role in Fenton catalysis when used as a support for iron oxide nanoparticles, by donating electrons to the Fe sites to regenerate Fe^{II}, while some GO C=C regions are oxidised.[169]

1.10 Rieske Dioxygenases and Biomimetic Investigation of Their Catalytic Properties

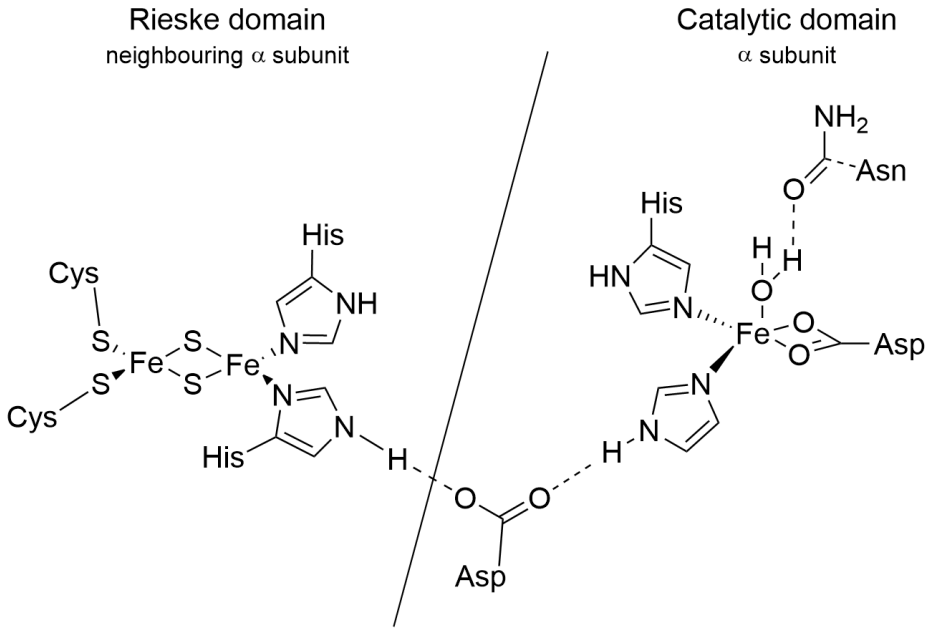

Fig. 1.7 The active site of naphthalene dioxygenase, showing the 2-His-1-carboxylate facial triad common to many Fe^{II}-containing metalloenzymes. Based on the diagram from Bassan *et al*.[187]

Should graphene find its way into the environment, the most likely class of organisms that will degrade it would be soil bacteria, particularly those species already able to degrade

aromatic organic matter from detritus. As graphene has been shown to partake in many reactions based on organic aromatic chemistry as mentioned above, it is possible that agents that degrade aromatic compounds could also degrade graphene.

Pseudomonas sp possess a class of metalloenzyme known as Rieske dioxygenases. These metalloenzymes, despite not containing heme, operate in a similar manner to that of heme-containing enzymes such as cytochrome P450 in that they activate O_2 or H_2O_2 to generate high valent Fe species that can perform C-H activation or oxygen insertion into substrates.[188] These contain an iron centre bonded to histidine and aspartate moieties, with a labile water ligand and a so-called Rieske iron-sulphur [2Fe-2S] cluster nearby. The active site is arranged as in Figure 1.7. The enzyme family itself is very diverse, with only the presence of the [2Fe-2S] cluster, ligated by two histidines and two cysteines with sulfide bridges, and the mononuclear Fe^{II} centre being preserved throughout the family.[189] The cofactors and redox switch change between different branches of the family. There is even variation in the placing of these parts of the active site within the enzyme, with the cluster being found in the ferredoxin component of the enzyme in biphenyl dioxygenase in *Pseudomonas sp* and found in the reductase component in naphthalene dioxygenase of related *Camomonas sp*.[190]

These enzymes incorporate oxygen atoms into substrates either *via* O_2 or H_2O_2, therefore destroying the aromaticity and kick-starting the degradation of substrates such as naphthalene. The accepted mechanism is that 2 electrons are donated from a pyridine nucleotide to the flavin cofactor in the enzyme. These electrons are then singly transferred to the [2Fe-2S] cluster, then the mononuclear Fe^{II} site, and both electrons are used in the oxygenation of one molecule of the substrate. The electrons are passed to the active site and are used to activate molecular O_2 or ambient H_2O_2. This forms either a side-on bound peroxide or a hydroperoxide. Experimental evidence points towards this being a hydroperoxide, suggesting that a proton could be taken up from water, which occupies the fifth coordination site of the resting active site.[191] This can then undergo O-O bond cleavage or radical reaction, forming

the postulate active oxidant, O=Fe^{V}-OH. A nearby substrate, for example, naphthalene, is then oxidised *via* one of the two postulated mechanisms (Figure 1.8).[192]

Oxygenases are well studied and have been researched for applications in bioremediation of industrial pollutants.[190] However, the care and limited conditions enzymes can stand precludes their use in industrial waste management. An alternative to using enzymes is the development of inorganic complexes that mimic enzymatic activity: biomimetic catalysts. The biomimetic catalysts used in this study were first synthesised and used as alkene/arene oxidants by Que *et al*[193, 194] in the late 1990s and throughout the 2000s but the ligands tris(2-pyridylmethyl)amine (TPA) and *N,N*'-dimethyl-*N,N*'-bis-(2-pyridylmethyl)-1,2-diaminoethane (BPMEN) were originally synthesised much earlier by Anderegg and Toflund *et al*.[195, 196] Que and his group studied the ability of the complexes to mimic the Rieske dioxygenases by *cis*-dihydroxylating alkenes and arenes. The structure of both complexes are shown in Figure 1.8.

As with the mononuclear active sites of the Rieske dioxygenases, the complexes possess neutral amine donors to the metal, and two labile solvent sites. With the addition of H_2O (the labile H_2O ligand required for enzymatic action) and the oxidant, H_2O_2, both complexes

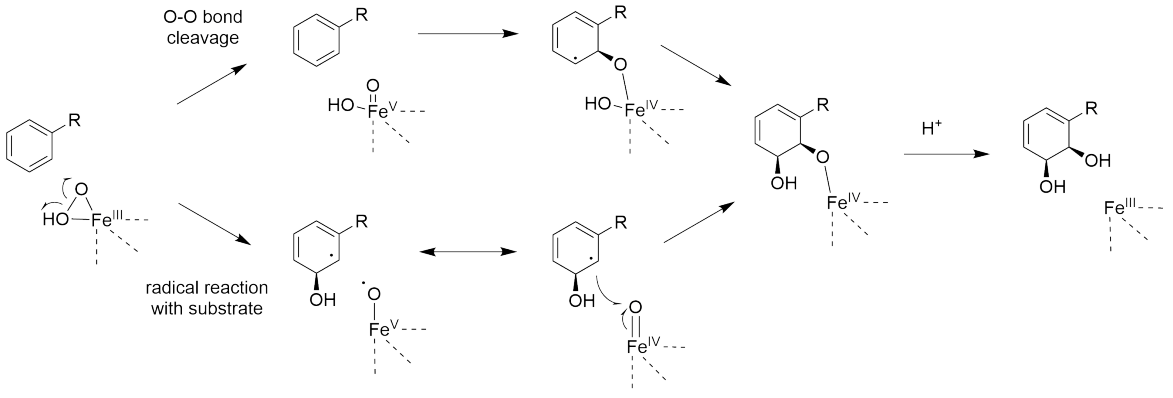

Fig. 1.8 The postulated mechanisms for cis-dihydroxylation of arenes by Rieske enzymes. Based on the mechanism proposed by Ramaswamy *et al*.[189]

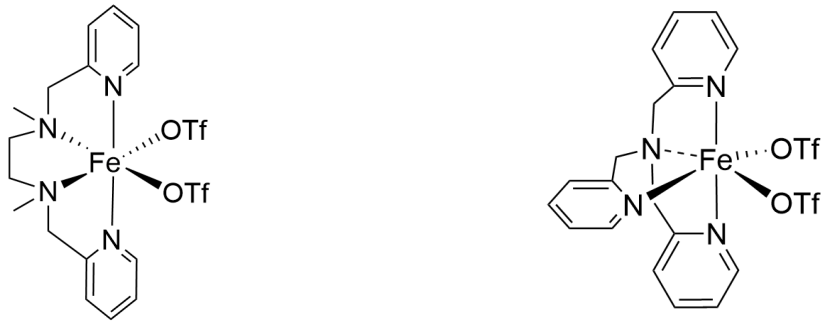

Fig. 1.9 The complexes investigated in this study: (a) $[Fe^{II}(BPMEN)(OTf)_2]$ (b) and $[Fe^{II}(TPA)(OTf)_2]$.

were reported to form a high-valent Fe^{V} species that could cis-dihydroxylate alkene and arene bonds, as evidenced by isotopic studies using $H_2{}^{18}O_2$.[193]

Over more than a decade of studies, Que's group in particular showed that the catalysts, $[Fe^{II}(BPMEN)(ClO_4)_2]$ and $[Fe^{II}(TPA)(ClO_4)_2]$, in the presence of H_2O and H_2O_2, could successfully hydroxylate alkenes such as cyclohexane and 1,2-dimethylcyclohexane,[193] either epoxidise or *cis*-dihydroxylate cyclooctene,[197] and *cis*-hydroxylate *ortho*- or *para*-substituted benzoic acids to their respective salicylates, or with decarboxylation, to phenolates.[198] The $[Fe^{II}(BPMEN)(ClO_4)_2]$ complex shows greater selectivity towards *cis*-diol products, which is more typical of the behaviour of Rieske dioxygenases, whereas the $[Fe^{II}(TPA)(ClO_4)_2]$ complex tends to give almost equal amounts of the epoxide product as well.[197] The reactive intermediate thought to be responsible for oxidation in these experiments is the $O{=}Fe^{V}$-OH species generated from the heterolytic cleavage of the O-O bond in the Fe^{III}-OOH intermediate seen in Rieske dioxygenases, though this is still under debate.[199, 200] Homolytic cleavage of the O-O bond can also oxidise substrates *via* a radical pathway.[201]

Further studies by other groups have shown that these complexes form reactive intermediates not only with H_2O_2 and acetic acid, but also peracetic acid, *tert*-butyl hydroperoxide,

meta-chloroperbenzoic acid, and iodosobenzene.[202] The reactivity of these potential oxidants will be touched upon in this thesis but could also be tested with the biomimetic catalysts for reactivity towards carbon nanomaterials in future work.

1.11 Research Aims and Scope of Thesis

Graphene and MoS_2 have proven to be useful materials for a hydrogen-fuelled, nano-driven future. To this end, this thesis contributes to the areas of graphene and MoS_2 chemistry, their reactivity and also their application as HER catalysts. A techniques chapter will detail the preparation of each of the three nanomaterials used in this thesis, and the analytical techniques used to characterise and compare them.

The first project described here will focus on the reactivity of graphene, detailing the efforts to degrade it using first simple laboratory oxidants and oxygen donating agents, secondly through the use of Fenton's reagent, and finally by reacting with two biomimetic complexes described previously. The ultimate destination of some if not all commercially produced graphene will be the environment, and how this can be broken down by soil bacteria and water treatment plants is important to know, as single-layer or functionalised graphene has very different properties to that of graphite. Therefore, this project will provide insight into the potential pathways of bioremediation of waste graphene.

Next, the formation of van der Waals heterostructures of graphene and 2H- or 1T-phase MoS_2 will be attempted with a view to analysing the chemical interaction of these materials during heterostructure formation. This will be the first comprehensive analysis of the interaction of MoS_2 and graphene from a purely chemical point of view. The catalytic activity towards HER of both 2H-MoS_2/graphene and ce-1T-MoS_2/graphene will also be tested and compared to the 2H- or ce-1T-MoS_2 alone.

The final project will detail the formation of a heterostructure of 1T-MoS_2 and graphene joined together covalently by the coupling of functionalised graphene and functionalised MoS_2. The functionalisation and subsequent conversion of functional groups has not been widely reported on graphene or MoS_2, and particular care will be afforded to the full characterisation of these materials and the spectroscopic handles used for identifying functional groups and the alterations they cause to the properties of graphene and MoS_2. Preliminary studies into the HER activity of these covalently linked heterostructures will also be discussed.

References

[1] K. S. Novoselov, A. K. Geim, S. V. Morozov, D. Jiang, Y. Zhang, S. V. Dubonos, I. V. Grigorieva and A. A. Firsov, *Science*, 2004, **306**, 666–669.

[2] V. Singh, D. Joung, L. Zhai, S. Das, K. S. I. and S. S., *Progress in Materials Science*, 2001, **56**, 1178–1271.

[3] A. K. Geim and S. Novoselov, *Nature Materials*, 2007, **6**, 183–191.

[4] R. Mas-Balleste, C. Gomez-Navarro, J. Gomez-Herrero and F. Zamora, *Nanoscale*, 2011, **3**, 20–30.

[5] K. S. Novoselov, V. I. Falko, L. Colombo, P. R. Gellert, M. G. Schwab and K. Kim, *Nature*, 2012, **490**, 192–200.

[6] V. C. Sanchez, A. Jachak, R. H. Hurt and A. B. Kane, *Chemical Research in Toxicology*, 2012, **25**, 15–34.

[7] M. Cole, P. Lindeque, C. Halsband and T. S. Galloway, *Marine Pollution Bulletin*, 2011, **62**, 2588–2597.

[8] S. Ziajahromi, P. A. Neale and F. D. L. Leusch, *Water Science and Technology*, 2016, **74**, 2253.

[9] G. W. Crabtree, M. S. Dresselhaus and M. V. Buchanan, *Physics Today*, 2004, **57**, 39–44.

[10] F. Wang, T. A. Shifa, X. Zhan, Y. Huang, K. Liu, Z. Cheng, C. Jiang and J. He, *Nanoscale*, 2015, **7**, 19764–19788.

[11] J. K. Nørskov, T. Bligaard, A. Logadottir, J. R. Kitchin, J. G. Chen, S. Pandelov and U. Stimming, *Journal of the Electrochemical Society*, 2005, **152**, 23–26.

[12] M. A. Lukowski, A. S. Daniel, F. Meng, A. Forticaux, L. Li and S. Jin, *Journal of the American Chemical Society*, 2013, **135**, 10274–10277.

[13] Y. Li, H. Wang, L. Xie, Y. Liang, G. Hong and H. Dai, *Journal of the American Chemical Society*, 2011, **133**, 7296–7299.

[14] S. Z. Butler, S. M. Hollen, L. Cao, Y. Cui, J. A. Gupta, H. R. Gutiérrez, T. F. Heinz, S. S. Hong, J. Huang, A. F. Ismach, E. Johnston-Halperin, M. Kuno, V. V. Plashnitsa, R. D. Robinson, R. S. Ruoff, S. Salahuddin, J. Shan, L. Shi, M. G. Spencer, M. Terrones, W. Windl and J. E. Goldberger, *ACS Nano*, 2013, **7**, 2898–2926.

[15] Y. Chen, B. Song, X. Tang, L. Lu and J. Xue, *Small*, 2014, **10**, 1536–1543.

[16] X. Du, M. Xiao, Y. Meng and A. Hay, *Carbon*, 2005, **43**, 195–197.

[17] V. Georgakilas, A. B. Otyepka, M.and Bourlinos, V. Chandra, N. Kim, K. C. Kemp, P. Hobza, R. Zboril and K. S. Kim, *Chemical Reviews*, 2012, **112**, 6156–6214.

[18] G. Abellán, M. Schirowski, K. F. Edelthalhammer, M. Fickert, K. Werbach, H. Peterlik, F. Hauke and A. Hirsch, *Journal of the American Chemical Society*, 2017, **139**, 5175–5182.

[19] E. Siegfried, E.-H. Michael, G. Stefan, H. Philipp, K. Wolfgang, G. Andreas, D. Christoph, R. Michael, X. Jie, P. Christian, L. Ole, S. Hans-Peter, M. Paul and H. Andreas, *Advanced Materials*, 2013, **25**, 3583–3587.

[20] X. Chen and A. R. McDonald, *Advanced Materials*, 2016, **28**, 5738–5746.

[21] K. Pramoda, U. Gupta, I. Ahmad, R. Kumara and C. N. R. Rao, *Journal of Materials Chemistry A*, 2016, **4**, 8989–8994.

[22] B. K. Barman, D. Dasa and K. K. Nanda, *Journal of Materials Chemistry A,*, 2017, **5**, 18081–18087.

[23] J. E. Mates, I. S. Bayer, M. Salerno, P. J. Carrol, Z. Jiang, L. Liu and C. L. Megaridis, *Carbon*, 2015, **87**, 163–174.

[24] F. Torrisi, T. Hasan, W. Wu, Z. Sun, A. Lombardo, T. S. Kulmala, G. S. Hsieh, S. Jung, B. F., P. Paul, D. Chu and A. C. Ferrari, *ACS Nano*, 2012, **6**, 2992–3006.

[25] I. Lahiri, V. P. Verma and W. Choi, *Carbon*, 2011, **49**, 1614–1619.

[26] L. G. De Arco, Y. Zhang, C. W. Schlenker, K. Ryu, M. E. Thompson and C. Zhou, *ACS Nano*, 2010, **4**, 2865–2873.

[27] L. F. Dumee, L. He, Z. Wang, P. Sheath, J. Xiong, C. Feng, M. Y. Tan, F. She, M. Duke, S. Gray, A. Pacheco, P. Hodgson, M. Majumder and L. Kong, *Carbon*, 2015, **87**, 395–408.

[28] R. Sharma, J. H. Baik, C. J. Perera and M. S. Strano, *Nano Letters*, 2010, **10**, 398–405.

[29] E. Clar, in *The Aromatic Sextet and its Significance in Relation to the Stability of Aromatic Systems*, Springer Berlin Heidelberg, Berlin, Heidelberg, 1964, pp. 32–39.

[30] O. V. Yazyev, R. B. Capaz and S. G. Louie, *Journal of Physics: Conference Series*, 2011, **302**, 012016.

[31] K. Nakada, M. Fujita, G. Dresselhaus and M. S. Dresselhaus, *Physical Reviews B*, 1996, **54**, 17954–17961.

[32] K. He, G.-D. Lee, A. W. Robertson, E. Yoon and J. H. Warner, *Nature Communications*, 2014, **5**, 3040.

References

[33] A. Bellunato, H. Arjmandi Tash, Y. Cesa and G. F. Schneider, *ChemPhysChem*, 2016, **17**, 785–801.

[34] N. Alem, R. Erni, C. Kisielowski, M. D. Rossell, W. Gannett and A. Zettl, *Physical Reviews B*, 2009, **80**, 155425.

[35] L. Li, Y. Yu, G. J., Q. Ye, X. Ge, H. Ou, D. Wu, X. Feng, H. Chen and Y. Zhang, *Nature Nanotech.*, 2014, **9**, 372–377.

[36] F. Reis, G. Li, L. Dudy, M. Bauernfeind, S. Glass, W. Hanke, R. Thomale, J. Schäfer and R. Claessen, *Science*, 2017, **357**, 287–290.

[37] K. S. Novoselov, D. Jiang, F. Schedin, T. J. Booth, V. V. Khotkevich, S. V. Morozov and A. K. Geim, *Proceedings of the National Academy of Sciences of the United States of America*, 2005, **102**, 10451—10453.

[38] W. Choi, N. Choudhary, G. H. Han, J. Park, D. Akinwande and Y. H. Lee, *Materials Today*, 2017, **20**, 116–130.

[39] D. Wang, W. Yan and G. G. Botte, *Electrochemical Communications*, 2011, **13**, 1135–1138.

[40] N. Michael, K. Murat, P. Volker, L. Jun, N. Junjie, H. Min, H. Lars, G. Yury and B. M. W., *Advanced Materials*, 2011, **23**, 4248–4253.

[41] M. Chhowalla, H. S. Shin, G. Eda, L.-J. Li, K. P. Loh and H. Zhang, *Nature Chemistry*, 2013, **5**, 263–275.

[42] G. Eda, H. Yamaguchi, D. Voiry, T. Fujita, M. Chen and M. Chhowalla, *Nano Letters*, 2011, **11**, 5111–5116.

[43] P. Joensen, R. Frindt and S. Morrison, *Materials Research Bulletin*, 1986, **21**, 457–461.

[44] S. Presolski and M. Pumera, *Materials Today*, 2016, **19**, 140–145.

[45] Q. Tang and D.-e. Jiang, *Chemistry of Materials*, 2015, **27**, 3743–3748.

[46] T. Moldt, A. Eckmann, P. Klar, S. V. Morozov, A. A. Zhukov, K. S. Novoselov and C. Casiraghi, *ACS Nano*, 2011, **5**, 7700–7706.

[47] K. Paton, E. Varrla, C. Backes, V. Nicolosi, J. N. Coleman and et al, *Nature Materials*, 2014, **13**, 624–630.

[48] U. Khan, A. O'Neill, H. Porwal, P. May, K. Nawaz and J. N. Coleman, *Carbon*, 2012, **50**, 470–475.

[49] S. Stankovich, D. A. Dikin, R. D. Piner, K. A. Kohlhaas, A. Kleinhammes, J. Y., Y. Wu, S. T. Nguyen and R. S. Ruoff, *Carbon*, 2007, **45**, 1558–1565.

[50] D. R. Cooper, B. D'Anjou, N. Ghattamaneni, B. Harrick, M. Hilke, A. Horth, N. Majlis, M. Massicotte, L. Vandsburger, E. Whiteway and V. Yu, *ISRN Condensed Matter Physics*, 2012, **2012**, 56–62.

[51] J. Yu, J. Li, W. Zhang and H. Chang, *Chemical Science*, 2015, **6**, 6705–6716.

[52] M. Yi and Z. Shen, *Journal of Materials Chemistry A*, 2015, **3**, 11700–11715.

[53] Y. R. Lim, Y. B. Lee, S. K. Kim, S. J. Kim, Y. Kim, C. Jeon, W. Song, S. Myung, S. S. Lee, K.-S. An and J. Lim, *Applied Surface Science*, 2017, **392**, 557–561.

[54] V. Nicolosi, M. Chhowalla, M. G. Kanatzidis, M. S. Strano and J. N. Coleman, *Science*, 2013, **340**, 1420–1438.

[55] K. P. Lee, N. C. Chromey, R. J. Culik, R. Barnes and P. W. Schneider, *Toxicol. Sci.*, 1987, **9**, 222–235.

[56] J. N. Coleman, M. Lotya, A. O'Neill, S. D. Bergin, P. J. King, U. Khan, K. Young, A. Gaucher, S. De, R. J. Smith, I. V. Shvets, S. K. Arora, G. Stanton, H.-Y. Kim, K. Lee, G. T. Kim, G. S. Duesberg, T. Hallam, J. J. Boland, J. J. Wang, J. F. Donegan, J. C. Grunlan, G. Moriarty, A. Shmeliov, R. J. Nicholls, J. M. Perkins, E. M. Grieveson, K. Theuwissen, D. W. McComb, P. D. Nellist and V. Nicolosi, *Science*, 2011, **331**, 568–571.

[57] M. Buzaglo, I. P. Bar, M. Varenik, L. Shunak, S. Pevzner and O. Regev, *Advanced Materials*, 2017, **29**, 1603528.

[58] W. S. J. Hummers and R. E. Offeman, *Journal of the American Chemical Society.*, 1958, **80**, 1339.

[59] D. R. Dreyer, S. Park, C. Bielawski and R. S. Ruoff, *Chemical Society Reviews*, 2010, **39**, 228–240.

[60] J. M. Englert, C. Dotzer, G. Yang, M. Schmid, C. Papp, J. M. Gottfried, H.-P. Steinrück, E. Spiecker, F. Hauke and A. Hirsch, *Nature Chemistry*, 2011, **3**, 279–286.

[61] S. Majee, M. S. Shi-Li and Z. Z.-B. Zhang, *Carbon*, 2016, **102**, 51–57.

[62] S. Bae, H. Kim, Y. Lee, X. Xu, J.-S. Park, Y. Zheng, J. Balakrishnan, T. Lei, H. R. Kim, Y. I. Song, Y.-J. Kim, K. S. Kim, B. Özyilmaz, J.-H. Ahn, B. H. Hong and S. Iijima, *Nature Nanotechnology*, 2010, **5**, 574–578.

[63] T.-H. Han, Y. Lee, M.-R. Choi, S.-H. Woo, S.-H. Bae, B. H. Hong, J.-H. Ahn and T.-W. Lee, *Nature Photonics*, 2012, **6**, 105–110.

[64] M. Farrokhi, K. Dindarloo and H. A. Jamali, *Research Journal of Environmental Toxicity*, 2015, **9**, 274–289.

References

[65] M. E. Garah, S. Bertolazzi, S. Ippolito, M. Eredia, I. Janica, G. Melinte, O. Ersen, G. Marletta, A. Ciesielski and P. Samorì, *FlatChem*, 2018, **9**, 33–39.

[66] X. Fan, P. Xu, D. Zhou, Y. Sun, Y. C. Li, M. A. T. Nguyen, M. Terrones and T. E. Mallouk, *Nano Letters*, 2015, **15**, 5956–5960.

[67] E. Benavente, M. A. S. Ana, F. Mendizábal and G. González, *Coordination Chemistry Reviews*, 2002, **224**, 87–109.

[68] A. Jawaid, D. Nepal, K. Park, M. Jespersen, A. Qualley, P. Mirau, L. F. Drummy and R. A. Vaia, *Chemistry of Materials*, 2016, **28**, 337–348.

[69] S. Muralikrishna, K. Manjunath, D. Samrat, V. Reddy, T. Ramakrishnappa and D. H. Nagarajud, *RSC Advances*, 2015, **5**, 89389–89396.

[70] M. Li, D. Wang, J. Li, Z. Pan, H. Ma, Y. Jiang and Z. Tian, *RSV Advances*, 2016, **6**, 71534–71542.

[71] A. Zobel, A. Boson, P. M. Wilson, D. S. Muratov, D. V. Kuznetsov and A. Sinitskii, *Journal of Materials Chemistry C*, 2016, **4**, 11081–11087.

[72] Y. Xie, Z. Wang, Y. Zhan, P. Zhang, R. Wu, T. Jiang, S. Wu, H. Wang, Y. Zhao, T. Nan and X. Ma, *Nanotechnology*, 2017, **28**, 084001.

[73] D. Zhou, H. Shu, C. Hu, L. Jiang, P. Liang and X. Chen, *Crystal Growth & Design*, 2018, **18**, 1012–1019.

[74] K. Chang and W. Chen, *Chemical Communications*, 2011, **47**, 4252–4254.

[75] K. F. Mak, C. Lee, J. Hone, J. Shan and T. F. Heinz, *Physical Review Letters*, 2010, **105**, 136805.

[76] N. Choudhary, M. R. Islam, N. Kang, L. Tetard, Y. Jung and S. I. Khondaker, *Journal of Physics: Condensed Matter*, 2016, **28**, 364002.

[77] M. S. Fuhrer and J. Hone, *Nature Nanotechnology*, 2013, **8**, 146–147.

[78] T. F. Jaramillo, K. P. Jorgensen, J. Bonde, J. H. Nielsen, S. Horch and I. Chorkendorff, *Science*, 2007, **317**, 100–102.

[79] H. Kato, K. Asakura and A. Kudo, *Journal of the American Chemical Society*, 2003, **125**, 3082–3089.

[80] X. Chia, A. Y. S. Eng, A. Ambrosi, S. M. Tan and M. Pumera, *Chemical Reviews*, 2015, **115**, 11941–11966.

[81] B. Hinnemann, P.-G. Moses, J. Bonde, K. P. Jørgensen, J. H. Nielsen, S. Horch, I. Chorkendorff and J. K. Nørskov, *Journal of the American Chemical Society*, 2005, **127**, 5308–5309.

[82] Z. W. Seh, J. Kibsgaard, C. F. Dickens, I. Chorkendorff, J. K. Nørskov and T. F. Jaramillo, *Science*, 2017, **355**, 6321.

[83] D. Voiry, M. Salehi, R. Silva, T. Fujita, M. Chen, T. Asefa, V. B. Shenoy, G. Eda and M. Chhowalla, *Nano Letters*, 2013, **13**, 6222–6227.

[84] X. Chia, A. Ambrosi, D. Sedmidubský, Z. Sofer and M. Pumera, *Chemistry – A European Journal*, 2014, **20**, 17426–17432.

[85] S. M. Tan, A. Ambrosi, Z. Sofer, Š. Huber, D. Sedmidubský and M. Pumera, *Chemistry – A European Journal*, 2015, **21**, 7170–7178.

[86] X. Xie, Z. Ao, D. Su, J. Zhang and G. Wang, *Advanced Functional Materials*, 2015, **25**, 1393–1403.

[87] K. Chang and W. Chen, *ACS Nano*, 2011, **5**, 4720–4728.

[88] K.-J. Huang, L. Wang, J. Li and Y.-M. Liu, *Sensors and Actuators B: Chemical*, 2013, **178**, 671–677.

[89] J. E. Lee, J. Jung, T. Y. Ko, S. Kim, S.-I. Kim, J. Nah, S. Ryu, K. T. Nam and M. H. Lee, *RSC Advances.*, 2017, **7**, 5480–5487.

[90] X. Wan, K. Chen, Z. Chen, F. Xie, X. Zeng, W. Xie, J. Chen and J. Xu, *Advanced Functional Materials*, 2017, **27**, 1603998–1604005.

[91] X. Xu, Y. Sun, W. Qiao, X. Zhang, X. Chen, X. Song, L. Wu, W. Zhong and Y. Du, *Applied Surface Science*, 2017, **396**, 1520–1527.

[92] L. Zhao, C. Hong, L. Lin, H. Wu, Y. Su, X. Zhang and A. Liu, *Carbon*, 2017, **116**, 223–231.

[93] X. Zheng, J. Xu, K. Yan, H. Wang, Z. Wang and S. Yang, *Chemistry of Materials*, 2014, **26**, 2344–2353.

[94] S. Bertolazzi, D. Krasnozhon and A. Kis, *ACS Nano*, 2013, **7**, 3246–3252.

[95] X. Chen, Y. J. Park, T. Das, H. Jang, J.-B. Leea and J.-H. Ahn, *Nanoscale*, 2016, **8**, 15181–15188.

[96] X. Ling, Y. Lin, Q. Ma, Z. Wang, Y. Song, L. Yu, S. Huang, W. Fang, X. Zhang, A. L. Hsu, Y. Bie, Y.-H. Lee, Y. Zhu, L. Wu, J. Li, P. Jarillo-Herrero, M. Dresselhaus, T. Palacios and J. Kong, *Advanced Materials*, 2016, **28**, 2322–2329.

[97] D. Pierucci, H. Henck, J. Avila, A. Balan, C. H. Naylor, G. Patriarche, Y. J. Dappe, M. G. Silly, F. Sirotti, A. T. C. Johnson, M. C. Asensio and A. Ouerghi, *Nano Letters*, 2016, **16**, 4054–4061.

References

[98] Z. Ding, Q.-X. Pei, J.-W. Jiang, W. Huang and Y.-W. Zhang, *Carbon*, 2016, **96**, 888–896.

[99] R. Liu, B. Liao, X. Guo, D. Hu, H. Hu, L. Du, H. Yu, G. Zhang, X. Yang and Q. Dai, *Nanoscale*, 2017, **9**, 208–215.

[100] A. P. Murthy, J. Theerthagiri, J. Madhavan and K. Murugan, *Physical Chemistry and Chemical Physics*, 2017, **19**, 1988–1998.

[101] H.-J. Shin, K. K. Kim, A. Benayad, S.-M. Yoon, H. K. Park, I.-S. Jung, M. H. Jin, H.-K. Jeong, J. M. Kim, J.-Y. Choi and Y. H. Lee, *Advanced Functional Materials*, 2009, **19**, 1987–1992.

[102] M. Chatti, T. Gengenbach, R. King, L. Spiccia and A. N. Simonov, *Chemistry of Materials*, 2017, **29**, 3092–3099.

[103] Y. Shang, D. Zhang, Y. Liu and C. Guo, *Bulletin of Materials Science*, 2015, **38**, 7–12.

[104] W. Chen, Y. Yang, Z. Zhang and E. Kaxiras, *2D Materials*, 2017, **4**, year.

[105] S. Eigler and A. Hirsch, *Angewandte Chemistry International Edition*, 2014, **53**, 7720–7738.

[106] V. K. Thakur and M. K. Thakur, *Chemical Functionalisation of Carbon Nanomaterials: Chemistry and Applications*, CRC Press, United States of America, 2015.

[107] S. Pei and H. M. Cheng, *Carbon*, 2012, **50**, 3210–3228.

[108] L. Shang, T. Bian, B. Zhang, D. Zhang, L. Wu, C. Tung, Y. Yin and T. Zhang, *Angewandte Chemistry International Edition*, 2014, **53**, 250–254.

[109] M. Pumera and C. A. H. Wong, *Chemical Society Reviews*, 2013, **42**, 5987–5997.

[110] D. C. Elias, R. R. Nair, T. M. G. Mohiuddin, S. V. Morozov, P. Blake, M. P. Halsall, A. C. Ferrari, D. W. Boukhvalov, M. I. Katsnelson, A. K. Geim and K. S. Novoselov, *Science*, 2009, **323**, 610–613.

[111] A. J. Birch, *Journal of the Chemical Society*, 1944, 430–436.

[112] Z. Yang, Y. Sun, A. L. B., T. N. Narayanan and W. E. Billups, *Journal of the American Chemical Society.*, 2012, **134**, 18689–18694.

[113] Y. Wang, J. Xu, M. Lin, Q. Bao, B. Ozyilmaz and K. P. Loh, *ACS Nano*, 2010, **4**, 6146–6152.

[114] D. D. Chronopoulos, A. Bakandritsos, M. Pykal, R. Zbořil and M. Otyepka, *Applied Materials Today*, 2017, **9**, 60–70.

[115] J. T. Robinson, J. S. Burgess, C. E. Junkermeier, S. C. Badescu, T. L. Reinecke, F. K. Perkins, M. K. Zalalutdniov, J. W. Baldwin, J. C. Culbertson, P. E. Sheehan and E. S. Snow, *Nano Letters*, 2010, **10**, 3001–3005.

[116] R. R. Nair, W. Ren, R. Jalil, I. Riaz, V. G. Kravets, L. Britnell, P. Blake, F. Schedin, A. S. Mayorov, S. Yuan, M. I. Katsnelson, H.-M. Cheng, W. Strupinski, L. G. Bulusheva, A. V. Okotrub, I. V. Grigorieva, A. N. Grigorenko, K. S. Novoselov and A. K. Geim, *Small*, 2010, **6**, 2877–2884.

[117] S. H. Cheng, K. Zou, F. Okino, H. R. Gutierrez, A. Gupta, N. Shen, P. C. Eklund, J. O. Sofo and J. Zhu, *Physical Reiews B*, 2010, **81**, 205435–205440.

[118] R. Zbořil, F. Karlický, A. B. Bourlinos, T. A. Steriotis, A. K. Stubos, V. Georgakilas, K. Šafářová, D. Jančík, C. Trapalis and M. Otyepka, *Small*, 2010, **6**, 2885–2891.

[119] D. A. Kosynkin, A. L. Higginbotham, A. Sinitskii, A. Lomeda, J. R. Dimiev, B. K. Price and J. M. Tour, *Nature*, 2009, **458**, 872–876.

[120] A. Sinitskii, A. Dimiev, D. A. Corley, A. A. Fursina, D. V. Kosynkin and J. M. Tour, *ACS Nano*, 2010, **4**, 1949–1954.

[121] E. Bekyarova, M. E. Itkis, P. Ramesh, C. Berger, M. Sprinkle, W. A. de Heer and R. C. Haddon, *Journal of the American Chemical Society*, 2009, **131**, 1336–1337.

[122] J. R. Lomeda, C. D. Doyle, D. V. Kosynkin, W.-F. Hwang and J. M. Tour, *Journal of the American Chemical Society*, 2008, **130**, 16201–16206.

[123] C. Hadad, X. Ke, M. Carraro, A. Sartorel, C. Bittencourt, G. Van Tendeloo, M. Bonchio, M. Quintana and M. Prato, *Chemical Communications*, 2014, **50**, 885–887.

[124] J. M. Englert, K. C. Knirsch, C. Dotzer, B. Butz, F. Hauke, E. Spiecker and A. Hirsch, *Chemical Communications.*, 2012, **48**, 5025–5027.

[125] G. Abellan, M. Schirowski, K. F. Edelthalhammer, M. Fickert, K. Werbach, H. Peterlik, F. Hauke and A. Hirsch, *Journal of the American Chemical Society.*, 2017, **139**, 5175–5182.

[126] S. Sarkar, E. Bekyarova, S. Niyogi and R. C. Haddon, *Journal of the American Chemical Society*, 2011, **133**, 3324–3327.

[127] C. K. Chua, A. Ambrosia and M. Pumera, *Chemical Communications*, 2012, **48**, 5376–5378.

[128] A. T. Strom, E. P. Dillon, C. E. Hamilton and A. R. Barron, *Chemical Communications*, 2010, **46**, 4097–4099.

[129] L. H. Liu and M. Yan, *Journal of Materials Chemistry*, 2011, **21**, 3273–3276.

[130] X. Zhong, J. Jin, S. Li, Z. Niu, H. W., R. Li and J. Ma, *Chemical Communications*, 2010, **46**, 7340.

[131] E. Kaiser, R. L. Colescot, C. D. Bossinge and P. I. Cook, *Analytical Biochemistry*, 1970, **34**, 595–598.

[132] M. Quintana, K. Spyrou, M. Grzelczak, W. Browne, P. Rudolf and M. Prato, *ACS Nano*, 2010, **4**, 3527–3533.

[133] S. Bertolazzi, M. Gobbi, Y. Zhao, C. Backes and P. Samori, *Chemical Society Reviews*, 2018, **47**, 6845–6899.

[134] U. Müller, in *Symmetry Relationships between Crystal Structures: Applications of Crystallographic Group Theory in Crystal Chemistry*, Oxford University Press, 2013, ch. 3, p. 16.

[135] K. C. Knirsch, N. C. Berner, H. C. Nerl, C. S. Cucinotta, Z. Gholamvand, N. McEvoy, Z. Wang, I. Abramovic, P. Vecera, M. Halik, S. Sanvito, G. S. Duesberg, V. Nicolosi, F. Hauke, A. Hirsch, J. N. Coleman and C. Backes, *ACS Nano*, 2015, **9**, 6018–6030.

[136] D. Voiry, A. Goswami, R. Kappera, C. de Carvalho Castro e Silva, D. Kaplan, T. Fujita, M. Chen, T. Asefa and M. Chhowalla, *Nature Chemistry*, 2014, **7**, 45–49.

[137] L. Zhou, B. He and Y. He, *RSC Advances*, 2014, **61**, 32570–32578.

[138] R. Anbazhagan, H. J. Wang, H. C. Tsai and R. J. Jeng, *RSC Advances*, 2014, **81**, 42936–42942.

[139] C. Backes, N. C. Berner, X. Chen, P. Lafargue, P. LaPlace, M. Freeley, G. S. Duesberg, J. N. Coleman and A. R. McDonald, *Angewandte Chemie International Edition*, 2016, **54**, 2638–2642.

[140] H. Lee, S. Bak, S. J. An, J. H. Kim, E. Yun, M. Kim, S. Seo, M. S. Jeong and H. Lee, *ACS Nano*, 2017, **11**, 12832–12841.

[141] H. Lee, S. Bak, S.-J. An, J. H. Kim, E. Yun, M. Kim, S. Seo, M. S. Jeong and H. Lee, *ACS Nano*, 2017, **11**, 12832–12839.

[142] X. Chen, N. C. Berner, C. Backes, G. S. Duesberg and A. R. McDonald, *Angewandte Chemie International Edition*, 2016, **55**, 5803–5808.

[143] M. Jeong, S. Kim and S. Y. Ju, *RSC Advances*, 2016, **6**, 36248–36254.

[144] S. G. McAdams, E. A. Lewis, J. R. Brent, S. J. Haigh, A. G. Thomas, P. O'Brien, F. Tuna and D. J. Lewis, *Advanced Functional Materials*, 2017, **27**, 1703646.

[145] A. B. Laursen, S. Kegnaes and I. Chorkendorff, *Energy Environmental Science*, 2012, **5**, 5577–5591.

[146] J. Xie, J. Zhang, S. Li, F. Grote, X. Zhang, H. Zhang, R. Wang, Y. Lei, B. Pan and Y. Xie, *Journal of the American Chemical Society*, 2013, **135**, 17881–17888.

[147] A. Forster, S. Gemming, G. Seifert and D. Tomanek, *ACS Nano*, 2017, **11**, 9989–9996.

[148] P. Li, B. Zhang and T. Cui, *Biosensors and Bioelectronics*, 2015, **72**, 168–174.

[149] M. Liu, J. Song, S. Shuang, C. Dong, J. D. Brennan and Y. Li, *ACS Nano*, 2014, **8**, 5564–5573.

[150] Z. Liu, J. T. Robinson, X. Sun and H. Dai, *Journal of the American Chemical Society*, 2008, **130**, 10876–10877.

[151] X. Sun, Z. Liu, K. Welsher, J. T. Robinson, A. Goodwin, S. Zaric and H. Dai, *Nano Research*, 2008, **1**, 203–212.

[152] S. Goenka, V. Sant and S. Sant, *Journal of Controlled Release*, 2014, **173**, 75–88.

[153] J. Wang, S. A. Kondrat, Y. Wang, G. L. Brett, C. Giles, J. K. Bartley, L. Lu, Q. Liu, C. J. Kiely and G. J. Hutchings, *ACS Catalysis*, 2015, **5**, 3575–3587.

[154] K. Yang, L. Feng, X. Shi and Z. Liu, *Chemical Society Reviews*, 2013, **42**, 530–547.

[155] K. Yang, H. Gong, X. Shi, J. Wan, Y. Zhang and Z. Liu, *Biomaterials*, 2013, **34**, 2787–2795.

[156] E. L. K. Chng and M. Pumera, *RSC Advances*, 2015, **5**, 3074–3080.

[157] S. Vranic, A. F. Rodrigues, M. Buggio, L. Newman, M. R. H. White, D. G. Spiller, C. Bussy and K. Kostarelos, *ACS Nano*, 2018, **12**, 1373–1389.

[158] R. Li, L. M. Guiney, C. H. Chang, N. D. Mansukhani, Z. Ji, X. Wang, Y.-P. Liao, W. Jiang, B. Sun, M. C. Hersam, A. E. Nel and T. Xia, *ACS Nano*, 2018, **12**, 1390–1402.

[159] S. Liu, T. H. Zeng, M. Hofmann, E. Burcombe, J. Wei, R. Jiang, J. Kong and Y. Chen, *ACS Nano*, 2011, **5**, 6971–6980.

[160] L. Liu, J. Liu, Y. Wang, X. Yana and D. D. Sun, *New Journal of Chemistry*, 2011, **35**, 1418–1423.

[161] S. Agarwal, X. Zhou, F. Ye, Q. He, G. C. K. Chen, J. Soo, F. Boey, H. Zhang and P. Chen, *Langmuir*, 2010, **26**, 2244–2247.

[162] O. Akhavan, E. Ghaderi and A. Akhavan, *Biomaterials*, 2012, **33**, 8017–8025.

[163] W. Hu, C. Peng, W. Luo, M. Lv, X. Li, D. Li, Q. Huang and C. Fan, *ACS Nano*, 2010, **4**, 4317–4323.

[164] T. Lammel, P. Boisseaux, M.-L. Fernández-Cruz and J. M. Navas, *Particle and fibre toxicology*, 2013, **10**, 27.

[165] Y. Li, Y. Liu, Y. Fu, T. Wei, L. L. Guyader, G. Gao, R.-S. Liu, Y.-Z. Chang and C. Chen, *Biomaterials*, 2012, **33**, 402–411.

[166] W. L. Xing, G. Lalwani, I. Rusakova and B. Sitharaman, *Particles and Particle Systems Characterisation*, 2014, **31**, 745–750.

[167] G. Zhao, D. Shao, C. Chen and X. Wang, *Applied Physics Letters*, 2011, **98**, 183114–183147.

[168] X. Zhou, Y. Zhang, C. Wang, X. Wu, Y. Yang, B. Zheng, H. Wu, S. Guo and J. Zhang, *ACS Nano*, 2012, **6**, 6592–6599.

[169] N. A. Zubir, C. Yacou, J. Motuzas, X. Zhang, X. S. Zhao and J. C. Diniz da Costa, *Chemical Communications*, 2015, **51**, 9291–9293.

[170] C. Yu, F. Wang and S. Chen, *Scientific Reports*, 2016, **6**, year.

[171] L. Peng, Z. Xu, Z. Liu, Y. Wei, H. Sun, Z. Li, X. Zhao and C. Gao, *Nature Communications*, 2015, **6**, year.

[172] H. Yu, B. Zhang, C. Bulin, R. Li and R. Xing, *Scientific Reports*, 2016, **6**, year.

[173] Z. Sofer, J. Luxa, O. Jankovský, D. Sedmidubský, T. Bystroň and M. Pumera, *Angewandte Chemie International Edition*, 2016, **55**, 11965–11969.

[174] L. Yang and J. He, *Chemical Communications*, 2014, **50**, 15722–15725.

[175] G. P. Kotchey, B. L. Allen, H. Vedala, N. Yanamala, A. A. Kapralov, Y. Y. Tyurina, J. Klein-Seetharaman, V. E. Kagan and A. Star, *ACS Nano*, 2011, **5**, 2098–2108.

[176] G. Lalwani, W. Xing and B. Sitharaman, *Journal of Materials Chemistry B*, 2014, **2**, 6354–6362.

[177] H. J. H. Fenton, *Journal of the Chemical Society Transactions*, 1894, **65**, 899–910.

[178] H. Bataineh, O. Pestovsky and A. Bakac, *Chemical Science*, 2012, **3**, 1594–1599.

[179] J. Yoon, Y. Lee and S. Kim, *Water Science and Technology*, 2001, **44**, 15–21.

[180] M. L. Kremer, *Journal of Inorganic Biochemistry*, 2000, **78**, 255–257.

[181] E. Neyens and J. Baeyens, *Journal of Hazardous Materials*, 2003, **98**, 33–50.

[182] A. Boveris and E. Cadenas, *IUBMB Life*, 2000, **50**, 245–250.

[183] K. Metz, A. Mangham, M. Bierman, S. Jin, R. Hamers and J. Pedersen, *Environmental Science and Technology*, 2009, **43**, 1598–1604.

[184] G. Ruppert, R. Bauer, G. Heisler and S. Novalic, *Chemosphere*, 1993, **27**, 1339–1347.

[185] Y. Feng, K. Lu, L. Mao, X. Guo, S. Gao and E. J. Petersen, *Water Research*, 2015, **84**, 49–57.

[186] H. Bai, W. Jiang, G. P. Kotchey, W. A. Saidi, B. J. Bythell, J. M. Jarvis, A. G. Marshall, R. A. S. Robinson and S. A., *Journal of Physical Chemistry C*, 2014, **118**, 10519–10529.

[187] A. Bassan, M. R. A. Blomberg, T. Borowski and P. E. M. Siegbahn, *Journal of Physical Chemistry B*, 2004, **108**, 13031–13041.

[188] K. P. Bryliakov and E. P. Talsi, *Coordination Chemistry Reviews*, 2014, **276**, 73–96.

[189] D. J. Ferraro, L. Gakhar and S. Ramaswamy, *Biochemical Biophysical Research Communications*, 2005, **338**, 175–190.

[190] L. Wackett, *Enzyme and Microbial Technology*, 2002, **31**, 577–587.

[191] A. Karlsson, J. V. Parales, R. E. Parales, D. T. Gibson, H. Eklund and S. Ramaswamy, *Science*, 2003, **299**, 1039–1042.

[192] M. Costas, M. P. Mehn, M. P. Jensen and L. Que, *Chemical Reviews*, 2004, **104**, 939–986.

[193] K. Chen and L. J. Que, *Chemical Communications.*, 1999, **15**, 1375–1376.

[194] K. Chen, M. Costas, J. Kim, A. K. Tipton and L. J. Que, *Journal of the American Chemical Society*, 2002, **124**, 3026–3035.

[195] G. Anderegg and F. Wenk, *Helvetica Chimica Acta*, 1967, **50**, 2330.

[196] E. Toftlund, H. Pedersen and S. Yde-Andersen, *S. Acta Chemistry Scandia.*, 1984, **38A**, 693–697.

[197] R. Mas-Balleste, and L. J. Que, *Journal of the American Chemical Society.*, 2007, **129**, 15964–15972.

[198] O. Markhylnyats, P. Das, S. Taktak, M. Flook, R. Mas-Balleste, E. V. Rybak-Akimova and L. J. Que, *Chemistry–A European Journal*, 2009, **15**, 13171–13180.

[199] K. K. Singh, M. K. Tiwar, B. B. Dhar, K. Vanka and S. S. Gupta, *Inorganic Chemistry*, 2015, **54**, 6112–6121.

[200] I. Prat, J. S. Mathieson, M. Güell, X. Ribas, J. M. Luis, L. Cronin and M. Costas, *Nature Chemistry*, 2011, **3**, 788–793.

[201] P. D. Oldenburg and L. J. Que, *Catalysis Today*, 2006, **117**, 15–21.

[202] O. Y. Lyakin, K. P. Bryliakov and E. P. Talsi, *Inorganic Chemistry*, 2011, **50**, 5526–5538.

Chapter 2

Preparation and Characterisation of Liquid Phase Exfoliated Graphene, 2H-MoS_2 and Chemically Exfoliated 1T-MoS_2

2.1 Introduction

The materials prepared here (graphene, ce-1T-MoS_2 and 2H-MoS_2) and the spectroscopic techniques used to characterise them will be referenced frequently in the following chapters. This Techniques chapter introduces each material in order for the reader to gain a quick understanding of their preparation and general properties as ascertained through spectroscopy.

2.2 Preparation and Characterisation of Liquid Phase Exfoliated Graphene

Two sources of graphite were used herein to produce graphene: SGN18, a synthetic graphite powder, and Timrex PP10, a natural graphite powder. Dispersions of graphene based on SGN18 graphite were prepared *via* probe sonication in IPA for 3 h, and centrifugation at 1500 rpm for 1.5 h. This method was a slightly modified version of the liquid exfoliation techniques pioneered by Coleman's group.[1] When using Timrex PP10 graphite, dispersions were prepared by shear exfoliation[2] at 4500 rpm for 1.5 h in dimethyl sulfoxide (DMSO) or *N*-methyl-2-pyrollidinone (NMP), centrifugation at 1500 rpm for 1.5 h, vacuum filtration and re-dispersion in other solvents by probe sonication for 3 h. This method was also according to the Coleman group methods for shear exfoliation of 2D materials.[2] Dispersions of SGN18 in IPA would fully reaggregate in three months, with PP10 in DMSO or NMP lasting at least this long, potentially longer.[2] Both dispersions were routinely used within three weeks of preparation. Shear exfoliated graphene in acetonitrile (MeCN) re-aggregated over much shorter time periods, typically 24 h and were used as soon as prepared. The pristine graphene and re-aggregated graphene samples were analysed by UV-vis spectroscopy, attenuated total reflectance infrared (ATR-IR) spectroscopy and diffuse reflectance infrared Fourier transform (DRIFT) spectroscopy, thermogravimetric analysis (TGA), coupled TGA-infrared (IR) spectroscopy, Raman spectroscopy, atomic force microscopy (AFM), X-ray photoelectron spectroscopy (XPS), powder X-ray diffraction (pXRD) and scanning electron microscopy (SEM).

UV-vis Spectroscopy

In materials science, UV-vis spectroscopy is used to calculate the concentration in mg/ml of prepared dispersions or suspensions of nanomaterials by measuring the absorbance at specific nm and relating this to the reported extinction coefficient and length of the path of

light through the dispersion (Beer-Lambert Law). In the case of graphene, the extinction coefficient as reported by Coleman's group was 6600 ml mg^{-1} m^{-1} at 660 nm in water, stabilised by surfactants.[3] As the dispersions were prepared in different solvents, calculation of the concentration of the dispersions was also carried out by taking 3 x 10 ml aliquots of the dispersion, reducing it to dryness and weighing the residue. Freshly prepared dispersions typically showed concentrations of 0.3 mg/ml by residual weight and by the Beer-Lambert Law (Figure 2.1).

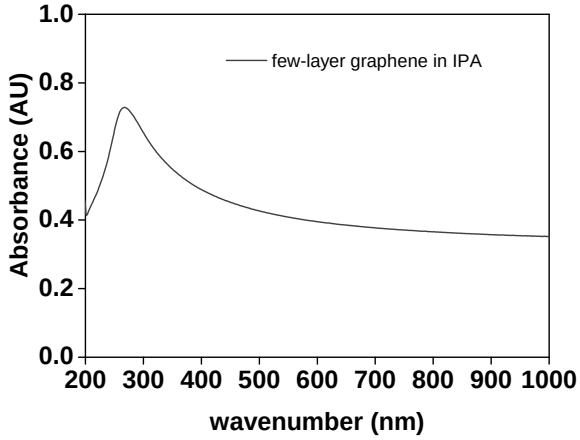

Fig. 2.1 UV-vis spectrum of SGN18 graphene in IPA.

Attenuated Total Reflectance and Diffuse Reflectance FT-IR

Graphene and graphite have been reported to show featureless IR spectra, due to the lack of dipoles in graphite.[4] The baseline of spectra from graphene and other carbonaceous or inorganic forms of carbon can suffer from the Christiansen effect[5] from the refraction of IR light at lower wavenumbers, particularly in ATR-IR as the IR light can be highly refracted instead of transmitting through the material (Figure 2.2). Organic residues such as carbonyls (typically found around 1700 cm^{-1}), hydroxyls (3500 cm^{-1}), epoxides (750–950 cm^{-1}) and also aromatic stretches and bends (peaks in the regions of 1000–1200 cm^{-1}, 1400–1500 cm^{-1}, and 2900–3000 cm^{-1}) that can exist as defects or form as a result of oxidation of graphene[6] can be easily detected using IR spectroscopy.[7] IR spectroscopy can pick up any functional

groups that may form on the basal plane of graphene, with more surface sensitive techniques such as DRIFT spectroscopy able to pick up signals from the graphene edges and surface of re-aggregated samples.

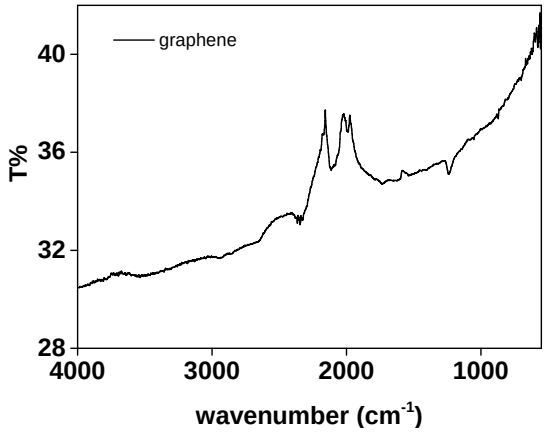

Fig. 2.2 ATR-IR spectrum of SGN18 graphene.

DRIFT spectroscopy measures the energy of reflected IR light and therefore shows better surface sensitivity than ATR-IR spectroscopy. In this way, small levels of functionalisation can be detected. The pristine graphene produced from both SGN18 and PP10 gave very low intensity peaks, which was expected with pristine graphene (Figure 2.3). The DRIFT spectrum from SGN18 graphene gave very low intensity peaks, as did graphene from PP10 graphite. Peaks detected gave reflectance values of 98% or higher, suggesting that there were very low levels of inherent defects, which was expected for pristine graphene (Figure 2.3).

Raman Spectroscopy

Raman spectroscopy is known as a complimentary technique to IR spectroscopy, as it relies on the polarisability of bonds in response to absorption of light, rather than dipole moments. A monochromated laser is used to excite the material to what are known as virtual excited states; *i.e.*, states that are higher than vibrational energy states but lower than electronic excitation states. The material relaxes and releases this energy, and some energy is released through a number of vibrational states.

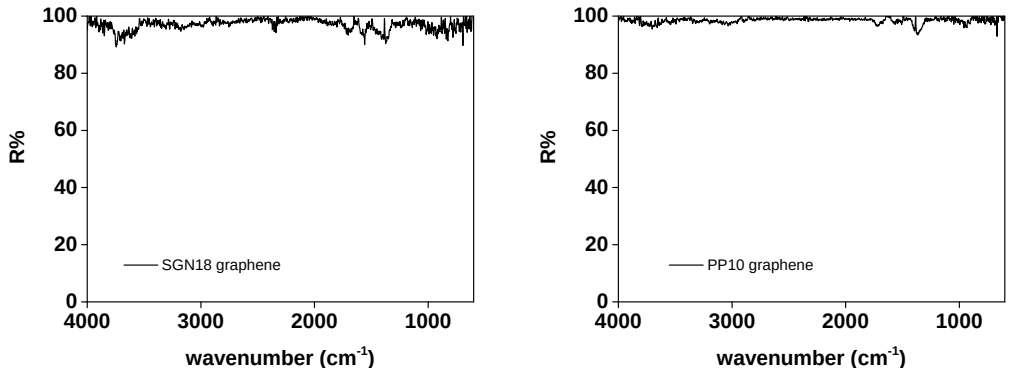

Fig. 2.3 DRIFT spectra of graphene from (a) SGN18 graphite and (b) PP10 graphite.

Most of the light energy is scattered elastically, in what is known as Rayleigh scattering. This scattering generates the main relaxation peak in the Raman spectrum, which is normally left out. The important peaks come from inelastic scattering—either Stokes scattering, where the energy released is less than that of the original power of the laser, or Anti-Stokes scattering, where the energy released is more than that of the original laser. In the case of Stokes scattering, some energy is lost when the material relaxes back to a higher vibrational mode than it occupied before excitation, whereas Anti-Stokes scattering occurs when the material relaxes back to a lower vibrational mode than it originally occupied. These kinds of scattering cause peaks to appear in the spectrum that are shifted with respect to that generated from Rayleigh scattering. These are unique to each material and are used to characterise and mark changes in a material with Raman-active vibrational modes.[8]

Graphite and its related compounds have very clear Raman spectra. The Raman spectrum of few-layer graphene typically showed three main peaks: the G peak at 1580 cm^{-1}, which is the result of in-plane vibrations of the sp^2 sheet, the D peak at 1350 cm^{-1}, which is related to the 'breathing' mode of edge sites, defect or functional group concentration of the graphene sheets, and the third peak, the '2D' peak at 2690 cm^{-1}, an overtone of the D peak which can give information on the thickness or number of sheets in the reaggregated sample.[9]

The increase in intensity of the D peak and D' (1620 cm^{-1}), a shoulder of the G peak, can occur as a result of increasing disorder, or functionalisation, of the graphene lattice. The intensity ratio of the D peak to the G peak can therefore be employed as a measure of the defect density in graphite or graphene.[10]

The graphene dispersions used in this thesis showed a typical I_D:I_G ratio of 0.25 for SGN18 graphene and 0.12 for PP10 graphene in spectra obtained using the 532 nm laser line (Figure 2.4). The higher value for SGN18 graphite as well as dispersibility in IPA are indicative of higher levels of defects.[11] The difference in ratio between the two types of graphene could be linked to the size distribution, which can be seen in the SEM below (Figure 2.9). The asymmetric shape of the 2D peak in the Raman spectra given by both prepared graphene dispersions was indicative of a multilayer structure; monolayer graphene typically has a symmetric 2D peak that is of equal or higher intensity to that of the G peak.[12, 9] In general, these values indicate a low concentration of inherent defects.[13]

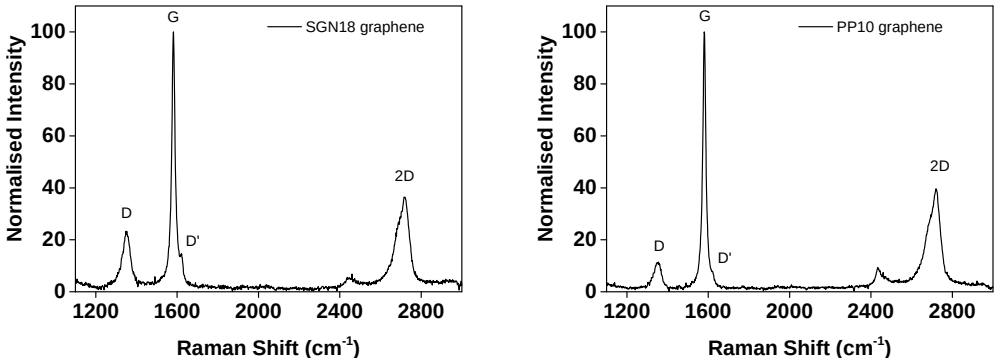

(a) (b)

Fig. 2.4 Raman spectra of graphene from (a) SGN18 graphite (b) PP10 graphite normalised to the 'G' peak (1580 cm^{-1}) of graphene.

Thermogravimetric Analysis

Thermogravimetric analysis (TGA) measures the change in weight of a sample as it is heated, normally at a set rate of heating, in a furnace. The atmosphere of the furnace can be air, nitrogen, other inert gases such as argon, or a vacuum. The weight loss measurements

obtained from TGA give insight into the amount and nature of adsorbed species on the material of interest, depending on the temperature at which weight loss occurs. The 1*st* derivative of the TGA trace is used to determine points of maximum rate of weight loss (inflection points).[14] Temperatures of over 250 °C are usually required to thermally break covalent bonds, whereas any weight loss below this is inferred to be due to material that is merely physisorbed to the surface.[15] TGA traces of re-aggregated SGN18 graphene and PP10 graphene both showed less than 1% weight loss up to 600 °C in air, after which point the graphene itself started to degrade, and there was a steep decline in weight to 900 °C.[16] The 1st derivative traces of the graphene TGA traces also reflected no change in the rate of weight loss until after the degradation temperature for both types of graphene (Figure 2.5, right). This supports the high quality and low-defect nature of the prepared graphene, with insignificant levels of physisorbed material and covalently bound functional groups present.

Coupled TGA-IR

This technique facilitates further identification of the gases given off during the thermal decay of a sample by continuously obtaining ATR-IR spectra of the carrier gas of the TGA as it passes through the furnace. Re-aggregated graphene from both graphite sources was also subjected to coupled TGA-IR (Figure 2.6). The IR spectra obtained from SGN18 graphene detected no change from the background spectrum until 570 °C, at which point asymmetric and symmetric CO_2 stretches (2320 and 2350 cm^{-1}) began to grow, reaching a maximum of 15 T% at 880 °C.[17] There were no other peaks detected. This matched the very low weight loss seen in the TGA trace before degradation of graphene itself occurred after 600 °C and identified the resulting weight loss as graphene undergoing oxidation in air, or from trace amounts of oxygen trapped in between the re-aggregated layers when the carrier gas was nitrogen.

X-ray Photoelectron Spectroscopy

X-ray photoelectron spectroscopy can support these other techniques by giving a qualitative

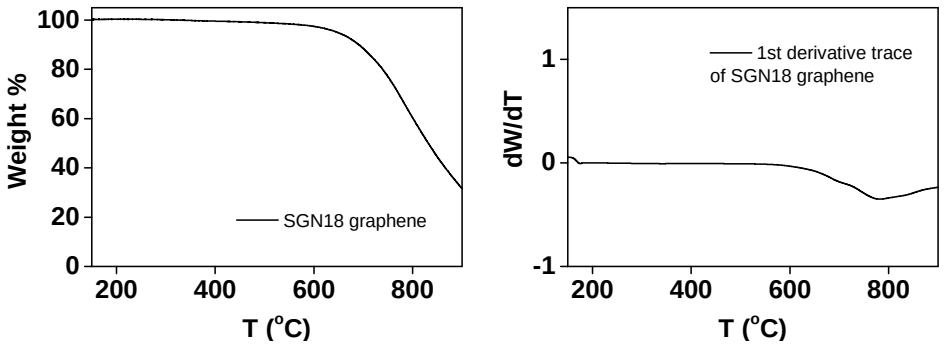

(a)

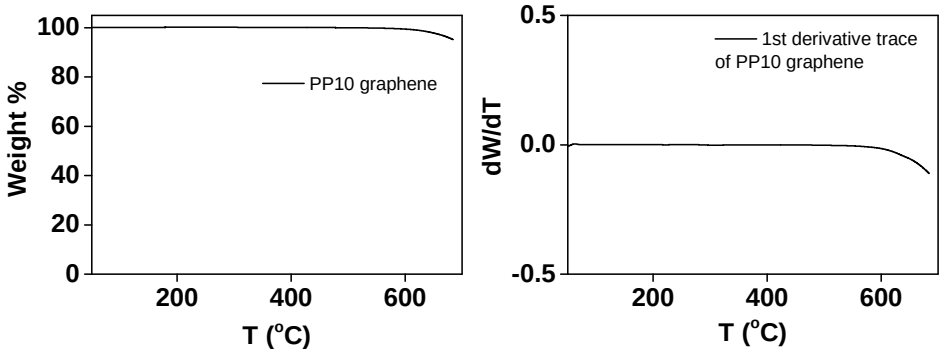

(b)

Fig. 2.5 (a) TGA trace and 1st derivative of SGN18 graphene, (b) TGA trace and 1st derivative of PP10 graphene.

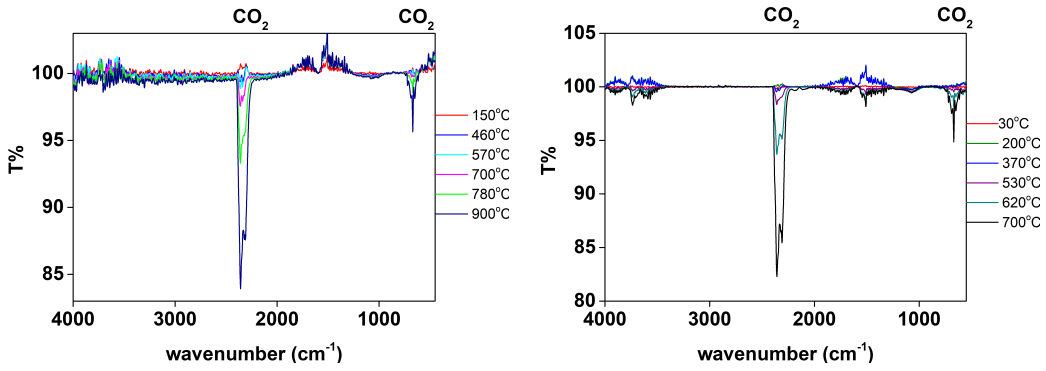

(a) (b)

Fig. 2.6 Coupled TGA-IR spectra of (a) SGN18 graphene and (b) PP10 graphene at specific temperatures.

and quantitative measure of functionalisation or doping. This is achieved by obtaining survey spectra to identify the atomic species present and core level spectra give an idea of the

chemical environment of the atomic species, *i.e.*, the nature of the hetero- and homo-nuclear bonds it is taking part in. The shifts in binding energy seen in carbon 1s spectra can be attributed to adjacent functional groups which change the charge distribution around the carbon atom, and can be assigned by how much they shift the binding energy.[18] The survey spectra of the pristine graphene sources used here showed that both C and O were present, with no other atomic species detected. From core level area calculations, the concentration of C and O (respectively) was determined as 95% and 5% for SGN18 graphene and 97% and 3% for PP10 graphene. The oxygen content is believed to derive from adventitious solvent or water.[19]

The C 1s core level spectrum of SGN18 graphene displayed a feature at 284.4 eV, attributed to sp^2 hybridised graphitic carbon, (88% of the total area) and a shake-up feature at 291 eV commonly observed in pristine graphite samples (5% of the total area).[20] This left 7% to be assigned as sp^3-hybridised carbon (284.8–285.5 eV), present as inherent defects in an imperfect crystal and/or adventitious carbon.[19] The core level spectrum of PP10 graphene also showed the graphitic carbon signal at 284.4 (92% of the total area) and a shake up feature at 291.0 eV (5% of the total area). The last feature, for saturated or oxidised carbon was fitted at 284.8–285.5 eV and came to 3% of the total area. These results again demonstrated the pristine nature of the sources used.

Powder X-ray Diffraction

Powder XRD (pXRD) is a form of X-ray diffraction which is useful for determining the d-spacing (the space between atoms) of a material. Unlike single crystals, which are highly ordered and anisotropic, and can produce extremely detailed diffractograms, powders are randomly orientated (isotropic) and therefore a diffractogram will show practically all of the possible crystal orientations as peaks at which diffraction occurs. As this is a diffraction technique, the peaks correspond to *hkl* planes of the reciprocal lattice of the material, and Bragg's equation can be used to determine d spacing.

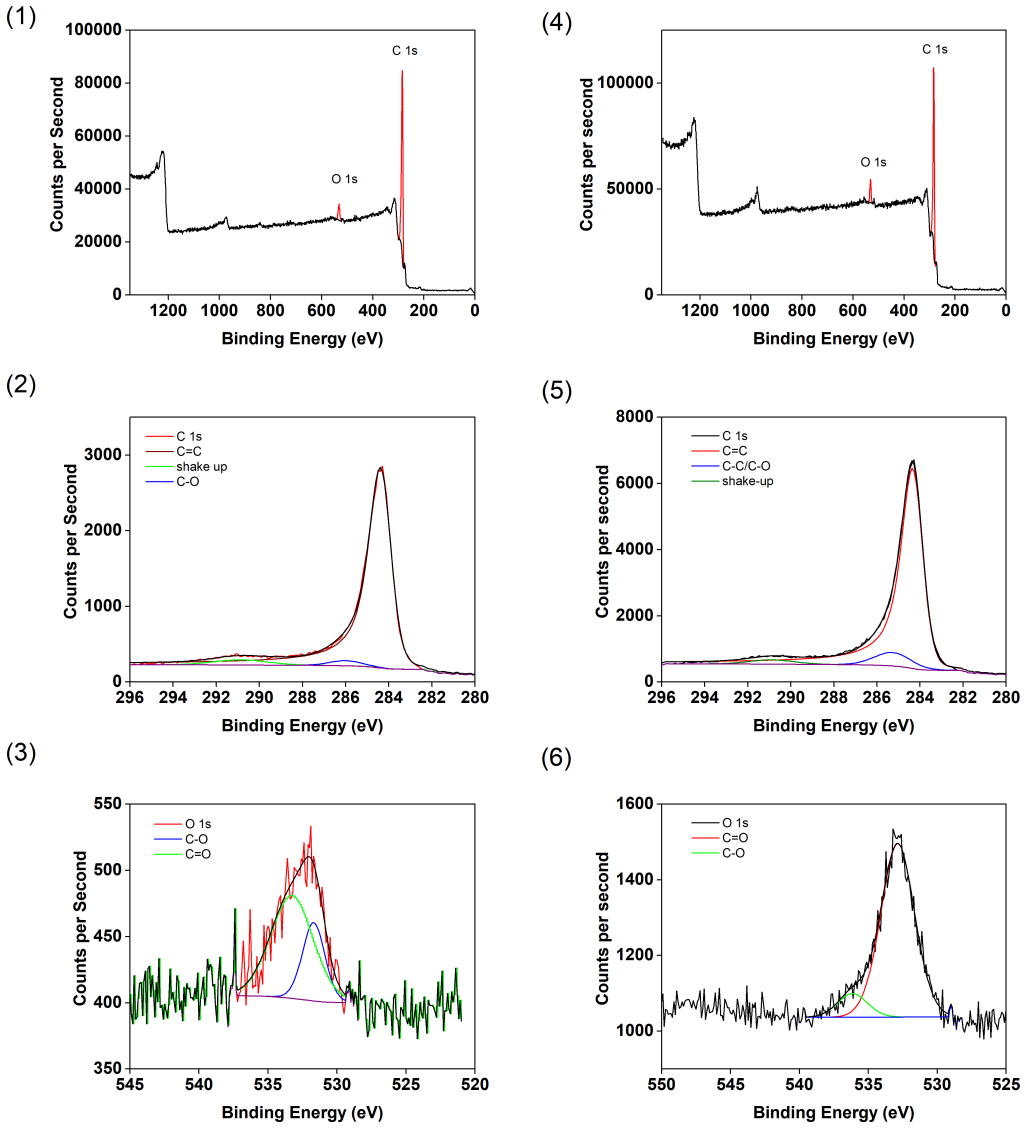

(a) (b)

Fig. 2.7 (a) Survey spectrum (1), C 1s (2) and O 1s (3) core level spectra of graphene from SGN18 graphite, and (b) survey spectrum (4), C 1s (5) and O 1s (6) core level spectra of graphene from PP10 graphite.

$$n\lambda = 2dsin\theta \tag{2.1}$$

Where n is an integer, λ is the wavelength of the incident X-rays, d is the atomic spacing, and θ is the scattering angle of the incident X-ray. PXRD is useful for determining the identity and phase of a material, and obtained diffraction patterns can be compared to a database of patterns for quick identification of a material.[21]

PXRD patterns of re-aggregated graphene from SGN18 and PP10 graphite were obtained from re-aggregated powders of the graphene dispersions (Figure 2.8). The pXRD pattern of SGN18 graphene and PP10 graphene gave peaks at 2θ that matched those of the reference graphite. Comparing the peaks at 42° (100), 43° (101) and others, the higher relative intensity of the peak at 26.5° for (002) was taken as evidence for partial exfoliation.[22]

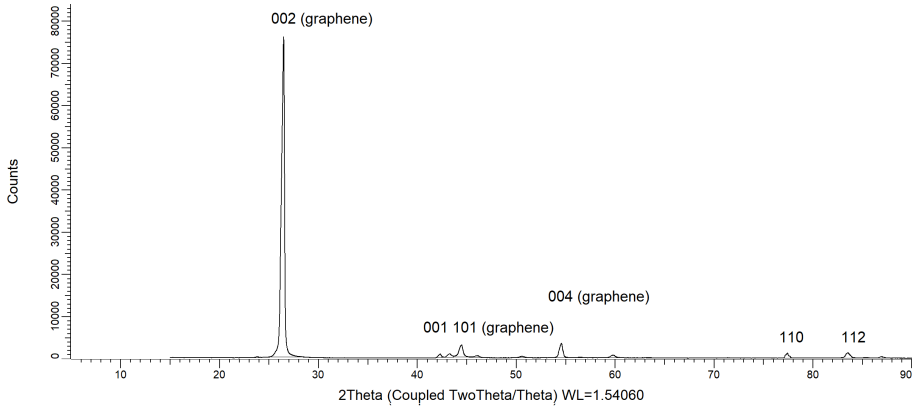

(a)

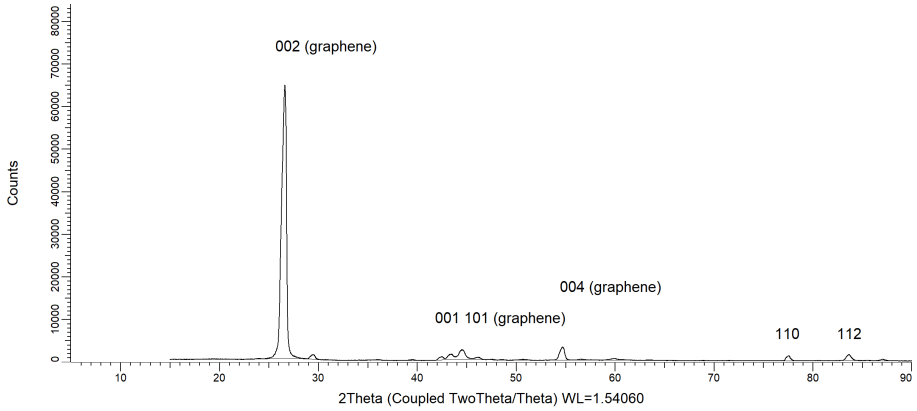

(b)

Fig. 2.8 Powder X-ray diffractograms of graphene from (a) SGN18 graphite, and (b) PP10 graphite.

Scanning Electron Microscopy & Atomic Force Microscopy

Scanning electron microscopy, similar to transmission electron microscopy is a form of microscopy in which an electron beam is focussed through a series of condenser lenses and objective lenses, generated by electric fields, and then used to probe a sample. In TEM, the electron beam is powerful enough to transmit through the sample with some diffraction occurring, be refocussed by the objective lens and interact with a fluorescent screen to produce an image of the sample down to the nanometer or even angstrom scale. SEM uses an electron beam of a much lower energy and produces an image of the sample through raster scanning of the electron beam across an area of the sample. The electrons are scattered (elastically or inelastically) by their interaction with the sample, and the detection of scattered electrons and the energy lost from their interaction with the sample forms the image.[23]

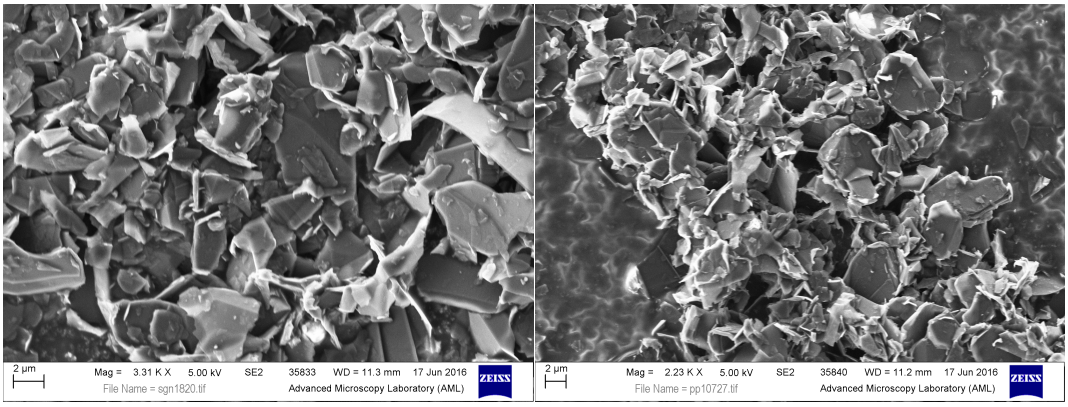

(a) (b)

Fig. 2.9 SEM (in secondary electron mode) images of drop-cast exfoliated graphene from (a) SGN18 and (b) PP10 graphite.

The multiple modes of SEM are based on the collection of different kinds of scattered electrons: secondary electron mode, backscatter mode and in lens mode, which are used in this thesis. Secondary electrons are produced from the top few nm of a sample and are electrons that have overcome the work function of the material with minimal interactions. They are the easiest to detect, and are acquired with a beam energy of 2–5 eV. Backscatter mode collects electrons that have been scattered at wide angles and have undergone many

interactions, and can give information on the bulk of the sample. They normally require a beam energy of 20—50 eV to detect. In Lens mode uses a low energy beam of 1–2 eV to probe only the first couple of nm of the sample and can give detailed surface information.[24]

Scanning electron microscopy provides more information on the physical properties of the graphene flakes after exfoliation, including the size distribution. SEM images were recorded in secondary electron and in-lens mode for both prepared graphene samples, and the average size of flakes was estimated to be 1.82 $\pm$ 0.19 μm for SGN18 graphene and 2.90 $\pm$ 0.41 μm for PP10 graphene. The larger D peak seen in the Raman spectrum for SGN18 graphene can be explained by the smaller size range and larger proportion of edges compared to PP10 graphene, as seen in the SEM. (Figure 2.9)

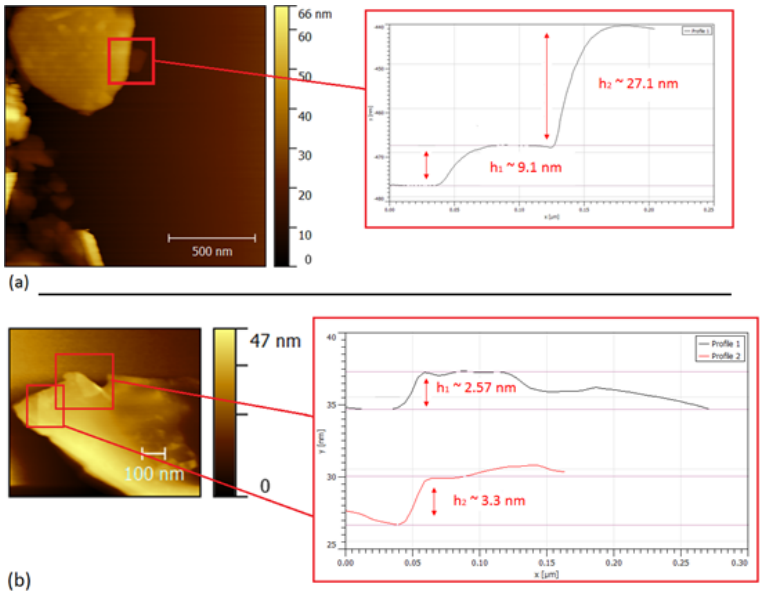

Fig. 2.10 AFM images of few-layer graphene from (a) SGN18 and (b) PP10 graphite, kindly provided by Mr Owen Brasil.

Atomic force microscopy uses a very fine tip, usually within the nanometer scale and made of silicon, attached to a cantilever to probe the thickness and surface topography of samples through the interaction of the tip with the surface of a material. The movement of the cantilever as the tip interacts with the surface causes the reflection of a laser, pointed at and reflecting off the cantilever, to change. This change is picked up by a photodiode.[25] There

are several modes of AFM, which differ by how to the tip interacts with the surface—tapping mode, contact mode and non-contact mode, each with slightly different processes, but these are beyond the scope of this thesis. AFM was conducted on Si plates that were spin coated with graphene from SGN18 and graphene from PP10 and analysed by Mr. Owen Brazil (Figure 10). Measurement of the dried flakes of each type of graphene gave thicknesses of 9–10 layers for SGN18 graphene and over 20 layers for PP10 graphene, with folds on the surface equalling 3–4 layers.

2.3 Preparation and Characterisation of ce-1T-MoS_2

Chemically exfoliated 1T-MoS_2 was prepared based on a method employed by Morrison *et al*, using *n*-BuLi to produce Li intercalated MoS_2.[26] This Li.MoS_2 was then exfoliated by bath sonication in water producing a stable, black dispersion of highly charged nanosheets of MoS_2. The alkaline dispersion was centrifuged for 1 h at 700 rpm and the unexfoliated powder was discarded. The remaining dispersion was centrifuged at 11000 rpm for 1 h and the supernatant discarded. The exfoliated powder was redispersed in water and this centrifugation step was repeated until the pH of the dispersion dropped below 8. The dispersions of ce-1T-MoS_2 have been reported to revert to 2H-MoS_2 phase over time and reaggregate. [27] The prepared dispersions re-aggregated fully in two weeks. To minimise this, ce-1T-MoS_2 dispersions were used within one week of preparation, and kept at 2–8°C while not in use. The dispersion and the re-aggregated powder obtained after vacuum filtration were characterised by UV-vis spectroscopy, ATR-IR, TGA, TGA-IR, Raman spectroscopy, XPS, pXRD and SEM.

UV-vis Spectroscopy

The concentration of ce-1T-MoS_2 in water was determined to be 1.9 mg/ml, using the extinction coefficient reported by Backes *et al* (Figure 2.11).[28] UV-vis can provide much information on MoS_2, such as the phase, thickness and size of the sheets in dispersion. Using absorption spectra, emission spectra and derivative spectra of these, Backes *et al* discerned much of this through in depth studies.[28, 29]

The 1T phase of MoS_2 can be identified from the absorption spectra by the μ_{max} at 260 and 300 nm (Figure 2.11). The shoulder at 400 nm grows steadily with reversion to the 2H phase, joined by peaks at 450, 610 and 670 nm. The peak at 300 nm disappears and the peak at 260 nm decreases in intensity. A new peak also appears at 227 nm (Figure 2.19).

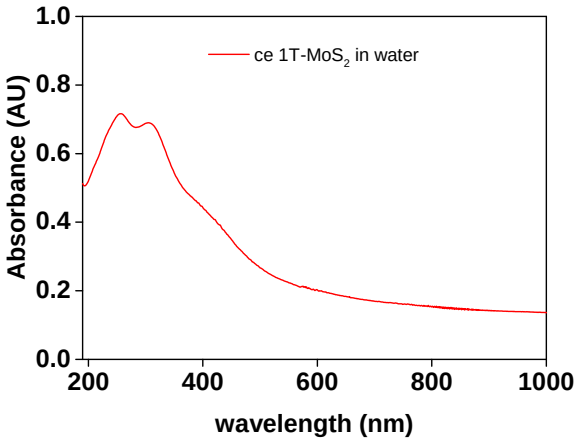

Fig. 2.11 UV-vis spectrum of ce-1T-MoS_2 in water.

ATR-IR Spectroscopy

ATR-IR spectroscopy was also used to characterise ce-1T-MoS_2. As with graphene, MoS_2 does not show any strong signals in the IR, but impurities and organic groups can be detected with this method. The spectrum of ce-1T-MoS_2 prepared for these studies displayed very weak features (Figure 2.12). Combining this with the XPS results showing the presence of carbon and oxygen, it was inferred that these bonds were due to residual solvent or intercalating agent from the chemical exfoliation process.

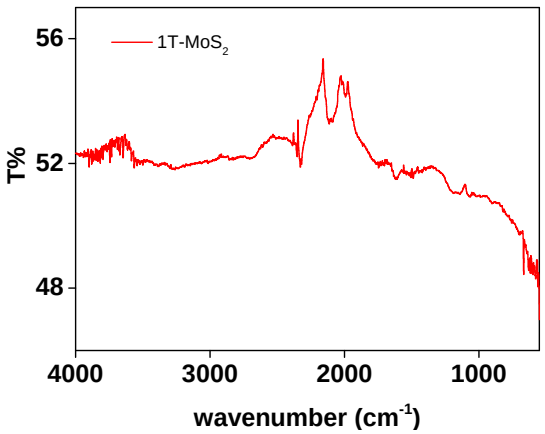

Fig. 2.12 ATR-IR spectrum of ce-1T-MoS_2 powder.

Thermogravimetric Analysis

The TGA trace of ce-1T-MoS_2 was similar to that of the graphene sources. 1% weight loss was recorded before 200 °C, which slowly increased to 2% up to 400 °C. The total weight loss before 600 °C was 8%, at which point the parent material starts to degrade. The derivative of the trace showed no obvious inflection points or changes in the rate of weight loss (Figure 2.13). This weight loss could be due to the adventitious species that were seen in the ATR-IR spectrum and the XPS data. Coupled TGA-IR was employed to test this.

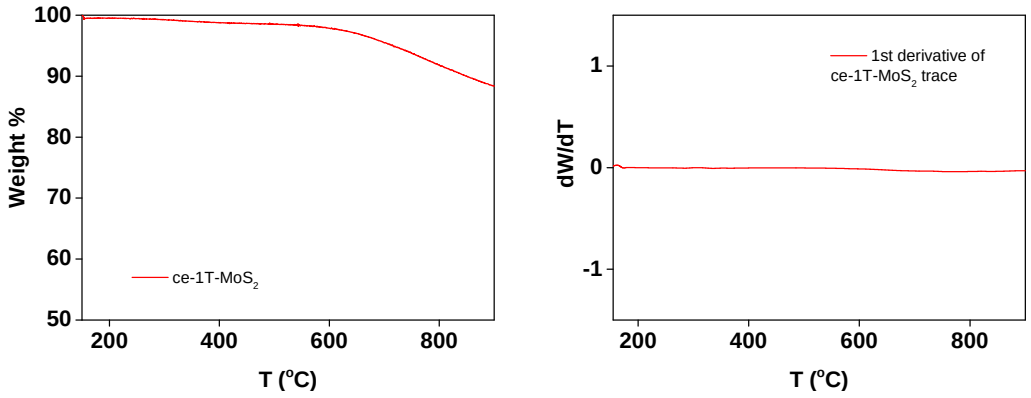

Fig. 2.13 TGA trace (a) and its corresponding 1st derivative trace (b) of ce-1T-MoS_2 under nitrogen.

Coupled TGA-IR

No peaks were detected in the spectra of TGA-IR until approximately 420 °C. These were very weak (<2 T%) and were tentatively identified as C-O stretching peaks in the range (1050–1150 cm^{-1}) (Figure 2.14).[7] These could possibly be from leftover intercalants from the preparation of the 1T phase, or residual solvent, and could explain the impurities seen using other spectroscopic techniques. Above 600 °C, CO_2 stretching peaks at 2350 and 2320 cm^{-1} appeared, though these were much less intense than the peaks seen for graphene (1% T). In agreement with the clean S 2p core level spectrum, no evidence for SO_x (1400–1300 cm^{-1}) species was seen *via* TGA-IR.

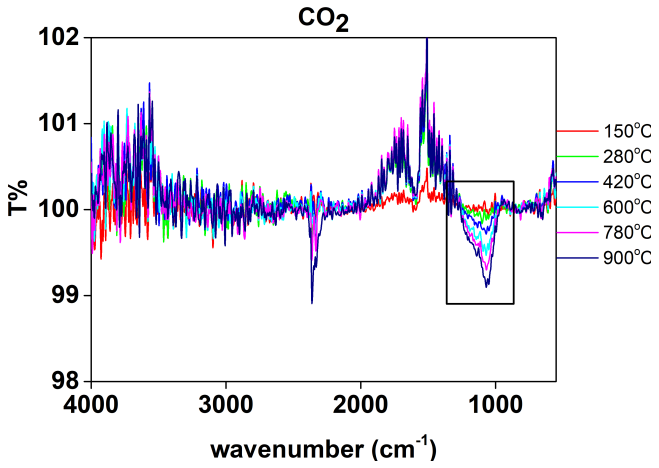

Fig. 2.14 TGA-IR spectra of ce-1T-MoS_2 at the stated temperatures.

Raman Spectroscopy

The Raman spectrum of ce-1T-MoS_2 displayed several characteristic peaks: three peaks at 150, 225, 340 cm^{-1} known as J_1, J_2, J_3 which are only observed for ce-1T-MoS_2,[30] as well as 383 (E^1_{2g}), 408 (A_{1g}) and 460 cm^{-1} (2LA(M)). The E^1_{2g} (383 cm^{-1} which is also IR active) and A_{1g} (408 cm^{-1}) signals can provide insight into the number of layers of MoS_2.[31]

For the pristine ce-1T-MoS_2 used in this study, the E^1_{2g}–A_{1g} distance was 26.3 cm^{-1} (Figure 2.15a). The resonant signal 2LA(M) (460 cm^{-1}), can vary in intensity with respect to (A_{1g}) in response to changes in the surface properties of MoS_2 and can be used as a measure of structural change.[32] The ratio of intensity of the resonant signal 2LA(M) to A_{1g} was 0.97 for the prepared ce-1T-MoS_2, using the 633 nm line (Figure 2.15b). The 532 nm laser line gave similar peaks, the major difference being the drastic reduction in intensity of the 2LA(M) peak to 0.11, as it does not resonate with the 532 nm line.

X-Ray Photoelectron Spectroscopy

Films of ce-1T-MoS_2 were also analysed by XPS (Figure 2.16). The survey spectrum confirmed the presence of both Mo and S, as well as small amounts of C and O, as remnants of the intercalation process and as adventitious material not removed by the ultra high vacuum. No other atomic species were detected. The quantity of each species calculated from the

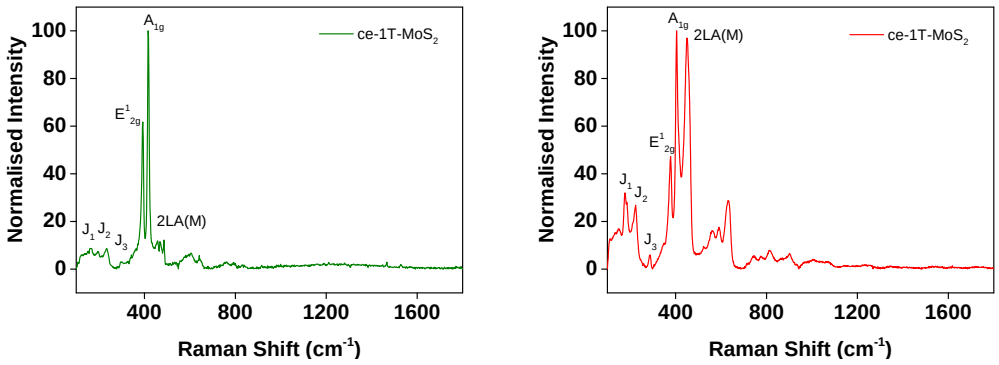

(a) (b)

Fig. 2.15 Raman spectrum of ce-1T-MoS_2 taken using (a) the 532 nm laser line and (b) the 633 nm laser line.

core level spectra and relative sensitivity factors was 23% Mo, 50% S, 15% C, and 12% O. The considerable amount of carbon and oxygen present, in comparison to their relative insignificance in ATR-IR and TGA suggested that during the preparation of the samples for XPS, a lot of adventitious carbon was deposited.[33]

The Mo 3d core level spectrum was fitted as 63% contribution from the 1T phase of MoS_2 at 229 and 230.5 eV and 25% from 2H-MoS_2 at 229.5 and 231 eV, with the remaining contribution (12%) from the overlapping S 2s region at 227 eV.[33] The S 2p core level spectrum showed the two components (3/2 and 1/2) of S 2p sulfide at 162 and 163.5 eV and no sign of oxidised sulfur. The small, low resolution feature in the C 1s spectrum of pristine ce-1T-MoS_2 was assigned as 40% oxygenated carbon (284.8 eV) and 60% saturated adventitious carbon (285.5 eV). The O 1s core level spectrum also showed a low resolution feature that was approximately assigned as 47% C=O (533.1 eV) and 53% C-O (534.6 eV).[19] The large fitting of the 1T phase of MoS_2 and the low concentration of adventitious carbon and oxygen demonstrated the success of the intercalation and exfoliation process.

Powder X-ray Diffraction

The pXRD pattern for ce-1T-MoS_2 matched that of 1T-phase MoS_2 (Figure 2.17).[34]The

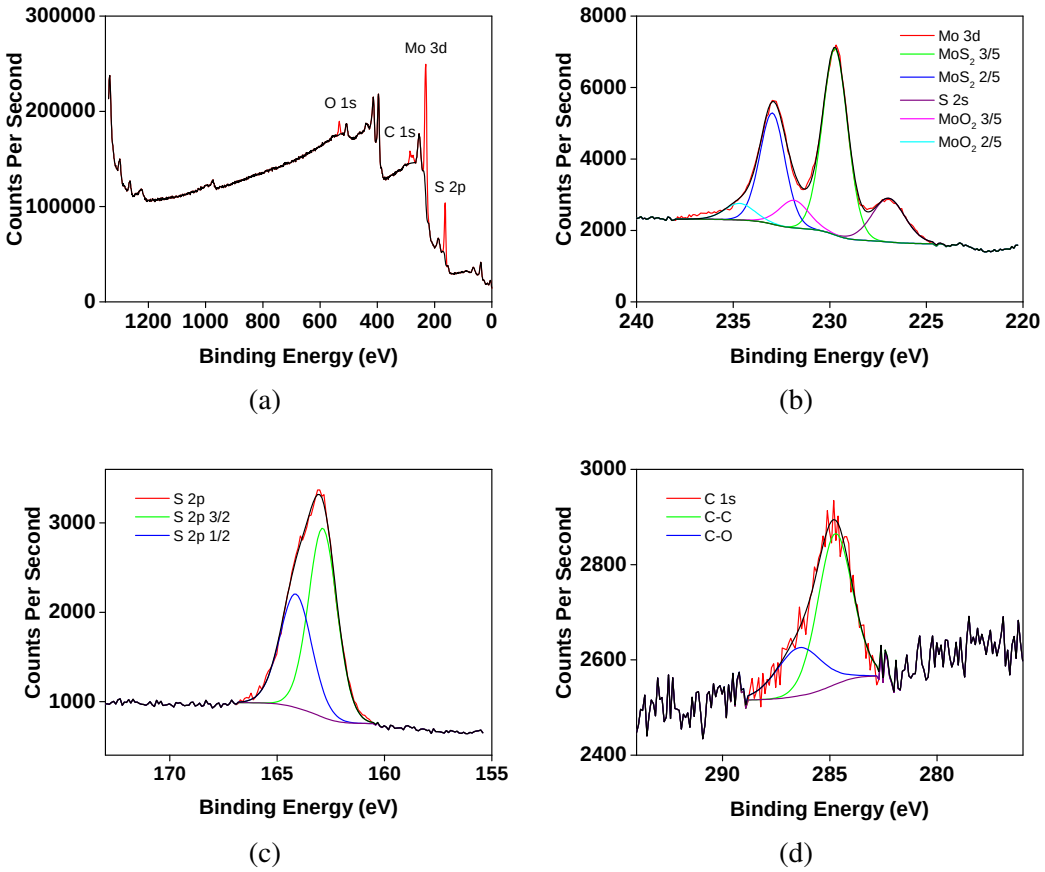

Fig. 2.16 (a) Survey spectrum, (b) Mo 3d, (c) S 2p and (d) C 1s core level spectra of ce-1T-MoS_2.

most intense of the peaks were two broad peaks at $2\theta = 9°$, corresponding to the (001) plane and 14°, for the (002) plane. The peak at 9° (001) suggested a considerable increase in interlayer distance, as previously reported.[34] As with re-aggregated graphene, the low relative intensity of the peaks at higher 2θ was taken as a sign of partial exfoliation. This effect was more pronounced in ce-1T-MoS_2 due to the increased concentration of monolayers produced in chemical exfoliation.

Scanning Electron Microscopy

The SEM images of ce-1T-MoS_2 revealed considerably wrinkled flakes of MoS_2 (Figure 2.18). With an average size of 0.22 ± 0.01 μm, flakes of ce-MoS_2 were much smaller than those of the liquid exfoliated 2H-MoS_2 flakes and graphene. The relatively high concentration

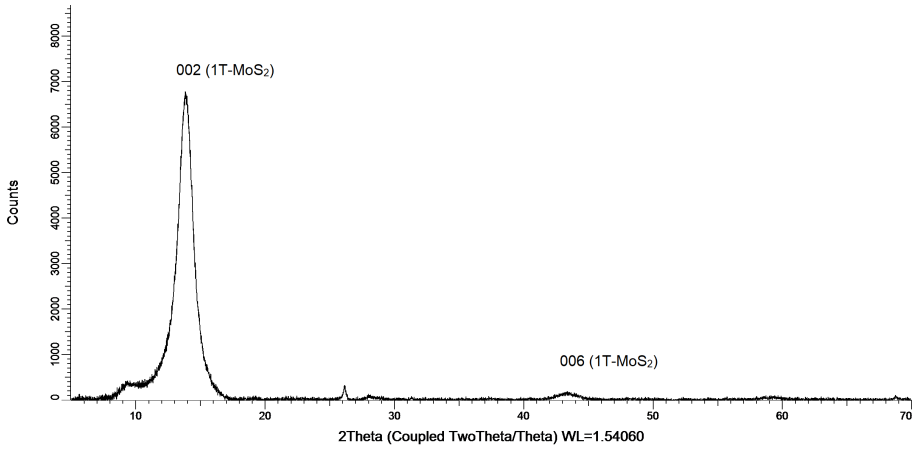

Fig. 2.17 Powder X-Ray diffractogram of ce-1T-MoS_2.

of ce-1T-MoS_2 is apparent in the SEM from the increased number and density of flakes on the sample holder.

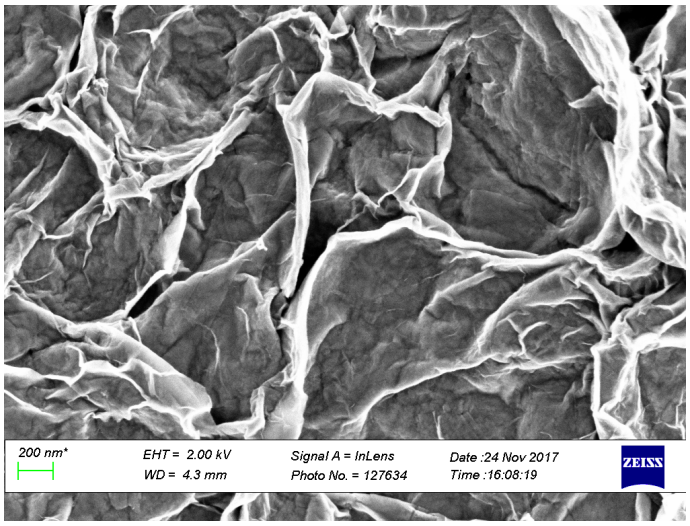

Fig. 2.18 SEM image showing flakes of ce-1T-MoS_2 in In Lens mode.

2.4 Preparation and Characterisation of 2H-MoS_2

Two dimensional 2H-MoS_2 nanosheets were prepared in a similar manner to SGN18 graphite. Typically, 2 g of MoS_2 powder was probe sonicated for 1 h in IPA, centrifuged for 1 h at 7000 rpm, then the 2H-MoS_2 powder was collected and the blue supernatant discarded. The powder was then redispersed in IPA by probe sonication for 4 h, followed by centrifugation at 1500 rpm for 1 h, yielding a grey-green dispersion of 2H-MoS_2 nanosheets. The dispersion of MoS_2 in IPA was quite stable, taking more than 3 months to fully re-aggregate. To minimise the re-aggregation, dispersions of 2H-MoS_2 were used within two weeks of preparation. The dispersion and the re-aggregated powder obtained after vacuum filtration were characterised by UV-vis spectroscopy, ATR-IR, TGA, TGA-IR, Raman spectroscopy, pXRD and SEM.

UV-vis Spectroscopy

UV-vis was used to determine the concentration of liquid exfoliated 2H-MoS_2 in IPA as 0.4 mg/ml, using the extinction coefficient determined by Coleman's group (Figure 2.19).[28] As described in the UV-vis section for ce-1T-MoS_2, the characteristic excitons were recorded for the dispersion of MoS_2 in IPA (Figure 2.19) at 230, 270, 400, 450 (A exciton), 610 (B exciton) and 670 nm (C exciton).[35] The thickness of the MoS_2 sheets can be estimated from the following equation:

$$N = 2.3 \times {}^{36}_{10}e^{(54888/\lambda_A)} \tag{2.2}$$

where N is equal to the number of layers and λ_A is the wavelength of the A exciton in nm. This was developed by Backes *et al* for the quick and accurate measurement of TMD thicknesses in dispersion, reducing the need for time consuming AFM and electron microscopy measurements. For the dispersion prepared here using 670 nm as the wavelength of A exciton, this gives an average thickness of 6 layers per sheet of MoS_2.[28]

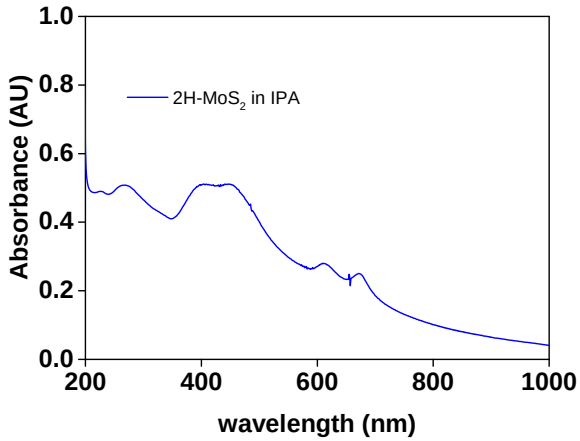

Fig. 2.19 UV-vis spectrum of 2H-MoS_2 in IPA.

ATR-IR Spectroscopy

The IR spectrum of 2H-MoS_2 was expected to be featureless, similar to the spectra of graphene and ce-1T-MoS_2. The spectrum of the prepared 2H-MoS_2 detected very weak peaks which were attributed to small amounts of intercalated IPA from liquid exfoliation (Figure 2.20).

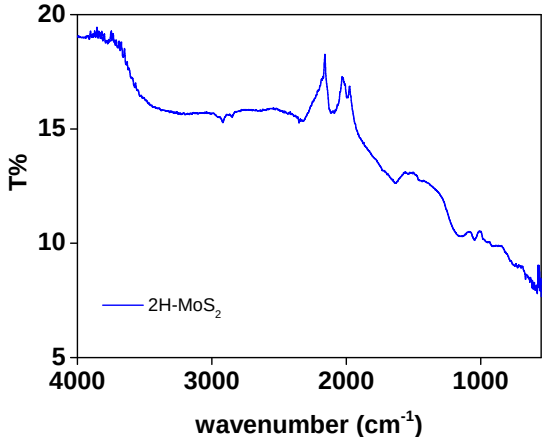

Fig. 2.20 ATR-IR spectrum of 2H-MoS_2.

Thermogravimetric Analysis

The TGA trace of 2H-MoS_2 showed weight losses of 1% below 200 °C, 2% below 400 °C and 8% observed below 600 °C (Figure 2.21). These small amounts of weight loss

at lower temperatures, with the help of ATR-IR, were assigned to residual solvent from liquid exfoliation. The nature of the weight loss at these and higher temperatures was later investigated through the use of coupled TGA-IR.

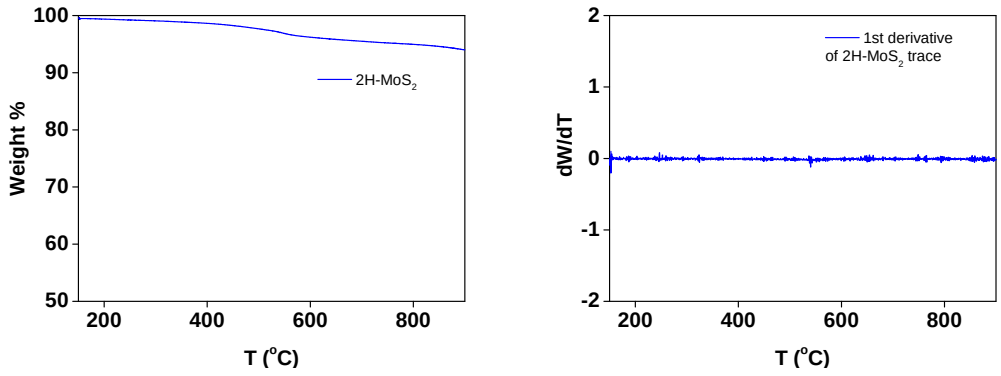

(a) (b)

Fig. 2.21 TGA trace (a) and its corresponding 1st derivative trace (b) of 2H-MoS_2 under nitrogen.

Coupled TGA-IR

TGA-IR analysis showed weak CO_2 stretches (max. 5 T%) at 2350 and 2320 cm^{-1} starting at 480 °C. SO_2 stretches (max. 15 T%) were detected at 1380 and 1350 cm^{-1}, from 480 °C, and grew to their highest T% at 600 °C before disappearing at 690 °C (Figure 2.22).[36] The detection of SO_2 may point to oxidative damage from long sonication times during exfoliation, or the presence of oxides in the starting material, which was also noted in XPS.[37] The presence of a small amount of CO_2 was in agreement with the organic residue detected in the ATR-IR and below, in the XPS analysis. The low concentrations of CO_2 and SO_2 detected by TGA-IR supported the formation of a dispersion of pristine 2H-MoS_2.

Raman Spectroscopy

The Raman spectrum also confirmed the presence of pristine 2H-MoS_2. It displayed several characteristic peaks: three peaks at 385 (E^1_{2g}), 407 (A_{1g}) and 460 cm^{-1} (2LA(M)). The E^1_{2g} (385 cm^{-1} which is also IR active) and A_{1g} (407 cm^{-1}) signals, as explained in the previous section, provide insight into the number of layers of MoS_2.[31] For the 2H-MoS_2 used here,

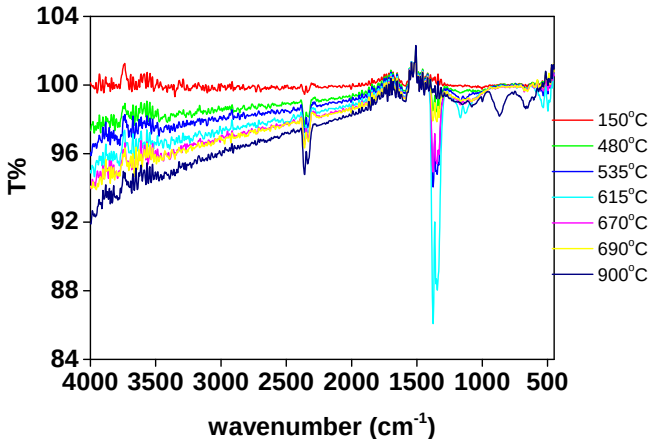

Fig. 2.22 TGA-IR spectra of 2H-MoS_2 at the stated temperatures.

the E^1_{2g}-A_{1g} distance was 22 cm^{-1} (Figure 2.23a). The resonant signal 2LA(M) (453 cm^{-1}), can vary in intensity with respect to (A_{1g}) in response to changes in the surface properties of MoS_2.[32] The ratio of intensity of the resonant signal 2LA(M) to A_{1g} was 0.94 for the 2H-MoS_2, using the 633 nm line (Figure 2.23b). The 532 nm laser line gave a lower intensity of the 2LA(M) peak of 0.10.

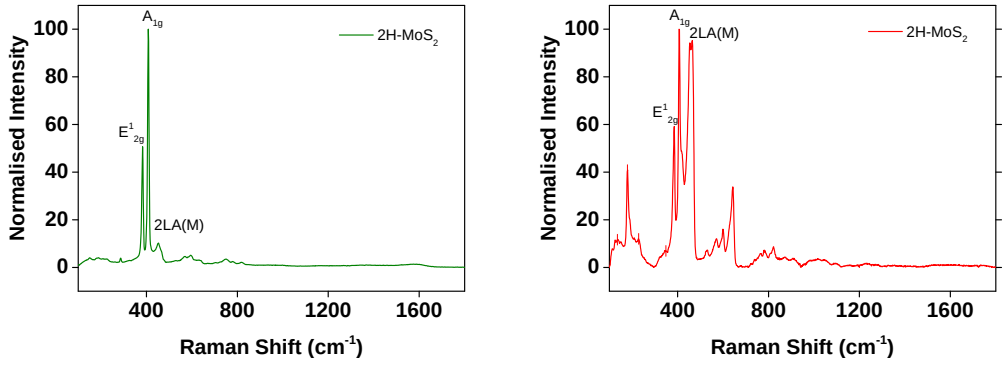

Fig. 2.23 Raman spectra of 2H-MoS_2 taken using the (a) 532 nm and (b) 633 nm laser lines.

X-Ray Photoelectron Spectroscopy

The survey spectra of 2H-MoS_2, as with ce-1T-MoS_2 confirmed the presence of Mo and S with C and O also detected (Figure 2.24). The concentration of each species was calculated to

be 51% S, 26% Mo, 16% C and 7% O. As with ce-1T-MoS_2, the high concentration of carbon and oxygen, compared to other spectroscopic techniques, was inferred to be adventitious carbon and oxygen deposited during preparation of the films for XPS.[33] No other elements were detected. Analysis of the Mo 3d core level spectrum gave a total of 84% 2H-MoS_2 at 229.5 (3/5) and 231 eV (2/5) with S 2s contributions at 227 eV (11%) and small quantities of Mo oxides at 235 eV (5%). The two components of S 2p were fitted at 163.0 and 164.5 eV respectively. The C 1s spectrum of 2H-MoS_2 showed a small feature that could be approximately assigned as 60% saturated carbon at 284.8 eV and 40% oxygenated carbon at 285.5 eV.

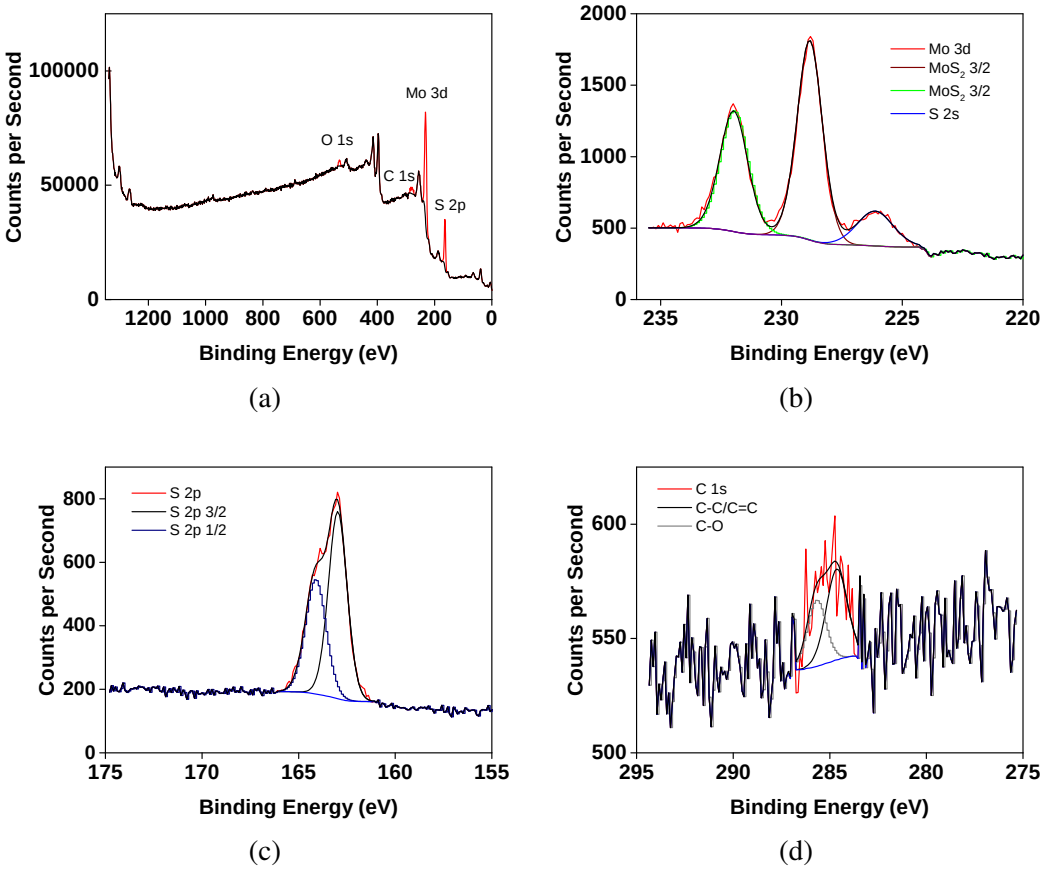

Fig. 2.24 (a) Survey spectrum, (b) Mo 3d, (c) S 2p and (d) C 1s core level spectra of 2H-MoS_2.

Powder X-ray Diffraction

The pXRD pattern for 2H-MoS_2 matched those of the reference pattern for 2H-MoS_2 well, in contrast to ce-1T-MoS_2 (Figure 2.25) demonstrating the pristine nature of liquid exfoliated 2H-MoS_2. The largest peak appeared at $2\theta = 14°$, corresponding to the (002) plane of MoS_2. The relative intensity of (002) compared to the other peaks present was much greater than that seen for ce-1T-MoS_2, suggesting a lesser degree of exfoliation. This was to be expected, as chemical exfoliation produces more monolayer MoS_2 than liquid exfoliation alone.[38]

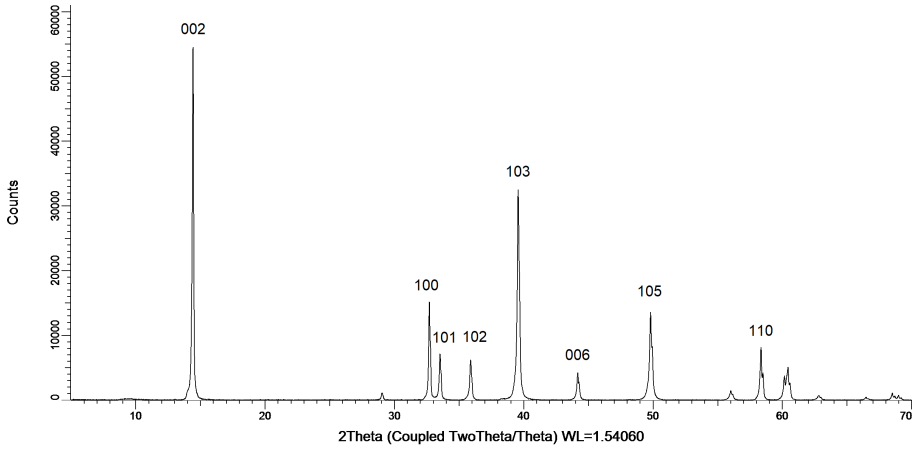

Fig. 2.25 Powder X-ray diffractogram of 2H-MoS_2 with diffraction planes labelled.

Scanning Electron Microscopy

SEM images of 2H-MoS_2 displayed smooth flakes of similar morphology but much smaller size compared to graphene, at 0.39 ± 0.04 μm in length (Figure 2.26). These small flakes were larger than those seen in the SEM images of ce-1T-MoS_2, demonstrating the harsher nature of chemical exfoliation compared to liquid exfoliation.

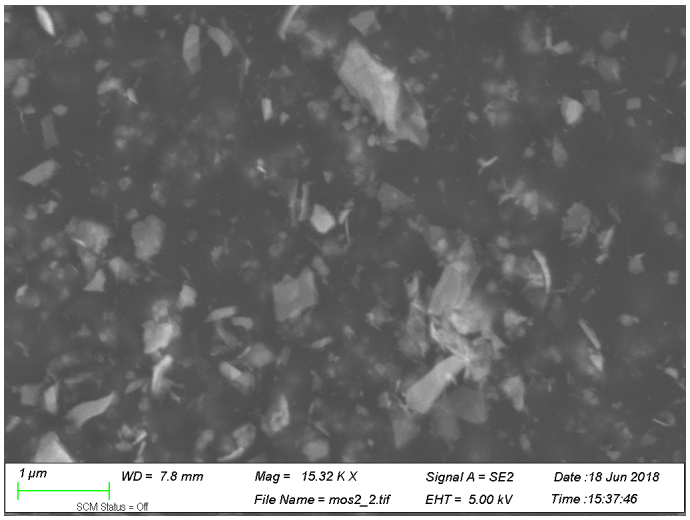

Fig. 2.26 SEM image of 2H-MoS_2 in secondary electron mode.

2.5 Methods and Instrumentation

HPLC-grade IPA and dimethyl sulfoxide were purchased from Fisher Scientific UK. Deionised water, SGN18 synthetic graphite and PP10 natural graphite were used as received. Bulk MoS_2 powder and n-BuLi (1.6 M in hexanes) were purchased from Sigma-Aldrich Co. Bulk MoS_2 was sonicated using a Sonics Vibra Cell solid tip under ice cooling (60% amplitude, pulse 6s on 2s off) for 1 h, centrifuged in a Thermo Scientific Heraeus Megafuge 16 using a Fibrolite carbon fibre rotor, at 11000 rpm for 1 h and the supernatant discarded to dispose of any inorganic salts present before exfoliation. Graphene was exfoliated using a Sonics Vibra Cell solid tip under ice cooling (60% amplitude, pulse 6s on 2s off) without pre-treatment. Rough dispersions of graphene, 2H-MoS_2 and ce-1T-MoS_2 were centrifuged in a Thermo Scientific Heraeus Megafuge 16 with a Fibrolite carbon fibre rotor. If sonication was required for further studies, the collected graphene, 2H-MoS_2 and ce-1T-MoS_2 were bath sonicated using a Branson 3800 ultrasonic bath.

UV-vis spectra were recorded using an Agilent 8453 UV-vis spectrometer. ATR-IR spectra were obtained using a Perkin Elmer Spectrum 100 FT-IR spectrometer with a Universal ATR sampling accessory with a minimum of 10 scans. DRIFT spectra were obtained on a

Perkin Elmer Spectrum One spectrometer and diffuse reflectance accessory, using powdered KBr as a blank and matrix with a minimum of 10 scans. Raman spectra were obtained on a Witec Alpha 300 R confocal Raman microscope with a laser wavelength of 532 nm or 633 nm at a power of 0.5 mW. Raman maps were collated from 49 spectra taken over a 20 μm $\times$ 20 μm range, and overlaid spectra were normalised to the G peak for graphene or the A_{1g} of MoS_2. TGA and TGA-IR traces were obtained using a Perkin Elmer Pyris 1 TGA and Perkin Elmer TG-IR-GCMS Interface TL 8000 spectrometer, and traces were obtained under nitrogen gas, at a rate of 10 °C/min from 150—900 °C. X-ray photoelectron spectra were taken using monochromated Al K X-rays from an Omicron XM1000 MkII X-ray source and an Omicron EA125 energy analyser. The analyser pass energies were 20 eV for the core-level spectra and 200 eV for the survey spectra. Powder X-ray diffraction patterns were obtained using a Bruker D2 Phaser, Cu Kα radiation (λ = 1.54178 Å), scanned over a range of 10°-70° 2θ. SEM images (secondary electron, in lens and backscatter modes) were taken using a Zeiss SEM Ultra. AFM images were taken on an Asylum AFM. Films of materials were spin coated on O_2 plasma-cleaned Si plates before analysis.

References

[1] U. Khan, A. O'Neill, H. Porwal, P. May, K. Nawaz and J. N. Coleman, *Carbon*, 2012, **50**, 470–475.

[2] K. Paton, E. Varrla, C. Backes, V. Nicolosi, J. N. Coleman and et al, *Nature Materials*, 2014, **13**, 624–630.

[3] M. Lotya, P. J. King, U. Khan, S. De and J. N. Coleman, *ACS Nano*, 2010, **4**, 3155–3162.

[4] E. Y. Choi, T. H. Han, J. Hong, J. E. Kim, S. H. Lee, H. W. Kim and S. O. Kim, *Journal of Materials Chemistry*, 2010, **20**, 1907–1912.

[5] R. Prost, *Clays and Clay Minerals*, 1973, **21**, 363–368.

[6] D. R. Dreyer, S. Park, C. Bielawski and R. S. Ruoff, *Chemical Society Reviews*, 2010, **39**, 228–240.

[7] H. Gunzler and H.-U. Gremlich, *IR Spectroscopy*, Wiley VCH, Weinheim, Germany, 2002.

[8] N. Colthup, *Introduction to Infrared and Raman Spectroscopy*, Elsevier, 2012.

[9] V. Singh, D. Joung, L. Zhai, S. Das, K. S. I. and S. S., *Progress in Materials Science*, 2001, **56**, 1178–1271.

[10] L. Malard, M. Pimenta, G. Dresselhaus and M. Dresselhaus, *Physics Reports*, 2009, **473**, 51–87.

[11] V. K. Thakur and M. K. Thakur, *Chemical Functionalisation of Carbon Nanomaterials: Chemistry and Applications*, CRC Press, United States of America, 2015.

[12] A. C. Ferrari, J. C. Meyer, V. Scardaci, C. Casiraghi, M. Lazzeri, F. Mauri, S. Piscanec, D. Jiang, K. S. Novoselov, S. Roth and A. K. Geim, *Physical Review Letters*, 2006, **97**, 187401.

[13] D. Yang, A. Velamakanni, G. Bozoklu, S. Park, M. Stoller, R. D. Piner, S. Stankovich, I. Jung, D. A. Field, C. A. Ventrice and R. S. Ruoff, *Carbon*, 2009, **47**, 145–152.

[14] A. W. Coats and J. P. Redfern, *The Analyst*, 1963, **88**, 906.

[15] N. A. Daud, B. W. Chieng, N. A. I. Talib and Z. Abidin, *Journal of Engineering Science*, 2017, **13**, 1–17.

[16] J. A. Venables, G. D. T. Spiller and M. Hanbucken, *Reports on Progress in Physics*, 1984, **47**, 399.

[17] J. W. London and A. T. Bell, *Journal of Catalysis*, 1973, **31**, 32–40.

[18] P. D. Ghosh, *Introduction to Photoelectron Spectroscopy*, John Wiley & Sons, United States of America, 1984.

[19] M. Velicky, M. A. Bissett, P. S. Toth, H. V., S. D. Worrall, A. N. J. Rodgers, E. W. Hill, I. A. Kinloch, K. S. Novoselov, T. Georgiou, L. Britnell and R. A. W. Dryfe, *Physical Chemistry Chemical Physics*, 2015, **17**, 17844–17853.

[20] L. Liu, M. An, P. Yang and J. Zhang, *Scientific Reports*, 2015, **5**, 9055.

[21] B. E. Warren, *X-Ray Diffraction*, Dover Publications Inc., 1990.

[22] G. Wang, J. Yang, J. Park, X. Gou, B. Wang, H. H. Liu and J. Yao, *Journal of Physical Chemistry C*, 2008, **112**, 8192–8195.

[23] L. Reimer, *Scanning electron microscopy: physics of image formation and microanalysis*, Springer, 2013, vol. 45.

[24] D. C. Joy and C. S. Joy, *Micron*, 1996, **27**, 247–263.

[25] E. Meyer, *Progress in Surface Science*, 1992, **41**, 3–49.

[26] P. Joensen, R. Frindt and S. Morrison, *Materials Research Bulletin*, 1986, **21**, 457–461.

[27] F. Wypych and R. Schöllhorn, *Journal of the Chemical Society Chemical Communications*, 1992, 1386–1388.

[28] C. Backes, R. J. Smith, N. McEvoy, N. C. Berner, D. McCloskey, H. C. Nerl, A. O. Neill, P. J. King, T. Higgins, D. Hanlon, N. Scheuschner, J. Maultzsch, L. Houben, G. S. Duesberg, J. F. Donegan, V. Nicolosi and J. N. Coleman, *Nature Communications*, 2014, **5**, 4576.

[29] C. Backes, B. M. Szydłowska, A. Harvey, S. Yuan, V. Vega-Mayoral, B. R. Davies, P.-l. Zhao, D. Hanlon, E. J. G. Santos, M. I. Katsnelson, W. J. Blau, C. Gadermaier and J. N. Coleman, *ACS Nano*, 2016, **10**, 1589–1601.

[30] E. E. Benson, H. Zhang, S. A. Schuman, S. U. Nanayakkara, N. D. Bronstein, S. Ferrere, J. L. Blackburn and E. M. Miller, *Journal of the American Chemical Society*, 2018, **140**, 441–450.

[31] H. Li, Q. Zhang, C. C. R. Yap, B. K. Tay, T. H. T. Edwin, A. Olivier and D. Baillargeat, *Advanced Functional Materials*, 2012, **22**, 1385–1390.

[32] S. Mignuzzi, A. J. Pollard, N. Bonini, B. Brennan, I. S. Gilmore, M. A. Pimenta, D. Richards and D. Roy, *Physical Review B*, 2015, **91**, 195411.

[33] N. M. Brown, N. Cui and A. McKinley, *Applied Surface Science*, 1998, **134**, 11–21.

[34] K. E. Dungey, M. D. Curtis and J. E. Penner-Hahn, *Chemistry of Materials*, 1983, **10**, 2152–2161.

[35] A. Castellanos-Gomez, J. Quereda, H. P. van der Meulen, N. Agraït and G. Rubio-Bollinger, *Nanotechnology*, 2016, **27**, 115705.

[36] J. P. Dunn, P. R. Koppula, H. G. Stenger and I. E. Wachs, *Applied Catalysis B: Environmental*, 1998, **19**, 103–117.

[37] D. M. Sim, H. J. Han, S. Yim, M.-J. Choi, J. Jeon and Y. S. Jung, *ACS Omega*, 2017, **2**, 4678–4687.

[38] G. Eda, H. Yamaguchi, D. Voiry, T. Fujita, M. Chen and M. Chhowalla, *Nano Letters*, 2011, **11**, 5111–5116.

Chapter 3

Graphene and Its Reactivity towards the Fenton Reagent and High-Valent Iron-Containing Biomimetic Catalysts

3.1 Introduction

Liquid exfoliation, either by sonication or shear forces remains the most cost-effective and scalable method for the production of high quality graphene.[1] This method produces dispersions of graphene and other 2D materials that are more accessible to functionalisation or other modifications using wet chemistry. Therefore, it is one of the most likely forms of graphene to be industrially produced, and as a result, the most likely form of graphene post-consumer waste. This raises the question of what can be done to remove graphene from waste water or landfills, or what adverse effects may arise from graphene coming in contact with the natural world post-exfoliation or functionalisation.[2, 3]

Graphene and Its Reactivity towards the Fenton Reagent and High-Valent Iron-Containing Biomimetic Catalysts

Graphene, as illustrated in the introduction, possesses greatly increased reactivity relative to its parent material, graphite, but is still resistant to chemical attack, similar to other polyaromatic substances.[4] There have been a few attempts to oxidise or degrade different kinds of graphene or graphite reported in the literature—the most well know being the improved preparation of graphite oxide in 1958 by Hummer and Offeman.[5] Subsequent sonication of this graphite intercalated compound (GIC) yielded what is now known as graphene oxide, a defective, oxygen-rich graphene-like compound.[6, 7] However, this method requires high temperatures (98 °C) and the use of several oxidants and acids——$KMnO_4$, H_2SO_4 and H_2O_2 to form the initial GIC. This was later adapted to form oxo-graphene, a form of graphene oxide that still possesses large areas of pristine hexagonal graphitic domains—using $KMnO_4$ and H_2SO_4 at lower temperatures (<10 °C).[8, 9] Aside from incomplete chemical degradation or formation of graphene oxide, only the use of extremely high temperature (>2000 K) laser processing of suspended multilayer graphene in air has been shown to oxidise entire individual layers of graphene to CO_2. This method also has limitations—as the 'burning' progresses, incomplete oxidation of underlying layers results in CO amorphous carbon production instead of the thermodynamic product CO_2. Rather than large scale degradation of graphene, this was developed as a method for the thinning of multilayer graphene or graphite samples.[10]

Partial degradation or functionalisation of graphene has been achieved through adapting electrophilic aromatic substitution and using radical based chemistry[11] such as diazonium functionalisation[12] which will be explored in other chapters. Functionalisation of graphene using H_2O_2 and metal-based oxidants is a nascent area in the field of graphene functionalisation, with only a few somewhat conflicting reports on the efficacy of the Fenton reagent on epitaxial and synthetic graphene.[13–15] There have been some reports on the enzymatic degradation of graphene oxide by horse radish peroxidase (HRP)[16] and human myeloperoxidase[17] but neither of the enzymes have been reported to successfully degrade

pristine graphene. Reduced graphene oxide nanoribbons have been degraded by bacterial lipase[18] and lignin peroxidase[19] but again, rGO-based materials, despite being similar to pristine graphene, are more defective and therefore more susceptible to degradation. To the best of our knowledge there have been no reports of the successful degradation of graphene by enzymatic means. This chapter attempts to address this problem, and expand on the efficacy of a series of inorganic and organic oxidants or oxygenating agents in oxidising or degrading liquid phase exfoliated graphene dispersions.

3.2 Reacting Common Laboratory Oxidants with Graphene

This section deals with the treatment of dispersions of few-layer graphene with hydrogen peroxide (H_2O_2), tert-butyl hydroperoxide (^{t}BuOOH), peracetic acid ($PhCO_3H$), *meta*-chloroperbenzoic acid (*m*-CPBA), diacetoxy iodosylbenzene (DAIB) and iodosylbenzene (PhIO). 1 mM dispersions of few-layer graphene were freshly prepared and stirred overnight at room temperature with 10 equivalents of an oxidant. Each sample was subjected to TGA, ATR-IR or DRIFT-IR spectroscopy and Raman spectroscopy for analysis, while some samples were also analysed by XPS. In all cases, flocculation of graphene occurred when stirred with the oxidants overnight, but no change in colour of the re-aggregated graphene was observed.

3.2.1 Reactivity of Peroxides towards Few-Layer Graphene

As H_2O_2 was the primary oxidant used in the preparation of high valent Fe species used later in this chapter, it was imperative to establish the effect, if any, that H_2O_2 had on pristine graphene before combining it with Fenton's reagent or the other Fe catalysts. The results presented here show the effect of H_2O_2 on few-layer graphene prepared from synthetic (SGN18) and natural (PP10) graphite.

A 10 mM solution of H_2O_2 was added to a graphene dispersion and stirred at room temperature overnight. The graphene was collected by centrifuge and dried prior to analysis. The powders obtained were analysed by TGA, TGA-IR, XPS and Raman spectroscopy. The TGA results showed very little weight loss (1%) before 600 °C (Figure 3.2b). This was comparable with the weight loss demonstrated by the SGN18 graphene control in the same temperature range (<1%, Figure 2.5). That the mass remained unchanged before 250 °C showed sufficient drying of the samples before analysis and a lack of physisorbed material. Any covalently bonded functional groups on the carbon framework would have been lost in

the temperature range of 300–500 °C before re-aggregated graphene decomposition at 600 °C and this was not seen. When this experiment was repeated with PP10 graphene, similar results were obtained—TGA also showed little (<1%) to no weight loss. The derivative traces of the TGA also show no major changes in the rate of weight loss until the degradation temperature at 600°C (Figure 3.2c). Therefore, by TGA analysis, H_2O_2 treatment had no effect on the prepared graphene dispersions.

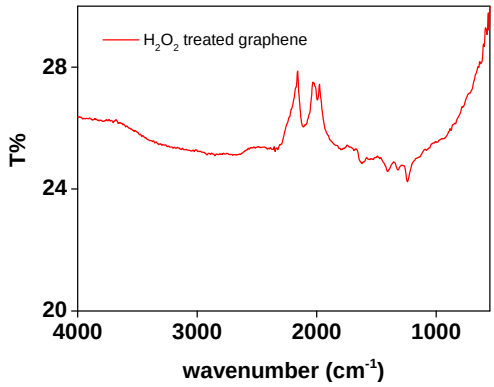

Fig. 3.1 ATR-IR spectrum of H_2O_2 treated graphene.

The ATR-IR spectrum of the H_2O_2 treated PP10 graphene (Figure 3.1), also showed no difference to either of the control graphene spectra. Any peaks that were seen in graphene treated with H_2O_2 were also seen in the spectra of graphene control (Figure 2.2) and showed no sign of shifting or an increase in intensity. Thus, the IR spectra are in agreement with the TGA results, showing no evidence of oxidation occurring.

As seen in the Raman spectrum of H_2O_2 treated graphene in Figure 3.2a, no change in the ratio of D to G peak intensity (I_D:I_G) outside of experimental error was observed for graphene from SGN18 graphite (0.26 for H_2O_2 treated graphene, within experimental error of 0.25) or for PP10 graphene (no change from 0.12). In agreement with the TGA and IR spectra, this suggested that an insignificant amount of oxidation/degradation of graphene has occurred. The slight change in SGN18 graphene could be due to its increased reactivity from its higher concentration of existing defects.[11]

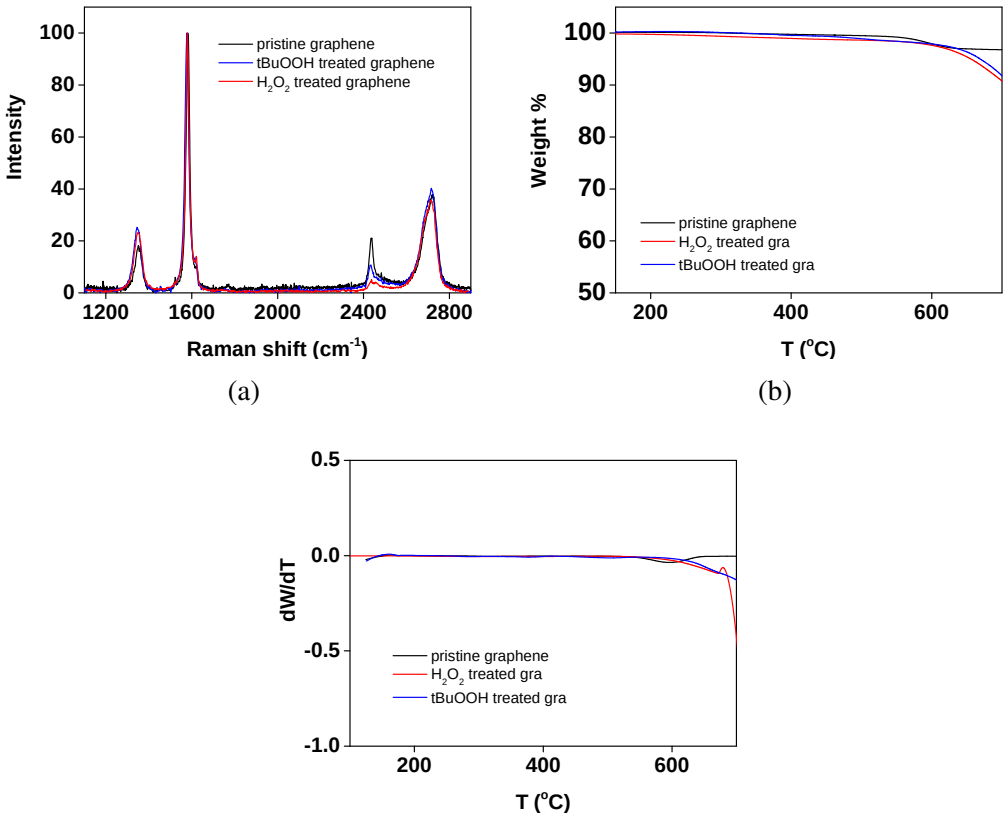

Fig. 3.2 (a) The Raman spectra of H_2O_2 treated SGN18 graphene (red) ^{t}BuOOH treated graphene (blue) and pristine SGN18 graphene (black). (b) TGA traces and (c) 1st derivative traces showing H_2O_2 treated graphene (red) ^{t}BuOOH treated graphene (blue) and pristine graphene (black).

The effect of H_2O_2 on PP10 graphene was also investigated *via* XPS—in agreement with other techniques, the spectrum did not show any new peaks that would be characteristic of new functional groups (Figure 3.3). Carbon and oxygen were the only elements detected in the survey spectrum (with concentrations of 97% and 3% respectively) and when compared to pristine graphene, the level of oxygen present in the survey spectrum were within experimental error (96% C, 4% O). In the core spectra, specifically the C1s spectrum, the levels of C-O and COOH remained at 3%. All analytical techniques employed in the characterisation of these samples showed no sign of functionalisation, allowing the conclusion to be drawn that H_2O_2 is not a strong enough oxidant to degrade the few-layer graphene dispersions

prepared herein. This is in agreement with the literature regarding the limited action of H_2O_2 on epitaxial graphene.[14] This is particularly true for few-layer graphene, which shows lowered reactivity compared to mono- or bilayer graphene.[20]

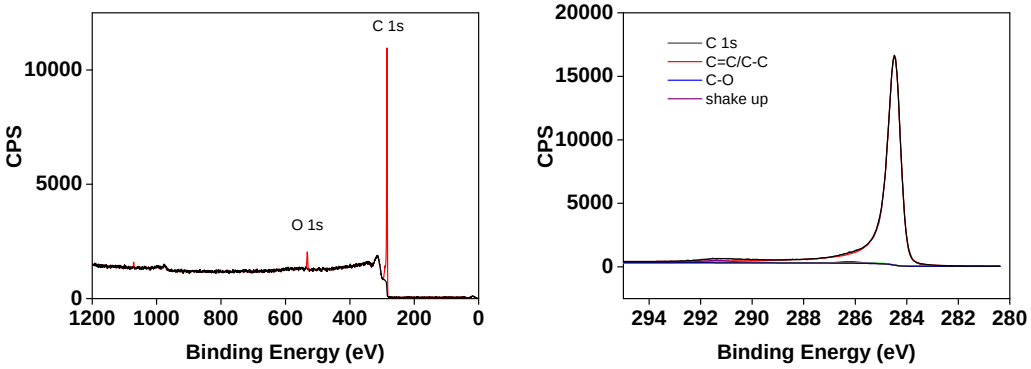

(a) (b)

Fig. 3.3 The survey spectrum (a) and C 1s spectrum (b) of H_2O_2 treated graphene.

Tert-butyl hydroperoxide (^{t}BuOOH), an organic peroxide, is used to oxidise alkenes in reactions such as Sharpless epoxidation.[21] This was also tested to investigate whether organic peroxides could oxidise graphene. It also produces highly reactive radicals on decomposition[22] and in so far as the author is aware, the reactivity of ^{t}BuOOH towards graphene has not been reported. The procedure was similar to that used for treating graphene dispersions with H_2O_2—10 equivalents of ^{t}BuOOH (70% in H_2O) were added to a dispersion of SGN18 graphene in IPA or a dispersion of PP10 graphene in MeCN and stirred for 12 hours at RT, before the material was centrifuged down and washed with solvent.

When analysed by TGA and Raman spectroscopy, ^{t}BuOOH treated graphene samples demonstrated no detectable levels of functionalisation, similar to that seen in H_2O_2 (Figure 3.1). TGA traces of samples after treatment with ^{t}BuOOH showed weight losses between 200–600 °C of less than 1%, again suggesting that no functionalisation has occurred. This was consistent for both sources of graphene. Similarly to H_2O_2, the Raman spectrum for ^{t}BuOOH treated graphene showed little difference in I_D:I_G ratio for either SGN18 or

PP10 graphene, changing slightly for SGN18 graphene (from 0.25 for pristine to 0.26) and remaining at 0.12 for PP10 graphene. This again showed that no significant defect formation has occurred in the graphene from exposure to this oxidant. Therefore, LPE graphene did not undergo degradation upon treatment with either peroxide used in this study.

3.2.2 Reactivity of Peracids towards Few-Layer Graphene

Peracetic acid was chosen as an oxidant as it is often used with metal complexes and catalysts to generate powerful oxidants. It could be used in conjunction with high valent iron complexes, used later in the study, to form highly oxidising intermediates that may have the potential to degrade graphene.[23, 24] Similar to the experiments using H_2O_2, 10 equivalents of peracetic acid (32% in dilute acetic acid) was added to a fresh dispersion of graphene (either SGN18 in IPA or PP10 in MeCN) and left to stir for 12 h, with centrifuging at 4500 rpm and washing with solvent as work up. In conjunction with this experiment, a control experiment in which acetic acid was added to the graphene dispersion was carried out (Figure A.3) to account for the presence of acetic acid in the peracetic acid solution. The samples were then analysed by DRIFT-IR, TGA, and Raman spectroscopy.

DRIFT-IR (Figure A.2) gave a spectrum showing good overlap with the pristine graphene control. Despite this, some peaks showed lower R% and therefore higher intensity in the areas of ν = 3500 cm^{-1} (O-H stretch), some peaks around 3000 cm^{-1} (C-H stretch) and possibly a very weak C=O stretch at approximately 1650 cm^{-1}. These could be assigned as oxidised areas of graphene, but also as residual acid. TGA and Raman spectroscopy were employed to further investigate the nature of the peaks seen in DRIFT-IR.

Initial TGA results showed that graphene treated with peracetic acid underwent the most significant weight loss of all of the oxidants tested. The bulk of this occurred before 200 °C and can be disregarded as thermal decomposition of physisorbed acid and solvent evaporation.

Similar weight loss was also detected for graphene treated with acetic acid, as shown in the TGA trace in Figure A.3. This was believed to be physisorption, not functionalisation. To overcome this, samples were washed and centrifuged, then subjected to drying at 150 °C to remove any residual acid. The TGA traces were run under N_2, and continued to show weight loss at temperatures of >200 °C, as seen in Figure 3.4b below, up to 4%. This was also reflected in the inflection step at 400°C in the derivative trace (Figure 3.4c). This was the highest in this temperature range for any of the oxidants tested with graphene. This could be attributed to the decomposition of covalently bonded oxygen groups on graphene, introduced by the peracid. This would support the assignment of some oxygen-containing bonds as seen in the DRIFT-IR.

The Raman spectrum (Figure 3.4a) for peracetic acid treated graphene showed an insignificant decrease in I_D:I_G, from 0.25 for the pristine SGN18 graphene control, to 0.24. The Raman spectrum of the control experiment, acetic acid treated graphene, showed an I_D:I_G of 0.25 compared to the pristine graphene control. For PP10 graphene, this ratio remained unchanged as 0.12 for both peracetic acid treated graphene and for acetic acid treated graphene. A lack of change in this ratio points to little or no functionalisation, as the increase in intensity of the D peak corresponds to an increase in defects in the graphene structure, which can be caused by the insertion of functional groups and the destruction of aromaticity/saturation of carbon bonds.

Both IR and TGA analysis pointed to some functionalisation of graphene occurring in the presence of peracetic acid. However, Raman spectroscopy showed minimal change in the spectra of treated samples compared to pristine samples. The use of AFM or pXRD should provide insight into whether functionalisation has occurred, or the acid has intercalated between the sheets of re-aggregated graphene. This could explain the weight loss seen in TGA and the lack of functionalisation noted in the Raman spectrum. With regards to

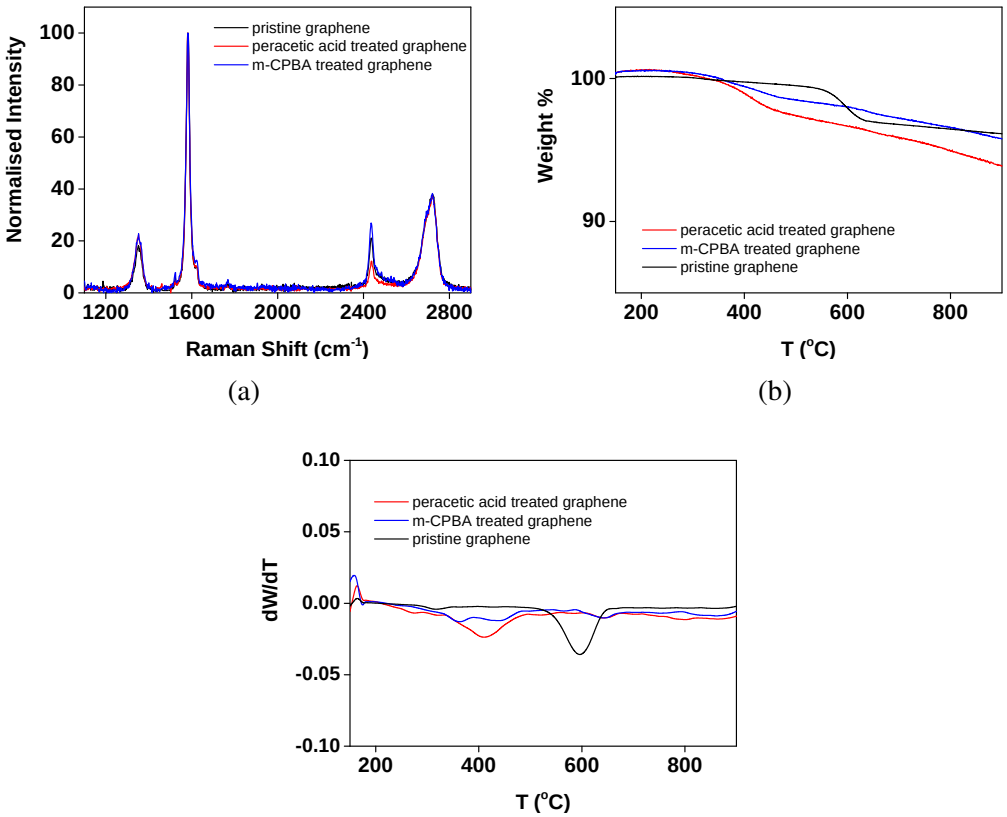

Fig. 3.4 (a) Raman spectra of peracetic acid treated graphene (red) *m*-CPBA treated graphene (blue) and pristine graphene (black). (b) TGA traces and (c) 1st derivative traces of peracetic acid treated graphene (red), *m*-CPBA treated graphene (blue) under N_2.

degradation of graphene, it may be more useful to look into the efficacy of peracetic acid in generating an oxidant with the Fe catalysts that will be discussed later.

Like peracetic acid, *meta*-chloroperbenzoic acid (*m*-CPBA) is a peracid, used as an oxygenating donating agent,[25] and possesses an aromatic ring which could assist in intercalation into the graphene structure and facilitate oxidation. The literature for *m*-CPBA acting on graphene is sparse but does show *m*-CPBA having some ability to functionalise graphene with epoxide groups.[26] After treating a dispersion of few layer graphene with 10 equivalents of *m*-CPBA, the samples were centrifuged and washed in a similar manner to the oxidant tests described previously and analysed using TGA, DRIFT-IR and Raman spectroscopy.

The TGA trace displayed some weight loss after washing (1%) but this did not reach the weight losses seen for peracetic acid (Figure 3.4b, A.4). The 1st derivative trace similarly showed very small changes in rate over the temperature range (Figure 3.4c). The DRIFT-IR spectrum (Figure A.3) was similar to the peracetic acid results, with what could be weak carbonyl and C-O stretches at approximately 1700 cm^{-1} and 1500 cm^{-1} respectively. As it has been previously reported that *m*-CPBA can functionalise epitaxial graphene, this could be interpreted as low level functionalisation of few-layer graphene. However, unlike peracetic acid treated graphene, the weight loss in the TGA did not support this.[26]

The Raman spectra for *m*-CPBA showed no significant change in I_D:I_G for SGN18 graphene, although the D+D" peak, centred around 2440 cm^{-1} showed a marked increase in relative intensity (Figure 3.4a). This peak is not often directly associated with defect formation, and tends to increase in conjunction with the D peak. To see it increase without a corresponding increase in the D peak was unusual. This change was not seen in PP10 graphene, showing only a small change within experimental error in the I_D:I_G ratio to 0.14 from 0.12. The Raman spectra for graphene treated with either peracid showed no significant increase in the intensity of the D peak, which normally signifies an increase in defect concentration. Instead of being used to degrade graphene alone, these oxidants could be used in conjunction with the metal-based catalysts in future to produce highly reactive species that may show greater reactivity towards few-layer graphene.

3.2.3 Reactivity of Iodosyl Arene Oxidants Towards Graphene

Two iodine-containing oxo transfer agents, diacetoxy iodobenzene (DAIB) and iodosyl benzene (PhIO) were also investigated for reactivity towards few layer graphene. DAIB and PhIO are oxygen atom transfer reagents that are commonly used in conjunction with metal catalysts,[27] much like *m*-CPBA. As with the other oxidants tested, 10 equivalents of DAIB

or PhIO were added to a dispersion of graphene and left to stir for 16 hours before work up and analysis.

TGA traces of graphene treated with DAIB or PhIO (Figure 3.5b) obtained were almost identical to those of the control graphene—weight losses at high temperatures are <1% before reaching the degradation temperature of re-aggregated graphene in air. Prior to washing, the TGA showed particularly large weight losses of 70% at 200 °C for DAIB-treated graphene and 10% at 420 °C for PhIO treated graphene. These were reflected in the inflection points of the 1st derivative traces (Figure A.4b). Control TGA traces of DAIB and PhIO revealed that the thermal decomposition temperatures of the oxidants matched the mass loss observed in the TGA traces for DAIB treated graphene (200 °C, Figure A.4), thus implying that the oxidant was merely physisorbed to the re-aggregated graphene surface after treatment. This was believed to be due to the strong $\pi - \pi$ interactions between the aromatic groups of DAIB and PhIO and the basal planes of graphene. The weight loss for PhIO occurred at much higher temperatures (420 °C) than the degradation temperature of PhIO in the furnace (two steps, 100 °C and 210 °C, Figure A.4). This could have been assigned to functionalisation of the underlying graphene by PhIO. However, the weight losses observed for both DAIB and PhIO treated graphene were eliminated after three washing and centrifuging cycles, confirming the physisorbed nature of the material on graphene.

The Raman spectra supported the TGA analysis—the I_D:I_G for SGN18 graphene treated with either iodosyl reagent showed no increase (0.25) when treated with either DAIB or PhIO, and similarly, in PP10, the I_D:I_G remained at 0.12 (Figure 3.5a). This clearly showed that no oxygen-donation occurred using these oxidants.

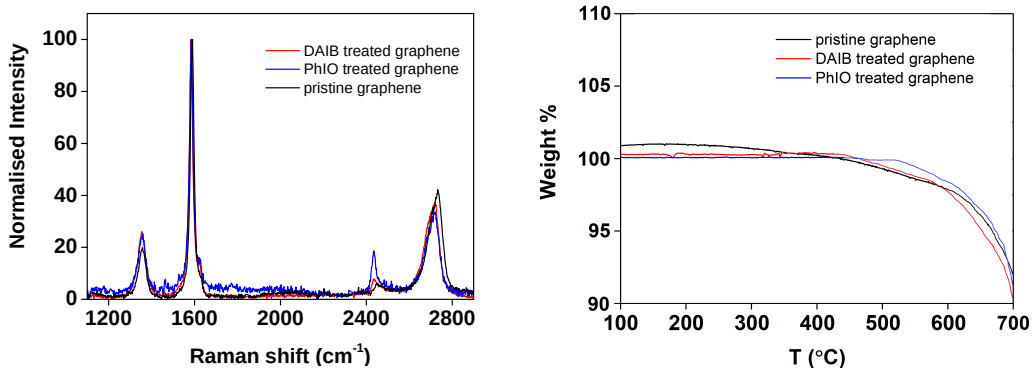

(a) (b)

Fig. 3.5 (a) Raman spectra of graphene treated with DAIB (red) and PhIO (blue) with pristine graphene (black). (b) TGA traces run under nitrogen, showing DAIB treated graphene (red) or PhIO treated graphene (blue).

3.2.4 Summary

In summary, evidence for the oxidation of graphene by the oxidants presented here was mixed. Importantly for the next section, in which catalysts are used in conjunction with H_2O_2, no functionalisation of graphene by H_2O_2 and tBuOOH was observed by DRIFT-IR, TGA or XPS. Clearly, peroxides alone are not reactive enough to functionalise few-layer graphene.

For the peracids, peracetic acid and *m*-CPBA, low levels of functionalisation were seen in the DRIFT-IR for peracetic acid and *m*-CPBA, but only peracetic acid showed a corresponding increase in weight loss observed compared to pristine graphene. All of the oxidants showed no significant increase to the I_D:I_G in the Raman spectra which precluded defect formation occurring. However, there was an increase in the D+D" peak which is associated with defect formation for *m*-CPBA, but without corresponding changes in the D and G' peaks. There was no change in the Raman spectrum for peracetic acid treated graphene. The TGA traces for peracetic acid, despite washing, regularly showed mass loss at low temperatures as well as loss at thermolysis temperatures, up to 4% in total. The persistent

weight loss from the TGA trace of peracetic acid despite repeated drying and washing could be a result of the intercalation of the acid between the re-aggregated graphene sheets, rather than functionalisation. More comprehensive testing of this would be to measure the increase, if any, of the interlayer spacing *via* XRD. It may also be worth investigating the reaction of *m*-CPBA with graphene further by these methods, despite the minimal weight loss (typically 1%) for *m*-CPBA.

TGA also showed some anomalies with DAIB and PhIO treated graphene. Copious washing was needed to remove physisorbed DAIB and PhIO from graphene, eliminating weight loss from the TGA. Both iodosyl oxidants are structurally very similar; both contain an aromatic ring with an iodosyl substituent, in the case of DAIB, and this may lead to π-π interactions exacerbating normal physisorption of material on graphene.

In conclusion, the results of peracetic acid and to a lesser extent, *m*-CPBA treated graphene suggested small amounts of functionalisation, whereas H_2O_2, tBuOOH, DAIB and PhIO showed no ability to functionalise or degrade graphene by Raman, DRIFT-IR, TGA and XPS analysis.

3.3 Reactivity of Fenton's Reagent Toward Graphene

In order to test the reactivity of Fenton's reagent with few-layer pristine graphene, Fenton's reagent—here, $FeCl_2$ and 10 equivalents of H_2O_2, each in 5 mL MeCN, were simultaneously added in aliquots to a degassed dispersion of PP10 graphene that was sonicated in MeCN for 3 h prior to addition. The mixture was then kept under N_2 and left to stir overnight. Flocculation of graphene would occur when stirring was halted. The mixture was then subjected to three cycles of washing/centrifuging—– twice with 0.1 M HCl and once with MeCN prior to analysis, in order to remove the large amounts of iron oxide that formed as a by-product of the Fenton chemistry.[28] The Fenton-treated graphene was then analysed by TGA, TGA-IR, DRIFT-IR, Raman spectroscopy, and XPS. Control experiments included a graphene dispersion stirred in MeCN without any metal salt or oxidant, the Fenton reagent stirred in MeCN in the absence of graphene, and $FeCl_2$ without H_2O_2 added to a graphene dispersion in MeCN, all under N_2.

Three different concentrations of Fenton's reagent (with respect to graphene) were investigated in this study. The ratios studied were stoichiometric (100% mol/mol), 50% mol/mol and 10% mol/mol of Fe catalyst to graphene, with graphene taken as the mass of carbon (12 g/mol). For all experiments, [H_2O_2] were maintained at 10 times [$FeCl_2$] and the pH kept under 4 to ensure optimal Fenton conditions.[29]

3.3.1 Results

TGA analysis was conducted under N_2 on washed and dried samples of re-aggregated graphene that had been treated with Fenton's reagent as detailed above. The TGA traces for washed Fenton-treated graphene then showed <1% weight loss up to 250 °C, confirming the removal of solvent and physisorbed material through adequate washing. The samples then consistently showed an average of 3% weight loss up to 600 °C for stoichiometric and

50% mol/mol (Figure 3.6a) and 4% for 10% mol/mol. The weight losses for these were larger than that seen in the control experiments (<1% for pristine, 1% for $FeCl_2$ treated graphene) and can be attributed to the thermolysis of small levels of functional groups from the re-aggregated graphene. It appeared that 10% and 50% mol/mol concentrations of Fenton reagent were enough to oxidise graphene to a detectable level according to TGA. However, the 1^2 derivative traces showed no obvious changes in rate of weight loss. This could mean that any weight lost from the Fenton treated graphene was lost very gradually over a considerable range, with no sudden drops in weight which matches the TGA trace. This was likely either due to the low loading and heterogeneous nature of the oxidation that could be induced by the Fenton reagent. In the case of heterogeneous groups, these would be lost at several different temperatures, and could contribute to a steady loss of weight over a large temperature range (Figure 3.6b).

Initially, TGA traces of the unwashed stoichiometric and 50% mol/mol samples showed weight losses of 15% before 200 °C. The mass loss then increased to 27% (stoichiometric amounts of Fenton reagent) and 36% (50% mol/mol) before 400 °C (Figure A.5). However, these losses could not be directly attributed to covalent bonding to the graphene sheets. These were compared to the control experiment in which the Fenton reagent was stirred without graphene in MeCN. These traces showed that the iron oxides formed lost an average 32% of total mass below 200°C rising to 49% before 400 °C and 71% was lost by 600 °C (Figure A.5). Comparing the data to the control TGA trace and the 1^{st} derivative trace, it was inferred that most of the mass loss from unwashed, Fenton-treated graphene was indeed coming from the decomposition of the spent catalyst. This was hiding any possible mass lost from the treated graphene. As mentioned above, this was counteracted by employing multiple solvent and acid (0.1 M HCl) washing/centrifuging cycles to eliminate the spent iron catalyst from dried samples.

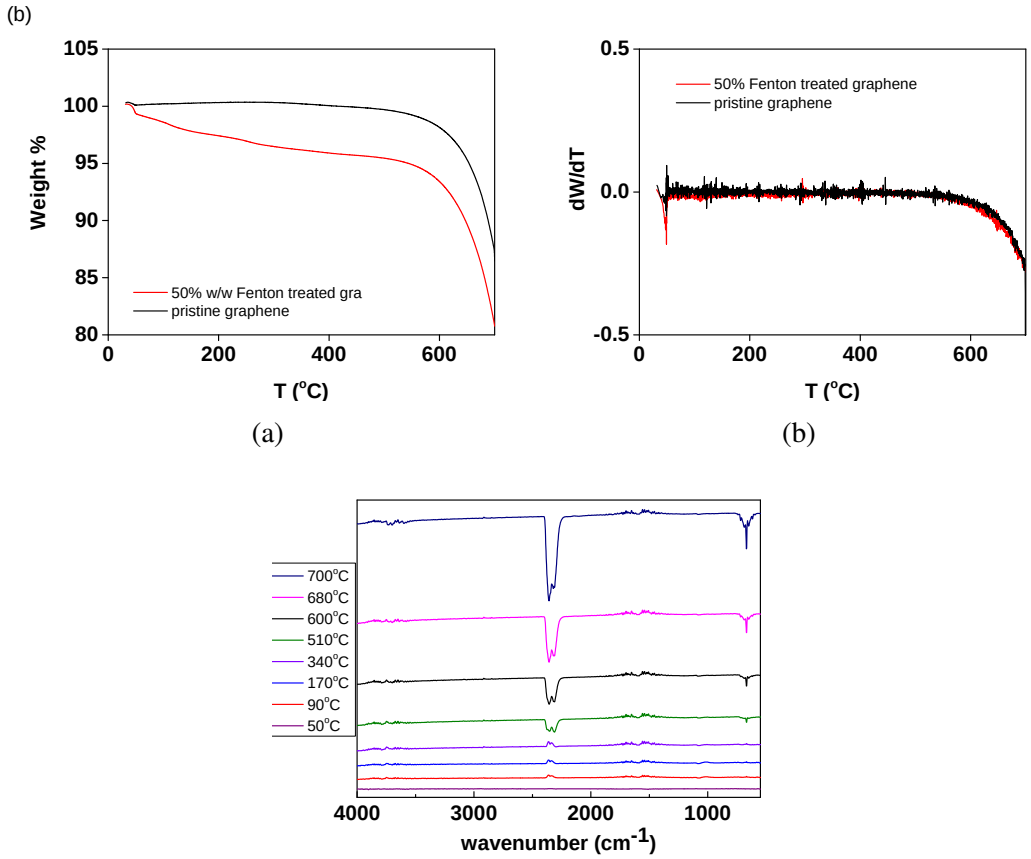

Fig. 3.6 (a) The TGA traces and (b) 1st derivatives of 50% Fenton treated graphene (red) and pristine graphene (black). (c) the TGA-IR spectra showing the evolution of CO_2 as T increases from 50% mol/mol Fenton-treated graphene.

To identify any of the functional groups coming off the graphene samples, washed samples of 50% mol/mol experiments were further investigated by coupled TGA-IR (Figure 3.6c). Comparing the Fenton treated graphene TGA-IR to pristine graphene, spectra up to 250 °C were similar, but a distinct CO_2 stretching vibration at 2358 and 2308 cm^{-1} consistently became visible at lower temperatures (500 °C) and at higher intensity in the IR spectra from 10% mol/mol, 50% mol/mol and stoichiometric Fenton treated graphene compared to the pristine graphene (600 °C). Coupled with the small increase in weight loss seen at the same temperature range in the TGA, this suggested that low-level functionalisation of the graphene by Fenton's reagent had occurred.

Possible sources for the CO_2 observed in the TGA-IR spectra could be seen in the DRIFT-IR spectra for the 50% mol/mol Fenton-treated graphene (Figure 3.7). In the DRIFT-IR spectrum of pristine graphene, an O-H stretch was visible at approximately 3600 cm^{-1} and other low intensity peaks are seen in the region of 1000-1500 cm^{-1}, which could be attributed to C-O/C=C stretches at higher wavenumbers and C-O bends at lower wavenumbers. The DRIFT-IR spectra highlighted showed signals corresponding to O-H stretches (3500-3700 cm^{-1}), C=O stretches (1691 cm^{-1}) and C-O stretches (1259 cm^{-1}), all of which are higher in intensity compared to the control. Coupled with the low levels of mass loss in the TGA, DRIFT-IR spectra could mean that these functional groups are present only on the surface/edges or top layer of few-layer graphene.

X-ray photoelectron spectroscopy was employed in the analysis of the Fenton experiments to detect any changes in the levels of functionalisation of the Fenton-treated graphene compared to the control in the C 1s core spectrum. The survey spectra for 10% mol/mol Fenton-treated graphene showed the presence of C, O and despite washing, residual Fe. This was also seen in the spectra for 50% mol/mol and stoichiometric or equivalent mol/mol Fenton-treated graphene (Figures A.6–A.8). The concentration of the elements detected in

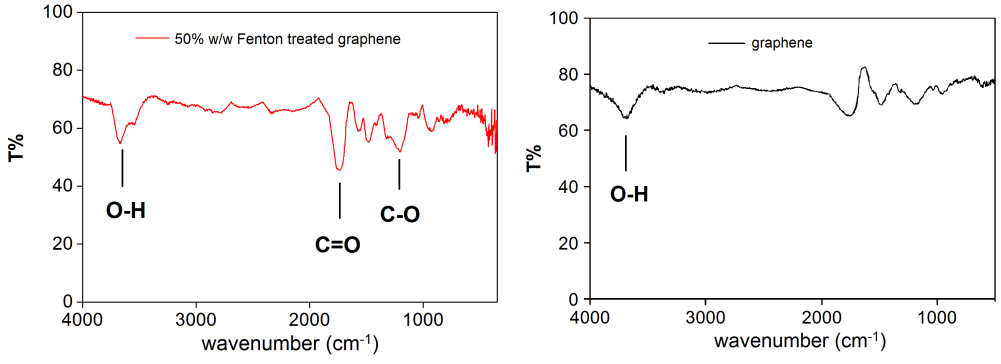

(a) (b)

Fig. 3.7 The DRIFT-IR spectra for (a) 50% mol/mol Fenton-treated graphene and (b) pristine graphene.

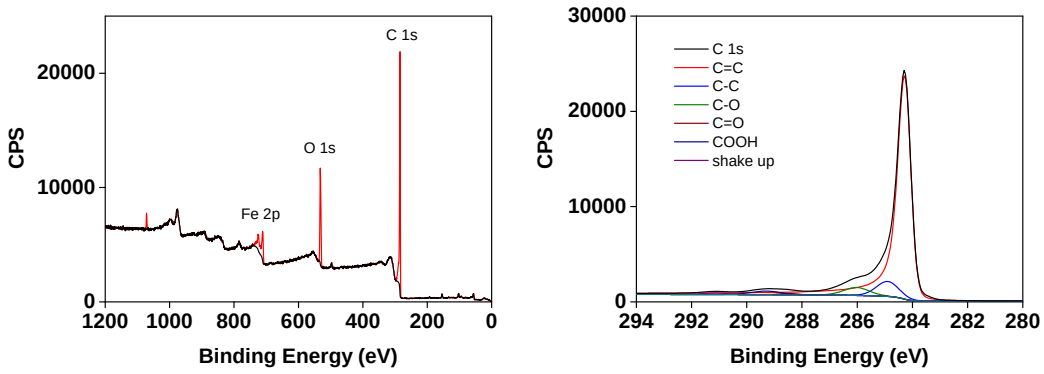

(a) (b)

Fig. 3.8 High resolution (a) survey spectrum and (b) C 1s core level spectrum of 50% mol/mol Fenton treated graphene. The scan and fitting were provided by Dr. Nina Berner.

the survey spectrum for Fenton-treated graphene samples was approximately 84% C, 14% O and 2% Fe for for 10% mol/mol, 86% C, 11% O and 3% Fe for Fe 50% mol/mol and 86% C, 12% O and 2% Fe for stoichiometric Fenton treated graphene, compared to 96% C and 4% O for graphene (Figure 3.8a). This showed an increase in overall oxygen content which could be attributed to oxidative functionalisation of graphene.

The C 1s core level spectrum was analysed for evidence of oxidation (Figure 3.8b). For 10% Fenton-treated graphene, the components of the C 1s peak were fitted as 77% C=C (284.4 eV), 15% C-C/C-O (284.8-285.5 eV), 3% C=O (287.0 eV) and 5% as a shake up feature (291 eV). Compared to the C 1s peak of pristine graphene, where C=C contributed to 89%, this shows that a degree of oxidation has taken place. In the case of 50% mol/mol, the C 1s peak could be fitted as 87% C=C (284.4 eV), 8% C-C/C-O (284.8-285.5 eV), 1% C=O (287.0 eV), and 3% shake-up (291 eV). The last sample, stoichiometric mol/mol, gave a C 1s core level spectrum that was fitted as such: 80% C=C (284.4 eV), 14% C-C/C-O (284.8-285.8 eV) and 4% shake-up (291 eV). In terms of oxygen content, 10% mol/mol Fenton reagent was the only sample fitted with >1% C=O groups as well as possible C-O groups within the saturated carbon peak, and showed higher levels of oxygen in the survey

spectrum. For XPS at least, graphene treated with lower concentration of Fenton's reagent seemed to undergo the most oxidation.

Fittings of O 1s core level spectra are never accurate due to the contributions from atmospheric oxygen even in UHV,[30] but the O 1s core level spectra were analysed to detect any metal oxides and infer what their contribution to the oxygen content of the sample was. For 10% mol/mol Fenton-treated graphene, the O 1s core level peak was fitted as two components: 74% C-O (531 eV) and 26% Fe-O (529 eV). The O 1s core level spectrum of 50% mol/mol was fitted as 64% C-O (531 eV) and 36% Fe-O (529 eV), and stoichiometric Fenton treated graphene was fitted as 66% C-O (531 eV) and 34% Fe-O (529 eV). The core level spectrum of Fe 2p, in three Fenton-treated samples (10% mol/mol, 50% mol/mol and stoichiometric) showed the presence of iron oxides, therefore the increase in oxygen content could be partially attributed to iron oxide residue that remained even after washing (Figures A.6–A.8). These results demonstrated that approximately one third of the oxygen detected in the survey spectra came from iron oxides and the increase from 4% to 11–14% was partly from increased oxygen content in graphene.

Therefore, according to XPS, mild oxidation of graphene occurs during treatment with Fenton's reagent, with lower concentrations (a catalytic amount, such as 10% mol/mol used here) able to more efficiently oxidise graphene. This may be due to the increased concentration of graphene relative to the catalyst, increasing the chance of the Fenton reagent coming into contact with graphene, as opposed to reacting with itself. Also interesting to note is the appearance of carbide species in XPS, seen in the C 1s spectrum in Figure 3.8—these could be iron species interacting with the edges or basal plane defects of graphene that were not removed during washing, but no evidence for this was observed using other spectroscopic techniques.

The Raman spectra of the samples treated with stoichiometric, 50% mol/mol and 10% mol/mol Fenton reagent were very similar to that of pristine graphene, with I_D:I_G of approxi-

mately 0.13, compared to 0.12 for graphene (Figure 3.9) after washing. Increasing the range of the Raman spectra of the washed samples from 100 cm^{-1} to 2800 cm^{-1} also showed no remaining iron oxide peaks, highlighting the efficacy of the washing method for removing residual Fe.

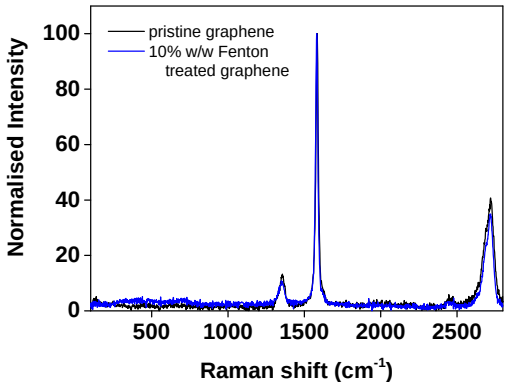

Fig. 3.9 A Raman spectrum showing no change in D peak (1350 cm^{-1}) intensity compared to pristine graphene after treatment with 10% mol/mol Fenton reagent.

Prior to washing, the Raman spectra of graphene treated with stoichiometric levels of Fenton reagent showed an increase in I_D:I_G from 0.12 up to 0.25 for graphene.(Figure A.9) Comparing the Raman spectra of pure iron oxide revealed that there was a risk of an overlap of one of the peaks associated with iron oxides such as haematite[31] and the D peak characteristic of graphene. As explained above, the changing intensity of the D peak is diagnostic for the functionalisation or degradation of the graphene, and obscuring this peak makes characterisation much more difficult.[32] This overlap was illustrated clearly in an iron oxide nanoparticle-carbon composite paper by Song *et al*,[33] and also in the Raman spectrum in Figure A.9. After washing, spectroscopic evidence of the iron oxides (peaks from 134–712 cm^{-1} and at 1338 cm^{-1}, Figure A.9) disappeared and the D and G peaks of graphene could be seen clearly. the Raman spectrum suggested that no increase in defects or functionalisation had occurred, and the I_D:I_G of the Fenton-treated samples was similar to the graphene control.

3.3.2 Summary

XPS, DRIFT-IR and TGA analysis of Fenton treated graphene suggested that some oxidation has taken place. A tentative trend was identified for the studies, with 10% mol/mol showing increased oxidation of graphene compared to 50% mol/mol Fenton reagent and stoichiometric Fenton reagent. Lower concentrations of the Fenton reagent gave weight losses of 3–4% above 250 °C, slightly higher than the mass loss seen in the pristine graphene trace. XPS results showed a clear increase in oxygen content and core level spectra demonstrated the presence of carbonaceous oxygen species as well as some carbide. The presence of carbide could be a result of residual intermediates from Fenton's reagent interacting with graphene—there have been previous reports of Fe interacting with the edges of graphene, in the case of Zhau *et al*,[34] treatment of CVD-grown graphene with 1 M solution of $FeCl_3$ resulted in Fe-assisted growth of monolayer graphene, by catalytically adding carbon to the edges of the sheet.

This could be further investigated by the use of EDX in SEM to search for iron atoms or clusters on the surface or edges of Fenton-treated graphene. DRIFT-IR also showed evidence of incorporation of oxygen-containing groups in the appearance of stretches and bends that could be associated with carbonyl and hydroxyl groups, supporting the XPS assignments. According to Raman spectroscopy, for all concentrations of Fenton reagent, samples showed little to no change in I_D:I_G, giving spectra that were almost identical to the graphene control in the range measured. There is a risk that any degraded graphene, particularly graphene of very few or one layer that may be present in the reaction mixture could be lost in the supernatant despite intense centrifugation. In future, precipitating out the iron oxide by adding base to the supernatants may facilitate analysis of graphene remaining in the supernatant.

In conclusion, treatment of few layer graphene dispersions with Fenton's reagent results in low levels of oxidation compared to pristine graphene in this study. The evidence for

oxidation apparent in the XPS, DRIFT-IR and TGA/TGA-IR, and the lack of evidence in the Raman spectrum suggest that new defects were not formed, but oxidation was occurring at pre-existing defects such as the edges of the few-layer graphene sheets or isolated defects on the basal plane.

3.4 Reactivity of Biomimetic Catalysts toward Graphene

The last set of studies tested the ability of two biomimetic catalysts, first developed and studied by Que's group throughout the late 1990s and 2000s.[35, 36] [Fe(BPMEN)$(OTf)_2$] (BPMEN = N,N'-dimethyl-N,N'-bis-(2-pyridin-2-ylmethyl)-1,2-ethanediamine) and [Fe(TPA) $(OTf)_2$] (TPA = 2-(trispyridylmethyl)amine) in the presence of H_2O_2, to degrade or functionalise graphene. As well as being potent oxygenating catalysts capable of oxidising alkanes such as cyclohexane,[37] these catalysts also mimic the reactivity of the Rieske dioxygenase enzyme family. These non-heme iron-containing enzymes are used by soil bacteria to degrade aromatic and substituted aromatic substrates,[38] as described in Chapter 1. The interaction of H_2O_2 and other peroxides such as ^{t}BuOOH with these catalysts forms a highly reactive intermediate that performs cis-dihydroxylation of the C=C bonds of a substrate to form cis-diols or epoxides. The postulated intermediate is an Fe(V) oxo hydroxo, commonly written as $Fe^V(O)(OH)$.[39, 40] The study of the interaction of these biomimetic catalysts with few-layer graphene should give some insight into the fate of graphene in soil bacteria, and offer some contrast to the effect of a simpler metal-based oxidant found in biology, Fenton's reagent, as described previously.

The ligands BPMEN and TPA were synthesised *via* reductive amination as described in previously reported syntheses.[37, 41, 42] The complexations were carried out with [$Fe(OTf)_2$ $(MeCN)_4$] under N_2 according to literature procedures.[41, 43] The reactivity studies involving both biomimetic catalysts were carried out in a similar manner to the Fenton experiments, as both catalysts were air-sensitive. H_2O_2 was added slowly to the reaction mixture to obtain the postulated active oxidant, [$Fe^V(L)(O)(OH)$], where L is BPMEN or TPA. For this set of experiments, 10% mol/mol complex to carbon was investigated, with [H_2O_2] kept at 10 equivalents with respect to the complex concentration. TGA, DRIFT-IR, XPS and Raman

data were employed to analyse the experiments involving [Fe^{V}(BPMEN)(O)(OH)], and TGA, DRIFT-IR and Raman data for [Fe^{V}(TPA)(O)(OH)] studies.

3.4.1 Results

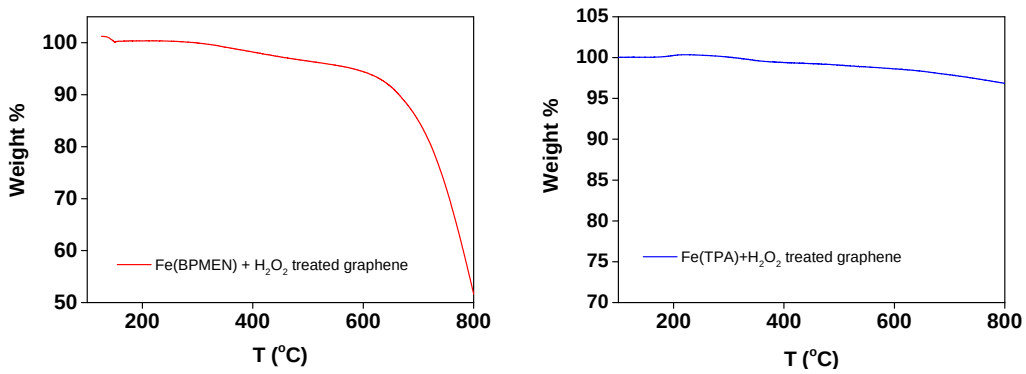

(a) (b)

Fig. 3.10 The TGA traces of washed SGN18 graphene treated with (a) 10% mol/mol [Fe^{V}(BPMEN)(O)(OH)] and (b) 10% mol/mol [Fe^{V} (TPA)(O)(OH)] showing weight loss before 600 °C (Figure A.12 shows the full traces).

Re-aggregated graphene, treated with either [Fe^{V}(BPMEN)(O)(OH)] or [Fe^{V}(TPA)(O)(OH)] was analysed by TGA. Graphene treated with 10% mol/mol [Fe^{V}(BPMEN)(O)(OH)] gave average weight losses between 250–600 °C of 7%, while for graphene treated with 10% mol/mol [Fe^{V}(TPA)(O)(OH)], weight losses in this temperature region were 3% on average (Figure 3.10). This suggests that some oxidation of the graphene has occurred as the weight loss occurred below graphene degradation temperatures (600 °C) but above the temperatures normally required to remove most physisorbed material (250 °C). These values were similar than those observed by the samples treated with the most effective concentration of the Fenton reagent, 10% mol/mol (4%). The TGA results also suggested that [Fe^{V}(BPMEN)(O)(OH)] could be more effective than [Fe^{V}(TPA)(O)(OH)] at oxidising graphene.

The TGA traces for the unwashed graphene treated with [Fe^{V}(BPMEN)(O)(OH)] showed several separate weight losses (totalling 18%) at temperatures above 250 °C (Figure A.13).

This was attributed to the decomposition of leftover complex and iron oxide degradation and cannot be conclusively attributed to functionalisation of the graphene. Hence, cycles of washing/centrifuging with 0.1 M HCl and solvent were employed again to remove spent catalyst.

Two typical DRIFT-IR spectra of graphene treated with 10% mol/mol [Fe^{V}(BPMEN)(O)(OH)] and 10% mol/mol [Fe^{V}(TPA)(O)(OH)] are illustrated in Figure 3.11. Compared to pristine graphene, the spectra of graphene treated with both [Fe^{V}(BPMEN)(O)(OH)] and [Fe^{V}(TPA)(O)(OH)] showed an increase in number of peaks and an increase in relative intensity of existing peaks, indicating functionalisation. Though the region in which O-H stretches would be expected to appear was less defined as in the Fenton-treated graphene spectra, there appeared to be much more peaks centering on 2900–3100 cm^{-1} (alkyl or aromatic C-H stretches) which could be indicative of some loss of aromaticity in graphene. This was seen in graphene samples treated with either catalyst. The largest signals detected were 1590 cm^{-1} and 1484 cm^{-1} (C=C stretches), for [Fe^{V}(BPMEN)(O)(OH)]. Some smaller signals could be assigned as C-O stretches and bends for epoxide groups at 1232 cm^{-1} and 1090 cm^{-1}. For [Fe^{V}(TPA)(O)(OH)], similar signals were observed at 1590 cm^{-1} and 1451 cm^{-1} (C=C), and smaller C-O stretches at 1222 cm^{-1} and 1080 cm^{-1}. As mentioned, O-H signals (approx. 3500-3600 cm^{-1}) were noticeably weak. The catalysts used were expected to introduce hydroxyl groups, epoxide groups or a combination of both, and to see no clear sign of O-H groups was unusual.

10% [Fe^{V}(BPMEN)(O)(OH)] treated graphene was also analysed by XPS, as shown in Figure 3.12. The survey spectrum indicated the presence of carbon (91%) and oxygen (9%) with no detectable levels of iron, unlike the traces seen in the survey and core level spectra of the Fenton experiments (Figures A.6–A.8). The C 1s spectrum was fitted as follows: 76% C=C (284.4 eV), 13% C-C/C-O component, 4% C=O, and 4% contributions from the shake-up feature (291 eV). This was encouraging, as 17% oxidation was much higher than

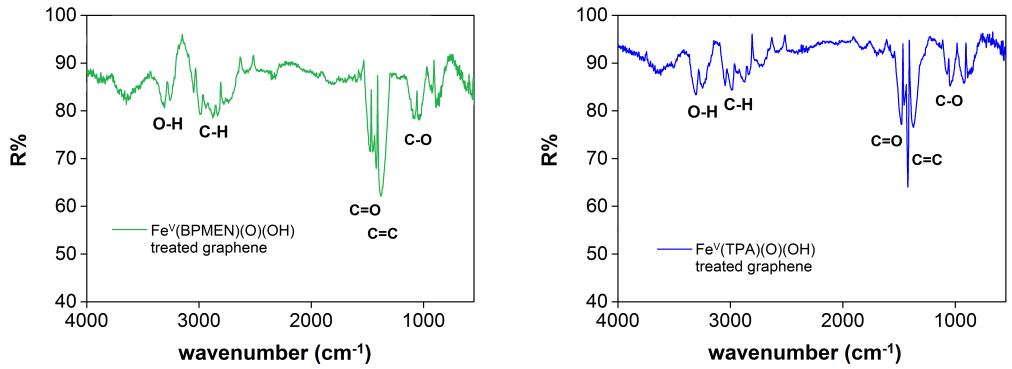

(a) (b)

Fig. 3.11 Typical DRIFT-IR spectra obtained for graphene treated with [Fe^{V}(BPMEN)(O)(OH)] (green) and [Fe^{V}(TPA)(O)(OH)] (blue).

that seen in the control spectra (Figure 2.7). The O 1s core level spectrum, though not as reliable as the C 1s peak, also showed contributions from carbonaceous oxygen and none from iron oxides. The Fe 2p core level spectrum showed that no Fe species were present, in agreement with the survey spectrum. This showed that the washing employed in the catalyst studies was sufficient in removing the Fe catalyst, most likely due to its higher solubility in MeCN and dilute acid. The level of C-O was higher than that observed in pristine PP10 graphene (3%) which suggested that oxidation had occurred, even at low loadings of catalyst.

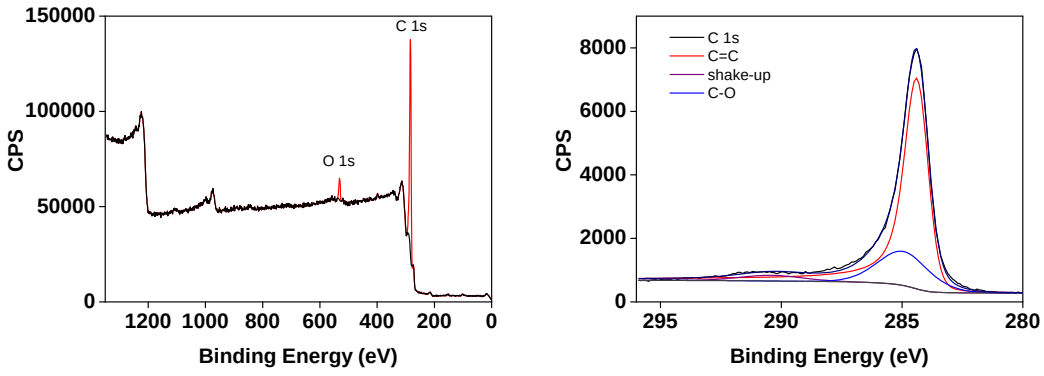

(a) (b)

Fig. 3.12 (a) Survey spectrum and (b) the C1s core level spectrum of 10% [Fe^{V}(BPMEN)(O)(OH)] treated PP10 graphene.

The Raman spectra for the [Fe^{V}(BPMEN)(O)(OH)] treated graphene prior to washing gives distinct features to those seen in the Fenton experiments. A large shift in the baseline around the D and G peaks, as seen in Figure 3.13, was observed in the [Fe^{V}(BPMEN)(O)(OH)] treated sample, which was likely due to the presences of the ligands of the residual physisorbed catalysts. A spectrum like this has been reported before as the intercalation of a Ni(II)-tetra[14]annulene complex into few layer graphene.[44] This could occur with this complex too, as π–π interactions similar to those of the Ni complex are possible due to the aromatic nature of the pyridyl ligands. Due to this baseline shift, however, it is difficult to quantify the change, if any, in the I_D:I_G of the Raman spectra. This baseline shift was not seen for unwashed or washed samples treated with [Fe^{V}(TPA)(O)(OH)], and occurred at higher wavenumbers than that of the iron oxides seen in unwashed Fenton treated graphene.

Raman analysis of washed samples of [Fe^{V}(BPMEN)(O)(OH)] treated graphene gave comparable results to Fenton-treated graphene. There were minimal changes in I_D:I_G for either graphene source (0.26 for SGN18 and 0.12 for PP10) as shown in the spectra to the right in Figure 3.13 (Figure A.11 shows the PP10 spectra). This can be interpreted as no functionalisation or increase in disorder or defects of the graphene basal plane and was very similar to the Fenton spectra spectra employed in this project.

3.4.2 Summary

In summary, similarly to the results given by studies using the Fenton reagent, there is evidence in TGA, DRIFT-IR and XPS spectra for functionalisation occurring in both types of graphene treated with both catalysts. However, except for the baseline shift seen in unwashed samples of [Fe^{V}(BPMEN)(O)(OH)] treated graphene, the Raman spectra remain essentially the same. This leads to a tentative conclusion of edge functionalisation occurring

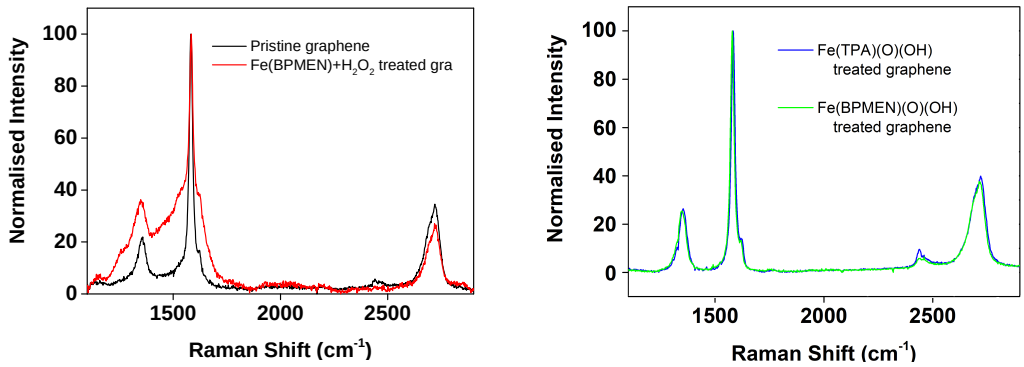

(a) (b)

Fig. 3.13 The Raman spectrum of [Fe^{V}(BPMEN)(O)(OH)] treated graphene showing shifted baseline, and the SGN18 graphene control. (b) The Raman spectra of SGN18 graphene treated with (green) [Fe^{V}(BPMEN)(O)(OH)] and (blue) [Fe^{V}(TPA)(O)(OH)], showing no change.

in few-layer graphene treated with either [Fe^{V}(BPMEN)(O)(OH)] or [Fe^{V}(TPA)(O)(OH)], at concentrations below those required for the Fenton reagent to achieve the same result, but not full degradation of the graphene structure due to the increased reactivity of the edge with respect to the basal plane.[45, 46] In future, further XPS analysis, particularly of [Fe^{V}(TPA)(O)(OH)] treated samples will support this conclusion. Dispersion studies of the postulated edge functionalised graphene in more hydrophilic solvents should also give some insight into whether this mild functionalisation can stabilise dispersions of few-layer graphene in more common or safer solvents than those normally used, such as NMP and DMF. Positive results in these dispersion studies would also support the assignment of edge functionalisation.[47]

3.5 Conclusions

Although complete degradation of graphene was not achieved in this study, it demonstrated an interesting trend in terms of reactivity towards graphene. H_2O_2 and the other organic

peroxide, peracids, and iodosyl agents did not have a significant effect on graphene, showing very little evidence of alteration to the pristine graphene structure, by several spectroscopic techniques. Few of those agents tested had previously been reported to react or not react with graphene,[14, 15, 25] and this study presents the first study of the effect of all of these oxidants on few-layer graphene.

Looking beyond the reactivity of H_2O_2 and organic oxidants, the Fenton's reagent used in the second part of the study displayed increased reactivity towards few-layer graphene, and the biomimetic catalysts used in the latter section showed greater reactivity again. These metal-based oxidants are naturally more aggressive due to their ability to form highly reactive radical or metal-oxo/hydroxide species that are longer-lived and better positioned to attack substrates than radicals produced almost at random by organic oxidants.[48] The demonstrated oxidative functionalisation of graphene in the study, while undoubtedly higher than that seen for H_2O_2 for example, still remained below 5% by TGA and 10% according to XPS. The few-layer nature of the graphene substrate may have limited the access of these oxidants to the edges and exposed surfaces of the substrate, while the basal planes hidden inside the 9–10 layer stack remained untouched. More interesting was the improvement in efficacy seen in the complexed Fe species relative to Fenton's reagent. Low levels of oxidation, most likely at the edges and existing defects on graphene, was confirmed through the use of various spectroscopic techniques. Beyond this, the exact nature of the functional groups introduced by each of the oxidising or oxygen-donating agents used should be the focus of further studies. It has been established that [Fe^{V}(BPMEN)(O)(OH)] can introduce both dihydroxyl groups and epoxides into smaller aromatic substrates to break aromatic systems, whereas [Fe^{V}(TPA)(O)(OH)] primarily inserts oxygen atoms into substrates to produce epoxides,[35, 36] and detection of either of these species on graphene could be attempted using assays to identify particular species.[49] Repeating the study with monolayer graphene, possibly by cascading centrifuging graphene dispersions, in order to isolate the

most exfoliated sheets,[50] or preparing epitaxial graphene and soaking this in a solution of oxidant, may give more insight into the efficacy of these oxidants on the more reactive monolayer graphene.

In terms of a study into the life of few-layer graphene, which is more easily produced and can also result from mono-/bilayer graphene, etc. re-aggregating post-consumer or industrial life, this chapter highlights the difficulty of treated waste graphene. It also proposes the possibility of waste graphene, when take up by soil bacteria or exposed to waste water treatment, being converted into functionalised graphene. As depicted in the introduction, this form of graphene can cause more damage *in vivo* due to its increased bioavailability and reactivity, therefore, more destructive techniques will need to be employed to break it down further.

3.6 Experimental Methods

^{1}H NMR spectra were recorded using a Bruker DPX 400 MHz NMR Spectrometer. IR spectra were recorded using a Perkin-Elmer 100 Series FT-IR Spectrometer and a Perkin Elmer Spectrum One spectrometer and diffuse reflectance accessory. ESI mass spectra were obtained using a Micromass TOF spectrometer interfaced to a Waters 2690 HPLC. MALDI-TOF were obtained using a MALDI TOF Premier MS system. UV-vis spectra were recorded using an Agilent 8453 UV-vis spectrometer. Raman spectra were obtained on a Witec Alpha 300 R confocal Raman microscope with laser wavelengths of 532 and 633 nm at a power of 0.5 mW. Raman maps were collated from 49 spectra taken over a 20 μm $\times$ 20 μm range, and overlaid spectra were normalised to the G peak for graphene, and the A_{1g} peak for MoS_2. TGA and TGA-IR traces were obtained using a Perkin Elmer Pyris 1 TGA and Perkin Elmer TG-IR-GCMS Interface TL 8000 spectrometer, and traces were obtained under nitrogen gas or air, at a rate of 10 °C/min from 50–900 °C. X-ray photoelectron spectra were taken using monochromated Al Kα X-rays from an Omicron XM1000 MkII X-ray source and an Omicron EA125 energy analyser. The analyser pass energies were 20 eV for the core level spectra and 200 eV for the survey spectra.

Graphene and oxidant reactivity tests

Graphene-oxidant tests were carried out at room temperature for 12 h. 1 mmol of graphene was stirred with 10 mmol of the chosen oxidant as a dispersion in either IPA or MeCN. The dispersion was then allowed to re-aggregate by centrifugation or left to stand overnight and washed once with IPA/MeCN and twice with water. The re-aggregated samples were characterised by Raman, TGA, and DRIFT-IR.

Graphene and Fenton reagent reactivity tests

Re-aggregated shear exfoliated graphene (Timrex PP10 powder, 12 mg–120 mg) was re-dispersed in MeCN at the start of each experiment. The dispersion was then degassed with

N_2. Two vials, each containing $FeCl_2$ (0.064g–0.127g, 0.5–1 mmol) in 10 ml MeCN were made up in a N_2 atmosphere glovebox and sealed with septa. The oxidant solution was made up using 3% H_2O_2 solution (10 mM) in 9:1 MeCN:H_2O. The graphene dispersion was divided in two. One aliquot of $FeCl_2$ was added to one portion of dispersion and kept under N_2. $FeCl_2$ and the H_2O_2 solution were added in aliquots to the other dispersion, with a 1 ml addition of each occurring every 10 min. The pH was monitored *via* indicator paper, and was adjusted with NaOH solution to 2–4. Upon completion of the additions, the dispersions were left to stir overnight. The samples were then washed with acetonitrile and dilute acid and centrifuged at 3000 rpm for 30 min to collect the re-aggregated graphene. The supernatant was also kept for analysis. The re-aggregated graphene samples were analysed by Raman, TGA, DRIFT-IR, and XPS.

Syntheses of ligands and iron precursor

The ligands TPA (tris(2-pyridylmethyl)amine) and BPMEN (N,N'-dimethyl-N,N'-bis-(2-pyridin-2-ylmethyl)-1,2-ethanediamine) were synthesised by alkylation of 2-picolyl amine by 2-picolyl chloride, and reductive amination of 2-pyridine carboxaldehyde by 2-picolyl amine and sodium triacetoxyborohydride, respectively, as detailed in the literature.[41, 42, 37] 2-Picolyl amine, N,N'-dimethylamine and 2-pyridine carboxaldehyde were vacuum distilled prior to use and the reactions were carried out in dry DCM. TPA was then purified by recrystallisation, BPMEN by extraction with hexane, and both characterised by ^{1}H NMR and MS. Average percentage yields: TPA 60%, BPMEN 50%.

BPMEN: δ_H (400 MHz, $CDCl_3$): 2.30 (s, 6H, N-CH_3) 2.70 (s, 4H, -CH_2-CH_2) 3.72 (s, 4H, N-CH_2-Pyr) 7.14-7.17 (tr, 3H, J = 6 Hz, 5-Pyr-H) 7.57-7.59 (d, 3H, J = 8 Hz, 3-Pyr-H) 7.64-7.68 (d, 3H, J = 16 Hz, 4-Pyr-H) 8.54-8.55 (d, 3H, J = 4 Hz, 6-Pyr-H) ppm.

ESI-MS: $[M+H]^+$ (271.1916) detected.

TPA: δ_H (400 MHz, $CDCl_3$): 3.90 (s, 6H, N-CH_2-Pyr) 7.13-7.16 (tr, 3H, J = 6 Hz, 5-Pyr-H) 7.56-7.58 (d, 3H, 8 Hz, 3-Pyr-H) 7.63-7.67 (tr, 3H, J = 8 Hz, 4-Pyr-H) 8.53-8.54 (d, 3H, J =

4 Hz, 6-Pyr-H) ppm.

ESI-MS: $[M+H]^+$ (291.1646) detected.

The iron precursor, $[Fe(OTf)_2(MeCN)_4]$ was synthesised according to the literature.[51] $FeCl_2$ (1 g, 80 mmol) was dissolved in dry, degassed MeCN in the glovebox, and trimethylsilyl trifluoromethanesulfonate (3.07 ml, 170 mmol) was added dropwise. The white powder formed was collected, filtered, washed with diethyl ether and characterised by FT-IR and MS.

ATR-IR: ν = 3455 (O-H stretch), 2310, 2270 (MeCN nitrile stretch), 1655 (C=O stretch), 1243, 1185 (S=O stretch), 1028, 767, 633 (C-F stretch) cm^{-1}.

ESI-MS: $[M+H]_+$ (518.3541) detected.

Syntheses of biomimetic catalysts

The catalysts, $[Fe(BPMEN)(OTf)_2]$ and $[Fe(TPA)(OTf)_2]$, were both prepared with labile triflate ligands as reported in the literature.[41, 43] $[Fe(OTf)_2(MeCN)_4]$ was dissolved in dry, degassed THF in the glovebox and the desired ligand was added stoichiometrically. Upon reduction of solvent volume, the desired complex precipitated. This polycrystalline material was filtered and washed with diethyl ether and characterised by paramagnetic ^1H NMR and MALDI-TOF MS.

Paramagnetic ^1H NMR (400 MHz, $CDCl_3$) $[Fe(BPMEN)(OTf)_2]$: δ_H = 160.02 (s, Pyr-H), 128.60, 91.25 (s, Pyr-H), 74.67 (s, -CH_2-), 54.31 (s, Pyr-H), 24.09, 16.61 (s, -CH_3) ppm.

MALDI-TOF: $[M-OTf]^+$ detected, 475.0714.

Paramagnetic ^1H NMR (400 MHz, $CDCl_3$) $[Fe(TPA)(OTf)_2]$: δ_H = 135.79 (s, Pyr-H), 63.45 (s, -CH_2-), 52.20 (s, Pyr-H), 49.98 (s, Pyr-H), 12.52 (s, Pyr-H) ppm.

MALDI-TOF: $[M-OTf]^+$ detected, 495.3033.

Graphene and Fe(II) catalyst reactivity tests

This was carried out in a similar fashion to the Fenton experiments, although both complex solutions were made up in 5 ml MeCN in the glovebox, and two graphite sources (Timrex

PP10 in MeCN and SGN18 in IPA) were used. As well as H_2O_2 solution, acetic acid solution (10 mmol in 10 ml MeCN) was also used to generate the active oxidant. The pH was not monitored in these reactions. The washed re-aggregated samples were analysed by Raman, TGA, DRIFT-IR and XPS, while the supernatant were analysed by Raman, TGA, UV-vis and ATR-IR/DRIFT-IR.

References

[1] M. Yi and Z. Shen, *Journal of Materials Chemistry A*, 2015, **3**, 11700–11715.

[2] X. Hu and Q. Zhou, *Chemical Reviews*, 2013, **113**, 3815–3835.

[3] A. M. Pinto, I. C. Gonçalves and F. D. Magalhães, *Colloids and Surfaces B: Biointerfaces*, 2013, **111**, 188–202.

[4] I. A. Popov, K. V. Bozhenko and A. I. Boldyrev, *Nano Research*, 2012, **5**, 117–123.

[5] W. S. J. Hummers and R. E. Offeman, *Journal of the American Chemical Society.*, 1958, **80**, 1339.

[6] S. Stankovich, R. D. Piner, X. Chen, N. Wu, S. T. Nguyen and R. S. Ruoff, *Journal of Materials Chemistry*, 2006, **16**, 155–158.

[7] X. Du, M. Xiao, Y. Meng and A. Hay, *Carbon*, 2005, **43**, 195–197.

[8] E. Siegfried, E.-H. Michael, G. Stefan, H. Philipp, K. Wolfgang, G. Andreas, D. Christoph, R. Michael, X. Jie, P. Christian, L. Ole, S. Hans-Peter, M. Paul and H. Andreas, *Advanced Materials*, 2013, **25**, 3583–3587.

[9] C. E. Halbig, T. J. Nacken, J. Walter, C. Damm, S. Eigler and W. Peukert, *Carbon*, 2016, **96**, 897–903.

[10] V. A. Ermakov, A. V. Alaferdov, A. R. Vaz, E. Perim, P. A. S. Autreto, R. Paupitz, D. S. Galvao and S. A. Moshkalev, *Scientific Reports*, 2015, **5**, 11546.

[11] V. K. Thakur and M. K. Thakur, *Chemical Functionalisation of Carbon Nanomaterials: Chemistry and Applications*, CRC Press, United States of America, 2015.

[12] J. R. Lomeda, C. D. Doyle, D. V. Kosynkin, W.-F. Hwang and J. M. Tour, *Journal of the American Chemical Society*, 2008, **130**, 16201–16206.

[13] A. Boveris and E. Cadenas, *IUBMB Life*, 2000, **50**, 245–250.

[14] G. Zhao, D. Shao, C. Chen and X. Wang, *Applied Physics Letters*, 2011, **98**, 183114–183147.

[15] W. L. Xing, G. Lalwani, I. Rusakova and B. Sitharaman, *Particles and Particle Systems Characterisation*, 2014, **31**, 745–750.

[16] G. P. Kotchey, B. L. Allen, H. Vedala, N. Yanamala, A. A. Kapralov, Y. Y. Tyurina, J. Klein-Seetharaman, V. E. Kagan and A. Star, *ACS Nano*, 2011, **5**, 2098–2108.

[17] K. Rajendra, R. Julie, S. M. A., T. Emanuele, M.-M. Cécilia, D. R.-C. A. Esaú, V. Ester, S. Paolo, P. Vincenzo and B. Alberto, *Small*, 2015, **11**, 3985–3994.

[18] E. Murray, B. C. Thompson, S. Sayyar and G. G. Wallace, *Polymer Degradation and Stability*, 2015, **111**, 71–77.

[19] G. Lalwani, W. Xing and B. Sitharaman, *Journal of Materials Chemistry B*, 2014, **2**, 6354–6362.

[20] P. Serp and B. Machado, *Nanostructured Carbon Materials for Catalysis*, Royal Society of Chemistry, 2015, pp. 226–228.

[21] T. Katsuki and K. B. Sharpless, *Journal of the American Chemical Society*, 1980, **102**, 5974–5976.

[22] B. Zhu, H. Zhao, B. Kalyanaraman, J. Liu, G. Shan, Y. Du and B. Frei, *Proceedings of the National Aacademy of Sciences*, 2007, **104**, 3698–3702.

[23] S. V. Barkanova, O. L. Kaliya and E. A. Lukyanets, *Mendeleev Communications*, 2001, **11**, 116–118.

[24] A. P. Pandell, *Journal of Organic Chemistry*, 1976, **41**, 3992–3996.

[25] Z. Pan and M. Newcomb, *Inorganic Chemistry*, 2007, **46**, 6767–6774.

[26] S. Yaragalla, G. Anilkumar, T. V. Vineeshkumar, N. Kalarikkal and S. Thomas, *Advanced Materials Letters*, 2015, **6**, 848–852.

[27] B. T. V. Srinivas, V. S. Rawat and B. Sreedhar, *Advanced Synthesis & Catalysis*, 2015, **357**, 16–17.

[28] H. J. H. Fenton, *Journal of the Chemical Society Transactions*, 1894, **65**, 899–910.

[29] M. Farrokhi, K. Dindarloo and H. A. Jamali, *Research Journal of Environmental Toxicity*, 2015, **9**, 274–289.

[30] P. D. Ghosh, *Introduction to Photoelectron Spectroscopy*, John Wiley & Sons, United States of America, 1984.

[31] F. Froment, A. Tournie and P. Colomban, *Journal of Raman Spectroscopy*, 2008, **39**, 560–568.

[32] V. Singh, D. Joung, L. Zhai, S. Das, K. S. I. and S. S., *Progress in Materials Science*, 2001, **56**, 1178–1271.

[33] K. Song, Y. Lee, M. R. Jo, K. M. Nam and Y. M. Kang, *Nanotechnology*, 2012, **23**, 505401.

[34] J. Zhao, Q. Deng, S. M. Avdoshenko, L. Fu, J. Eckert and M. H. Rümmeli, *Proceedings of the National Academy of Sciences*, 2014, **111**, 15641–15646.

[35] K. Chen and L. J. Que, *Chemical Communications.*, 1999, **15**, 1375–1376.

[36] P. Das and L. J. Que, *Inorganic Chemistry*, 2010, **49**, 9479–9485.

[37] G. J. P. Britovsek, J. England and A. J. P. White, *Inorganic Chemistry*, 2005, **44**, 8125–8134.

[38] D. J. Ferraro, L. Gakhar and S. Ramaswamy, *Biochemical Biophysical Research Communications*, 2005, **338**, 175–190.

[39] K. K. Singh, M. K. Tiwar, B. B. Dhar, K. Vanka and S. S. Gupta, *Inorganic Chemistry*, 2015, **54**, 6112–6121.

[40] I. Prat, J. S. Mathieson, M. Güell, X. Ribas, J. M. Luis, L. Cronin and M. Costas, *Nature Chemistry*, 2011, **3**, 788–793.

[41] A. Iturrospe, B. Artetxe, S. Reinoso, L. San Felices, P. Vitoria, L. Lezama and J. M. Gutierrez-Zorrilla, *Inorganic Chemistry*, 2013, **52**, 3084–3093.

[42] Z. Tyeklar, R. R. Jacobson, N. Wei, N. N. Murthy, J. Zubieta and K. D. Karlin, *Journal of the American Chemical Society*, 1993, **115**, 2677–2689.

[43] D. Alain, and S. H. Karl, *Inorganic Chemistry*, 1998, **37**, 215–223.

[44] E. V. Basiuk, M. Martinez-Herrera, E. Alvarez-Zauco, L. V. Henao-Holguin, I. Puente-Lee and V. A. Basiuk, *Dalton Transactions*, 2014, **43**, 7413–7428.

[45] A. Bellunato, H. Arjmandi Tash, Y. Cesa and G. F. Schneider, *ChemPhysChem*, 2016, **17**, 785–801.

[46] R. Sharma, J. H. Baik, C. J. Perera and M. S. Strano, *Nano Letters*, 2010, **10**, 398–405.

[47] V. Georgakilas, A. B. Otyepka, M.and Bourlinos, V. Chandra, N. Kim, K. C. Kemp, P. Hobza, R. Zboril and K. S. Kim, *Chemical Reviews*, 2012, **112**, 6156–6214.

[48] E. Neyens and J. Baeyens, *Journal of Hazardous Materials*, 2003, **98**, 33–50.

[49] Z. Xiang, Q. Dai, J.-F. Chen and L. Dai, *Advanced Materials*, 2016, **28**, 6253–6261.

[50] C. Backes, B. M. Szydłowska, A. Harvey, S. Yuan, V. Vega-Mayoral, B. R. Davies, P.-l. Zhao, D. Hanlon, E. J. G. Santos, M. I. Katsnelson, W. J. Blau, C. Gadermaier and J. N. Coleman, *ACS Nano*, 2016, **10**, 1589–1601.

[51] J. M. Hagadorn, L. J. Que and W. B. Tolman, *Inorganic Chemistry*, 2000, **39**, 6086–6090.

Chapter 4

The Interaction of Graphene with MoS_2 and the Use of their Heterostructures as HER Catalysts

This chapter is partially based on an unpublished manuscript entitled "On the Reaction between Two Dimensional MoS_2 and Graphene" by Ciara McGlynn, Xin Chen and Aidan R. McDonald.

4.1 Abstract

Although the benefits of combining catalytic MoS_2 with conductive graphene have been established, very little attention has been given to the chemical interaction of the two materials, and experimental evidence of this is also lacking. To provide in depth analysis of the interaction of these two materials, this chapter describes a series of heterostructures composed of ce-1T-MoS_2/graphene and 2H-MoS_2/graphene prepared *via* liquid phase exfoliation

of 2H-MoS_2 and graphene and chemical exfoliation of 1T-MoS_2. The heterostructures were extensively characterised using XPS, TGA-IR, ATR-IR, pXRD, SEM and Raman spectroscopy. Particular attention was paid to the chemical interaction of the materials during heterostructure preparation. The new features observed were tentatively assigned as low levels of saturated carbon introduced into the graphene component of the heterostructures by its interaction with either 2H- or ce-1T-MoS_2, revealing a degree of chemical interaction which has so far been overlooked by the materials community. The growth of saturated carbon appears to be dependent on [MoS_2] and MoS_2 phase, with more saturation induced by the defect rich chemically exfoliated 1T-MoS_2.

4.2 Introduction

Two-dimensional (2D) nanomaterials, including graphene and transition metal dichalcogenides (TMDs, such as MoS_2) have been employed together as composites or heterostructures for a wide variety of applications. Most commonly, these heterostructures are used in applications where conductivity, strength, and catalytic activity are required.[1, 2] MoS_2/graphene hybrids are prepared and studied in the hopes of producing a composite or heterostructure that possesses the properties of both parent materials: for example, the catalytic activity of MoS_2 towards hydrogen evolution,[3, 4] coupled with the robust, inert, and conductive nature of graphene.[5] Such heterostructures have found applications as anode materials for lithium or sodium ion batteries[6, 7] for transistors and information storage,[8] as sensors for small organics,[9] as well as catalysts for hydrogen evolution. These heterostructure materials are usually prepared *via* hydrothermal or solution based syntheses,[10–12] chemical vapour deposition,[13, 14] or from the combination of films of liquid phase exfoliated materials.[15]

This study aims to further the understanding of the interaction of both solvent-exfoliated 2H-MoS_2 and ce-1T-MoS_2 with solvent-exfoliated few-layer graphene when subjected to

sonication. Non-innocent interactions between TMDs such as MoS_2 and graphene, while noted,[11, 15–18] have been addressed in mainly physical terms in the literature. Heterostructures or composites of MoS_2 and graphene have shown increased conductivity and even increased catalytic activity compared to MoS_2 alone. According to DFT calculations on heterostructures, the presence of MoS_2 causes p-type doping in graphene which facilitates hydrogen binding on the graphene side as well as the MoS_2 side.[19] However, in-depth experimental and chemical analysis is lacking, despite the significant volume of published research combining the two materials as devices, supports, and catalysts for a wide range of applications as mentioned earlier. Much of the research approached from a chemistry viewpoint is limited to graphene oxide (GO) or reduced graphene oxide (rGO) as a conducting base for MoS_2 in applications such as HER.[20] However, significant defects are formed during oxidation to GO, and reduction often cannot heal holes or remove all oxygenated groups in the structure of rGO.[20, 21] This can make it impossible to discern any additional chemical changes that may result from the interaction between MoS_2 and graphene during heterostructure formation, particularly when hydrothermal methods are used.[3, 10]

Therefore, this study specifically looks at the preparation of mixed MoS_2/graphene films by combining liquid-exfoliated dispersions of graphene and both 2D polymorphs of MoS_2. It aims to explore the chemical interaction of the two materials during the formation of the heterostructure, and the potential effect this has on the heterostructure films of both 2H-MoS_2 and ce-1T-MoS_2.

4.3 Results

For the reactions between graphene and 2H-MoS_2, separate IPA dispersions of 2H-MoS_2 and graphene were combined at different molar ratios (1:25, 1:15, 1:1, 2:1, 5:1 2H-MoS_2:graphene), subjected to bath sonication for 2 h, and then stirred using a magnetic stir bar at room temper-

ature for 16 h. For the reaction between graphene and ce-1T-MoS_2, solid ce-1T-MoS_2 was added to a dispersion of graphene in IPA at varying molar equivalencies (1:20, 1:12, 1:10, 1:5, 1:2 ce-1T-MoS_2:graphene). At high ce-1T-MoS_2 concentrations (>1:1 molar ratios), very poor quality spectroscopic data was obtained (XPS, Raman spectra were saturated by ce-1T-MoS_2 signals making analysis inaccurate), therefore such ratios were not pursued further. After mixing of the dispersions the resulting heterostructure mixtures were subsequently subjected to bath sonication for 2 h followed by stirring using a magnetic stir bar at room temperature for 16 h. For both 2H-MoS_2/graphene and ce-1T-MoS_2/graphene heterostructures, flocculation of material was observed after magnetic stirring was ceased, indicating formation of larger heterostructured particles. The resulting mixtures were then filtered using a membrane of pore size 0.2 μm to yield films.

The pXRD pattern of the ce-1T-MoS_2/graphene heterostructures displayed 2θ peaks typical of both pristine ce-1T-MoS_2 and graphene at 9°, 14°, 26° and 59° (Figure 4.1a).[22–24] However, two changes from the pristine materials' pXRD patterns were observed: an increase in intensity alongside a small shift towards lower angles in the graphene (002) peak from 26.5° to 26°; similarly, a slight broadening of the 14° peak to include 13.5° in the (002) peak for ce-1T-MoS_2. These observations could suggest widening of the inter-planar distance of graphene, and to a greater extent, ce-1T-MoS_2, in the heterostructures. The powder X-ray diffraction (pXRD) pattern for 2H-MoS_2/graphene showed a shift in the (002) peak for 2H-MoS_2 from 14° to 13.5°, and a shift of approximately 0.5° for other 2H-MoS_2 peaks (Figure 4.1b).[23] Broadening of both the graphene (002) peak at 26° and the 2H-MoS_2 (002) peak at 13.5° was also observed. This broadening could be due to aggregation, but importantly, the shift of the (002) peaks to lower degrees suggested a slight increase in inter-layer distance.[22, 25] Overall, pXRD patterns for both of the heterostructured materials indicated the presences of both materials, and a small increase in interlayer distance for MoS_2 and broadening of the peaks associated with graphene and MoS_2. pXRD analysis of

other heterostructures in the literature also showed the presence of both materials in most cases, with some heterostructures achieving evidence of single layer species such as graphene intercalated between MoS_2 from the reduction or disappearance of the (002) from MoS_2 or graphene. The observed widening of the pXRD peaks has been reported as a result of exfoliation/reduction in thickness of the materials, and the increase in interlayer distance is also a sign of this.[26–28] The persistence of both materials and the small changes in the (002) peaks indicated that some exfoliation of the materials and heterostructure formation had occurred.

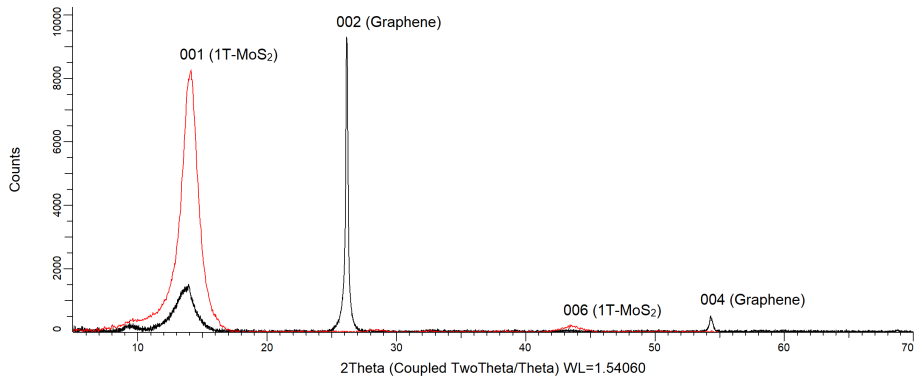

(a)

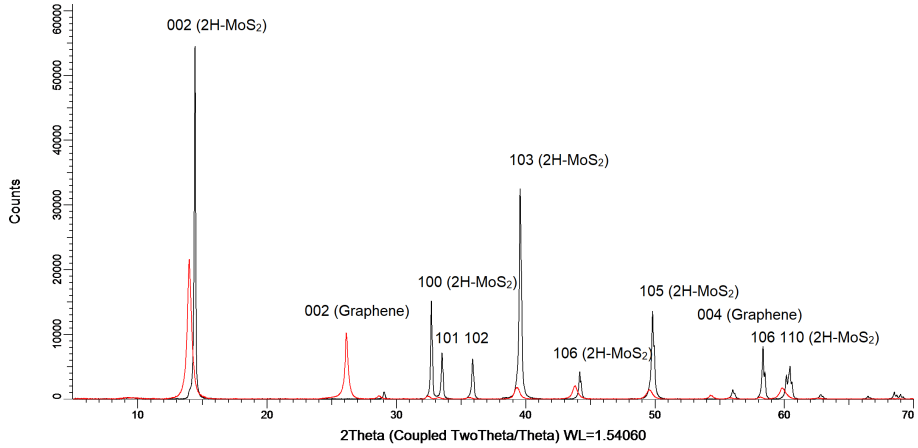

(b)

Fig. 4.1 (a) pXRD pattern of 1:5 ce-1T-MoS_2/graphene heterostructure (black trace) with ce-1T-MoS_2 (red trace). (b) pXRD pattern of 1:15 2H-MoS_2/graphene heterostructure (red trace) with 2H-MoS_2 overlaid (black trace).

Scanning electron microscopy (SEM) of the heterostructures showed the nanosheets were well-interspersed. ce-1T-MoS_2/graphene displayed an average particle size of 0.29 $\pm$ 0.02 μm for ce-1T-MoS_2 and 1.15 $\pm$ 0.12 μm for graphene (Figure 4.2). This was comparable in dimension to the pristine materials (0.22 $\pm$ 0.01 μm and 1.82 $\pm$ 0.19 μm, respectively, Figures 2.9, 2.18). The graphene flakes were initially larger than the ce-1T-MoS_2 because of the manner in which they are exfoliated. The same observations were made for 2H-MoS_2/graphene heterostructures. The MoS_2 flakes were identified *via* electron backscatter (ESB) in the SEM images of 1:15 2H-MoS_2/graphene (Figure 4.3). These flakes were 0.40 $\pm$ 0.04 μm on average, showing no change in size or morphology after heterostructure formation compared to the pristine materials (0.39 $\pm$ 0.04 μm for 2H-MoS_2, 1.15 $\pm$ 0.12 μm for graphene). Analysis of the heterostructure materials *via* electron backscatter mode, (showing MoS_2 as bright flakes and graphene as darker flakes, reflecting the atomic mass difference) showed that the two materials were present and well-interspersed (Figure 4.2). This demonstrated efficient mixing of the 2D nanomaterials and formation of heterostructured material. pXRD and SEM analyses thus suggested efficient mixing of the 2D nanosheets and formation of homogeneous heterostructures.

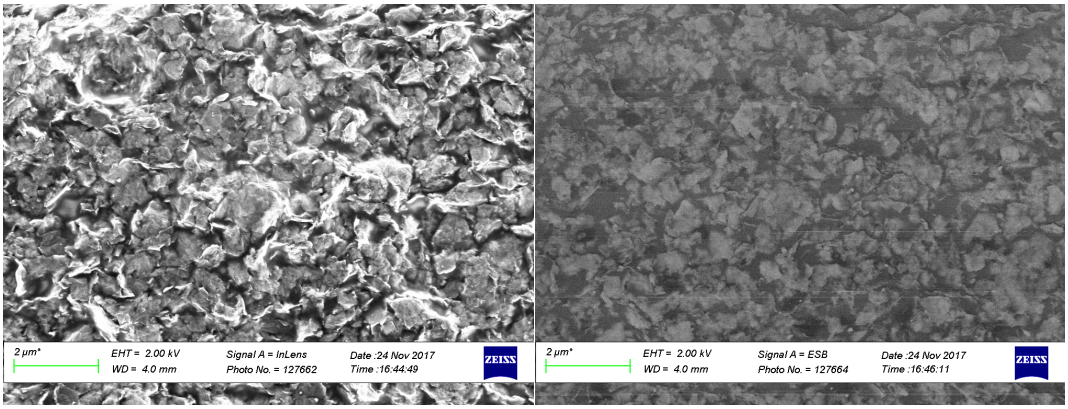

(a) (b)

Fig. 4.2 Top: InLens mode, bottom: ESB mode) of 1:5 ce-1T-MoS_2/graphene showing mix of ce-1T-MoS_2 and graphene flakes interspersed.

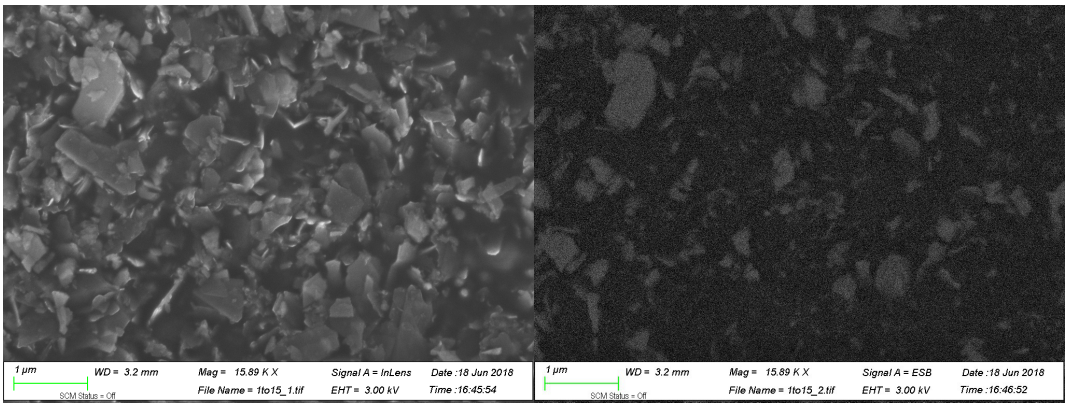

(a) (b)

Fig. 4.3 SEM images taken using (a) InLens mode and (b) ESB mode of 1:15 2H-MoS_2/graphene showing interspersed MoS_2 and graphene flakes.

X-ray photoelectron spectroscopy (XPS) was employed in order to explore the atomistic properties of the new heterostructures and to identify any potential changes in chemical environment in either the graphene, 2H-MoS_2, or ce-1T-MoS_2, graphene components of the heterostructures. The survey spectra of the heterostructure samples displayed the presence of S, Mo, C, and O confirming the presence of both MoS_2 and graphene (Figure 4.4a), as indicated by SEM and pXRD.

The core level XPS spectra of the heterostructure materials were compared to core level spectra of the pristine samples. Critically, in all of the C 1s core level spectra of the heterostructure materials we observed increased contributions from sp^3-hybridised C features (Figure 4.4b, 4.4d). Taking the average of 3 samples, in the ce-1T-MoS_2/graphene heterostructures the sp^2-hybridised C component of the C 1s spectrum (at 284 eV) decreased from representing 88% of the C present (pristine graphene) to 74% (1:20 ce-1T-MoS_2/graphene), 74% (1:12), 81% (for 1:10), 75% (for 1:5) and 66% (1:2). This was mirrored by an increase in saturated (sp^3-hybridised) C (284.8-285.5 eV) from an average of 7% in pristine graphene to 25% (1:20), 23% (1:12), 16% (1:10), 22% (1:5) and 34% (1:2) with the remaining small contribution coming from the shake-up feature at 291 eV. Comparing the C 1s spectra of the 2H-MoS_2/graphene heterostructures to pristine graphene, we observed a decrease in the

fitting of sp^2-hybridised C (284 eV) from 88% to 76% (for 1:15 2H-MoS_2/graphene), 75% (1:1) and 64% (2:1). For 1:25 2H-MoS_2/graphene, the graphitic carbon fitting stayed at 89%. This was thought to be due to the large excess of graphene present, meaning any saturation occurring was insignificant and not detected by XPS. A corresponding increase in saturated carbon (284.8-285.5 eV) was also observed from 7% in pristine graphene to 21% (for 1:15), 25% (1:1) and 36% (2:1), while the fit from the C1s spectrum of 1:25 2H-MoS_2/graphene was 10%. The shake-up feature at 291 eV made up the rest of the contribution to the C 1s peak. The decrease in the extent of saturation compared well to the decreasing ratio of 2H-MoS_2/graphene in the initial reaction mixture, indicating that the degree of sp^3-hybridised C was [2H-MoS_2] dependent. In summary, we consistently observed the appearance of a new C-feature in the C 1s core level XPS spectra that we have assigned as a new sp^3-hybridised (saturated) C atom in the heterostructures.

Fitting the C 1s core level spectrum of pristine graphene (Figure 2.7) demonstrated a feature at 284 eV (attributed to sp^2 hybridised graphitic carbon, 88%) with a shake-up feature at 291 eV commonly observed in pristine graphite samples (5%).[29] The remaining 7% was assigned as sp^3-hybridised carbon (284.8-285.5 eV), present as inherent defects in an imperfect crystal and/or adventitious carbon.[30] The quantity of sp^3-hybridised carbon fitted in the pristine material was thus considerably lower than that observed in the heterostructures. The core level C 1s spectra of 2H- and ce-1T-MoS_2 displayed negligible quantities of carbon (Figures 2.16, 2.24).

We surmise that the new sp^3-hybridised C feature is an indication of saturation of the graphene surface as a result of a reaction of the MoS_2 with graphene. The degree of saturation appeared to be [MoS_2] dependent for 2H-MoS_2/graphene (Figure 4.5b), whereas for ce-1T-MoS_2/graphene heterostructures the trend was less obvious, but an increase in saturated carbon was observed for the higher [ce-1T-MoS_2] (Figure 4.5a). This could be interpreted as a result of defects in the materials—2H-MoS_2 is not highly defective, so reaction with

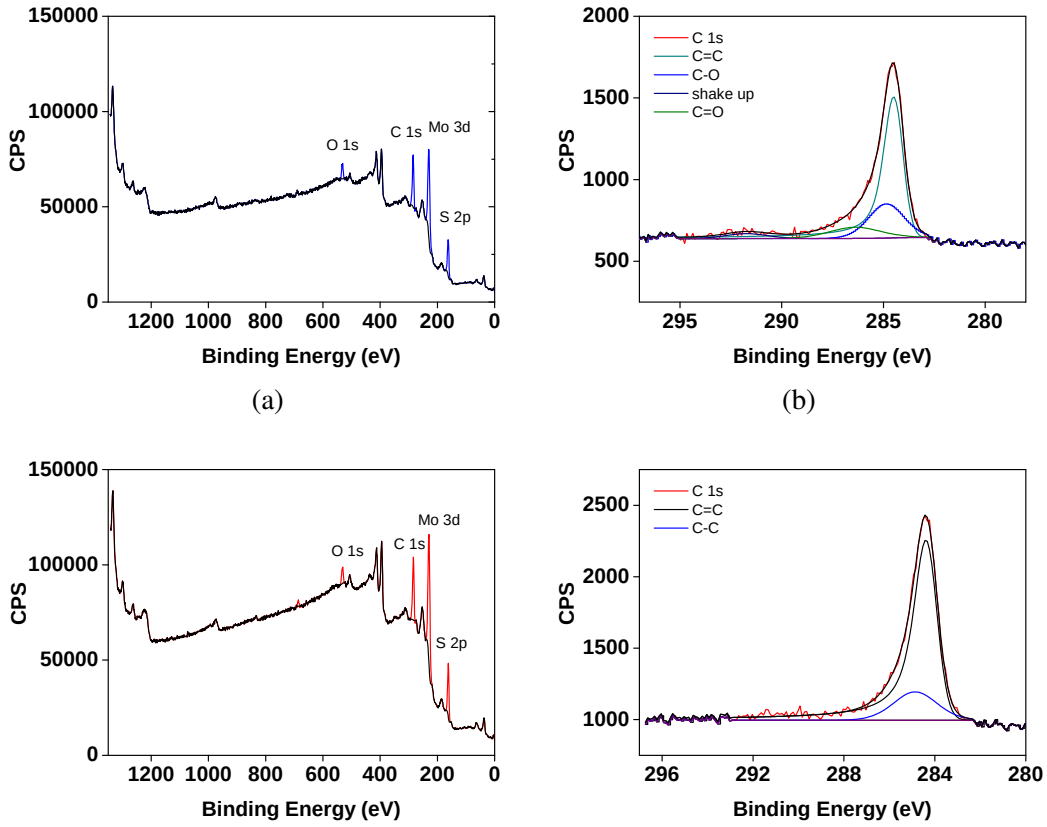

Fig. 4.4 (a) Survey and (b) C 1s core level spectra of a heterostructure of 1:5 ce-1T-MoS_2/graphene; (c) survey and (d) C 1s core level spectra of a heterostructure of 1:15 2H-MoS_2/graphene.

graphene would be [2H-MoS_2]-dependent, whereas different batches of chemical exfoliated MoS_2, despite efforts to make the exfoliation as consistent as possible, can possess different concentrations of defects. This could partially obscure any concentration dependence.

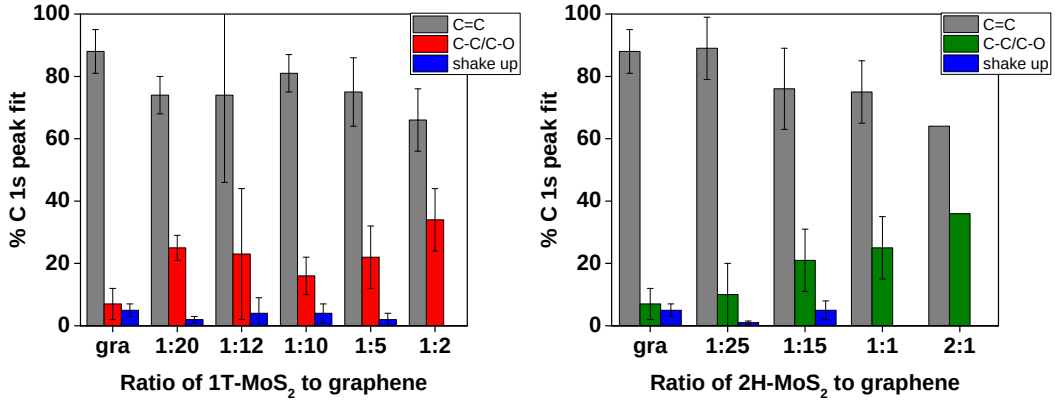

(a) (b)

Fig. 4.5 Histograms of the composition of the C 1s core level XPS spectra in a series of (a) ce-1T-MoS_2/graphene and (b) 2H-MoS_2/graphene heterostructures, showing the increase in sp^3-hybridised component. The error bars show the range of values obtained from 3 samples.

For all ratios of ce-1T-MoS_2/graphene and 2H-MoS_2/graphene the fitted components of the Mo 3d and S 2p core level spectra remained close to those seen in the pristine materials, *i.e.* there was no change in the 1T/2H ratio and the Mo remained chemically unchanged (Figures B.1, B.2 B.4).[31] Thus, according to XPS Mo 3d and S 2p core level spectra the MoS_2 components of the heterostructures demonstrated no evidence for chemical change/surface modification, while the core level C 1s spectra clearly demonstrated a chemical change to the graphene surface (Figure B.3).

In the difference attenuated total reflectance infra-red (ATR-IR) spectra (difference between pristine graphene and the 2H-MoS_2/graphene heterostructure (Figures 4.6, B.5, B.7), new features at ν = 2955, 2920 (C–H stretch), 1640 (C=O stretch), 1590 (C=C stretch), 1060 (C–O stretch), and 1000 cm^{-1} (C–H bend) were identified. Likewise, in the ce-1T-MoS_2/graphene heterostructure difference spectra, new features at ν = 3250 (O–H), 3080

(C–H), 1511 (C=C), and 950 (C–H bend) cm^{-1}, were observed (Figure B.6). As we have indicated, these features can be attributed to hydroxide (O–H), carbonyl (C=O), and aliphatic carbons (C–H) functionalities. The observation of such functionalities suggests the formation of aliphatic, alcoholic, carboxylic acid, or aldehyde functionalities on the graphene surface providing critical proof of the saturation/oxidation of the graphene surface.

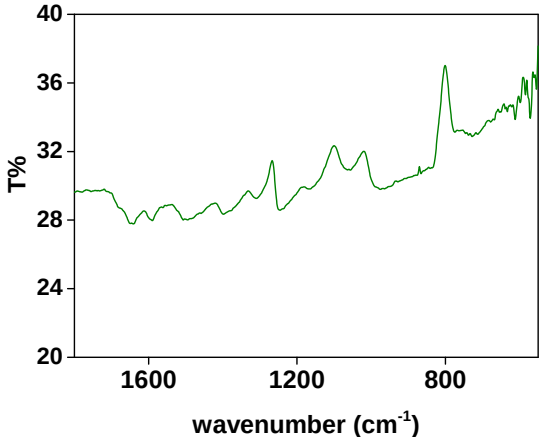

Fig. 4.6 ATR-IR difference spectra by subtracting heterostructure spectra from pristine graphene spectra: 1:15 2H-MoS_2/graphene.

Thermogravimetric analysis (TGA) and coupled thermogravimetric analysis/infrared spectroscopy (TGA-IR) were used to investigate the thermal decay properties of the heterostructures in order to gain further insight into the chemical functionalities on the graphene surface. As with the pristine materials, the heterostructures displayed no significant weight loss below 200 °C showing no residual solvent or smaller physisorbed molecules. Up to 600°C, the weight losses recorded for the heterostructures was markedly more than that seen in the control traces (Figure 4.7). There was a loss of 10% of the total weight of the heterostructure by 500 °C in both families of heterostructures (2H-MoS_2/ and ce-1T-MoS_2/graphene hybrids). In contrast, pristine graphene showed weight losses of less than 1% below 600 °C, while for 2H- and ce-1T-MoS_2 there was negligible weight loss below 600 °C with gradual decomposition of the material beyond 600 °C. (Figure 4.7, control traces)

The new weight loss in the heterostructured materials, prior to the degradation of the parent materials, supported the findings of the previous techniques as evidence for functional groups or less stable covalent defects being introduced into the MoS_2/graphene heterostructure. The defects cannot be physisorbed molecules because they are lost above 200 °C, in a region where covalently tethered entities normally appear.

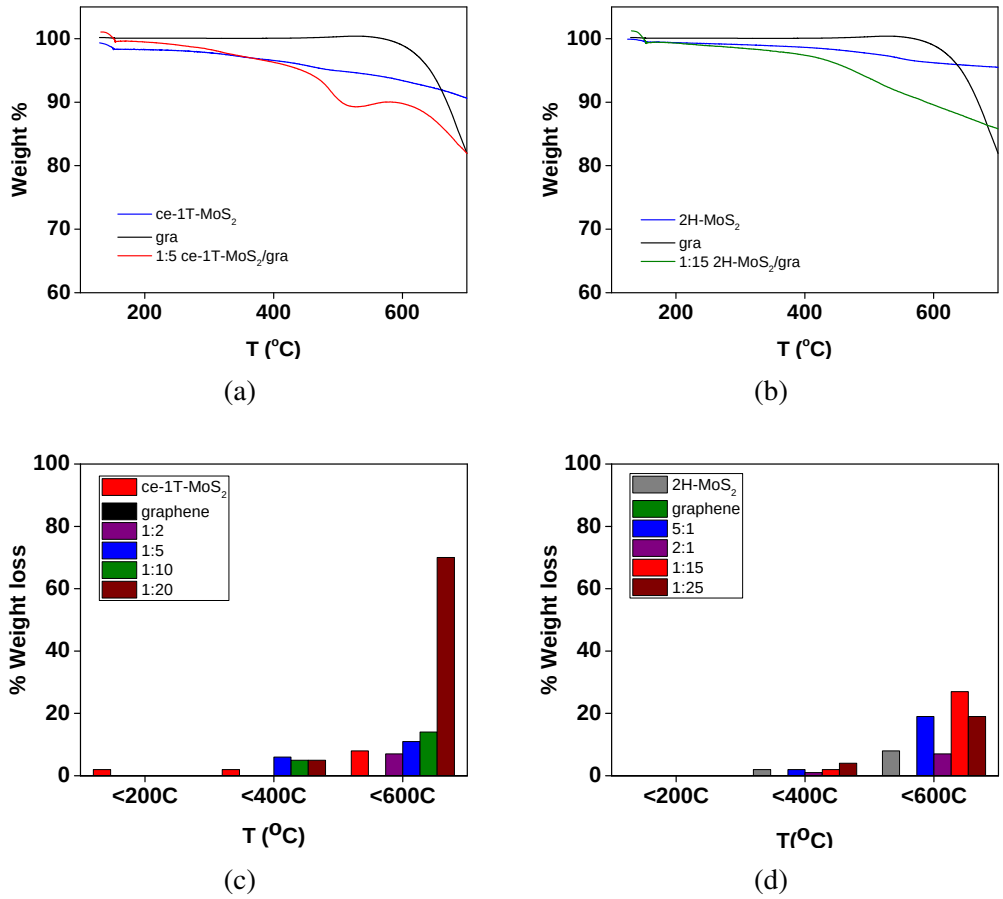

Fig. 4.7 TGA traces showing (a) the weight loss of a 1:5 molar ce-1T-MoS_2/graphene compared to the starting materials, (b) the weight loss of 1:15 2H-MoS_2/graphene compared to controls. (c) and (d) the cumulative weight loss between 200–600 °C for the different heterostructures of ce-1T-MoS_2/graphene and 2H-MoS_2/graphene.

In TGA-coupled infra-red (TGA-IR) spectroscopy, which performs IR analysis of the headspace of the TGA, CO_2 (ν = 2350 and 2320 cm^{-1}) was detected at much lower temperatures than that seen in pristine graphene (beginning at 390 °C) for the 2H-MoS_2/graphene

heterostructures (Figure B.8). In pristine few-layer graphene, such CO_2 features were observed only above 550 °C, which corresponded to the degradation of graphene around 600 °C (Figure 2.6).[32] In contrast no new SO_2 desorption was detected in the coupled TGA-IR spectra (any SO_2 loss was also observed in the pristine 2H- and ce-1T-MoS_2 materials at the same temperatures (Figures 2.14, 2.22)),[33, 34] showing that the MoS_2 components of the heterostructures were chemically unchanged and displayed no low temperature degradation. Likewise, the ce-1T-MoS_2/graphene heterostructure showed CO_2 formation at the relatively low temperature of 375 °C (Figures 4.8, B.8) further demonstrated chemical functionalisation of graphene had occurred. In summary, TGA and coupled TGA-IR of the MoS_2/graphene composites support the XPS and DRIFT-IR that indicated defective graphene in graphene/MoS_2 heterostructures.

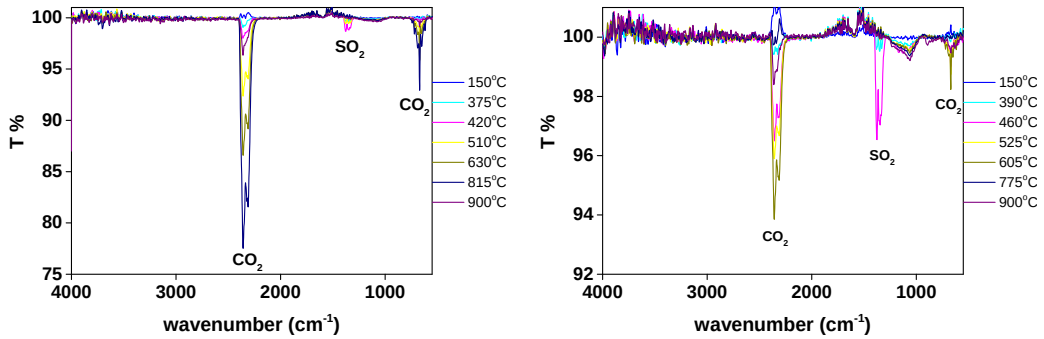

(a) (b)

Fig. 4.8 Overlaid IR spectra from coupled TGA-IR analysis of (a) a heterostructure of 1:5 ce-1T-MoS_2/graphene and (b) one of 1:15 2H-MoS_2/graphene showing the release of CO_2, SO_2 and anomalous organic matter (at 1200 cm^{-1}) with heating.

For the 2H-MoS_2 and ce-1T-MoS_2/graphene heterostructures the measured I_D:I_G ratio (0.26, 0.27) using the 532 nm line was similar to the measured value 0.29 for pristine few-layer graphene measured by Raman spectroscopy (Figure B.9, Tables B.1–4).[35, 36] The intensity ratio of the D/G bands I_D:I_G in graphene are used as a probe of defects in graphene-type materials. The lack of a difference in these values would indicate the degree of defect sites is low in the heterostructured materials, as indicated by TGA and XPS. For

the 2LA(M):A_{1g} mode of 2H-MoS_2 in the 2H-MoS_2/graphene heterostructure there were no significant changes from the pristine 2H-MoS_2 (Figure B.10).[37, 38] It can therefore be concluded that the heterostructures of MoS_2/graphene displayed no change in structure according to Raman spectroscopy from their parent materials.

4.4 Measuring the HER activity of ce-1T-MoS_2/graphene and 2H-MoS_2/graphene.

4.4.1 ce-1T-MoS_2/graphene Heterostructures

The catalytic activity and impedance of a film of ce-1T-MoS_2 and the ce-1T-MoS_2/graphene heterostructures was measured using linear sweep voltammetry and electrochemical impedance spectroscopy in a three electrode cell with a 0.5 M H_2SO_4 electrolyte. Three glassy carbon electrodes were coated with a film of ce-1T-MoS_2 or ce-1T-MoS_2/graphene as described in the experimental methods. Nafion (1% solution in IPA) was added to increase the adhesion of the film to the electrode and enable three linear sweeps to be performed on each electrode. The overpotential at which hydrogen evolution started and the Tafel slope as a measure of catalytic activity, were recorded for each electrode (Figure 4.9a). The resistance in the film, recorded using impedance spectroscopy, is also shown as a Nyquist plot of imaginary resistance to real resistance in Ω (Figure 4.9b).

For ce-1T-MoS_2, the overpotential at 5 mA/cm^2 was -380 mV with a Tafel slope of 90 mV/dec, which was similar to literature values for ce-1T-MoS_2.[39] The overpotential at 5 mA/cm^2 for each heterostructure tested was -470 mV (1:2 ce-1T-MoS_2/graphene), -360 mV (1:5), and -340 mV (1:10). The heterostructures were shown to demonstrate catalytic activity towards hydrogen evolution, comparable to that of the control ce-1T-MoS_2. 1:2 was the only heterostructure to show a large increase in overpotential, which was unusual for MoS_2/graphene catalysts. We then examined the Tafel slope of each heterostructure and compared it to ce-1T-MoS_2. The Tafel slope gives information on the mechanism of hydrogen evolution occurring at the catalyst, whether it is diffusion-limited or active site limited by determining which of the two steps of the HER reaction is rate limiting—the Volmer step (adsorption of H atom to metal surface) or the Tafel/Heyrovsky (reaction with

another absorbed H atom or proton to form H_2) step. For ce-1T-MoS_2, the Tafel slope was 90 mV/dec, compared to 178 mV/dec (1:2), 115 mV/dec (1:5) and 86 mV/dec (1:10). It was observed that low concentrations of graphene with ce-1T-MoS_2 have a detrimental effect on Tafel slope, while the higher concentration of graphene (1:10) resembles ce-1T-MoS_2. Therefore, ce-1T-MoS_2 and the 1:10 heterostructure demonstrated Volmer step rate dependence (the production of H_2 on the surface being rate determining) according to the lower Tafel slope. 1:5 gave a Tafel slope that was intermediate and therefore harder to assign the Volmer or Tafel/Heyrovsky step as rate determining. 1:2 showed a marked increase in both overpotential and Tafel slope, and therefore, the Tafel/Heyrovsky step was rate determining for this catalyst.

Lastly, the impedance of each heterostructure was compared to ce-1T-MoS_2. Resistance measured at -500 mV was 60 Ω for ce-1T-MoS_2, 160 Ω (1:2 ce-1T-MoS_2/graphene), dropping dramatically to 21 Ω (1:5) and 17 Ω (1:10) for these heterostructures. The resistance of the 1:5 and 1:10 films decreased relative to ce-1T-MoS_2, with 1:2 being the only heterostructure to show higher resistance then ce-1T-MoS_2. This drop in resistance was in agreement with the literature, in that the presence of graphene or other carbon nanomaterials increases the conductivity of the film.[40] The outlier, 1:2 which showed increased resistance relative to ce-1T-MoS_2, could be explained by the damage sustained by graphene from sonication with ce-1T-MoS_2 during the preparation of this heterostructure. This could have a deleterious effect on the conductivity of graphene, leading to a negation of the beneficial effect pristine graphene brings to the heterostructure. This could also explain the similar trend seen in the overpotential and Tafel slopes, in which the values for the 1:2 ce-1T-MoS_2/graphene heterostructure were considerably worse than for ce-1T-MoS_2 or the other heterostructures. The improved catalytic activity brought about by graphene is largely attributed to the improvement in conductivity, but DFT calculations also show that MoS_2 induces p type doping in graphene which facilitates H adsorption on both graphene and MoS_2 in van der Waals heterostructures which leads

to a build-up of negative charge on MoS_2 and improved catalysis.[41] For already defective or oxidised graphene, this charge transfer is hampered by the reduced negative charge on graphene, and therefore the charge transfer to MoS_2 also reduced, leading to no change, or in the worse case, a decrease in catalytic activity. This was offset in other heterostructures by the larger excess of graphene—in this way, large areas of graphene retained enough integrity and electron density to maintain higher conductivity and this led to improved catalytic performance. This was in agreement with the trends established in the XPS section above—lower concentrations of graphene relative to MoS_2 were subjected to more damage during heterostructure formation than higher concentrations of graphene, or graphene sonicated with 2H-MoS_2.

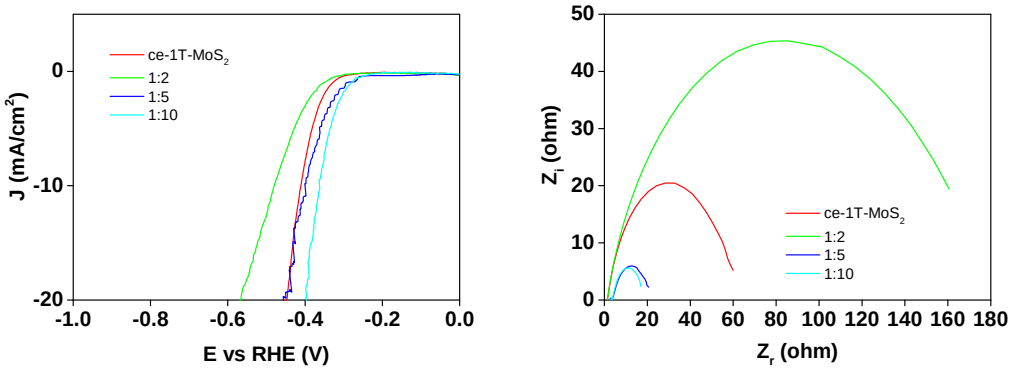

(a) (b)

Fig. 4.9 (a) LSV sweeps and (b) EIS Nyquist plots of ce-1T-MoS_2 and various heterostructures of ce-1T-MoS_2/graphene.

4.4.2 2H-MoS_2/graphene Heterostructures

2H-MoS_2 is known to have lower catalytic activity towards HER relative to ce-1T-MoS_2.[42] Therefore, the heterostructures composed of 2H-MoS_2/graphene were expected to show a greater change in activity than those of ce-1T-MoS_2, with the semi-conducting nature of 2H-MoS_2 paired with conductive graphene.[43] 2H-MoS_2 and 2H-MoS_2/graphene films

were prepared by filtering the dispersion through a membrane and cutting out a section of the membrane of an appropriate size for the glassy carbon electrode. The membrane was then removed by the acetone vapour method, as detailed in the experimental methods. No Nafion was used in the preparation of the 2H-MoS_2 or heterostructure films as they displayed better adhesion to the electrodes than ce-1T-MoS_2. For the control, a film of 2H-MoS_2 on a glass carbon electrode gave an overpotential of -630 mV (to RHE) at 5 mA/cm^2, and a Tafel slope of 112 mV/dec, demonstrating a decreased activity towards HER compared to ce-1T-MoS_2 and similar to that reported for the edges of 2H-MoS_2, and demonstrated Tafel/Heyrovsky step rate dependence.[44] The overpotential values for the heterostructures were as follows: -620 mV (2:1), -610 mV (1:5), -600 mV (1:15) and -600 mV (1:25) (Figure 4.10a). These were all very similar to the overpotential seen in 2H-MoS_2, demonstrating that the presence of graphene has a minimal effect on the overpotential. The Tafel slopes of the heterostructures were 118 mV/dec (2:1), 112 mV/dec (1:5), 115 mV/dec (1:15) and 120 mV/dec (1:25) mV/dec, compared to 2H-MoS_2 (112 mV/dec). These values are also within error of the control, demonstrating again that no change has occurred with respect to the activity of 2H-MoS_2. All heterostructures retained high Tafel slopes and overpotentials which could be attributed to Tafel/Heyrovsky step rate dependence.

The impedance spectra (Figure 4.10b) gave resistances of 55 Ω (2H-MoS_2), 35 Ω (2:1), 45 Ω (1:1), 50 Ω (1:15) and 35 Ω (1:25). The 2:1 and 1:25 MoS_2/graphene heterostructures showed the lowest resistance. The other samples 1:15, 1:1 also displayed lower resistance compared to the 2H-MoS_2 control, with some loss of conductivity. This correlated well to the overpotential data, which displayed a similar trend. 2:1 and 1:25 2H-MoS_2/graphene heterostructures seemed to perform better than other heterostructures and 2H-MoS_2 in terms of conductivity of the catalyst, and all heterostructures showed incremental improvement in catalytic activity compared to 2H-MoS_2. This could be due to the lower activity of 2H-MoS_2 towards introducing saturation into graphene when both materials were sonicated together

during heterostructure preparation. Possible reasons for the trend (2:1 ≈ 1:25 > 1:15 ≈ 1:1) could be that both 1:15 and 1:1 have defective graphene, whereas for 1:25 the graphene is mostly intact, giving greater conductivity, but this reasoning does not explain 2:1. Here, the minimal concentration of graphene, despite possible defects induced by MoS_2, seemed to improve the performance of the catalyst.

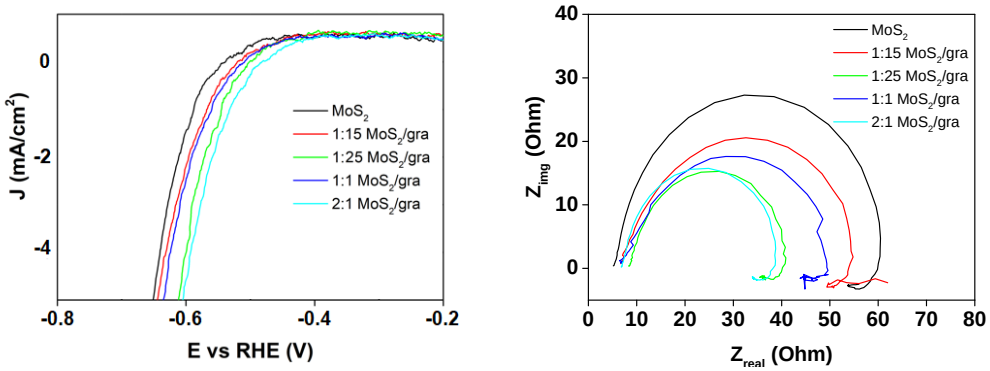

(a) (b)

Fig. 4.10 (a) LSV sweeps and (b) EIS Nyquist plots of 2H-MoS_2 and 2H-MoS_2/graphene heterostructures.

4.5 Conclusions

In conclusion, the preparation of composite films of 1T-MoS_2/graphene showed an increase in saturated and oxygenated carbon content compared to that of the starting materials alone under the same conditions. XPS analysis of the prepared heterostructures revealed an increase in the C-C/C-O component of the C 1s core level spectra for heterostructures composed of a series of ratios of ce-1T-MoS_2/graphene. The Raman results differed from the XPS as the C 1s core level spectra suggested some functionalisation was introduced into the graphene structure when combined with 1T-MoS_2. TGA-IR, ATR-IR and difference IR were employed next to ascertain the amount and nature of the disorder or functionality on graphene—using difference spectra new peaks were isolated and assigned as O-H, C=C, C-O and C-H moieties not found in pristine graphene.

2H-MoS_2/graphene heterostructures also showed the increase in saturated carbon that correlated with 2H-MoS_2 concentration by XPS. Raman spectroscopy for the 2H-MoS_2 heterostructures showed no obvious increase in defect formation for graphene or any variation in the structure of 2H-MoS_2. TGA-IR traces of 2H-MoS_2/graphene showed loss of CO_2 and SO_2 exceeding that of the parent materials, but lower levels than were observed for heterostructures containing ce-1T-MoS_2. The potentially higher levels of functionalisation of 1T-MoS_2/graphene compared to 2H-MoS_2/graphene can also be explained by the higher activity of 1T-MoS_2 compared to its other 2D polymorph.[45]

The decrease in efficacy seen in 2H-MoS_2 containing-samples compared to 1T-MoS_2, has been rationalised as the active sites for catalysis or reactivity being located at the edges or inherent defect sites for 2H-MoS_2. 1T-MoS_2 in contrast, has been shown to have a reactive basal plane as well as active edges.[46] Any functionalisation happening at few layer graphene from close proximity to the MoS_2 under sonication could be occurring at the easily accessible edges, causing small signals to appear in the XPS and TGA-IR/ATR-IR, but not changing the

overall concentration of defects detected by Raman spectroscopy. The presence of O_2 or H_2O in the solvent, combined with MoS_2, may be causing the formation of oxygen-containing groups on graphene. Further studies, conducted in the absence of O_2 may clarify this.

The consequences of the interaction between MoS_2 and graphene was further investigated through the study of the HER activity of the heterostructures relative to ce-1T-MoS_2 or 2H-MoS_2 alone. As shown in the main body of the report, although some disorder was introduced into graphene from 2H-MoS_2 in the 2H-MoS_2/graphene heterostructures, this was a lower degree of disorder/functionalisation than was seen in the ce-1T-MoS_2/graphene heterostructures. The HER data also appeared to support this, showing the presence of graphene generally improving conductivity in the 2H-MoS_2/graphene heterostructures, with a reduction or less pronounced effect the lower the graphene concentration relative to MoS_2. For ce-1T-MoS_2/graphene heterostructures, higher concentrations of graphene also displayed greater conductivity but for graphene below 5 equivalents the conductivity suffered due to the defects introduced during heterostructure formation. This followed the trend seen in the XPS, where more saturation was observed in heterostructures with a lower ratio of graphene to MoS_2. The reasoning for this could be linked to the defects introduced into the structure of graphene preventing the postulated charge transfer from pristine graphene to MoS_2 that has been shown by DFT calculations.[41]

The results of this study offer evidence for a non-innocent interaction between graphene and ce-1T-MoS_2 in the preparation of composite films by liquid exfoliation, also suggesting a weaker effect when 2H-MoS_2 is employed. The determination of the exact nature of these functionalities through the use of TGA-MS and ssNMR, and the study of heterostructure formation in degassed solvent and an inert atmosphere, will be the focus of further studies.

4.6 Experimental Methods

Materials

HPLC-grade 2-propanol was purchased from Fisher Scientific UK. Deionised water and SGN18 synthetic graphite were used as received. Bulk MoS_2 powder and n-BuLi (1.6 M in hexanes) were purchased from Sigma-Aldrich Co.

Preparation of 2H-MoS_2/graphene and 1T-MoS_2/graphene composites

Fresh dispersions of 2H-MoS_2 and few-layer graphene were combined while varying the concentration of either graphene or 2H-MoS_2 (0.3 mmol-3 mmol MoS_2 to 0.3 mmol-7.5 mmol graphene) and sonicated together in an ultrasonic bath for 2 h. The dispersion mixture was then stirred at RT for 12 h and filtered onto a membrane with a pore size of 0.025 μm. The dispersions were dropcast onto slides for Raman spectroscopic analysis. For XPS, TGA, ATR-IR, DRIFT-IR and pXRD analysis and HER studies, these dispersions were filtered using a membrane of pore size 0.2 μm to form composite films.

Preparation of Electrodes

Ce-1T-MoS_2/graphene: A dispersion of a ce-1T-MoS_2 or a heterostructure (1:2, 1:5, 1:10, 1:12 ce-1T-MoS_2/graphene), in total 0.2 mg of material, was mixed with 300 μm of 1% Nafion solution. This was then dropcast directly onto glassy carbon electrodes (with an area of 1 cm^2) and the electrodes left to dry in air completely before use.

2H-MoS_2/graphene: A dispersion of a 2H-MoS_2 or a heterostructure (2:1, 1:1, 1:15, 1:25 2H-MoS_2/graphene) was filtered onto a nitrocellulose membrane with a pore size of 0.025 μm. The heterostructure film was transferred to a glassy carbon membrane of size 0.7 cm^2 by the acetone vapour method: A circle of the membrane containing 0.2 mg of film was punched out and wetted with 2-propanol (IPA). This was applied to the electrode surface and the electrode was exposed to hot acetone vapour until the membrane became clear. It was then submerged in a series of three acetone baths spending 10 minutes in each to fully

remove the membrane. The electrode coated with the heterostructure film was left to dry in air before use.

Electrochemistry

Electrochemical measurements were performed in a cell consisted of a standard three-electrode setup: Pt wire counter electrode, glassy carbon working electrode, and an Ag/AgCl reference electrode, in 0.5 M H_2SO_4 electrolyte. Linear sweep voltammetry (LSV) and electrochemical impedance spectroscopy (EIS) were performed on a Gamry 3000 potentiostat at an overpotential of -0.5 V. Each working electrode was conditioned at -0.5 V before performing LSV and EIS. All data was iR corrected with respect to the electrolyte resistance.

ce-1T-MoS_2/graphene

Three electrodes coated with ce-1T-MoS_2 or one of each prepared heterostructure with graphene were subjected to three instances of linear sweep voltammetry (0.1 V to -1.0 V vs RHE) and one cycle of electrochemical impedance spectroscopy at -0.5 V vs RHE.

2H-MoS_2/graphene

Three electrodes coated with 2H-MoS_2 or one of each prepared 2H-MoS_2/graphene heterostructure were subjected to three instances of linear sweep voltammetry (0.1 V to -1.2 V vs RHE) and one cycle of electrochemical impedance spectroscopy at -0.5 V vs RHE.

References

[1] X. Xu, Y. Sun, W. Qiao, X. Zhang, X. Chen, X. Song, L. Wu, W. Zhong and Y. Du, *Applied Surface Science*, 2017, **396**, 1520–1527.

[2] L. Zhao, C. Hong, L. Lin, H. Wu, Y. Su, X. Zhang and A. Liu, *Carbon*, 2017, **116**, 223–231.

[3] X. Zheng, J. Xu, K. Yan, H. Wang, Z. Wang and S. Yang, *Chemistry of Materials*, 2014, **26**, 2344–2353.

[4] Y. Li, H. Wang, L. Xie, Y. Liang, G. Hong and H. Dai, *Journal of the American Chemical Society*, 2011, **133**, 7296–7299.

[5] V. Singh, D. Joung, L. Zhai, S. Das, K. S. I. and S. S., *Progress in Materials Science*, 2001, **56**, 1178–1271.

[6] X. Xie, Z. Ao, D. Su, J. Zhang and G. Wang, *Advanced Functional Materials*, 2015, **25**, 1393–1403.

[7] K. Chang and W. Chen, *Chemical Communications*, 2011, **47**, 4252–4254.

[8] S. Bertolazzi, D. Krasnozhon and A. Kis, *ACS Nano*, 2013, **7**, 3246–3252.

[9] K.-J. Huang, L. Wang, J. Li and Y.-M. Liu, *Sensors and Actuators B: Chemical*, 2013, **178**, 671–677.

[10] K. Chang and W. Chen, *ACS Nano*, 2011, **5**, 4720–4728.

[11] Z. Ding, Q.-X. Pei, J.-W. Jiang, W. Huang and Y.-W. Zhang, *Carbon*, 2016, **96**, 888–896.

[12] J. E. Lee, J. Jung, T. Y. Ko, S. Kim, S.-I. Kim, J. Nah, S. Ryu, K. T. Nam and M. H. Lee, *RSC Advances.*, 2017, **7**, 5480–5487.

[13] Y. R. Lim, Y. B. Lee, S. K. Kim, S. J. Kim, Y. Kim, C. Jeon, W. Song, S. Myung, S. S. Lee, K.-S. An and J. Lim, *Applied Surface Science*, 2017, **392**, 557–561.

[14] X. Wan, K. Chen, Z. Chen, F. Xie, X. Zeng, W. Xie, J. Chen and J. Xu, *Advanced Functional Materials*, 2017, **27**, 1603998–1604005.

[15] J. N. Coleman, M. Lotya, A. O'Neill, S. D. Bergin, P. J. King, U. Khan, K. Young, A. Gaucher, S. De, R. J. Smith, I. V. Shvets, S. K. Arora, G. Stanton, H.-Y. Kim, K. Lee, G. T. Kim, G. S. Duesberg, T. Hallam, J. J. Boland, J. J. Wang, J. F. Donegan, J. C. Grunlan, G. Moriarty, A. Shmeliov, R. J. Nicholls, J. M. Perkins, E. M. Grieveson, K. Theuwissen, D. W. McComb, P. D. Nellist and V. Nicolosi, *Science*, 2011, **331**, 568–571.

[16] D. Pierucci, H. Henck, J. Avila, A. Balan, C. H. Naylor, G. Patriarche, Y. J. Dappe, M. G. Silly, F. Sirotti, A. T. C. Johnson, M. C. Asensio and A. Ouerghi, *Nano Letters*, 2016, **16**, 4054–4061.

[17] R. Liu, B. Liao, X. Guo, D. Hu, H. Hu, L. Du, H. Yu, G. Zhang, X. Yang and Q. Dai, *Nanoscale*, 2017, **9**, 208–215.

[18] A. P. Murthy, J. Theerthagiri, J. Madhavan and K. Murugan, *Physical Chemistry and Chemical Physics*, 2017, **19**, 1988–1998.

[19] R. K. Biroju, D. Das, R. Sharma, S. Pal, L. P. L. Mawlong, K. Bhorkar, P. K. Giri, A. K. Singh and T. N. Narayanan, *ACS Energy Letters*, 2017, **2**, 1355–1361.

[20] H.-J. Shin, K. K. Kim, A. Benayad, S.-M. Yoon, H. K. Park, I.-S. Jung, M. H. Jin, H.-K. Jeong, J. M. Kim, J.-Y. Choi and Y. H. Lee, *Advanced Functional Materials*, 2009, **19**, 1987–1992.

[21] Y. Shang, D. Zhang, Y. Liu and C. Guo, *Bulletin of Materials Science*, 2015, **38**, 7–12.

[22] G. Wang, J. Yang, J. Park, X. Gou, B. Wang, H. H. Liu and J. Yao, *Journal of Physical Chemistry C*, 2008, **112**, 8192–8195.

[23] K. E. Dungey, M. D. Curtis and J. E. Penner-Hahn, *Chemistry of Materials*, 1983, **10**, 2152–2161.

[24] Y. Liu, X. Wang, X. Song, Y. Dong, L. Yang, L. Wang, D. Jia, Z. Zhao and J. Qiu, *Carbon*, 2016, **109**, 461–471.

[25] Y. Liu, L.-Z. Fan and L. Jiao, *Journal of Power Sources*, 2017, **340**, 104–110.

[26] V. H. Pham, K.-H. Kim, D.-W. Jung, K. Singh, E.-S. Oh and J. S. Chung, *Journal of Power Sources*, 2013, **244**, 280–286.

[27] X. Ren, X. Ren, L. Pang, Y. Zhang, Q. Ma, H. Fan and S. F. Liu, *International Journal of Hydrogen Energy*, 2016, **41**, 916–923.

[28] Z. Wang, T. Chen, W. Chen, K. Chang, L. Ma, G. Huang, D. Chenb and J. Y. Leeb, *Journal of Materials Chemistry A*, 2013, **1**, 2202–2210.

[29] L. Liu, M. An, P. Yang and J. Zhang, *Scientific Reports*, 2015, **5**, 9055.

[30] M. Velicky, M. A. Bissett, P. S. Toth, H. V., S. D. Worrall, A. N. J. Rodgers, E. W. Hill, I. A. Kinloch, K. S. Novoselov, T. Georgiou, L. Britnell and R. A. W. Dryfe, *Physical Chemistry Chemical Physics*, 2015, **17**, 17844–17853.

[31] N. M. Brown, N. Cui and A. McKinley, *Applied Surface Science*, 1998, **134**, 11–21.

[32] J. W. London and A. T. Bell, *Journal of Catalysis*, 1973, **31**, 32–40.

[33] J. P. Dunn, P. R. Koppula, H. G. Stenger and I. E. Wachs, *Applied Catalysis B: Environmental*, 1998, **19**, 103–117.

[34] D. M. Sim, H. J. Han, S. Yim, M.-J. Choi, J. Jeon and Y. S. Jung, *ACS Omega*, 2017, **2**, 4678–4687.

[35] D. Yang, A. Velamakanni, G. Bozoklu, S. Park, M. Stoller, R. D. Piner, S. Stankovich, I. Jung, D. A. Field, C. A. Ventrice and R. S. Ruoff, *Carbon*, 2009, **47**, 145–152.

[36] A. C. Ferrari, J. C. Meyer, V. Scardaci, C. Casiraghi, M. Lazzeri, F. Mauri, S. Piscanec, D. Jiang, K. S. Novoselov, S. Roth and A. K. Geim, *Physical Review Letters*, 2006, **97**, 187401.

[37] B. Pal, A. Singh, S. G. P. Mahale, A. Kumar, S. Thirupathaiah, H. Sezen, M. Amati, L. Gregoratti and U. V. Waghmare, *Physical Reviews B*, 2017, **96**, 195426.

[38] E. E. Benson, H. Zhang, S. A. Schuman, S. U. Nanayakkara, N. D. Bronstein, S. Ferrere, J. L. Blackburn and E. M. Miller, *Journal of the American Chemical Society*, 2018, **140**, 441–450.

[39] X. Chia, A. Ambrosi, D. Sedmidubský, Z. Sofer and M. Pumera, *Chemistry – A European Journal*, 2014, **20**, 17426–17432.

[40] K. Pramoda, U. Gupta, I. Ahmad, R. Kumara and C. N. R. Rao, *Journal of Materials Chemistry A*, 2016, **4**, 8989–8994.

[41] H. Li, K. Yu, C. Li, Z. Tang, B. Guo, X. Lei, H. Fu and Z. Zhu, *Scientific Reports*, 2015, **5**, 18730.

[42] T. F. Jaramillo, K. P. Jorgensen, J. Bonde, J. H. Nielsen, S. Horch and I. Chorkendorff, *Science*, 2007, **317**, 100–102.

[43] F. Wang, T. A. Shifa, X. Zhan, Y. Huang, K. Liu, Z. Cheng, C. Jiang and J. He, *Nanoscale*, 2015, **7**, 19764–19788.

[44] S. M. Tan, A. Ambrosi, Z. Sofer, Š. Huber, D. Sedmidubský and M. Pumera, *Chemistry – A European Journal*, 2015, **21**, 7170–7178.

[45] S. Presolski and M. Pumera, *Materials Today*, 2016, **19**, 140–145.

[46] M. A. Lukowski, A. S. Daniel, F. Meng, A. Forticaux, L. Li and S. Jin, *Journal of the American Chemical Society*, 2013, **135**, 10274–10277.

Chapter 5

The Formation of a Covalently Linked Heterostructure of Graphene and 1T-MoS_2 and its Use as a Catalyst for HER

5.1 Introduction

As seen in the previous chapter, heterostructures comprised of liquid exfoliated graphene and 2H-MoS_2 or chemically exfoliated 1T-MoS_2 can be prepared by sonicating and depositing materials together for use in applications such as HER. This chapter will take the formation of heterostructures one step further by illustrating the preparation, characterisation and application of a heterostructure of covalently bound MoS_2 and graphene from functionalised liquid exfoliated starting materials. The field of research concerning nanomaterial-based heterostructures, composed of carbon-based nanomaterials and two-dimensional transition

metal dichalcogenides, has been dominated by Van der Waals or other non-covalent interactions in the preparation of heterostructures, as was the case in the previous chapter. These methods involve chemical vapour co-deposition of graphene on MoS_2 or *vice versa*,[1, 2] hydrothermal/solvothermal synthesis of graphene oxide together with precursor salts such as MoO_3/NaS_2 or $(NH_4)_2MoS_4$ [3, 4] and the use of GO or rGO in the place of pristine graphene. Reports detailing the covalent linking of graphene and MoS_2 are few—one of the more promising methods was published by Rao *et al* utilised Sonogashira coupling (using a Pd(0) catalyst, CuI cocatalyst and TEA in 140 °C DMF) between sheets of iodobenzene functionalised MoS_2 and iodobenzene functionalised reduced graphene oxide.[5] The heterostructure formed displayed high CO_2 adsorption properties, and they used the same chemistry to create 3D assemblies of MoS_2 which showed enhanced HER activity. This paper continued the use of reduced graphene oxide as a substitute for pristine graphene, however. Other reports detailing the linking of graphene and TMDs by covalent means were mostly computational, as in Kaxiras' 2017 study of 'lateral heterojunctions' of these materials *i.e.*, the interaction of covalently linked materials joined together at the edges of the sheets where dangling bonds facilitated binding.[6] Therefore this chapter details the construction and study of a heterostructure of covalently bound MoS_2 and graphene, by functionalising liquid exfoliated starting materials and connecting the materials *via* these functional groups into a heterostructure capable of HER catalysis.

Here, graphene was produced from liquid exfoliating SGN18 graphite as detailed previously, and treated with 4-carboxybenzene diazonium tetrafluoroborate to produce benzoic acid functionalised graphene. The ability of diazonium salts to functionalise graphene *via* single electron transfer chemistry has been known since 2009, with Tour's group showing the functionalisation of graphene nanoribbons from CNTs in 2009[7, 8] and Strano's group publishing a study on the differing reactivity of the edges and surface of epitaxial graphene towards diazonium salt solutions.[9] MoS_2 was chemically exfoliated to produce

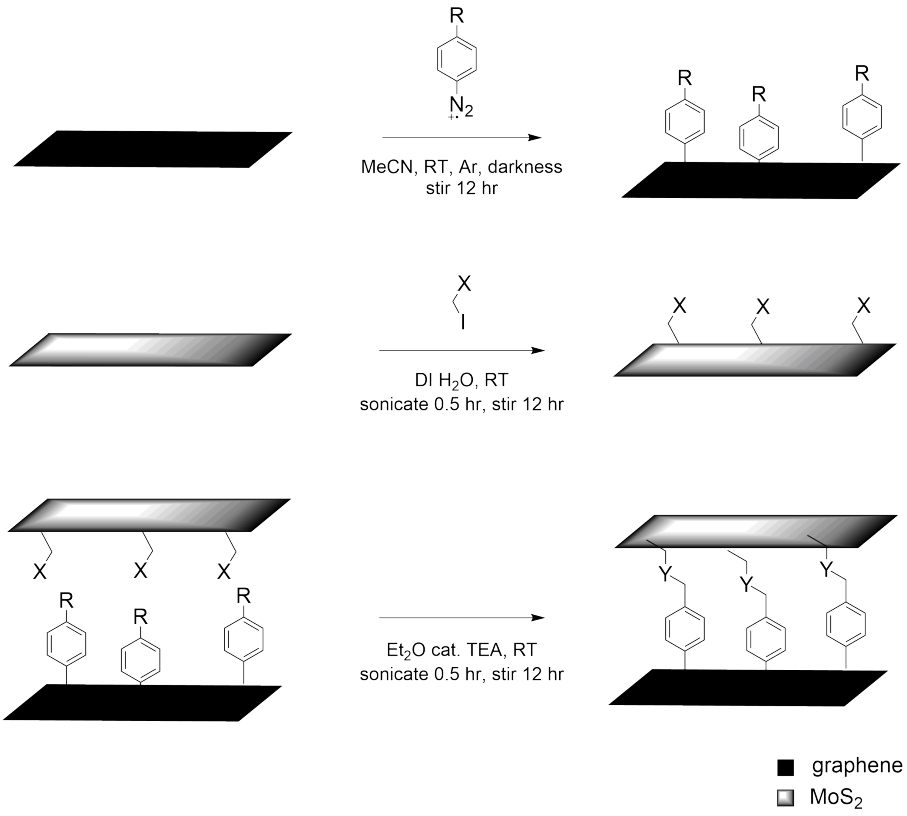

Scheme 5.1 The functionalisation of graphene, using diazonium salts, the conversion of these to a more reactive moiety, the halogen-based functionalisation of ce-1T-MoS_2 and the linking of functionalised graphene and MoS_2.

ce-1T-MoS_2. Iodoethanol was added to the dispersion of ce-1T-MoS_2 and after undergoing nucleophilic attack by the negatively charged nanosheets, resulted in ethanol functionalised MoS_2 (MoS_2-EtOH). The functionalisation of ce-1T-MoS_2 using halogenated substrates was first developed by Chhowalla's group in 2014.[10]

Next, benzoic acid functionalised graphene was converted to the more reactive benzoyl chloride functionalised graphene. Benzoyl chloride functionalised graphene and alcohol functionalised ce-1T-MoS_2 were reacted together to form an ester bridge between the two materials, and a summary of the main reactions is shown in Scheme 1. The carbonyl peak at 1680 cm^{-1} in gra-PhCOOH was an important spectroscopic handle that was used extensively to monitor the modification of the benzoic acid group in functionalised graphene. The shift of

the carbonyl peak in ATR-IR spectra also allowed for quick and accurate analysis of graphene functionalised with benzoyl chloride (gra-PhCOCl), iodoethyl benzoate (gra-PhCOOEt) and N-phenyl benzamide (gra-PhCONHPh), which became important intermediate steps in the synthesis of the covalently linked graphene and MoS_2 heterostructure. The linked graphene and MoS_2 heterostructure was then investigated for altered or enhanced HER activity compared to the ce-1T-MoS_2 starting material and the MoS_2-EtOH intermediate. It was also compared to the HER results of the heterostructures prepared from pristine materials, illustrated in the previous chapter.

5.2 Preparation of a Linked Heterostructure of Graphene and MoS_2

5.2.1 Preparation of Benzoic-Acid Functionalised Graphene

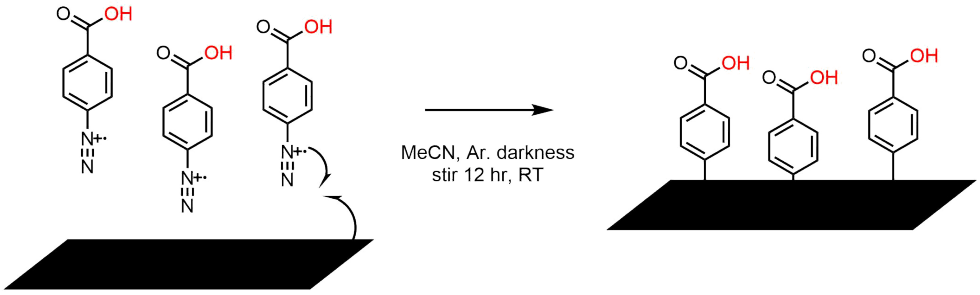

Scheme 5.2 The functionalisation of graphene with 4-carboxybenzenediazonium tetrafluoroborate.

To achieve the covalent linking of graphene to MoS_2, few-layer graphene was initially functionalised with benzoic acid groups *via* a modified version of diazonium salt based functionalisation of graphene.[11] Graphene was prepared as previously described, by probe sonicating and centrifuging graphite in order to produce a dispersion.[12] Next, this was filtered and then redispersed in MeCN by probe sonication for 3 h. 4-carboxybenzenediazonium tetrafluoroborate was prepared from *p*-aminobenzoic acid (PABA), tetrafluoroboric acid (HBF_4) and sodium nitrite ($NaNO_2$) in DI water as detailed in the experimental section.[13] This liquid exfoliated graphene was treated with 4-carboxybenzene diazonium tetrafluoroborate in MeCN, under N_2 and in darkness, for 16 h before work up, yielding a green solid from an initially black graphene dispersion and yellow 4-carboxybenzenediazonium tetrafluoroborate. This product, benzoic acid-functionalised graphene (gra-PhCOOH) was collected by centrifuging at 4500 rpm for 1 h, then subjected to several cycles of washing with MeCN and acetone and further centrifuging. It was then characterised by ATR-IR, TGA, Raman spectroscopy, XPS, SEM and pXRD.

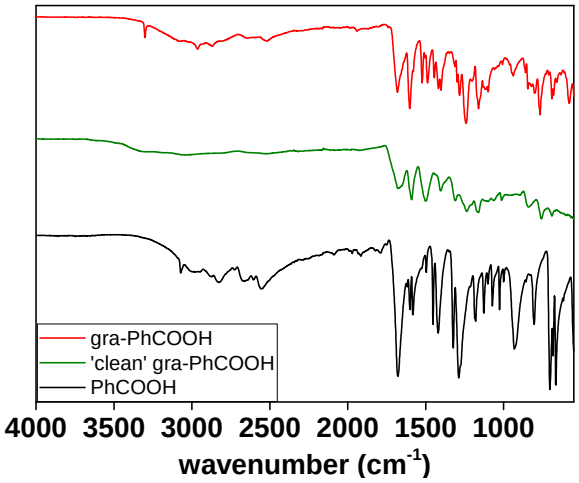

Fig. 5.1 ATR-IR spectra of benzoic acid (black) as-synthesised gra-PhCOOH (red) and 'clean' gra-PhCOOH (green) (Figure C.3 shows the region 2000–550 cm^{-1} in greater detail).

The ATR-IR spectrum of gra-PhCOOH was obtained and compared to that of free benzoic acid (Figure 5.1). As previously mentioned in the characterisation of graphene, pristine graphene has an almost featureless IR spectrum—this changed considerably upon functionalisation with the diazonium salt, to O-H stretches, C=O and C-O stretches, and a multitude of C-H and C=C stretches and bends that could be attributed to benzoic acid clearly present. For gra-PhCOOH, these were located at ν = 3304 (O-H stretch), 3070, 2995, 2879, 2819, (aromatic C-H stretches) 2650, 2602, 2525 (alkyl C-H stretches), 1680 (C=O stretch), 1600, 1581 (C=C stretch), 1517 (C-H bend), 1485, 1415 (O-H bend), 1326, 1284, 1246 (O=C-O sym stretch), 1160 (O=C-O asym stretch), 1124, 1070, 1025 (C-O bend), 930, 809, 764 (substituted aromatic C-H bend), 684, 576 cm^{-1}. The disappearance of the nitrogen triple bond of the diazonium salt (2307 cm^{-1}, Figure C.1) was also indicative of successful functionalisation. A number of the peaks overlapped directly with the peaks obtained for commercially available benzoic acid (Figure 5.1). Other than the carbonyl stretch at 1680 cm^{-1}, the peaks at ν = 3070, 2879, 2650, 2525, 1600, 1581, 1517, 1485, 1415, 1284, and 684 cm^{-1} could also be directly attributed to benzoic acid. The small shifts in other peaks could be due to the covalent bond to graphene, or from leftover starting material.

In order to remove any physisorbed or nitrogen-containing starting materials that might be contributing to the unassigned peaks in the ATR-IR spectrum, 50 mg of gra-PhCOOH powder was heated in an oven at 130 °C for 1 h, resulting in a colour change from green to brown. This heated gra-PhCOOH was analysed again by ATR-IR. The baseline shifted to lower transmission, which was characteristic of the graphene ATR-IR spectrum.[14] The majority of the peaks previously attributed to benzoic acid groups on graphene were still present, but at lower intensities. This suggested that part of the material covering the graphene had been removed. These peaks were ν = 3320 (O-H stretch), 3185, 3071, 3030, 2804 (aromatic C-H stretch), 2637, 2527 (alkyl C-H stretch), 1681 (C=O stretch), 1650, 1593 (C=C stretch), 1498, 1405 (O-H bend), 1310, 1236 (O=C-O sym stretch), 1163 (O=C-O asym stretch), 1100, 1065, 1016 (C-O bend), 835, 757 (substituted aromatic C-H bend), 688 cm^{-1}. Comparing the spectrum to free benzoic acid revealed that although many peaks still remained that overlapped with those in benzoic acid (specifically ν = 2527, 1590, 1405, 1310, 1236, 1163, 1065, 1016, 687 cm^{-1}) there was a shift in several peaks of more than 10 cm^{-1} wavenumbers (2650 to 2637, 1485 to 1498, 1326 to 1310, 1246 to 1236, and 930 to 895 cm^{-1}). This could be explained by conjugation of the benzoic acid groups to the graphene surface, which could occur after covalent bonding. This could cause a decrease in frequency, and therefore wavenumber, of the stretching conjugated bonds as electron density is shared across multiple close double bonds, effectively weakening them.

TGA analysis was employed in order to determine the extent of functionalisation of graphene and to confirm the nature of the functional groups (Figure 5.2a). Gra-PhCOOH was heated to 150 °C and kept at this temperature for 10 minutes, after which, the powder was heated to 900 °C at a rate of 10 °C/min, and the weight loss over this temperature range monitored. Weight losses below 200 °C are generally attributed to the degradation and release of physisorbed material from the surface of graphene, whereas weight loss above this and up to 600 °C is considered to be from the thermolysis of covalently bound species on

the graphene surface and edges with the graphene itself degrading in air above this. TGA analysis of gra-PhCOOH consistently showed weight loss in the range 260–270 °C of 20% which was determined to be free benzoic acid by TGA-IR (Figure 5.3). Upon removal of this species, there was no weight lost before 250 °C, confirming the removal of all solvent and volatile species. Above this, the average weight loss was 39% up to 600 °C which can be assigned as the loss of covalently bound functional groups from the surface and edges of graphene. This was supported by the 1st derivative of the TGA trace—the loss of free benzoic acid was seen with the highest rate of weight loss (the inflection point) at 210 °C (Figure 5.2b). Other weight loss stages were also present, with points at 250 °C and 450 °C, relating to the release of covalently bound functional groups from graphene. Coupled TGA-IR analysis of gra-PhCOOH identified that the first species given off was benzoic acid, along with CO_2 (Figure 5.3b). The peaks assigned to free benzoic acid disappeared from the ATR spectra above 300 °C, with concommitant growth in intensity of the CO_2 peaks at ν = 2350 and 2320 cm^{-1} from 375 °C onwards as the covalently bound groups thermolysed, and graphene itself began to degrade.

Taking 39% as the weight loss attributed to the loss of functional groups (initial decarboxylation and subsequent lysis of C-C bonds at substituted aromatic rings or on the

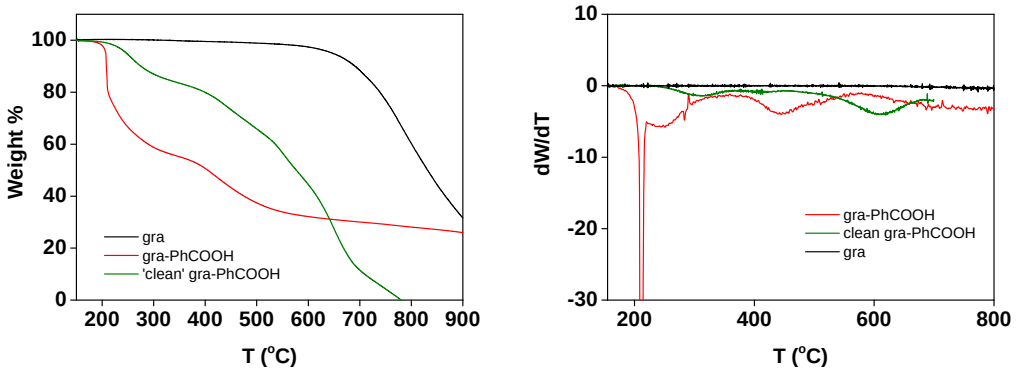

(a) (b)

Fig. 5.2 (a) TGA traces and (b) corresponding derivatives of pristine graphene (black), as-synthesised gra-PhCOOH (red) and cleaned gra-PhCOOH (green).

surface of graphene), with the 20% relating to physisorbed material disregarded, the degree of functionalisation was estimated. The weight of the sample minus 20% (2.0 mg from a total of 2.5 mg used for TGA) was recalculated to be 49% benzoic acid and 51% graphene. Calculating the amount in moles of each species gave 10% of the graphene functionalised with benzoic acid.

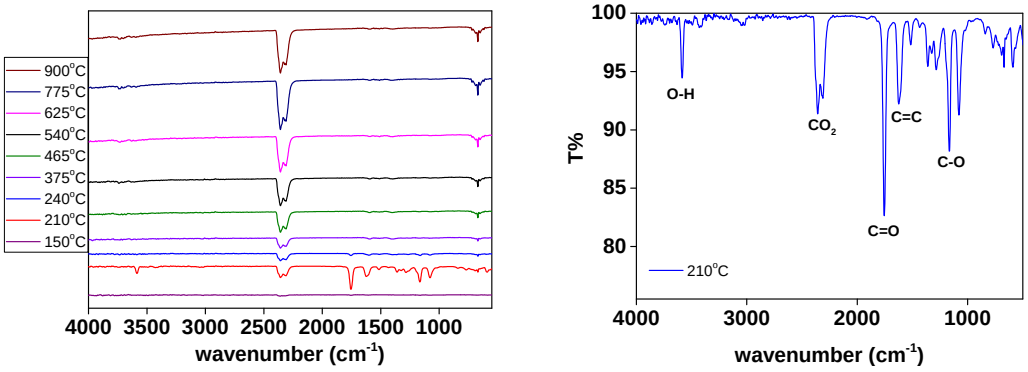

Fig. 5.3 (a) Coupled TGA-IR spectra of gra-PhCOOH at stated temperatures. (b) The spectrum at 210 °C showing benzoic acid and CO_2.

TGA analysis of 'clean' gra-PhCOOH—which had already undergone a heating step in an oven in order to remove volatile physisorbed surface groups—was also obtained. Here, insignificant weight loss below 250 °C was observed. In the range of 250–600 °C, a total of 36% weight loss occurred. This was similar than that seen for the original gra-PhCOOH powder in the same temperature range. From this, it was inferred that heating gra-PhCOOH to 260 °C removed physisorbed benzoic acid but did not seem to significantly change the concentration of covalently bonded functional groups according to TGA. The 1st derivative of the TGA trace of 'clean' TGA also differed from untreated gra-PhCOOH, reflecting the disappearance of the inflection point at 210 °C with a new point at 380 °C. It also retained the point seen at 450°C, and showed the weight loss step at 610 °C of the degradation of graphene (Figure 5.2b).

The total weight loss before 600 °C, 36%, demonstrated a similar amount of functionalisation as the as-prepared gra-PhCOOH minus the weight lost before 250 °C (39%). The approximate percentage of functionalised graphene for clean gra-PhCOOH by TGA was also 10% of the total graphene content.

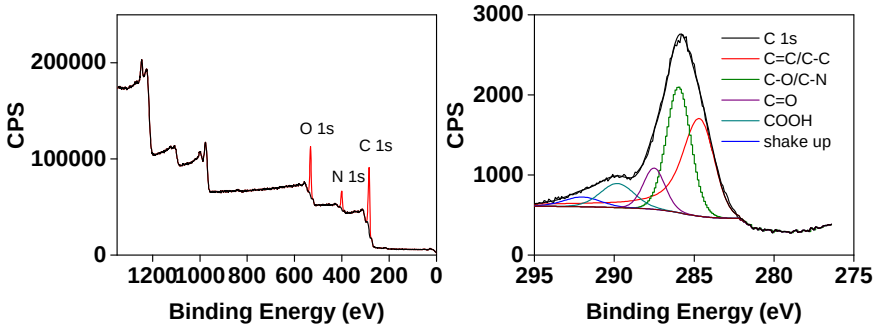

(a)

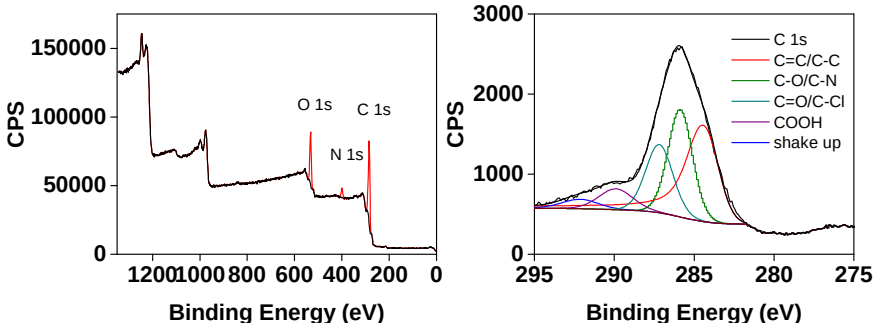

(b)

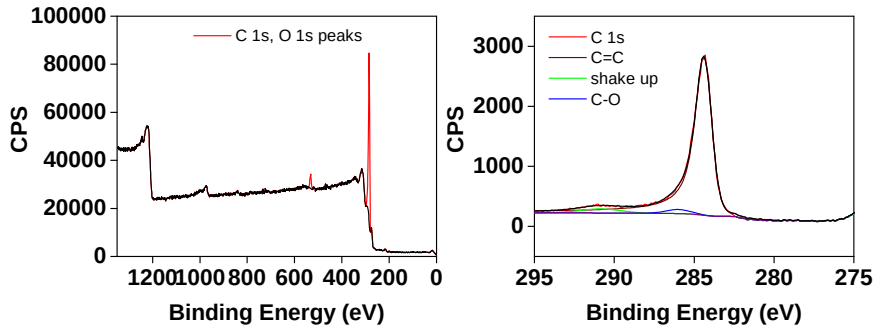

(c)

Fig. 5.4 (a) The survey spectrum and C 1s core level spectrum of gra-PhCOOH, showing components. (b) The survey spectrum and C 1s core level spectrum of 'clean' gra-PhCOOH, showing components. (c) The survey spectrum and C 1s core level spectrum of graphene for reference.

XPS analysis of gra-PhCOOH also supported the evidence of graphene functionalisation seen in the ATR-IR and TGA analysis (Figure 5.4a). The survey spectrum of gra-PhCOOH confirmed the presence of C, O and a small amount of N as residual diazonium or PABA on the surface of the re-aggregated graphene. The approximate concentrations of each element detected were 72% (C), 17% (O) and 11% (N), compared to pristine graphene (96% C and 4% O) showing a marked increase in oxygen content. Further analysis was confined to the C 1s, N 1s and O 1s core level spectra (Figures 5.4 and C.5–6). The C 1s spectrum was fitted as follows: 35% C=C/C-C (284.6 eV), reduced from a pristine graphene fitting of approximately 88%. Some of this peak was attributed to the formation of new C-C bonds, as a result of functionalisation by the diazonium salt, but the binding energy of these species were determined to be too close to separate with conviction. C-O and remaining C-N peaks were also fit with one feature at 286 eV, due to the binding energy of these species being too close for confident separate fitting, taking up 39% of the contribution to the C 1s peak. C=O and COOH (287.5 and 289.8 eV, respectively) were present as 11% and 10% of the C 1s peak. The presence of the carbon to oxygen peaks, in particular the obvious COOH peak demonstrated the presence of carboxylic acid species on graphene. The shake up feature (292.0 eV) seen in samples with large regions of sp^2 carbon was fitted as 5%. The N 1s core level spectrum showed two low resolution features at 400 and 401.5 eV that were assigned as N-C and N=N respectively, demonstrating that some diazonium/PABA remained. The O 1s core level spectrum showed an almost even split between C=O and C-O which was expected for the high number of carboxylic acid groups present (Figure C.5).[15]

The XPS survey spectrum of 'clean' gra-PhCOOH showed C (75% from core spectra calculations), O (20%) and N (5%), with a reduction in N concentration which could correspond to the loss of some of the residual diazonium on the surface, and a small increase in O. The C 1s core level spectrum was fitted as 33% C=C/C-C (284.6 eV), 32% C-O/C-N (285.9 eV), 23% C=O (287.1 eV) and 9% COOH (289.9 eV), with the shake up feature

taking up 4% (292.1 eV). The increase in C=O was supported by the increase in O seen in the survey. The loss of some residual diazonium may be accompanied by some oxidation as the sample was heated in air, which would also explain the increase in O and reduction in N seen in the survey compared to as-prepared gra-PhCOOH. As in the previous sample, the N 1s core level spectrum showed two low resolution features at 400 and 401.5 eV that were assigned as N-C and N=N respectively, and the O 1s core level spectrum showed an almost even split between C=O and C-O as expected (Figure C.5). Therefore, by XPS, 'clean' gra-PhCOOH showed a slight reduction in N but a large increase in O, suggesting some oxidation of graphene or the functional groups had occurred as well as removal of some residual amine or diazonium salt.

Powder X-ray diffraction was also employed to analyse gra-PhCOOH (Figure 5.5). Many more peaks were detected in the diffraction pattern of gra-PhCOOH compared to that of graphene. Most importantly, these were concentrated in the area of 2θ = 5–25°, where functionalised graphenes such as GO often have peaks due to the extension of the (002) *hkl* plane due to functionalisation between the layers of graphite.[16] For gra-PhCOOH, these were detected at 2 θ of 5°, 9°, 10°, 14°, 17°, 18°, 19° and 25°. 9° and 10° can be found in the diffraction pattern for GO[17], and therefore may be due to the increase in d spacing as a result of oxygen-containing groups between the layers of re-aggregated graphene. However, in gra-PhCOOH where the surface PABA and diazonium salts were removed, these peaks were reduced to 14°, 20° and 25°. None of these peaks match those observed in GO, and so the functionalisation or work up did not overly damage the underlying graphene, and the other peaks were likely due to the polycrystalline PABA or diazonium on the surface. Comparing these peaks with the literature values for pure benzoic acid, it was inferred that the peaks at 5°, 17°, 18° were found in both free benzoic acid crystals and in gra-PhCOOH, but not in cleaned gra-PhCOOH. The presence of peaks just below the main peak of 26°

suggested that some of the re-aggregated graphene sheets have a larger d spacing, due to the functional groups interfering with the re-stacking of the nanosheets.

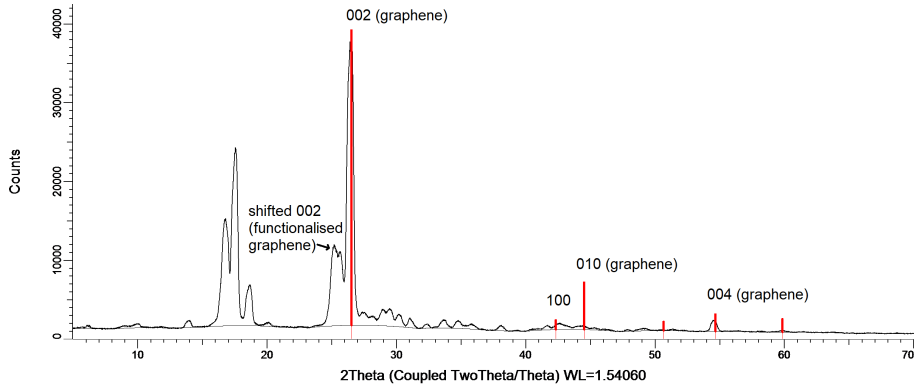

(a)

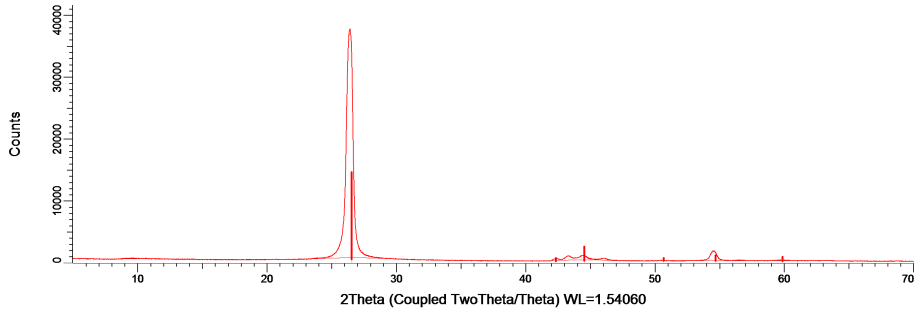

(b)

Fig. 5.5 (a) Powder X-ray diffraction of gra-PhCOOH (black) with graphite peaks from database for reference (red). (b) pXRD pattern of graphene showing 5–70° for comparison.

Raman spectroscopy of gra-PhCOOH displayed several signals that were shifted compared to those of benzoic acid, in particular, peaks at 1395, 1443 and 1607 cm^{-1}. A Raman spectrum of benzoic acid (Figure C.2) showed that it has Raman active modes at 1450, 1515, 1560 and 1650 cm^{-1}. However, the peaks for benzoic acid also overlapped the region of the characteristic D (approx 1360 cm^{-1}) peak for defective graphene, making the calculation of an I_D:I_G ratio for defect or functionalisation analysis difficult (Figure 5.6). The I_D:I_G for pristine graphene was 0.3. Gra-PhCOOH showed two peaks that did not belong to benzoic acid in the area of the D peak: 1400 and 1438 with a G peak at 1583 cm^{-1}, which have been previously reported in diazonium treated graphene.[18] The benzoic acid peak at 1608 cm^{-1} overlapped the shoulder of the G peak at 1620 cm^{-1} (also known as D') which could also

be used for defect analysis. The I_D:I_G ratios afforded by these two D peaks with respect to the peak at 1583 cm^{-1} were 0.56 and 0.47, considerably higher than pristine graphene (0.3). As well as the growth in D peak intensity, the blue shift relative to the G and 2D peaks has also been reported to be a sign of hole doping, which may also be due to functionalisation with the positively charged diazonium salts.[19] Considering this and the peaks attributed to diazonium functionalised graphene, the functionalisation appeared to have been successful by Raman analysis.

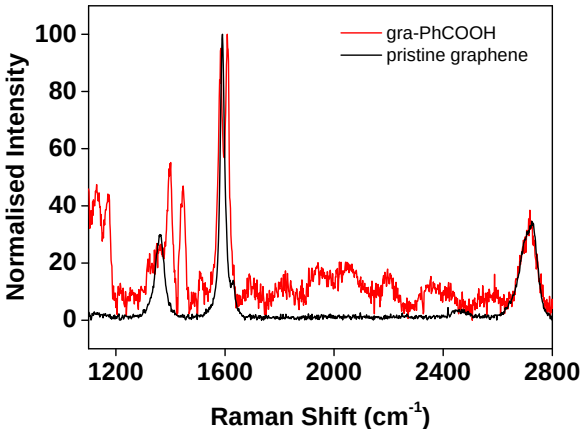

Fig. 5.6 The gra-PhCOOH Raman spectrum (red) and pristine re-aggregated graphene spectrum (black).

SEM images of gra-PhCOOH showed no changes in size from pristine graphene, remaining at the average size seen in graphene produced from SGN18 graphite discussed in the second chapter (2.96 $\pm$ 0.65 μm). Rod-shaped microcrystals, of length 0.65 $\pm$ 0.06 μm and width 0.15 $\pm$ 0.02 μm of unreacted PABA or diazonium salt were clearly seen in the SEM image of untreated gra-PhCOOH, showing the excess of physisorbed materials compared to chemisorbed functionalities. The SEM images of 'clean' gra-PhCOOH had significantly reduced numbers of these crystals, showing the efficacy of the heating process in removing the physisorbed material which was also seen in ATR-IR and TGA. The SEM also revealed

wrinkled upper layers on the functionalised re-aggregated graphene compared to smooth pristine graphene (Figure 5.7).

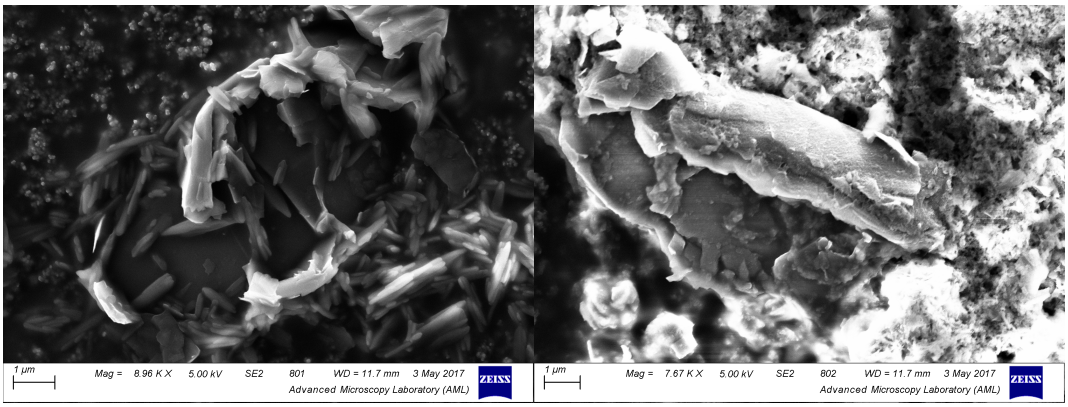

(a) (b)

Fig. 5.7 (a) SEM image of untreated gra-PhCOOH showing rod-shaped crystals of physisorbed material. (b) SEM image of 'clean' gra-PhCOOH.

The characterisation of gra-PhCOOH by a range of spectroscopic techniques supported the assertion that the functionalisation of liquid exfoliated graphene was a success. Many of these techniques matched the data seen in the literature for diazonium functionalised graphene (Raman, XPS, TGA, SEM) or the presence of benzoic acid (ATR-IR, TGA-IR, pXRD). This confirmed the conversion of the substituted diazonium salt to the acid on the surface of graphene as well as the presence of covalently bound species on graphene. In the next section, the reactivity of these functional groups on graphene was tested by the attempted conversion to acyl chloride and other groups before attempting the linkage with MoS_2.

5.2.2 Preparation of Benzoyl Chloride Functionalised Graphene

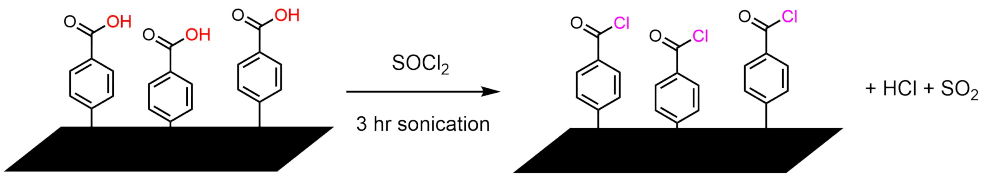

Scheme 5.3 The conversion of gra-PhCOOH to gra-PhCOCl.

The preparation of benzoyl chloride functionalised graphene (gra-PhCOCl) involved sonicating gra-PhCOOH powder in 5 mL of $SOCl_2$ for 3 h, followed by removal of the excess $SOCl_2$ by distillation and drying of the dark brown, flaky product under vacuum. Refluxing in $SOCl_2$ after or instead of sonication was found to slightly reduce the yield of acyl chloride, and was avoided. The preparation of gra-PhCOCl from both gra-PhCOOH and 'clean' gra-PhCOOH yielded the same product according to both ATR-IR and TGA, suggesting that sonication in $SOCl_2$ was enough to remove the physisorbed benzoic acid and excess diazonium salt that remained on gra-PhCOOH before washing and drying. ATR-IR analysis of gra-PhCOCl gave the spectrum seen in Figure 5.8. The following peaks were detected: ν = 2959, 2848 (aromatic C-H stretch) 1779, 1735 (C=O symmetric and asymmetric stretches), 1679 (C=O stretch of residual carboxylic acid) 1612, 1587 (C=C stretch), 1513, 1433, 1303, 1253, 1205, 1153 (residual O=C-O stretches, O=C-Cl stretches), 1026 (C-O bend), 806, 776, 752 (substituted aromatic C-H bend), 693 cm^{-1} (C-Cl stretch). As seen in the overlaid spectra, this correlated well with commericial tolyl chloride, with many peaks overlapping directly with those of the free acyl chloride (2959, 2848, 1779, 1735, 1612, 1587, 1433, 1303, 1205, 806, 776, 693 cm^{-1}). Some were also shifted slightly, again possibly due to the covalent bond to graphene (1170 to 1155, 820 to 806, 712 to 693 cm^{-1}). The symmetric and asymmetric C=O stretches characteristic to acyl chlorides were clearly visible,[20] as was the residual carbonyl from benzoic acid. The O-H stretch has been greatly reduced, and an C-Cl bend was assigned as the sharp peak at 693 cm^{-1}. As with 'clean' gra-PhCOOH, the IR

baseline has reduced T%, similar to the ATR-IR spectrum of graphene[14] and suggested that the physisorbed organic species covering the graphene had been removed, leaving the fewer, covalent species on the surface of graphene.

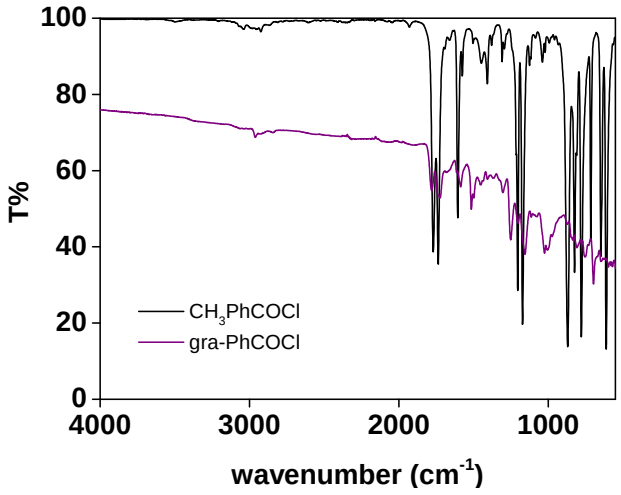

Fig. 5.8 ATR-IR spectra of gra-PhCOCl (purple) and free tolyl chloride (black) for comparison (Figure C.7 shows the range 2000–550 cm^{-1} in greater detail).

To add further support to the assignment of the C=O in the ATR-IR as acyl chloride peaks, hydrolysis of gra-PhCOCl and conversion back to the acid was attempted by bath sonication of gra-PhCOCl in DI water for 2 h and refluxing in DI water for a further 2 h. The product was filtered and dried before analysis by ATR-IR. The spectrum resembled that previously described for gra-PhCOOH: ν = 3339 (O-H stretch), 3064, 2962 (aromatic C-H stretches), 1680 (acid C=O stretch), 1657, 1591 (C=C stretch), 1504 (C-H bend), 1406 (O-H bend), 1310, 1233, 1205, 1157 (O=C-O stretches), 1093, 1055, 1010 (C-O bend), 844, 796, 755 (substituted aromatic C-H bend), 665 cm^{-1}. The reappearance of the O-H stretch and shift of the carbonyl stretch to 1680 cm^{-1}, as well as the simplification of the fingerprint region and disappearance of the C-Cl peak at 693 cm^{-1} demonstrated a return to the carboxylic acid (Figure C.9).

TGA analysis of gra-PhCOCl differed greatly from that seen for gra-PhCOOH. Weight loss before 200 °C averaged 4%, suggesting that some $SOCl_2$ remained on gra-PhCOCl despite drying. However, this was an improvement on the amount of physisorbed material that remained on gra-PhCOOH detected by TGA, and more closely matched that of 'clean' gra-PhCOOH. This could be due to the loss of much of the physisorbed material on graphene during the preparation of gra-PhCOCl. This would also explain the lower intensity of much of the peaks in the ATR-IR spectrum. Weight loss in the region of 200–400 °C averaged 12%, rising to a total of 34% for 200–600 °C, showing a similar weight loss compared to gra-PhCOOH (39% of the total weight for gra-PhCOOH and 36% for 'clean' gra-PhCOOH above 250 °C).

The 1st derivative of the TGA trace of gra-PhCOCl, other than the point seen at 130 °C from solvent or physisorbed material, showed three other rate changes, with inflection points at 250 °C and 430 °C which could be loss of functional groups (possibly HCl or CO_2 from the decarboxylation of the acid), and 550 °C which demonstrated the beginning of the degradation of functionalised graphene, at an earlier temperature than seen in the pristine material (Figure 5.9). Functionalisation may be responsible for this by increasing defects and therefore de-stabilising areas of the graphene, causing it to thermally decompose at lower temperatures than the pristine material.

The TGA-IR spectra showed no difference to the background until the relatively high temperature of 450 °C, at which point the symmetric and asymmetric signals for CO_2 start to grow steadily, peaking at 740 °C at 50 T% before decreasing slowly to 900 °C. TGA-IR spectra of gra-PhCOCl did not show any physisorbed material that could be identified as free benzoyl chloride, compared to the free benzoic acid seen in the TGA-IR spectra for gra-PhCOOH (Figure 5.10). This could be due to the low concentration of any organic species that may be carried to the detector from the furnace or their weak absorption of infrared light, or a combination of these.

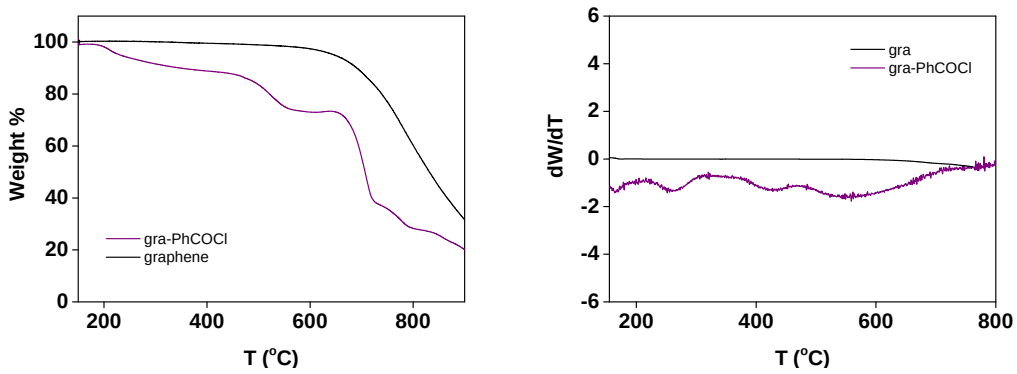

(a) (b)

Fig. 5.9 (a) TGA traces and (b) corresponding derivatives of gra-PhCOCl (purple) compared to pristine graphene (black).

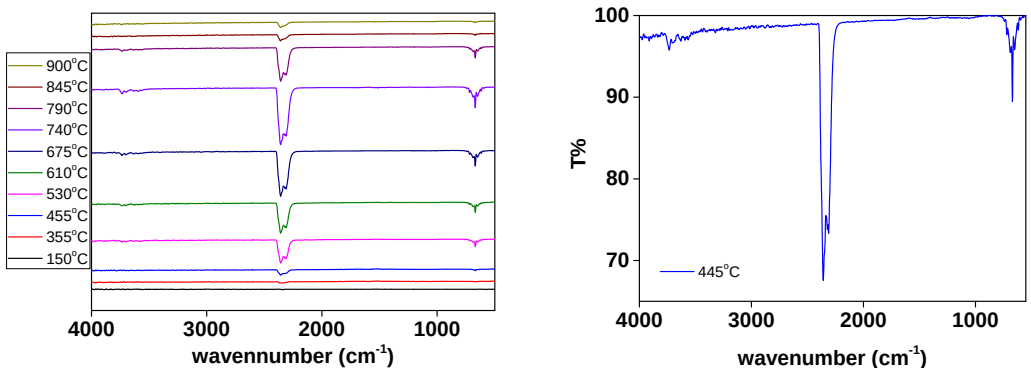

(a) (b)

Fig. 5.10 (a) TGA-IR spectra of gra-PhCOCl at a range of temperatures. (b) IR spectrum showing the evolution of CO_2 at 445°C.

XPS analysis of gra-PhCOCl demonstrated changes from both pristine graphene and gra-PhCOOH (Figure 5.11). The survey spectrum confirmed the presence of C (72%), O (17%), Cl (6%) and N (5%). Importantly, no S was detected, confirming the complete removal of $SOCl_2$. The presence of N, as in the survey spectrum of gra-PhCOOH could be residual diazonium salts or PABA on graphene. The core level spectra gave more detailed information on each of these species. The C 1s core level spectrum was fit similarly to the C 1s spectrum of gra-PhCOOH, with the addition of the C-Cl moiety seen the in ATR-IR spectrum. The fits gave contributions from C=C/C-C (284.5 eV) of 50%, 29% C-O/C-N

(285.7 eV), 8% C=O/C-Cl (287.0 eV), 8% COOH (289.5 eV) and 4% shake up (292.7 eV). The C-Cl and C=O species were difficult to separate confidently and so were both included in the fitting at 287.0 eV. The presence of acyl chloride and carboxylic acid species matched that seen in the ATR-IR, and illustrated the conversion of some of the carboxylic acid groups to acyl chloride.

Analysis of the N 1s core level spectrum revealed the presence of two nitrogen species at 399.4 eV and 401 eV which matched the literature value of C-N and N=N respectively (Figure C.8a). The Cl 2p core level spectrum also showed only one chemical species present at 201 eV relating to organic chloride, supported the assignment of such a species in the C 1s core level spectrum and in the ATR-IR spectrum.[15] The slight increase from the literature value of 200 eV could be due to the adjacent carbonyl species (Figure C.8b) detracting electron density from the chloride. The O 1s species, as in gra-PhCOOH, showed two species, both C-O and C=O, again showing residual carboxylic acid that is reflected in the ATR-IR spectrum (Figure C.8c).

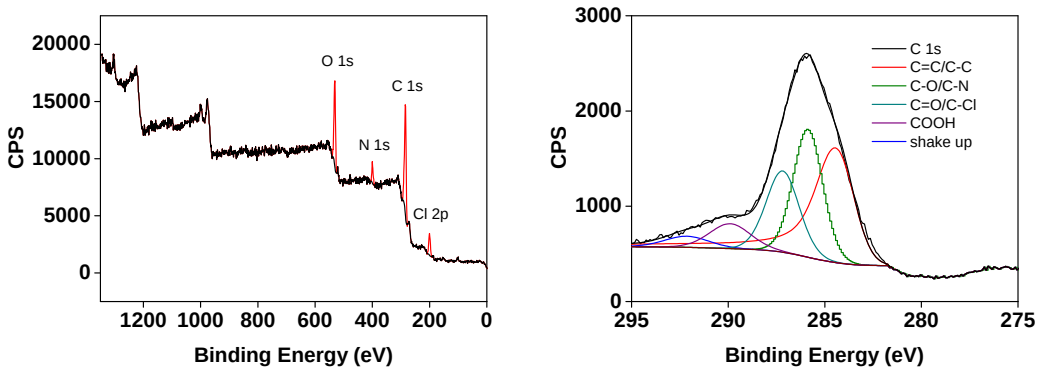

(a) (b)

Fig. 5.11 (a) Survey spectrum of gra-PhCOCl showing atomic species. (b) C1s core level spectrum of gra-PhCOCl.

The powder X-ray diffraction of gra-PhCOCl (Figure 5.12), compared to that of gra-PhCOOH, displayed fewer peaks, at 2θ of 9°, 10°, 14°, 25°, 26.5°, 27.5°, 30.5°, 32°, 33°, 39°, 54.5°, 58°, and 68 2°. The majority of these were also found in the spectrum for

gra-PhCOOH. However, the growth of the peaks at 9° and 14° suggested that an increase in interlayer distance has occurred: a peak at 9° is frequently reported in pXRD patterns of GO.[21] This may mean that the preparation of gra-PhCOCl used here caused some damage to the underlying graphene as well as converting the acid groups to acyl chlorides. However, the persistence and intensity of the (002) peak at 26.5° showed that much of the graphene remains intact. There were no significant changes to the peaks observed at higher degrees.

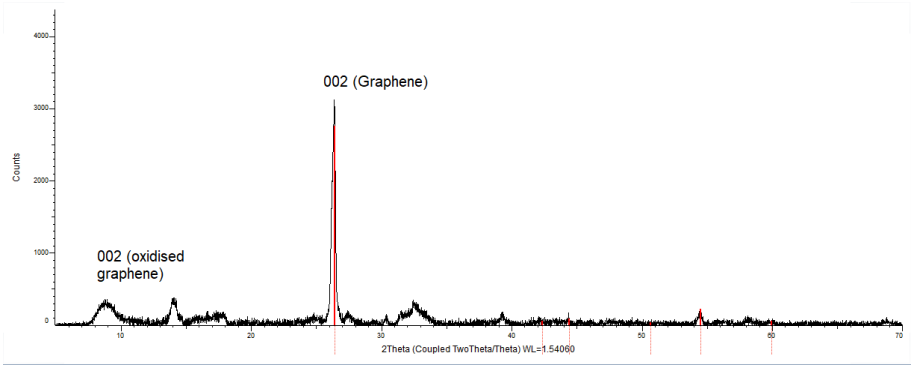

Fig. 5.12 Powder X-ray diffraction of gra-PhCOCl (black) with graphite peaks from database (red).

As a control experiment, pristine exfoliated graphene was sonicated in $SOCl_2$ for 4 h, after which the $SOCl_2$ was distilled off, the graphene isolated and analysed by ATR-IR and TGA-IR. This experiment was conducted to support the implication from earlier experiments that $SOCl_2$ was not functionalising the basal plane of graphene, and only the carboxylic acid moiety of the functional groups was affected. Previous literature reports have shown that $SOCl_2$ can dope SWCNTs, GO and chemically converted graphene (CCG) with chloride,[22, 23] but there are no reports as of writing that detail the effect $SOCl_2$ has on liquid exfoliated pristine graphene. Initial analysis *via* ATR-IR and comparison of the pristine graphene spectrum with the spectrum of graphene treated with $SOCl_2$ (Figure 5.13) showed little change had occurred after $SOCl_2$ treatment. The featureless spectrum of graphene with extremely low baseline seen in transmission IR spectra of graphene (35 T%) was retained,[14] new peaks were limited to those at ν = 2656, 1240 and 870 cm^{-1}. These peaks, as detailed in

the characterisation of pristine graphene could also be found in the spectra of liquid exfoliated graphene and so did not arise from $SOCl_2$ through doping or functionalisation.

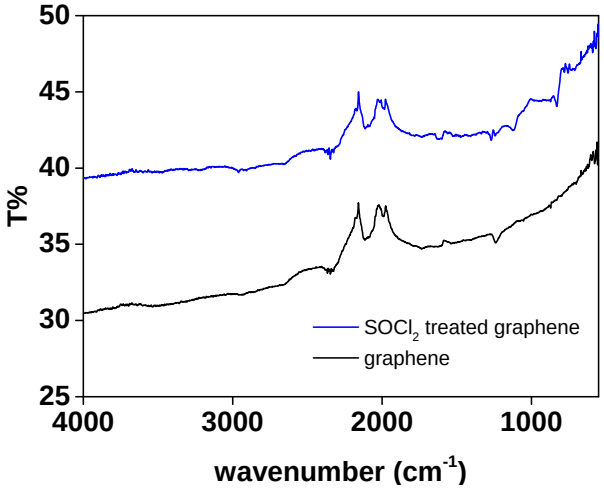

Fig. 5.13 ATR-IR spectra of graphene treated with $SOCl_2$ (blue) and pristine graphene (black).

TGA analysis of graphene treated with $SOCl_2$, however, showed weight loss during the isothermal step at 150 °C of 2% and a weight loss step of a further 10% between 220 and 350 °C (Figure 5.14). This is considerably higher than the weight loss seen in pristine graphene of <1% up to 600 °C in air, indicating possible thermolysis of functional groups from $SOCl_2$ treated graphene. This was supported by the IR spectra taken during coupled TGA-IR (Figure 5.31). The spectra showed CO_2 production at the marginally lower temperature of 560 °C as opposed to 600 °C for pristine graphene. Additionally, a peak at 1024 cm^{-1} as well as several weak peaks at 1260, 1144, 1085 and 813 cm^{-1} were seen in the temperature region of 220–350 °C in the TGA-IR spectra, corresponding to the 10% weight loss seen in the TGA trace of $SOCl_2$ treated graphene. These peaks did not match those of the literature values for $SOCl_2$, but the peak at 1024 cm^{-1} could be assigned as a sulfoxide and was similar to the sulfur-based peaks seen in exfoliated and functionalised MoS_2 TGA-IR spectra. The combination of ATR-IR and TGA-IR analysis suggested that the basal plane of graphene was not inert towards $SOCl_2$. As the level of functionalisation was low, it could be assumed that when

treating gra-PhCOOH with $SOCl_2$, the more readily accessible and reactive carboxylic acid functional groups should preferentially be targeted by $SOCl_2$, with some functionalisation of the basal plane. However, previous literature reports have established that functionalised graphene is more reactive than pristine graphene, and an already defective basal plane may be more susceptible to attack than a pristine one.[24]

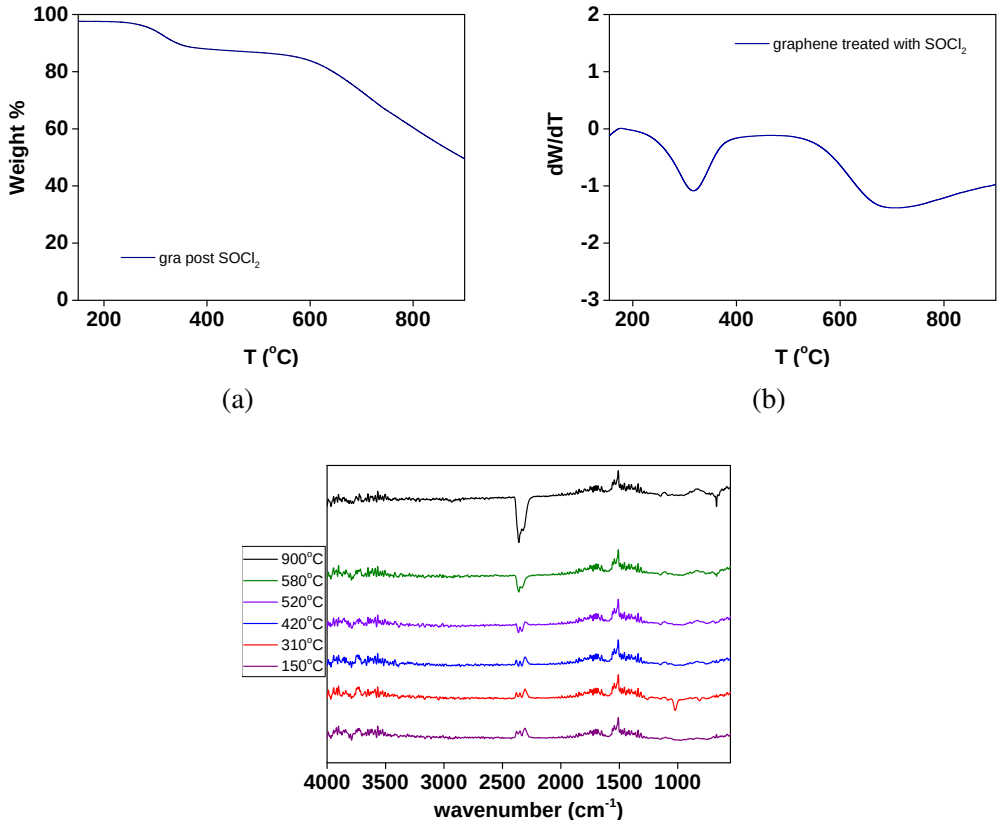

(a) (b)

(c)

Fig. 5.14 (a) TGA trace and (b) derivative of graphene treated with $SOCl_2$. (c) TGA-IR spectra taken at specific temperatures.

The preparation of gra-PhCOCl from gra-PhCOOH and $SOCl_2$ was confirmed by ATR-IR and XPS, with support from other techniques (TGA, TGA-IR, pXRD). The reduction in intensity of the peaks in ATR-IR, as well as the reduction in weight lost before 600 °C in the TGA was inferred to be due to the removal of physisorbed material on graphene during the harsh conditions used to convert the carboxylic acid groups on graphene to acyl chloride.

The presence of chloride in the XPS as well as the clear overlap of the C=O stretches with those of tolyl chloride were taken as evidence for the formation of the acyl chloride, whereas the other techniques supported the persistence of functional groups on graphene. Control experiments, including the monitoring of the hydrolysis of the acyl chloride by ATR-IR and the treatment of pristine graphene with $SOCl_2$ added further credibility to the conversion of gra-PhCOOH to gra-PhCOCl.

5.2.3 Preparation of Iodoethyl Benzoate Functionalised Graphene

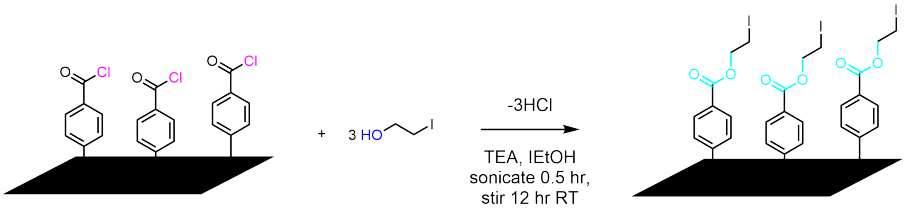

Scheme 5.4 Esterification of graPhCOCl and iodoethanol.

Esterification was performed using graphene functionalised with benzoyl chloride (gra-PhCOCl), as described above, dispersed in dry ether. Gra-PhCOCl was bath sonicated in dry Et_2O for 1 h before addition of iodoethanol. The dispersion was then stirred for 16 h, filtered on a membrane and washed with the solvent, or in the case of DMF, centrifuged at 4500 rpm and washed with MeCN 3 times. The alcohol was expected to attack the acyl chloride group causing the elimination of HCl gas and formation of the ester in a simple nucleophilic attack/elimination reaction. The ATR-IR spectrum of gra-PhCOOEtI prepared from the alcohol and gra-PhCOCl showed ν = 3331 (residual O-H), 3054, 2908 (C-H stretches), 1778 (acyl chloride C=O stretch), 1709 (ester C=O stretch), 1651, 1589 (C=C stretch), 1496 (C-H bend), 1401 (O-H bend), 1311, 1237 (O=C-O stretches), 1163, 1014 (C-O bend), 962, 897, 842, 752 (substituted aromatic C-H bend), 694 cm^{-1} (Figure 5.15). The carbonyl stretch associated with gra-PhCOCl disappeared, or decreased greatly, and a small signal at 1709 cm^{-1} became visible which was assigned as the ester C=O according to the literature.[20] This was supported by the good overlay of the C=O stretch of free ethyl benzoate with gra-PhCOOEtI and the shift in the acetate stretches from 1303 and 1253 cm^{-1} in gra-PhCOCl to 1311 and 1237 cm^{-1}. Peaks at ν = 1589, 1311, 1237, 1163, 1014, 842, 694 cm^{-1} also overlapped with that of the free ester, supporting the assignment of these as peaks from the ester product. Esterification attempts in other solvents (DMF, THF) also gave IR spectra similar to that produced by Et_2O.

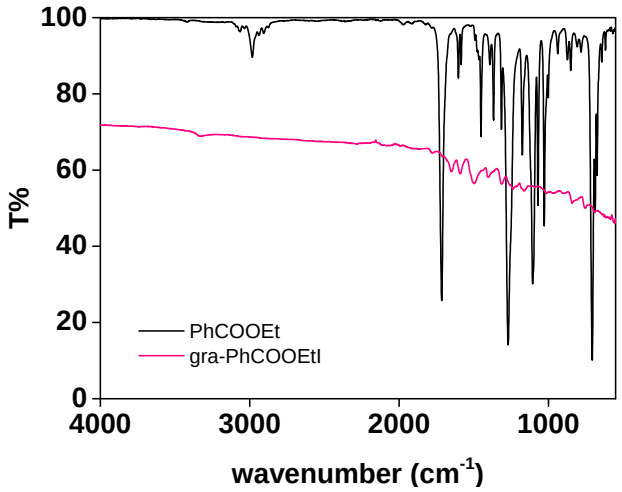

Fig. 5.15 ATR-IR of gra-PhCOOEtI from gra-PhCOCl and iodoethanol (pink) overlaid with a spectrum of ethyl benzoate (black) (Figure C.10 shows the labelled spectrum).

As was done for gra-PhCOCl, hydrolysis of the ester was attempted by bath sonicating gra-PhCOOEtI in DI water and subsequently refluxing it in 0.1 M HCl for 12 h. The product was then washed with DI water and analysed by ATR-IR. The IR spectrum showed significant changes from that of gra-PhCOOEtI (Figure C.11). The signals detected were ν = 3301 (O-H stretch), 2914, 2852, 2658 (aromatic and alkyl C-H stretches), 1682 (acid C=O stretch), 1645, 1602 (C=C stretches), 1524 (C-H bend), 1487, 1444, 1416, 1401 (O-H bend), 1284, 1240, 1151 (O=C-O stretches), 1095 (C-H bend), 946, 805, 761 cm^{-1} (substituted aromatic C-H bend). The disappearance of the residual acyl chloride carbonyl and C-Cl stretches, as well as the ester C=O at 1709 cm^{-1}, the reappearance of the O-H stretch and bend, and the shift of the fingerprint region to match the benzoic acid spectrum confirms the successful hydrolysis of gra-PhCOOEtI and residual gra-PhCOCl and return to gra-PhCOOH.

The putative ester was further analysed by TGA (Figure 5.16a). For gra-PhCOOEtI prepared by reacting gra-PhCOCl and iodoethanol, the weight loss was 12% over 200–400 °C, growing to 34% before the graphene degradation temperature of 600 °C, not including a 2% loss in weight before 200 °C. This was similar to that seen for gra-PhCOOH (39%)

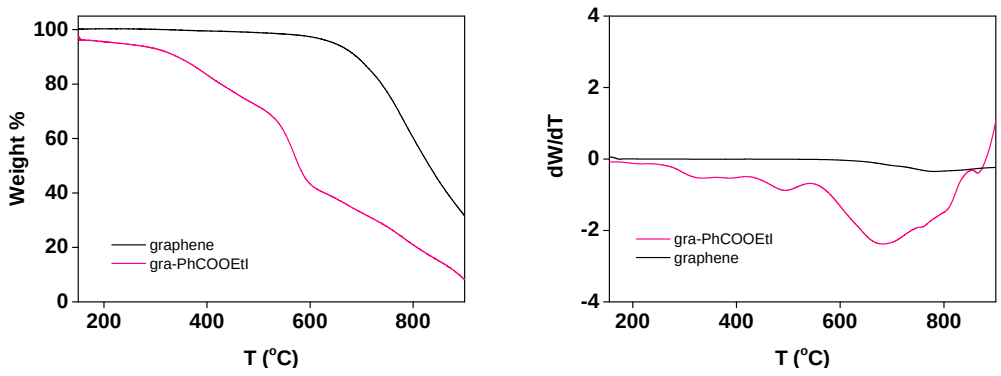

(a) (b)

Fig. 5.16 (a) TGA traces and (b) corresponding derivatives of gra-PhCOOEtI from gra-PhCOCl (pink) compared to re-aggregated graphene (black).

and the weight loss seen for gra-PhCOCl (34%). It was expected that the weight loss of the ester-functionalised graphene would be intermediate between gra-PhCOOH and gra-PhCOCl due to the differences in molecular weight between the OH^- of the acid, the chloride of the acyl chloride and the ethyl group of the ester, but the error in the TGA may be too great for such precise measurements. The 1st derivative of the TGA trace gave several inflection points: at 95 °C for the release of solvent or water from the destruction of the ester, 325 °C and 495 °C from the loss of functional groups from graphene and 680 °C as the fastest rate for the degradation of graphene (Figure 5.16b). These points were reflected in the TGA trace in Figure 5.14, and the increase in complexity of the TGA trace and the derivative trace suggested the loss of several species from the graphene surface. The ester itself is expected to thermolyse before the functional groups are lost from graphene,[25] therefore this increase in the number of thermolysis steps was expected.

The XPS survey spectrum of the putative ester-functionalised graphene detected C, O, N, Cl, and some I (Figure 5.17). The concentrations of each species from core level areas came to 72% C, 15% O, 7% N, 5% Cl and 1% I. The C 1s spectrum was fit as follows: 33% C=C/C-C (284.5 eV), 39% C-O/C-N (286.0 eV), 19% C=O/C-Cl (287.5 eV), 8% COOH (289.9 eV), 3% shake up feature (292.5 eV). For ester formation, an increase in C-C due to

the presence of ethyl groups and a reduction in Cl/increase in O would be expected and was observed here. According to the survey spectrum, the amount of Cl did decrease, and the retention of I supported ester formation. The use of a halogen-substituted ethanol supplied a marker for XPS analysis as the presence of iodine implied that the ethyl group remained attached to the functional groups on graphene despite washing.

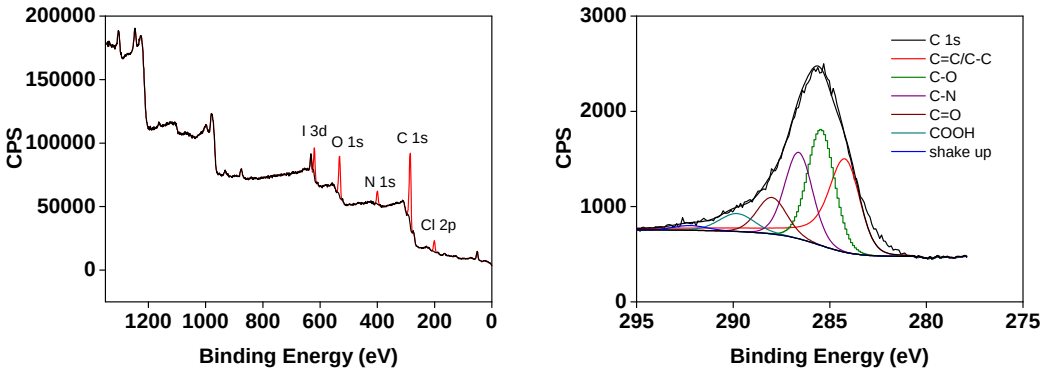

(a) (b)

Fig. 5.17 (a) Survey spectrum and (b) C 1s core level spectrum of gra-PhCOOEtI.

Looking at the powder X-ray diffraction pattern of graphene functionalised with iodoethyl benzoate (Figure 5.18), it was clear that changes had occurred—most clearly in the shift of peak at 14° shifting to 17°, and the peak at 25° shifting to 20° . The latter shift suggested that some of the re-aggregated graphene had a larger d spacing, due to the functional groups forcing the sheets apparent and interfering with re-stacking, to a larger extent than in gra-PhCOOH. There was also a reduction in intensity of the peak at 9° which usually indicates the presence of oxidised graphene, as was seen in gra-PhCOCl.[26] At higher 2θ, the pattern remained similar to that seen in the diffraction pattern for gra-PhCOOH. Considering the decrease in the peak at 9°, and the return to higher temperatures (>600°C) for graphene degradation, the preparation of the ester may undo some of the possible damage to the graphene basal plane that was observed after treatment with $SOCl_2$.

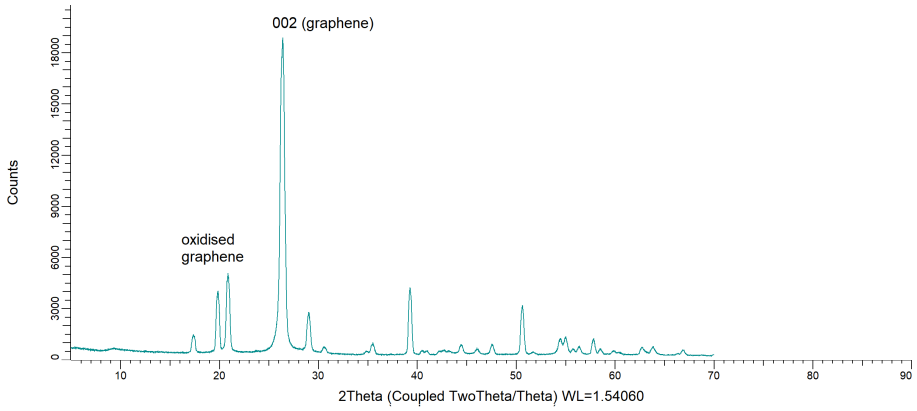

Fig. 5.18 Powder X-ray diffraction of gra-PhCOOEtI from gra-PhCOCl (cyan).

In addition to iodoethanol, gra-PhCOCl was reacted with aniline in order to prepare for the eventual formation of an amide linkage between graphene and MoS_2. Gra-PhCOCl and aniline were sonicated together for 30 min and stirred at RT for 16 h before work up. The addition of gra-PhCOCl to the amine was exothermic, and resulted in the immediate formation of HCl fumes. The ATR-IR spectrum was assigned as such: ν = 3325, 3347 (N-H stretch), 2930, 2874, 2651 (aromatic and alkyl C-H stretches), 1731 (C=O stretch, acyl chloride), 1672 (C=O stretch, amide), 1654, 1598 (C=C stretch), 1530 (N-H bend), 1496 (C-O stretch), 1438, 1401, 1323, 1238 (O-C=O stretches), 1151, 1052, 869, 768, 709 cm^{-1} (N-H oop). The appearance of the amide carbonyl at 1672 cm^{-1}, the presence of N-H stretches and out of plane bending all confirm the presence of the amide (Figure 5.19). The TGA trace showed some weight loss prior to 200 °C (5%), then a gradual loss of 15% in the region 250-600 °C. However, the total weight loss was much lower than expected and seemed to imply the loss of some functional groups during the esterification attempt, which may also explain the low intensity of the peaks in the ATR-IR spectrum. The potentially damaging effect of the amine should be studied in further detail in future experiments if amidation attempts are to be continued.

The esterification of gra-PhCOCl and the chosen alcohol, iodoethanol was confirmed by the overlap and identification of the ester C=O stretch with ethyl benzoate in ATR-IR. The

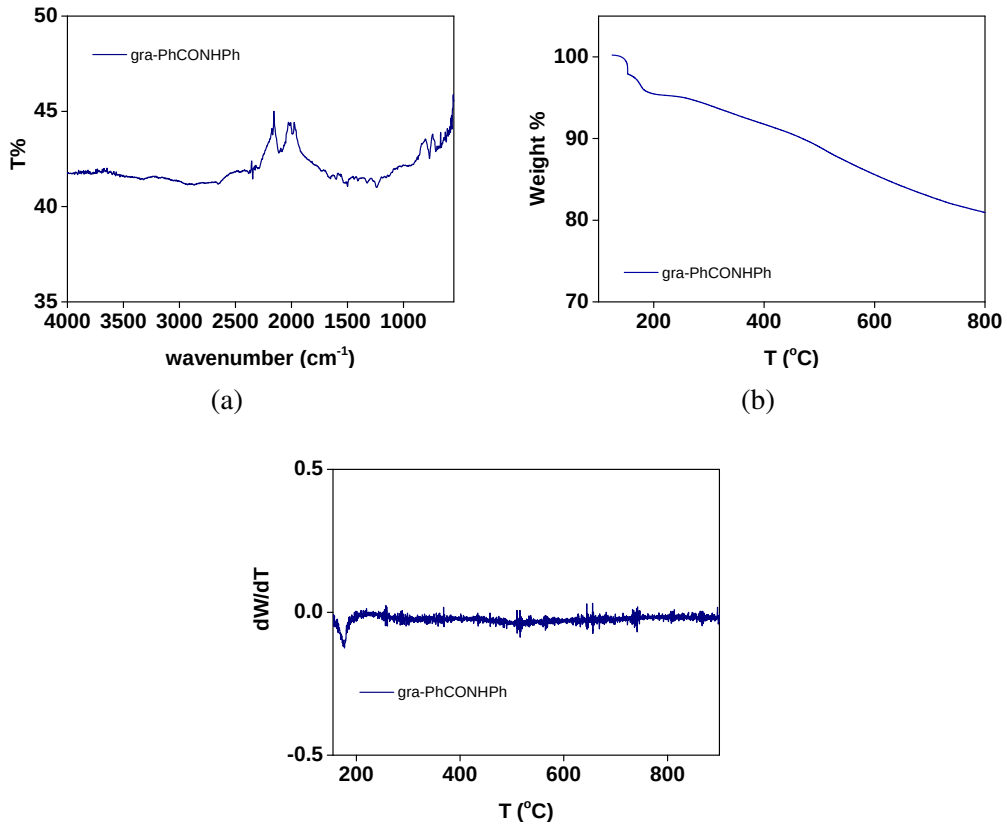

Fig. 5.19 (a) ATR-IR spectrum, (b) TGA trace and (c) 1st derivative rof gra-PhCONHPh.

TGA also showed many degradation steps and this may be due to a multitude of functional groups coming off of graphene: the breaking of the ester linkage and the loss of both remaining benzoyl chloride and benzoic acid species before the degradation of graphene itself. Further evidence supporting this came from XPS, showing the presence of functional groups remaining on graphene after conversion and washing. With functionalised graphene—gra-PhCOOH, gra-PhCOCl and gra-PhCOOEtI—synthesised and characterised, attention was now turned to the preparation of functionalised ce-1T-MoS_2, MoS_2-EtOH, and the formation of linked graphene-MoS_2.

5.2.4 Functionalisation of MoS_2 With Ethanol

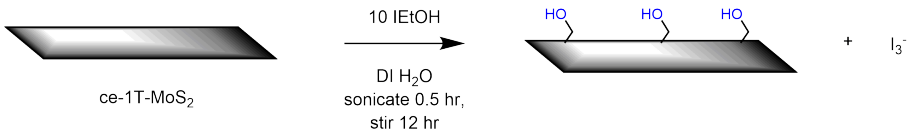

Scheme 5.5 Functionalisation of ce-1T-MoS_2 with iodoethanol.

Functionalisation of MoS_2 *via* iodide-containing organic groups was initially developed by Chhowalla's group in 2014, when they produced functionalised 1T-MoS_2 by treating ce-1T-MoS_2 with iodoacetimide and iodomethane.[10] The functionalisation proceeds *via* electron transfer from the negatively charged ce-1T-MoS_2 to the iodine-containing hydrocarbon. Iodide is lost and the alkyl group then binds to the sulfur atoms of MoS_2. This was established by the presence of a C-S stretch at approximately 750 cm^{-1} in the ATR-IR spectrum (Figure 5.20) and in XPS by a shoulder coming off the S 2p core level peak assigned as C-S (Figure 5.23c), as reported by Chhowalla's group. The functionalisation method used here was a modified version of this, employing dispersed sheets of ce-1T-MoS_2 in DI water and iodoethanol. These were bath sonicated in darkness for 1 h before stirring in darkness for 16 h, followed by centrifuging and washing with DI water and ethanol. The isolated grey-black sheets were analysed by ATR-IR, TGA, TGA-IR, XPS and Raman spectroscopy.

The ATR-IR of MoS_2-EtOH showed peaks at ν = 3325 (O-H stretch), 2978, 2926 (alkyl C-H stretch), 1651, 1469, 1413 (O-H bend), 1364, 1305 (C-O stretch), 1209, 1163, 1129, 1108, 1021 (C-O bend), 949, 817, 749 (C-S stretch) and 671 cm^{-1} (Figure 5.20). The appearance of several peaks that can be attributed to organic residues, particularly the peaks assigned to C-O and O-H moieties, suggested that functionalisation was successful. Most importantly, the weak signal at 749 cm^{-1} of the fingerprint region could be assigned as a C-S stretch[20] which would confirm the covalent nature of the interaction of ethanol to MoS_2. The weak intensities of the peaks could be due to the low loading of EtOH, as the functionalisation of MoS_2 in the literature normally amounts to only 10%.[27, 10] The TGA

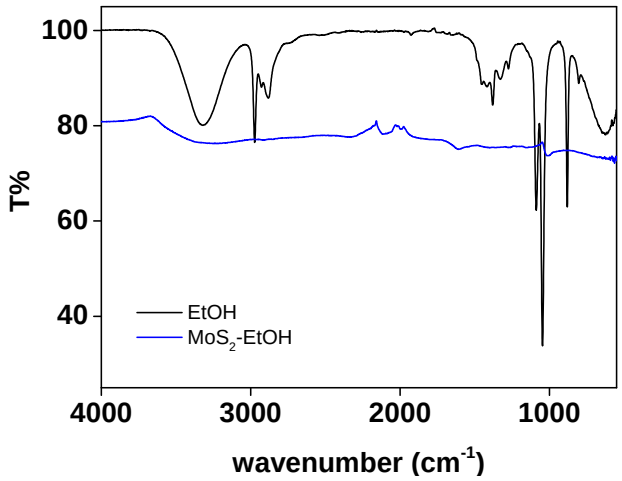

Fig. 5.20 ATR-IR spectrum of MoS_2-EtOH (blue) and ethanol (black).

trace of MoS_2-EtOH detected weight loss of 3% before 200 °C, increasing to 6% up to 400 °C and totalling 16% before 700 °C, seen in Figure 5.21. Disregarding the loss before 200 °C as residual volatiles and physisorbed material, this was a total of 13% mass lost attributed to the thermolysis of functional groups covalently bound to ce-1T-MoS_2. This was in agreement with the literature reports of functionalised ce-1T-MoS_2.[10]

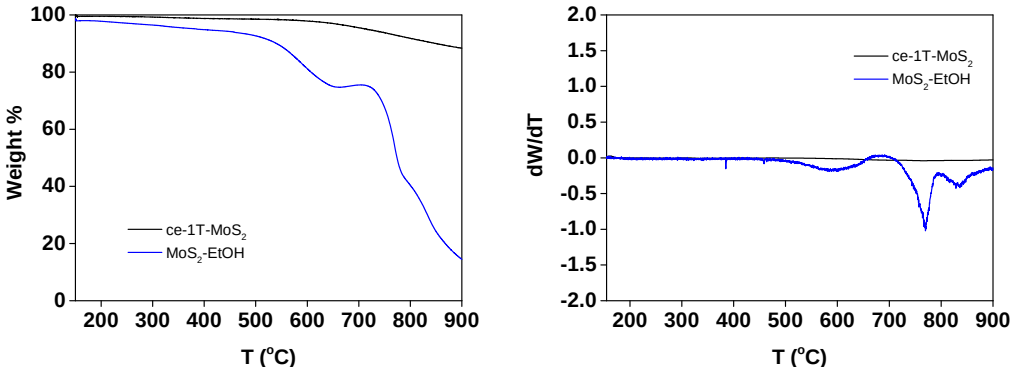

Fig. 5.21 TGA trace of MoS_2-EtOH (blue) with ce-1T-MoS_2 trace (black) for comparison.

The 1st derivative of the TGA trace showed inflection points at 143 °C and 211 °C, showing the loss of solvent and physisorbed material, 526 °C as the highest rate of loss of

covalently bound ethanol, and at 705 °C as the underlying MoS_2 began to degrade in air. The TGA-IR spectra of MoS_2-EtOH (Figure 5.22) obtained over the 200–700 °C period of weight loss showed the presence of CO_2 as well as several signals in the region of ν = 1378, 1347, 1328 (C-O/S=O/S-O stretches), 1165, 1090, 1040 (C-O bend) and 1009 cm^{-1} (C-H bends). These signals could be interpreted as ethanol, CO_2 and SO_2 coming off of ce-1T-MoS_2, indicating functionalisation and some oxidation of MoS_2. Signals from CO_2 and SO_2 both appear as early as 450 °C, with SO_2 vanishing by 600 °C. Signals at lower wavenumbers that can be attributed to alkyl C-H bends and C-O stretches started to grow at 600 °C, matching the step and inflection point in the TGA trace and derivative trace respectively. The peaks assigned to CO_2 persisted, though decreasing in intensity, along with the other organic species until 900 °C. As described in Chapter 2, the TGA-IR of pristine ce-1T-MoS_2 only showed very weak signals of CO_2 (from 700–900 °C), and the appearance of other peaks that can be assigned as organic matter in the TGA-IR of MoS_2-EtOH at lower temperatures (200–700 °C) could be taken as evidence for functionalisation and the loss of ethanol groups from MoS_2.

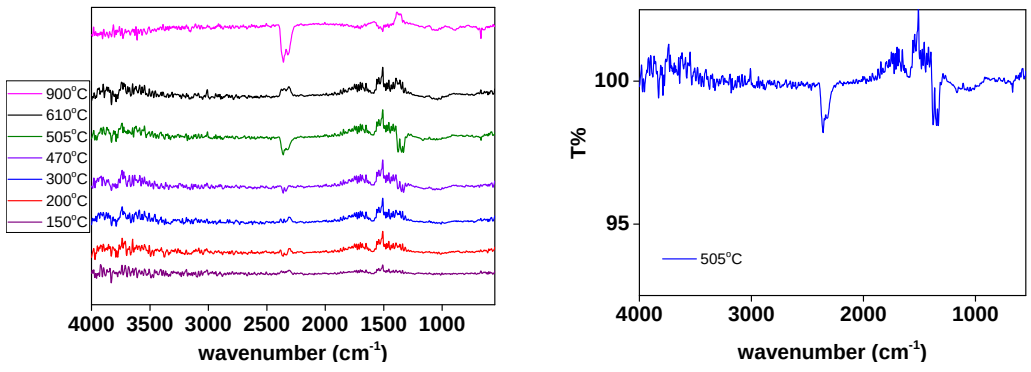

(a) (b)

Fig. 5.22 (a) TGA trace of MoS_2-EtOH (blue) with ce-1T-MoS_2 trace (black) for comparison. (b) TGA-IR spectrum showing the evolution of CO_2 at 500 °C.

XPS was also conducted on MoS_2-EtOH and compared with pristine ce-1T-MoS_2 (Figure 5.23). The survey spectrum of MoS_2-EtOH showed the presence of Mo, S, C and O, with no

I detected. The concentrations of each element calculated from the core level spectra and relative sensitivity factors were as follows: Mo (22%), S (44%), C (23%), O (11%) and I (<1%). The core level scan of the I 3d area revealed residual (<1%) I, however, this was lower than the iodine concentration of gra-PhCOOEtI, and displayed a very low signal-to-noise ratio (Figure C.13). This suggested that the majority of the iodine was lost through functionalisation. The Mo 3d core level spectrum was fitted as 59% 1T-phase and 24%

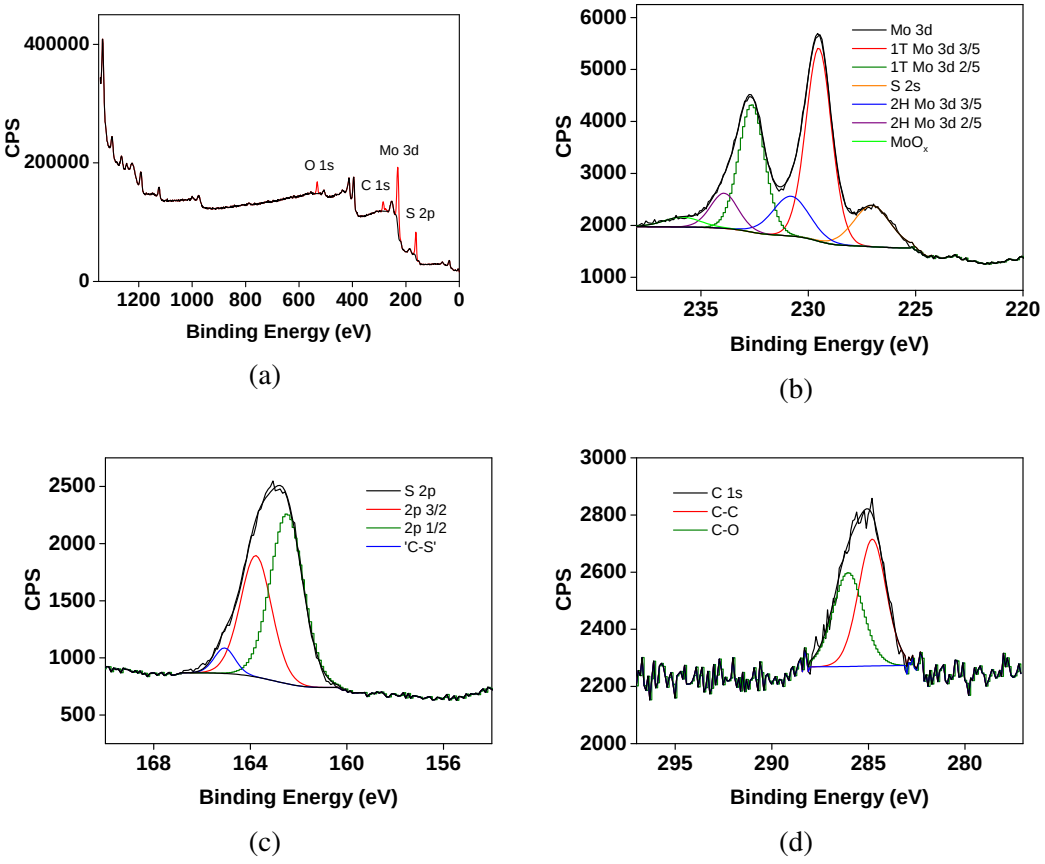

(a) (b) (c) (d)

Fig. 5.23 (a) Survey spectrum (b) Mo 3d (c) S 2p (d) C 1s core level spectrum of MoS_2-EtOH.

2H-phase within experimental error of the values found for pristine ce-1T-MoS_2 (63% and 25%). Other contributions were from the overlapping S 2s peak (14%) and some oxidised Mo (3%). It was possible to fit a small area at higher binding energies (165 eV) in the S 2p core level spectrum as functionalised S, to account for a widening of the full width half maximum

of the peak, though the contribution was low at 5%. The increase in C concentration (from 15% to 23%) and the fitting of the C 1s spectrum as approximately 2:1 C-C and C-O and the corresponding decrease in iodine supported successful functionalisation. The O 1s spectrum showed only one contribution (C-O) compared to adventitious material on ce-1T-MoS_2 or functionalised graphene, which was also taken as evidence for functionalisation of MoS_2.

Unlike the Raman spectra for functionalised graphene, functionalised MoS_2 gave much clearer spectra (Figure 5.24). The spectrum of MoS_2-EtOH retained the characteristic peaks for ce-1T-MoS_2: the A_{1g} (408 cm^{-1}), E^2_g (383 cm^{-1}) of MoS_2 and J_1 (150 cm^{-1}) J_2 (225 cm^{-1}) and J_3 (340 cm^{-1}) of the 1T phase. Functionalisation of MoS_2 usually results in the decrease in intensity or the disappearance of the J_1, J_2 and J_3 peaks, which are indicative of the existence of the 1T phase of MoS_2 in the sample.[28] Here, all three peaks remained, though the intensity relative to A_{1g} decreased. The Raman spectrum of MoS_2-EtOH taken using the 633 nm laser line gave much more defined peaks, especially of the 2LA(M) peak at 450 cm^{-1} due to the resonance induced by this laser line. The intensity ratio of 2LA(M) to A_{1g} in MoS_2-EtOH was 0.89 compared to 0.97 in the pristine ce-1T-MoS_2, demonstrating a change in the surface properties of ce-1T-MoS_2 that may be due to functionalisation.[29]

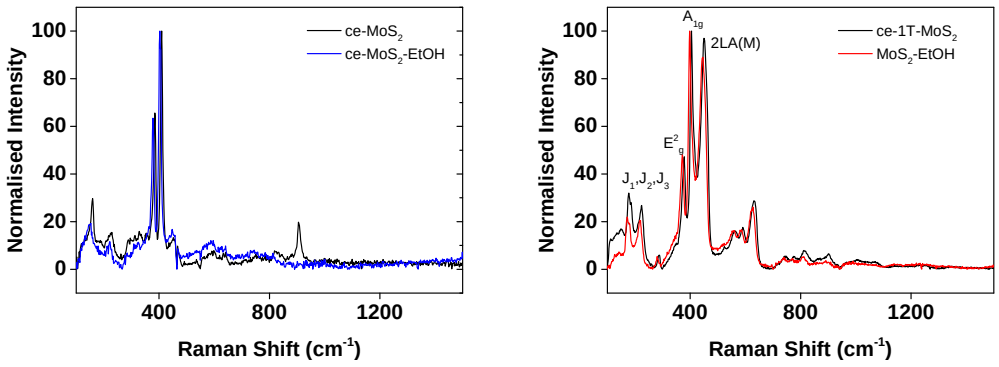

(a) (b)

Fig. 5.24 Raman spectra of (a) MoS_2-EtOH (blue) and ce-1T-MoS_2 (black) taken with 532 nm line. (b) MoS_2-EtOH (red) and ce-1T-MoS_2 (black) taken with 633 nm line.

In general, the analysis of MoS_2-EtOH by ATR-IR, TGA, TGA-IR, XPS and Raman all supported successful functionalisation by ethanol. ATR-IR, TGA-IR and XPS in particular were used to identify the species bound to MoS_2 as ethanol, and TGA in combination with XPS could be used to determine the degree of functionalisation, which amounted to 13%. With the preparation of MoS_2-EtOH complete, the linking of both functionalised materials was attempted.

5.2.5 Formation of Linked Graphene and MoS_2

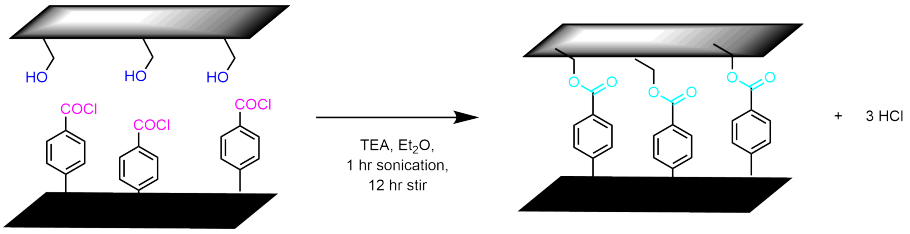

Scheme 5.6 Esterification of graPhCOCl and MoS_2-EtOH.

The formation of the ester linkage between acyl chloride functionalised graphene and ethanol functionalised MoS_2 was attempted using a similar method to the graphene-ester experiments. The two functionalised materials, 70 mg of gra-PhCOCl and 10 mg of MoS_2-EtOH, were bath sonicated for 1 h in a suitable dry solvent (Et_2O, THF or DMF) and stirred for a further 16 h before centrifuging and washing with Et_2O or ethyl acetate. The product, graphene and MoS_2 linked by an ethyl benzoate bridge (gra-PhCOOEt-MoS_2), was then analysed by ATR-IR, TGA, TGA-IR, pXRD and Raman spectroscopy.

The ATR-IR spectrum of gra-PhCOOEt-MoS_2 displayed signals at ν = 3285, 3183 (residual O-H stretches), 3066, 2964, 2924 (C-H stretches), 1713 (ester C=O stretch), 1642, 1605 (C=C stretch), 1536 (C-H bend), 1509 (aromatic C-O stretch), 1407 (O-H bend), 1321, 1246, 1203 (O=C-C asym and sym stretches), 1178, 1098, 1027 (C-O bend), 956, 823, 761 (substituted aromatic C-H bend), 731 (C-S stretch), 699 (C-Cl stretch) cm^{-1} (Figure 5.22). The peak assigned as a C-S stretch was shifted (749 to 731 cm^{-1}) with respect to the assigned peak in MoS_2-EtOH. Other than this, there was a good overlap of peaks with both MoS_2-EtOH (2924, 1642, 1407, 1203, 1027, 956, 823 cm^{-1}) and gra-PhCOCl (1509, 1203, 1027, 699 cm^{-1}), as well as the new carbonyl stretching mode at 1713 cm^{-1}. This carbonyl stretch was also in agreement with that found in the graphene-ester experiments described above (1709 cm^{-1} for gra-PhCOCl and iodoethanol). This shoulder off the acid carbonyl stretch also overlapped well with the synthesised free ethyl benzoate (Figure 5.25)

supporting the assignment of that as the ester carbonyl. Peaks at ν = 1605, 1407, 1321, 1246, 1178, 1098, 699 cm^{-1} in gra-PhCOOEt-MoS_2 also overlapped with those of ethyl benzoate, adding further credibility to their assignment. Much like the graphene-ester experiments, the intensity of the peaks attributed to the functional groups has decreased and the spectrum itself has low transmittance values normally seen in the ATR-IR spectra of both graphene and MoS_2 (2.2, 2.12) due to the loss of the physisorbed material and retention of covalently bound species only.

The formation of the ester was also reversed as in the graphene-ester experiments. The gra-PhCOOEt-MoS_2 product was bath sonicated in DI water, then refluxed in 0.1 M HCl for 16 h. It was then centrifuged and washed with DI water three times before being vacuum dried. The ATR-IR spectrum produced gave the following peaks: 3310, 3253 (O-H stretch), 2981 (C-H stretch), 1693 (C=O stretch), 1597 (C=C stretch), 1383, 1310, 1243 (O=C-O stretch), 761 cm^{-1} (substituted aromatic C-H bend) (Figure C.15). This resulted in the restoration of the O-H (3310 and 3253 cm^{-1}) and C=O (1693 cm^{-1}) stretches attributed to the carboxylic acid, as well as the disappearance of both the C=O stretch for the residual acyl chloride (1737, 1778 cm^{-1}) and the ester (1713 cm^{-1}), thus demonstrating the hydrolysis of both the ester and the acyl chloride and return to the carboxylic acid. This and the overlaid spectra both support the formation of the ester between graphene and MoS_2.

The TGA trace of the product, gra-PhCOOEt-MoS_2 displayed an average weight loss of 3% before 200 °C, increasing to 13% before 400 °C, to 38% before 600°C and to 68% before 700 °C (Figure 5.26). The gradual loss of weight before 200 °C despite washing and the isothermal step at 150 °C, suggested that a species of lower binding energy was being lost, whereas other functional groups were lost between 400 and 600 °C, similarly to the other functionalised graphenes described above. Therefore at least two species were being lost from gra-PhCOOEt-MoS_2, one at lower temperatures (200-400 °C) that remained despite washing, and at least one that occurred at higher temperature (400–600 °C) as the functional

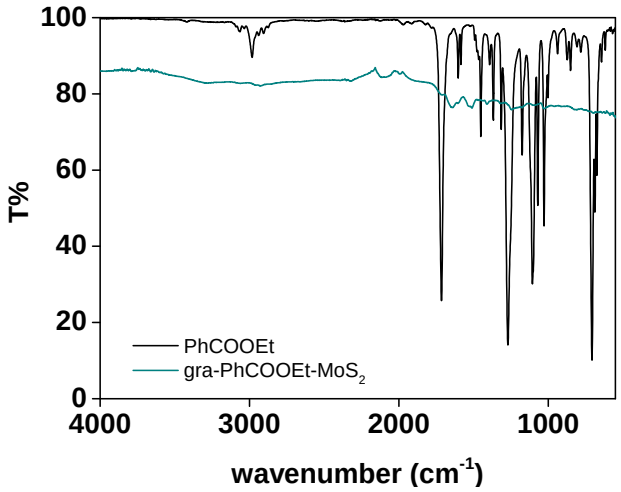

Fig. 5.25 ATR-IR spectrum of gra-PhCOOEt-MoS_2 from gra-PhCOCl and MoS_2-EtOH (teal) compared to free ethyl benzoate (black).

groups were inferred to come off the starting materials, gra-PhCOCl and MoS_2-EtOH. The weight lost at lower temperatures, matching that seen for the gra-ester product, could be water or CO_2 from the thermolysis of the ester bridge. Five steps of weight loss were identified by the inflection points in the 1st derivative of the TGA trace. These were observed at 145 °C for the loss of solvent, with the point at 260 °C likely to be due to ester degradation, and points at 405 °C, 460 °C and 510 °C corresponding to the loss of functional groups from both materials as well as the degradation of graphene beginning shortly after this, and 710 °C as the degradation of MoS_2, as identified from analysis of the pristine graphene and MoS_2. Combining this with the evidence seen in ATR-IR, this supported the formation of the ester. However, the low weight loss (13%) and the presence of many carbonyl species in the ATR-IR may also mean that while the ester was formed, the yield was low.

Further analysis using coupled TGA-IR afforded some insight into the nature of these steps. Stretching CO_2 peaks were detected at ν = 2350 and 2320 cm^{-1} at 380°C which corresponded to the first step of weight loss in the TGA trace. Accompanying the CO_2 were several weaker peaks at lower wavenumber (at approximately 1080 and 925 cm^{-1}).

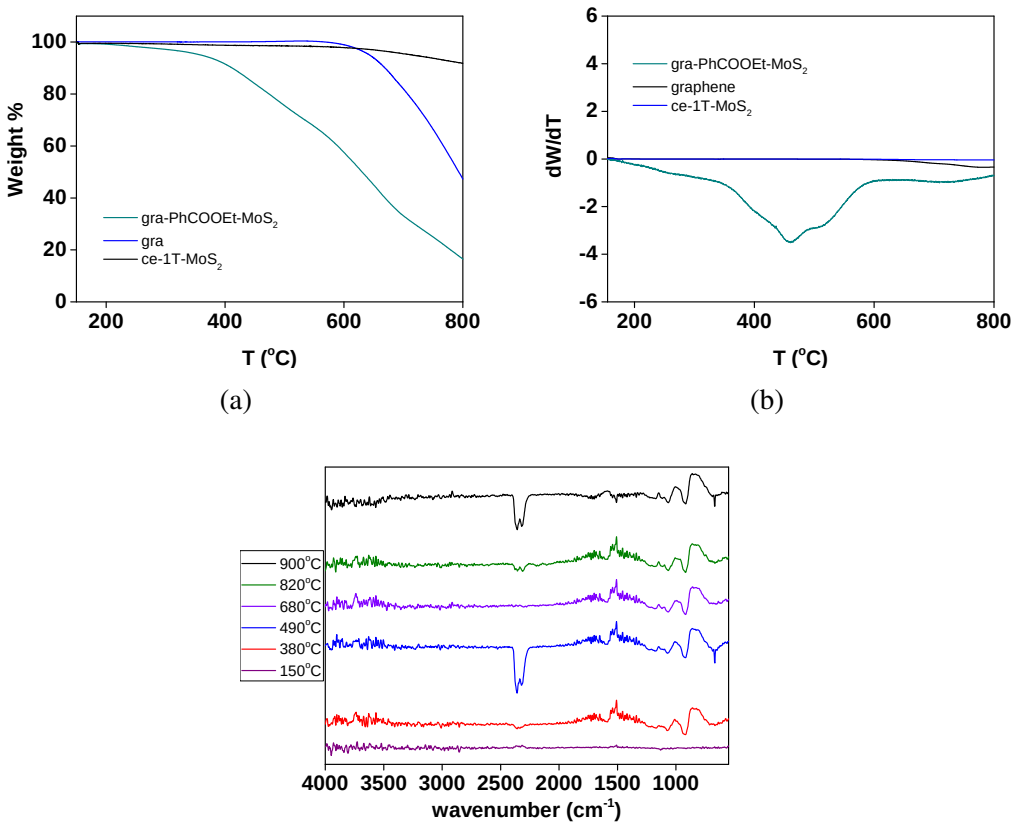

Fig. 5.26 (a) TGA traces and (b) derivatives of gra-PhCOOEt-MoS_2 (c) TGA-IR spectra showing the evolution of CO_2 at different temperatures in the furnace.

The peaks associated with CO_2 then decreased and had disappeared fully by 680 °C. The other peaks at ν = 1080 and 925 cm^{-1} persisted, and were also present when CO_2 was again detected at 820 °C. These peaks were seen in multiple samples and therefore were not considered adventitious. Peaks at or around these values were seen in MoS_2-EtOH (1040, 956 cm^{-1}) and in the ATR-IR for the ester-linked graphene and MoS_2 composite but not in the hydrolysed product and could be due to the loss of organic groups from MoS_2 whereas the first appearance of CO_2 matched that seen in functionalised graphene, the second step coming from the degradation of the underlying carbon framework. Here, the TGA-IR demonstrated the persistence of the functional groups on graphene and MoS_2 through decarboxylation

products and volatile organics at temperatures lower than the degradation temperatures of the nanomaterial base.

The powder X-ray diffraction pattern of linked graphene-MoS_2 presented peaks that were present in graphite (26.5°, 42.5°, 44.5°, 54.5° at 2θ) and functionalised graphite (9°, 14° at 2θ),[30] as well as in ce-1T-MoS_2 (19°, 25°, 32.5°, 39°, 42°, 48°, 50° at 2θ).[31] Although no direct evidence of ester formation can be obtained from this, it supported other techniques in showing the presence of both functionalised materials after reaction and work up (Figure 5.27).

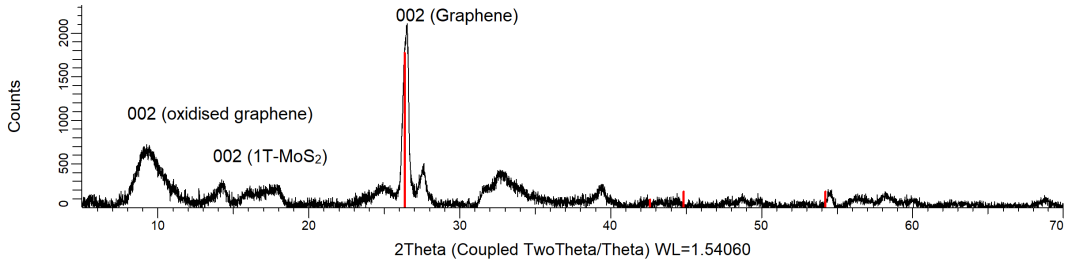

Fig. 5.27 Powder X-ray diffraction of gra-PhCOOEt-MoS_2 (black trace) with graphene pattern from database (red).

In summary, the analysis of the gra-PhCOOEt-MoS_2 product by ATR-IR identified peaks associated with an ester, and these were further supported by comparison with a sample of free ethyl benzoate and analysis of the product after hydrolysis which showed a return to the carboxylic acid product. TGA analysis detected several weight loss steps, which was likely due to the multitude of functional groups present, as well as the more heat-labile ester. At least two stages of CO_2 loss in the TGA-IR supported this. pXRD analysis and XPS confirmed the presence of both materials and their functional groups, respectively and therefore, the production of an ester-linked heterostructure of graphene and MoS_2 could be confirmed. These were later used for HER catalysis, and the effect of the graphene and linker compared with the HER studies of the pristine materials in the previous chapter, as well as with functionalised MoS_2. However, before this, another method of heterostructure formation was examined.

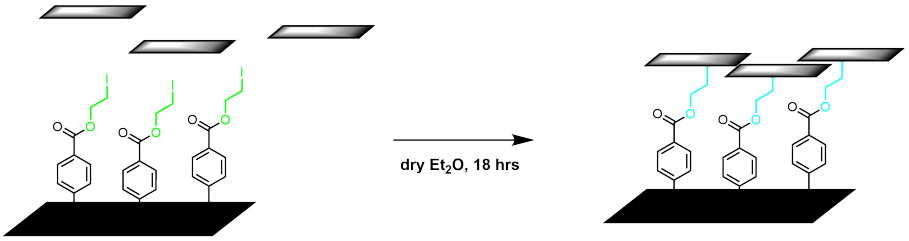

Fig. 5.28 Formation of heterostructure through the combination of ce-1T-MoS_2 and iodoethyl benzoate functionalised graphene (gra-PhCOOEtI).

The second method of heterostructure formation was attempted using the iodoester-functionalised graphene (gra-PhCOOEtI) and pristine ce-MoS_2 (Figure 5.28). The method employed was similar to the linked material (gra-PhCOOEt-MoS_2) prepared above. 50 mg of gra-PhCOOEtI and 5 mg of ce-1T-MoS_2 were bath sonicated for 1 h in a suitable dry Et_2O and stirred for a further 16 h before centrifuging and washing with Et_2O or ethyl acetate. The product (gra-PhCOOEtI+MoS_2) was then analysed by ATR-IR, TGA and XPS. The ATR-IR spectrum of this product had the following peaks: ν = 3299 (O-H stretch), 2955, 2919 (C-H stretches), 1728, 1712, 1702, 1674 (C=O stretches), 1652, 1592 (C=C stretch), 1503 (aromatic C-O stretch), 1401 (O-H bend), 1309, 1235 (O=C-C asym and sym stretches), 1163, 1088, 1009 (C-O stretches), 844, 756 (residual C-Cl), 667 cm^{-1} (Figure 5.29). The region of 1650-1750 cm^{-1} contained one wide C=O peak with several shoulders, which was likely due to the multitude of carbonyl containing species present. As above, the peak at 1712 cm^{-1} was assigned as the ester carbonyl, and the spectrum compared to that of ethyl benzoate. Peaks and shoulders off peaks directly overlapping with the free ester were at ν = 1712, 1592, 1503, 1401, 1309, 1009, 844, 766, 667 cm^{-1}, with other peaks (2919, 1652, 1309, 1163, 749 cm^{-1}) overlapping with that of MoS_2-EtOH. The presence of peaks from both materials as well as the presence of the ester carbonyl, although weaker in intensity than the ester produced from gra-PhCOCl and MoS_2, did suggest that this preparation may also work.

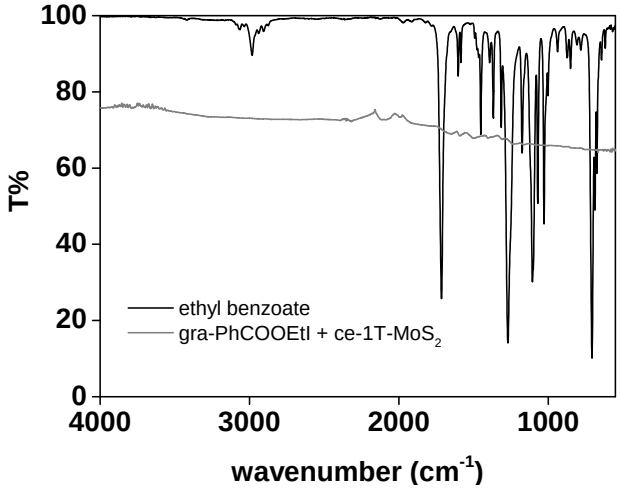

Fig. 5.29 ATR-IR spectrum of gra-PhCOOEt-MoS_2 from gra-PhCOOEtI and ce-1T-MoS_2 (grey) with ethyl benzoate (black).

The TGA trace of gra-PhCOOEtI+MoS_2 showed a steady decline in weight, totalling 25% from 200 °C to 600 °C with no obvious steps or inflection points in the 1st derivative of the trace, suggesting a mixture of physisorbed and covalently bound species coming off (Figure 5.30a). The weight loss from 400 °C onwards was less (10%) than that recorded for the ester formed from gra-PhCOCl and MoS_2-EtOH (24%) and coupled with the weaker intensity of the peaks in the ATR-IR spectrum, may mean that this method of linkage formation was not as effective as gra-PhCOCl and MoS_2-EtOH. The derivative again showed minimal steps, these were located at 300°C and 400°C (likely to be decarboxylation of the functional groups) with what could be the degradation step at approximately 500°C.

The XPS survey spectrum of the gra-ester-MoS_2 product from this method showed the presence of Mo, S, C, O and I in the survey spectrum (Figure 5.31). The concentrations of each species were calculated as 12% Mo, 20% S, 55% C, 12% O and <1% I. The loss of both N and Cl was indicative of the loss of the acyl chloride moiety and of residual amine/diazonium. The lingering presence of I in the survey spectrum compared to MoS_2-EtOH, suggested that functionalisation of MoS_2 with ester-functionalised graphene was not

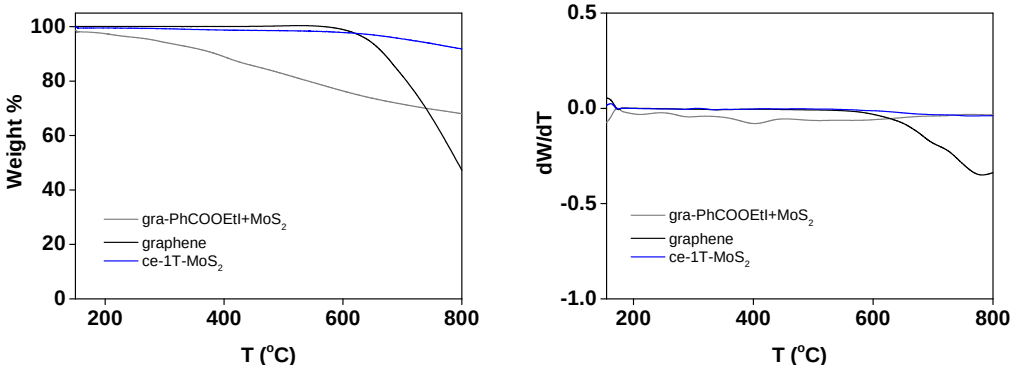

(a) (b)

Fig. 5.30 (a) TGA traces and (b) derivatives of gra-ester-MoS_2 from gra-PhCOOEtI and ce-1T-MoS_2.

as efficient as functionalisation with free iodoethanol, as expected. This was supported by the S 2p core level spectrum, which was fitted with a lower concentration (2.5%) of 'C-S' compared to MoS_2-EtOH (5%). The Mo 3d core level spectrum also showed a small increase in oxidised MoS_2 species (2%) similar to MoS_2-EtOH (3%). The C 1s core level spectrum was assigned as 52% C=C/C-C, 35% C-O, 5% C=O, 6% COOH, and 2% shake up. The increase in C=C/C-C could be indicative of the presence of the ethyl moiety on MoS_2. The decrease in C-O and C=O peaks, located at similar binding energies to C-N and C-Cl could also support the loss of N and Cl in the survey spectrum.

Analysis of the gra-PhCOOEtI+MoS_2 product in general was less clear than that seen for the gra-PhCOOEt-MoS_2 product. The ATR-IR spectrum detected the persistence of the ester group but evidence for a C-S stretch, necessary for linking to MoS_2, was less obvious. The TGA also displayed a reduction in weight loss between 200–600 °C. This may be due in part to the lower yield of ester formed on graphene (gra-PhCOOEtI) compared to acyl chloride (gra-PhCOCl), as seen above, and also the labile nature of the iodine leaving group. The XPS of gra-PhCOOEtI did detect iodine, but in low quantities, this may not be enough to form many connections with ce-1T-MoS_2 despite the excess of functionalised graphene used. In contrast, functionalisation of ce-1T-MoS_2 with iodoethanol typically requires 10

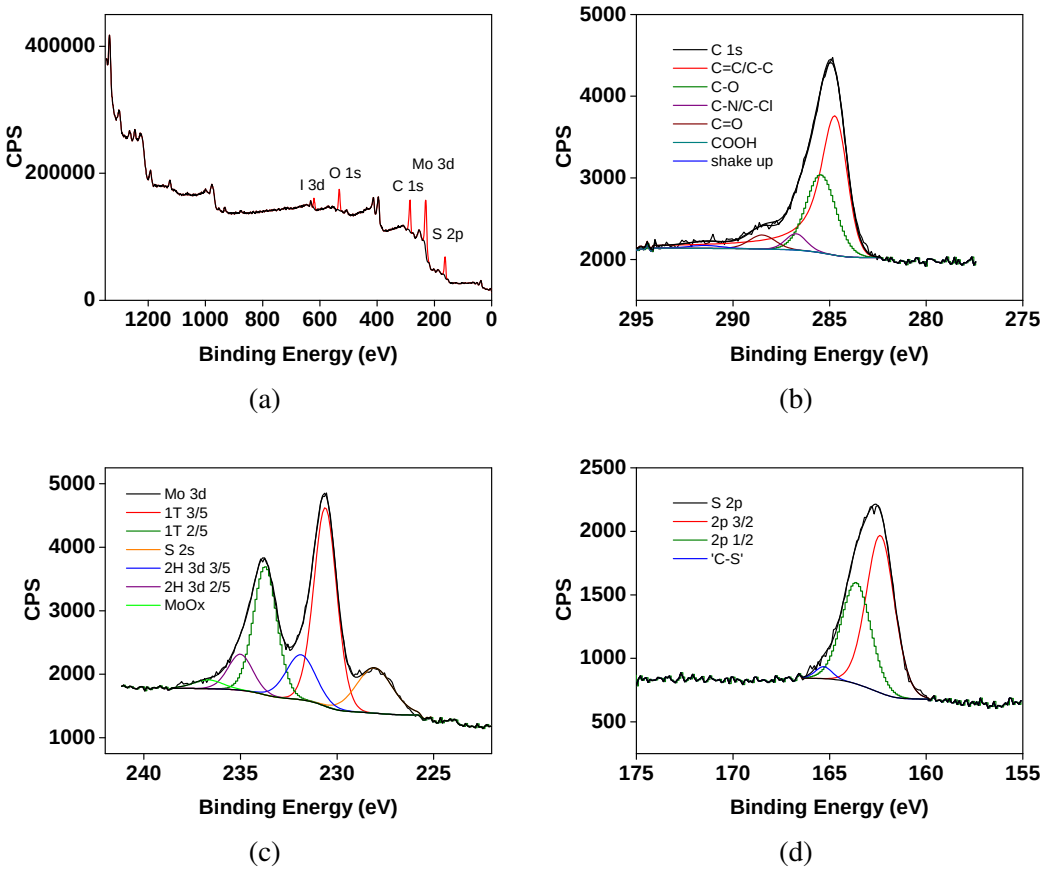

Fig. 5.31 (a) Survey spectrum, (b) C 1s, (c) Mo 3d and (d) S 2p core level spectra of gra-ester-MoS_2, from gra-PhCOOEtI and ce-1T-MoS_2.

equivalents of the alcohol. The XPS of gra-PhCOOEtI+MoS_2 showed a reduction in iodine content which may be from the successful reaction of graPhCOOEtI and ce-1T-MoS_2, but the feature assigned as C-S was smaller than that detected for gra-PhCOOEt-MoS_2. It was decided that the product that could more confidently be described as gra-PhCOOEt-MoS_2 would be tested for HER capability, as described in the next section.

5.3 Use of Covalently-linked Heterostructures as Catalysts for HER

The catalytic activity and impedance of films of gra-PhCOOEt-MoS_2 were measured using linear sweep voltammetry and electrochemical impedance spectroscopy in a three electrode cell with a 0.5 M H_2SO_4 electrolyte. Three glassy carbon electrodes were coated with a film of gra-PhCOOEt-MoS_2 as described in the experimental methods. Control films and HER studies were also prepared for ce-1T-MoS_2 and MoS_2-EtOH to compare their activity with that of the heterostructure. Nafion (1% solution in IPA) was added to increase the adhesion of the film to the electrode and three linear sweeps were performed on each electrode. The overpotential at which hydrogen evolution started and the Tafel slope, extracted from a plot of E as a function of log J, were recorded for each electrode. The LSV traces for ce-1T-MoS_2, MoS_2-EtOH and gra-PhCOOEt-MoS_2 are displayed below in Figure 5.32a. The film resistance was measured using impedance spectroscopy at -0.5 V and is also shown in Figure 5.32b as a Nyquist plot of imaginary resistance (Z_{img}) as a function of real resistance (Z_{real}).

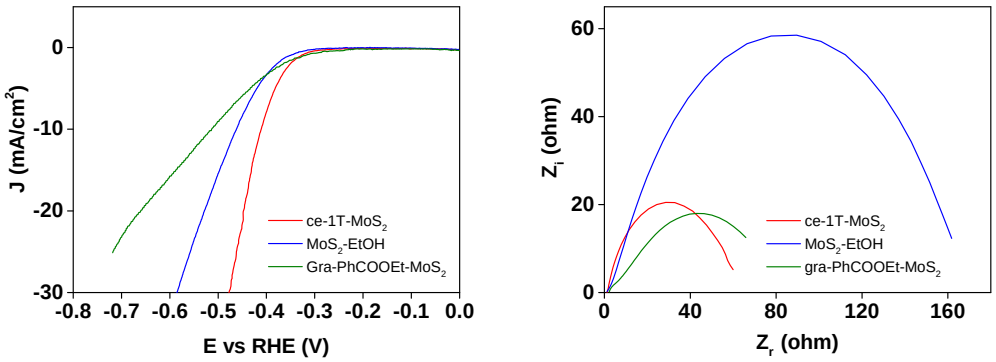

(a) (b)

Fig. 5.32 (a) The LSV runs of ce-1T-MoS_2 (red), MoS_2-EtOH (blue) and gra-PhCOOEt-MoS_2 (green). (b) The Nyquist plots of ce-1T-MoS_2 (red), MoS_2-EtOH (blue) and gra-PhCOOEt-MoS_2 (green).

Linear sweep voltammetry of ce-1T-MoS_2 gave a Tafel slope of 83 mV/dec and an overpotential at 5 mA/cm^2 of -0.38 V, with resistance remaining below 60 Ω. The functionalised sample, MoS_2-EtOH, despite the presence of the alcohol groups obstructing some of the active sites, had a Tafel slope of 89 mV/dec and an overpotential of -0.41 V at an exchange current density of 5 mA/cm^2 which were only slightly higher than ce-1T-MoS_2. The conductivity of the film was the only property that suffered significantly from the functionalisation of MoS_2, with impedance increased to a maximum of 160 Ω. Gra-PhCOOEt-MoS_2 showed worse catalytic activity than ce-1T-MoS_2 and MoS_2-EtOH. Most notably, the Tafel slope increased to 133 mV/dec, and the overpotential at 5 mA/cm^2 was -0.43 V. However, unlike MoS_2-EtOH, the conductivity was much closer to that of ce-1T-MoS_2 with the maximum impedance dropping to 65 Ω.

For both ce-1T-MoS_2 and MoS_2-EtOH, the rate-limiting step, inferred from the value of the Tafel slope, was most likely the Volmer step; the adsorption of hydrogen onto the surface of MoS_2/the active sites, however, due to its increase Tafel slope and overpotential, this may not be the case for gra-PhCOOEt-MoS_2.[32] The alcohol groups covalently binding to vacancies in the structures of MoS_2[10] are thought to reduce the number of putative active sites which can explain the small increase in overpotential and Tafel slope. The large increase in resistance of the film could be due to the electron-withdrawing nature of the functional groups. This correlated well with a study by Benson *et al* in 2018, on the trends in HER activity they discovered by testing 1T-MoS_2 functionalised with a series of *p*-substituted benzenes. They found that the more electron withdrawing the *para* substituent was (according to Hammett parameters), the worse the conductivity, Tafel slope and overpotential was in relation to ce-1T-MoS_2.[28] The drastic changes they observed were possibly due to the higher coverage and increased disorder introduced into MoS_2 afforded by diazonium functionalisation. The hydroxide group on ethanol can be electron withdrawing, and therefore MoS_2-EtOH could display much worse conductivity because of this.

Compared to gra-PhCOOEt-MoS_2, the presence of functional groups on MoS_2 and functionalised graphene appeared to have slightly more of a negative effect of the catalytic properties of MoS_2 compared to MoS_2-EtOH. Despite the increase in overpotential and substantial increase in Tafel slope however, the conductivity of the heterostructure was much improved compared to functionalised MoS_2. The ester linkage should be relatively electron donating, and the presence of the large, electron-rich graphene, as shown in the previous chapter, should also donate electron density to MoS_2 and increase conductivity. However, the combination of functionalised MoS_2 and functionalised graphene seemed to show an overall decrease in catalytic activity, with good conductance not enough to make up for the loss of active sites from functionalisation.

Comparing this to the HER results of the previous chapter, the use of pristine graphene with ce-1T-MoS_2 yielded the most efficient and stable catalytic activity, whereas the use of functionalised graphene seemed to have a deleterious effect on the activity of the film. The nature of the linkage or abundance of graphene may also have been a factor in the reduction of catalytic activity. In future, the use of a more stable amide bridge between MoS_2 and graphene may improve the activity of the covalently linked heterostructure. Although the heterostructure did not display activity as high as ce-1T-MoS_2, the presence of graphene is also postulated in the literature to improve the stability of the MoS_2 catalyst. Further studies examining this may show that the heterostructure shows improved catalysis over long periods of time.

5.4 Conclusions

This chapter detailed the preparation and characterisation of a series of functionalised graphenes (gra-PhCOOH, gra-PhCOCl, gra-PhCOOEtI) and functionalised MoS_2 (MoS_2-EtOH) with a view to forming a covalently linked heterostructure of graphene and MoS_2 (gra-PhCOOEt-MoS_2) by connecting the two functionalised materials. Benzoic acid functionalised graphene was prepared from liquid exfoliated graphene and 4-carboxybenzene diazonium tetrafluoroborate and characterised by ATR-IR, TGA, Raman spectroscopy, XPS, SEM and pXRD, which demonstrated good agreement with literature reports of the Raman spectra and ATR-IR spectra of diazonium functionalised graphene. Benzoic acid was identified directly by TGA-IR, although a certain amount of physisorbed material was detected by TGA and SEM, to be removed only by drying in an oven. Gra-PhCOOH was converted to benzoyl chloride functionalised graphene by sonication in $SOCl_2$ and characterised by ATR-IR, TGA, XPS and pXRD. Although the conversion was not quantitative, this conversion removed much of the physisorbed material and could be clearly identified by ATR-IR to contain the desired acyl chloride groups.

Esterification of gra-PhCOCl proved successful, although quantitative conversion of the acyl chloride to an ester was elusive, an ATR-IR handle for the ester was identified by overlaying with free ethyl benzoate and hydrolysis experiments. Amidation of gra-PhCOCl using aniline also yielded mixed results but enabled the assignment of a possible amide C=O stretching frequency in ATR-IR. The functionalisation of graphene in this way allowed for the quick and easy identification of the nature of the functional groups on graphene by the shift and broadening/splitting of the C=O peak in ATR-IR.

Ce-1T-MoS_2 was prepared by chemical exfoliation of 2H-MoS_2 and then functionalised with ethanol using a previously reported method, *via* nucleophilic attack on iodoethanol. The resultant ethanol-functionalised MoS_2 was characterised by ATR-IR, TGA, TGA-IR, XPS

and Raman spectroscopy, confirming the presence of the ethanol groups on MoS_2 conclusively by ATR-IR, XPS and TGA-IR, with evidence for functionalisation of MoS_2 coming from TGA and Raman spectroscopy. The two materials were linked by the esterification of the alcohol on MoS_2 and the acyl chloride on graphene by bath sonication and stirring, with a second attempt using the ester-functionalised graphene and pristine ce-1T-MoS_2. The linked heterostructure was characterised by ATR-IR, TGA, XPS and pXRD. The confirmation of ester formation was again inferred from ATR-IR after comparison with gra-PhCOOEtI and free ethyl benzoate, and the presence of both functionalised materials demonstrated by XPS and pXRD. The detection of many steps of weight loss in the TGA was taken as evidence for a multitude of functional groups present in the heterostructure. The second method of heterostructure formation, using ester-functionalised graphene and pristine ce-1T-MoS_2, did not give as clear indications of success, as the distinctive C-S peak in the ATR-IR spectrum was not obvious, and the XPS spectra also showed a reduction in the C-S contribution. Therefore, the gra-PhCOOEt-MoS_2 heterostructure produced from the first method (esterification) was used for HER studies. In terms of the functionalisation of nanomaterials, this chapter highlighted the viability of using diazonium salts on liquid exfoliated graphene as well as the more studied epitaxial graphene or more easily processed graphene oxide.[33, 34] It also demonstrated the possibility of altering the nature of the functional groups without overtly damaging the underlying graphene, by the production of benzoyl chloride and iodoethyl benzoate functionalised graphene.

The prepared heterostructure was tested for HER activity, and compared with the ce-1T-MoS_2 starting material and functionalised MoS_2 intermediate. The linked graphene-MoS_2 species showed a higher overpotential, higher Tafel slope than ce-1T-MoS_2 or MoS_2-EtOH, but similar conductance to ce-1T-MoS_2, which was much higher than that of MoS_2-EtOH, demonstrating that the presence of functionalised graphene did afford similar benefits to that of pristine graphene, as detailed in the previous chapter. Reasoning for the reduction in

catalytic efficiency for MoS_2-EtOH and gra-PhCOOEt-MoS_2 may be due to the proposed loss of active sites induced by the functionalisation of 1T-MoS_2. The presence of the linker to graphene however, aiming to lock the two materials together, retained the conductivity that MoS_2 can benefit from in the presence of graphene, although it did not outweigh the deficiency in catalytic efficiency caused by the defects introduced by functionalisation of MoS_2. The development of other, sturdier linkages or shorter linkages may afford more insight into this. Given the labile nature of the ester, future studies will concentrate on stability over time, and supported by the study of the reaction of gra-PhCOCl with amines, on the formation of an amide linkage between graphene and MoS_2.

5.5 Experimental Methods

40% HBF_4 in water, PABA, bulk MoS_2, HPLC MeCN, iodoethanol (99%), and 1.6 mL nBuLi in hexanes were purchased from Sigma Aldrich/Merck and used as received. $SOCl_2$, $NaNO_2$, aniline, HPLC IPA and EtOH were purchased from Fisher Scientific and used as received. SGN18 graphite was used as received. HPLC hexane and HLPC diethyl ether were purchased from Fisher Scientific, passed through a solvent purification system, degassed for 1 h with Ar and stored in a nitrogen-atmosphere glovebox. ^{1}H NMR spectra were recorded using a Bruker DPX 400 MHz NMR Spectrometer, in $CDCl_3$.

Preparation of Few-Layer Graphene for Functionalisation

Few-layer graphene was prepared as described in previous chapters: as a dispersion in IPA from ultrasonicating and centrifuging SGN18 synthetic graphite[12] and filtering the resultant dispersion using a nylon membrane of 0.2 μm. 100 mg (8.33 mmol) of the filtered graphene dispersions were then re-dispersed by sonication in MeCN for 3 h before addition of the diazonium salt.

Preparation of the Diazonium Salt

The diazonium salt was synthesised according to the literature procedure.[13] 2 g (14.46 mmol) of *para*-amino-benzoic acid (PABA) was dissolved in 8 mL of 24% HBF_4 in deionised (DI) water (5 mL of DI water and 3 mL of 40% HBF_4 in DI water). The solution was put on ice and a solution of $NaNO_2$ (1 g, 15 mmol in 5 mL DI water) was added slowly under nitrogen and in darkness over 30 minutes. After the addition of $NaNO_2$, the solution was warmed to room temperature and left to stir for 2 h to allow for formation of the diazonium salt. The solution, containing crystals of 4-carboxy-benzenediazonium tetrafluoroborohydrate was filtered to remove H_2O and added to the graphene dispersion in MeCN. A sample of the diazonium salt was analysed by ATR-IR (Figure C.1).

ATR-IR: ν = 3588, 3496 (residual N-H stretches), 3289 (O-H stretch), 3116, 2643, 2529

(C-H stretches), 2307 (N-N triple bond stretch), 1728, 1709 (acid C=O stretch), 1606, 1580 (C=C stretch), 1524, 1476, 1417 (C-O stretch), 1388, 1310, 1292, 1225, 1162 (O=C-O sym and asym stretches), 1034, 1011 (C-N stretch), 867, 760, 723, 701, 664, 638, 579 cm^{-1}.

Preparation of 4-Benzoic Acid Functionalised Graphene

The functionalisation of graphene *via* diazonium salts was based on the literature procedure and modified for liquid exfoliated graphene.[11] The mixture of 4-carboxy-benzenediazonium tetrafluoroborohydrate and graphene in MeCN was stirred in darkness under nitrogen at room temperature for 16 h. The resulting green solid and red supernatant were separated by centrifuging at 4500 rpm for 1 h. The solid was isolated and subjected to several cycles of centrifuging and washing with MeCN and acetone before it was vacuum dried. The green solid was analysed by ATR-IR, DRIFT-IR, TGA, TGA-IR, Raman spectroscopy, SEM and p-XRD.

Treatment of 4-benzoic acid functionalised graphene with heat (by heating the powder to 130 °C in an oven), a gas was evolved and the green colour of the solid was lost, forming a dark brown solid. ATR-IR/TGA/SEM analysis of this showed that the graphene remained covalently functionalised with benzoic acid, and the gas given off was believed to be excess diazonium salt physisorbed to the surface of the graphene. Heating of the green solid in the TGA also gave a sudden drop in mass at the 5 min long isothermal step at 150 °C which is believed to be the same substance coming off.

Conversion of Benzoic Acid-Functionalised Graphene to Benzoyl Chloride-Functionalised Graphene

300 mg of the 4-benzoic acid-functionalised graphene (green solid) isolated in the previous experiment was bath sonicated in 4 mL of $SOCl_2$ for 3 h. $SOCl_2$ was then vacuum-distilled off and the brown solid obtained was dried under vacuum. The brown solid was characterised by ATR-IR, DRIFT-IR, TGA, TGA-IR and SEM.

Preparation of Iodoethyl Benzoate-Functionalised Graphene

Esterification involved dispersing gra-PhCOCl in dry DMF or Et_2O with the addition of 10 equivalents of iodoethanol. This was bath sonicated for 30 min and stirred at RT for 16 h, before being centrifuged at 4500 rpm for 45 min and washed with MeCN before repeating the centrifuging step. Iodoethyl benzoate functionalised graphene (gra-PhCOOEtI) was characterised by ATR-IR, XPS and TGA.

Preparation of Ethanol-Functionalised ce-1T-MoS_2

Ce-1T-MoS_2 was prepared as described in a previous chapter.[35] The functionalised of ce-1T-MoS_2 has been described in the literature,[10] and the preparation here was based on this with some modification. Iodoethanol (0.36 mL, 5 mmol, 99%) was added to 40 mL (1.9 mg/mL, 0.5 mmol in DI water) of ce-1T-MoS_2 and bath sonicated for 1 h in darkness. The dispersion was then stirred at room temperature in darkness for 16 h. It was then centrifuged at 11000 rpm for 1 h and subsequently washed and centrifuged with ethanol and DI respectively. In order to characterise the functionalised MoS_2 and to use it in the linking experiment, the dispersion was filtered and dried using a nitrocellulose membrane with a pore size of 0.025 μm and a vacuum filtration setup.

Linking Benzoyl Chloride-Functionalised Graphene and Ethanol-Functionalised MoS_2

4-benzoyl chloride-functionalised graphene (70 mg, 0.5 mmol of functionalised graphene) and ethanol-functionalised MoS_2 (7 mg, 0.1 mmol functionalised MoS_2) were added as solids to 10 mL of dry Et_2O or DMF or THF and sonicated for 1 h. The dispersion was then stirred for 16 h, and filtered using a nylon membrane of 0.2 μm. The resultant powder was then characterised by ATR-IR, TGA, TGA-IR and pXRD.

Preparation of Electrodes for HER and HER Methods

0.5 mg of gra-ester-MoS_2 in ethyl acetate was dropcast onto three glassy carbon electrodes with an area of 1 cm^2. Nafion (0.2% in IPA) was added to the dispersion of gra-ester-MoS_2

before dropcasting for three additional electrodes. These made up six working electrodes. The counter electrode was composed of Pt wire, and aqueous Ag/AgCl was employed as the reference electrode. Each working electrode was subjected to a program of three cycles of conditioning and linear sweep voltammetry, followed by impedance measurement at -0.5 V. The best LSV run was chosen for each electrode and the Tafel slope calculated from this.

Synthesis of Benzoyl Chloride

Benzoyl chloride was synthesised according to the literature procedure.[36] Benzoic acid (1.22 g, 10 mmol) was refluxed in $SOCl_2$ (5.0 mL, 97%, 66 mmol) for 2 h. Excess $SOCl_2$ was distilled off and dried under vacuum. Filtering off residual solid benzoic acid gave benzoyl chloride as a clear liquid. This was characterised by ^{1}H NMR.

^{1}H NMR: Δ_H (400 MHz, $CDCl_3$): 7.50–7.54 (tr, J = 8 Hz, 2H), 7.67–7.71 (tr, J = 8 Hz, 1H), 8.12–8.14 (d, J = 8 Hz, 2H) ppm.

Synthesis of Ethyl Benzoate

Ethyl benzoate was synthesised according to the well-known procedure.[37] Triethyl amine (TEA) (1.0 mL, 7 mmol) were added to HPLC grade ethanol (15 mL, 240 mmol) and stirred. Benzoyl chloride (0.81 mL, 7 mmol) was added dropwise at 0 °C and the solution was left to stir at room temperature for 2 h. DI water (5 mL) was added and the product was extracted with ether (3 × 5 mL), dried over $MgSO_4$, filtered and the ether removed by rotary evaporator. The product was characterised by ^{1}H NMR and ATR-IR.

^{1}H NMR: Δ_H (400 MHz, $CDCl_3$): 1.31–1.34 (tr, J = 4 Hz, 3H), 4.29–4.34 (q, J = 4 Hz, 2H), 7.51–7.55 (d, J = 16 Hz, 2H), 7.66–7.68 (tr, J = 5.3 Hz, 1H), 7.96–7.97 (d, J = 4 Hz, 2H) ppm.

ATR-IR:ν = 3068, 2979, 2940, 2905, 1715, 1603, 1584, 1450, 1367, 1316, 1272, 1176, 1106, 1071, 1026, 937, 876, 850, 785, 707, 643, 611 cm^{-1}.

Preparation of Amide-Functionalised Graphene

These experiments were conducting using gra-PhCOCl and the amine in question in DMF.

100 mg of graPhCOCl and 2 mL of aniline were sonicated together in 10 ml dry DMF for 30 minutes, and then left to stir at RT for 16 h. The dispersions were then centrifuged at 4500 rpm for 45 min, washed with ethyl acetate three times, then filtered and air-dried as above. The products were analysed by ATR-IR and TGA.

Treatment of Pristine Graphene with Thionyl Chloride

To study the effect of $SOCl_2$ on pristine graphene, 90 mg (7 mmol) of re-aggregated graphene was bath sonicated in 5 mL (25 mmol) of $SOCl_2$ for 3 h, and refluxed for 4 h. $SOCl_2$ was distilled off and the graphene dried under vacuum. It was then characterised by ATR-IR and TGA.

References

[1] X. Chen, Y. J. Park, T. Das, H. Jang, J.-B. Leea and J.-H. Ahn, *Nanoscale*, 2016, **8**, 15181–15188.

[2] X. Ling, Y. Lin, Q. Ma, Z. Wang, Y. Song, L. Yu, S. Huang, W. Fang, X. Zhang, A. L. Hsu, Y. Bie, Y.-H. Lee, Y. Zhu, L. Wu, J. Li, P. Jarillo-Herrero, M. Dresselhaus, T. Palacios and J. Kong, *Advanced Materials*, 2016, **28**, 2322–2329.

[3] Y. Li, H. Wang, L. Xie, Y. Liang, G. Hong and H. Dai, *Journal of the American Chemical Society*, 2011, **133**, 7296–7299.

[4] B. K. Barman, D. Dasa and K. K. Nanda, *Journal of Materials Chemistry A,*, 2017, **5**, 18081–18087.

[5] K. Pramoda, U. Gupta, I. Ahmad, R. Kumara and C. N. R. Rao, *Journal of Materials Chemistry A*, 2016, **4**, 8989–8994.

[6] W. Chen, Y. Yang, Z. Zhang and E. Kaxiras, *2D Materials*, 2017, **4**, year.

[7] D. A. Kosynkin, A. L. Higginbotham, A. Sinitskii, A. Lomeda, J. R. Dimiev, B. K. Price and J. M. Tour, *Nature*, 2009, **458**, 872–876.

[8] A. Sinitskii, A. Dimiev, D. A. Corley, A. A. Fursina, D. V. Kosynkin and J. M. Tour, *ACS Nano*, 2010, **4**, 1949–1954.

[9] R. Sharma, J. H. Baik, C. J. Perera and M. S. Strano, *Nano Letters*, 2010, **10**, 398–405.

[10] D. Voiry, A. Goswami, R. Kappera, C. de Carvalho Castro e Silva, D. Kaplan, T. Fujita, M. Chen, T. Asefa and M. Chhowalla, *Nature Chemistry*, 2014, **7**, 45–49.

[11] J. M. Englert, C. Dotzer, G. Yang, M. Schmid, C. Papp, J. M. Gottfried, H.-P. Steinrück, E. Spiecker, F. Hauke and A. Hirsch, *Nature Chemistry*, 2011, **3**, 279–286.

[12] U. Khan, A. O'Neill, H. Porwal, P. May, K. Nawaz and J. N. Coleman, *Carbon*, 2012, **50**, 470–475.

[13] A. J. Blanch, C. E. Lenehan and J. S. Quinton, *The Journal of Physical Chemistry C*, 2012, **116**, 1709–1723.

[14] R. Prost, *Clays and Clay Minerals*, 1973, **21**, 363–368.

[15] P. D. Ghosh, *Introduction to Photoelectron Spectroscopy*, John Wiley & Sons, United States of America, 1984.

[16] N. A. Daud, B. W. Chieng, N. A. I. Talib and Z. Abidin, *Journal of Engineering Science*, 2017, **13**, 1–17.

[17] Y. Liu, L.-Z. Fan and L. Jiao, *Journal of Power Sources*, 2017, **340**, 104–110.

[18] D. B. Farmer, R. Golizadeh-Mojarad, V. Perebeinos, Y.-M. Lin, G. S. Tulevski, J. C. Tsang and P. Avouris, *Nano Letters*, 2009, **9**, 388–392.

[19] J. Liu, Q. Li, Y. Zou, Q. Qian, Y. Jin, G. Li, K. Jiang and S. Fan, *Nano Letters*, 2013, **13**, 6170–6175.

[20] H. Gunzler and H.-U. Gremlich, *IR Spectroscopy*, Wiley VCH, Weinheim, Germany, 2002.

[21] S. Stankovich, R. D. Piner, X. Chen, N. Wu, S. T. Nguyen and R. S. Ruoff, *Journal of Materials Chemistry*, 2006, **16**, 155–158.

[22] U. Dettlaff-Weglikowska, V. Skákalová, R. Graupner, S. H. Jhang, B. H. Kim, H. J. Lee, L. Ley, Y. W. Park, S. Berber, D. Tománek and S. Roth, *Journal of the American Chemical Society*, 2005, **127**, 5125–5131.

[23] M. A. Hamon, J. Chen, H. Hu, Y. Chen, M. E. Itkis, A. M. Rao, P. C. Eklund and R. C. Haddon, *Advanced Materials*, 1999, **11**, 834–840.

[24] D. R. Dreyer, S. Park, C. Bielawski and R. S. Ruoff, *Chemical Society Reviews*, 2010, **39**, 228–240.

[25] F. Najafi and M. Rajabi, *International Nano Letters*, 2015, **5**, 187–190.

[26] Y. Shang, D. Zhang, Y. Liu and C. Guo, *Bulletin of Materials Science*, 2015, **38**, 7–12.

[27] S. Presolski and M. Pumera, *Materials Today*, 2016, **19**, 140–145.

[28] E. E. Benson, H. Zhang, S. A. Schuman, S. U. Nanayakkara, N. D. Bronstein, S. Ferrere, J. L. Blackburn and E. M. Miller, *Journal of the American Chemical Society*, 2018, **140**, 441–450.

[29] S. Mignuzzi, A. J. Pollard, N. Bonini, B. Brennan, I. S. Gilmore, M. A. Pimenta, D. Richards and D. Roy, *Physical Review B*, 2015, **91**, 195411.

[30] G. Wang, J. Yang, J. Park, X. Gou, B. Wang, H. H. Liu and J. Yao, *Journal of Physical Chemistry C*, 2008, **112**, 8192–8195.

[31] K. E. Dungey, M. D. Curtis and J. E. Penner-Hahn, *Chemistry of Materials*, 1983, **10**, 2152–2161.

[32] F. Wang, T. A. Shifa, X. Zhan, Y. Huang, K. Liu, Z. Cheng, C. Jiang and J. He, *Nanoscale*, 2015, **7**, 19764–19788.

[33] E. Bekyarova, M. E. Itkis, P. Ramesh, C. Berger, M. Sprinkle, W. A. de Heer and R. C. Haddon, *Journal of the American Chemical Society*, 2009, **131**, 1336–1337.

[34] J. R. Lomeda, C. D. Doyle, D. V. Kosynkin, W.-F. Hwang and J. M. Tour, *Journal of the American Chemical Society*, 2008, **130**, 16201–16206.

[35] G. Eda, H. Yamaguchi, D. Voiry, T. Fujita, M. Chen and M. Chhowalla, *Nano Letters*, 2011, **11**, 5111–5116.

[36] S. Zuffanti, *Journal of Chemical Education*, 1948, **25**, 481.

[37] C. J. Maim, J. W. Mench, D. L. Kendall and G. D. Hiatt, *Industrial & Engineering Chemistry*, 1951, **43**, 684–688.

Chapter 6

General Conclusions and Future Work

The discovery of graphene and its unusual properties opened a door to the preparation of a wide range of two-dimensional materials for a myriad of applications.[1] Most commonly, these materials are proposed to be cheaper, more flexible and abundant replacements for more well-known, pre-existing materials. This can be seen in the studies of the use of graphene as an eventual replacement for tin indium oxide in flexible displays,[2] functionalised graphene or thin layer MoS_2 replacing silicon in transistors,[3] and 1T-phase MoS_2 equalling platinum in the catalysis of the hydrogen evolution reaction.[4] Beyond these examples, the unique and valuable properties of 2D materials such as graphene and MoS_2 mean that the study and use of these materials will continue long into the future. For this eventual ubiquity of these materials in everyday life, there must be a clear understanding of how they interact with one another, with living things and the environment, for both application purposes and their long-term bioremediation.

6.1 Key Findings and Contributions

Part 1 of this thesis has attempted to address this in terms of the interaction of liquid exfoliated graphene with organic lab oxidants and metal-based oxidants—namely, Fenton's reagent, used to degrade dyes in waste water management,[5] and two oxygenating catalysts based on soil bacteria metalloenzymes that degrade aromatic detritus.[6] Reactions of graphene with a series of lab oxidants and oxygen donating agents exhibited the inert nature of graphene, as H_2O_2, ^{t}BuOOH, the iodosyl benzene containing oxidants did not cause any significant change in the structure of the graphene by ATR-IR, TGA, Raman, or, in the case of H_2O_2, XPS. The peracids, peracetic acid and *m*-CPBA demonstrated tentative signs of functionalisation seen in ATR-IR spectrscopy and TGA, but nothing that could be assigned as degradation, as the structure of graphene remained intact. The use of Fenton's reagent on graphene yielded low level functionalisation and no degradation, as seen by ATR-IR, TGA, Raman and XPS. Compared with the sparse literature reports on other forms of graphene treated with Fenton's reagent, this study supported the view that the more defective the source graphene is, the higher level of functionalisation or degradation it undergoes—defective graphene and GO in the literature has been shown to degrade in the presence of Fenton's reagent, whereas the pristine graphene used in this thesis merely undergoes edge functionalisation.[7, 8]

In the case of liquid exfoliated graphene, or graphene comprised of a few layers, the Fenton reagent introduced some oxygen containing groups into the edges or pre-existing defects but did not have the ability to functionalise the basal plane, either from an inability to access it in re-stacked samples, or because the oxidant itself was not powerful enough. This was further tested with the use of the two biomimetic catalysts—both containing aromatic ligands, which should interact favourably with hydrophobic graphene and have the ability to generate reactive oxygen species capable of oxygenating aromatic bonds. [Fe(BPMEN)$(OTf)_2$] and [Fe(TPA)$(OTf)_2$] in the presence of H_2O_2 were used as metalloenzyme mimics. Graphene

treated with catalytic amounts of either complex again presented low levels of functionalisation, but more than originally seen for graphene treated with Fenton's reagent. The detection of intercalated complex by Raman suggested that the [Fe(BPMEN)$(OTf)_2$] complex at least could access the basal plane of graphene, but again, pre-existing defects were preferentially attacked and no noticeable defects were introduced into the basal plane for either this complex or [Fe(TPA)$(OTf)_2$]. These results highlighted the difficulty in degrading graphene and the high risk of waste graphene inadvertently being converted to functionalised graphene—more bioavailable and as shown by a number of studies, more cytotoxic.

The second part of this thesis elaborated on the general understanding of how 2D materials can interact with each other, using the preparation of heterostructures, of graphene and one of the two phases of 2D MoS_2, as examples. The vast majority of heterostructures presented in the literature use rGO or GO forms of graphene, which, already possessing abundant defects, mask the possible chemical interactions MoS_2, particularly the more reactive 1T phase, may have on graphene. The close proximity afforded by combining the materials in heterostructures facilitates this interaction, as seen in the computational report on the p doping effect of MoS_2 on graphene, and the well known increase in both stability and conductivity provided by the presence of graphene in previously prepared heterostructures.[9]

Through the preparation of a series of heterostuctures of differing concentrations of graphene and MoS_2, using both 2H-MoS_2 and ce-1T-MoS_2, this thesis demonstrated the chemical basis of the interaction between MoS_2 and graphene. Using XPS, ATR-IR, TGA-IR, pXRD, Raman and SEM to chemically and physically characterise the components of the heterostructures, it was found that a degree of saturation was induced in graphene during heterostructure formation. Furthermore, this was inferred to be concentration dependent for MoS_2, with the trend being clear for the 2H phase but less so for the more defective and reactive ce-1T-MoS_2. Regardless, ce-1T-MoS_2 showed increased saturation of graphene, in line with its increased reactivity relative to 2H-MoS_2 with respect to functionalisation and

catalytic activity.[10, 11] The HER activity of the prepared heterostructures also supported the assignment of an increase in disorder in the graphene component of the heterostructures; the combination of MoS_2 with graphene has been reported to increase the efficiency of the MoS_2 HER catalyst by increasing the electron flow through the catalyst (due to graphene's excellent conductivity).[12, 13] This is a trend seen in the 2H- and 1T-MoS_2-containing heterostructures for higher concentrations of graphene (although large excesses decrease the activity again), but the lower the graphene content, the worse the catalytic activity becomes. This may be due to the loss of conductivity suffered by defective graphene.

The third part of this thesis dealt with the preparation of a heterostructure of graphene and ce-1T-MoS_2, *via* the covalent tethering of functionalised graphene and functionalised MoS_2. The aim of this project was to form a heterostructure in which MoS_2 and graphene were chemically joined, in opposition to the van der Waals heterostructures prepared in the previous project and other reported in the literature.[14] The only clear example of a covalently bound composite of MoS_2 and graphene was reported by Rao *et al*,[15] using defective rGO as the graphene base before further functionalisation. Therefore, this project set out to achieve the synthesis of a heterostructure from liquid exfoliated graphene and MoS_2. In preparation for this, the functionalisation of liquid phase exfoliated graphene using diazonium salts was explored and characterised in detail using a host of spectroscopic techniques. The chemistry of the functional groups was investigated through the conversion of the starting carboxylic acid to an acyl chloride and then to an ester, before linking with functionalised MoS_2 was attempted. Two methods to form the linked heterostructure were tested and fully characterised, based on the preliminary experiments with functionalised graphene, and showed positive results, if not quantitative, for the formation of the linkage. This linked graphene/MoS_2 structure was then tested for HER activity and compared with that of unfunctionalised ce-1T-MoS_2 and functionalised MoS_2. While the functionalisation of MoS_2 is known to decrease its HER activity, possibly by the poisoning of some of its active

sites, the presence of functionalised graphene in this case did not improve conductivity or catalytic efficiency of the functionalised MoS_2, and unfunctionalised ce-1T-MoS_2 remained the most efficient catalyst.

6.2 Future Work

The most important step for the future work of the first project of this thesis is to properly identify the nature of the oxygen groups with which Fenton's reagent and the other Fe-based catalysts have functionalised liquid phase exfoliated graphene. The most likely kind of functionalisation from Fenton's reagent is hydroxylation; this can also be assumed to be one of the products of either [Fe(BPMEN)OTf_2] or [Fe(TPA)OTf_2] oxidation, the other being epoxidation.[16] Apart from ATR-IR or DRIFT spectroscopy, assays could be used to identify the edge-functional groups, such as the Kaiser test, successfully used to identify amine groups on functionalised graphene oxide.[17] Aside from this, the use of free metals such as Cu can coordinate to carboxylic groups on 2D nanomaterials, as demonstrated by Chen *et al* with acetate-functionalised MoS_2.[18] The edge-functionalisation demonstrated by the metal-based oxidants in the first part of this thesis can be used for future work, perhaps not on the degradation of graphene, but in applications that require the pristine basal plane of graphene, but with the enhanced solubility in polar solvents and delayed re-stacking that can come from functionalisation.[19] This edge-selective functionalisation has been proposed for conductive ink and conductive paper using dispersions and films of edge-functionalised graphene respectively.[20, 21] Edge-functionalisation can also be used in applications such as fuel cells and energy storage, where the functionalised edges of graphene can be further modified for fine-tuning of properties of graphene without overtly damaging it.[22] In order for the edge-functionalised graphene produced here to be applied in these fields, dispersion studies must first be conducted to ensure that it possesses the

required increased hydrophilicity relative to pristine liquid phase exfoliated graphene. In particular, the study of the dispersibility of Fe oxidant treated graphene in aromatic solvents such as toluene, and polar solvents such as alcohols, capable of hydrogen-bonding with oxygen-containing functional groups, should be the focus of the dispersion studies.

In depth analysis on how MoS_2 causes an increase in sp^3 hybridised carbon in graphene could be the focus of future work on the second project in this thesis. Repeating the experiments, using the ratios showing the highest levels of saturation, in the absence of air, or in different solvents, may elucidate the origin or aid the identification of the saturation in graphene—whether it is oxidation of graphene or hydrogenation. Sonication is widely used to aid functionalisation of two dimensional materials as well as in the preparation of liquid exfoliated materials. Whether sonication is necessary for the interaction to occur, or other experimental conditions lead to the same result, is also an area that could be expanded in the future. The use of dispersions composed of very thin MoS_2 and graphene to prepare heterostructures may also yield higher levels of saturation and would be a key area to investigate. It is well known that the thinner the materials, the more reactive they are. This could be realised using cascade centrifugation, pioneered by Backes *et al*.[23] Although this method produces dispersion of very fine materials, it is low yielding and difficult to scale up. Other methods for producing higher concentrations of monolayer graphene could be the use of surfactants in tandem with liquid phase exfoliation.[24, 25] However, the removal of surfactants and their possible interference in reactions on graphene need to be taken into consideration.

The study of the long-term stability of the ester-linked graphene/MoS_2 heterostructure, and the formation/characterisation of a more stable linker would be the main focus for future work, regarding the third part of this thesis. The prepared ester-linked graphene/MoS_2 is liable to hydrolyse, as seen in the ATR-IR spectra of the hydrolysis experiments on functionalised graphene and indeed the graphene/MoS_2 heterostructure. The choice of the

ester functionalisation was driven by the limited modes of MoS_2 functionalisation, therefore, further research into functionalisation that can afford groups such as amines or carboxylic acids on MoS_2 will facilitate the formation of stronger linkages such as amide, or high yielding, one-step coupling reactions such as azide/alkyne cycloadditions.[26] Other areas this project opens up would be to study the use of such heterostructures in applications other than HER activity—functionalisation of graphene and MoS_2 is known to delay or prevent re-stacking.[27] The presence of functional groups in re-stacked materials can also cause widening of the interlayer distance in a similar way to intercalated molecules.[28] Increased distance between layers means that more and larger atoms or molecules can be stored in between these layers—an attribute that is necessary for the storage of hydrogen for fuel cells, or lithium ions or sodium ions for batteries.[29–32] Therefore, these functionalised heterostructures could find use in any of these areas.

References

[1] V. Singh, D. Joung, L. Zhai, S. Das, K. S. I. and S. S., *Progress in Materials Science*, 2001, **56**, 1178–1271.

[2] K. S. Novoselov, V. I. Falko, L. Colombo, P. R. Gellert, M. G. Schwab and K. Kim, *Nature*, 2012, **490**, 192–200.

[3] F. Schwierz, *Nature Nanomaterials*, 2010, **5**, 487–496.

[4] M. A. Lukowski, A. S. Daniel, F. Meng, A. Forticaux, L. Li and S. Jin, *Journal of the American Chemical Society*, 2013, **135**, 10274–10277.

[5] S. Ziajahromi, P. A. Neale and F. D. L. Leusch, *Water Science and Technology*, 2016, **74**, 2253.

[6] D. J. Ferraro, L. Gakhar and S. Ramaswamy, *Biochemical Biophysical Research Communications*, 2005, **338**, 175–190.

[7] D. R. Dreyer, S. Park, C. Bielawski and R. S. Ruoff, *Chemical Society Reviews*, 2010, **39**, 228–240.

[8] X. Zhou, Y. Zhang, C. Wang, X. Wu, Y. Yang, B. Zheng, H. Wu, S. Guo and J. Zhang, *ACS Nano*, 2012, **6**, 6592–6599.

[9] M. Chatti, T. Gengenbach, R. King, L. Spiccia and A. N. Simonov, *Chemistry of Materials*, 2017, **29**, 3092–3099.

[10] S. Presolski and M. Pumera, *Materials Today*, 2016, **19**, 140–145.

[11] K. C. Knirsch, N. C. Berner, H. C. Nerl, C. S. Cucinotta, Z. Gholamvand, N. McEvoy, Z. Wang, I. Abramovic, P. Vecera, M. Halik, S. Sanvito, G. S. Duesberg, V. Nicolosi, F. Hauke, A. Hirsch, J. N. Coleman and C. Backes, *ACS Nano*, 2015, **9**, 6018–6030.

[12] Y. Li, H. Wang, L. Xie, Y. Liang, G. Hong and H. Dai, *Journal of the American Chemical Society*, 2011, **133**, 7296–7299.

[13] B. K. Barman, D. Dasa and K. K. Nanda, *Journal of Materials Chemistry A,*, 2017, **5**, 18081–18087.

[14] R. K. Biroju, D. Das, R. Sharma, S. Pal, L. P. L. Mawlong, K. Bhorkar, P. K. Giri, A. K. Singh and T. N. Narayanan, *ACS Energy Letters*, 2017, **2**, 1355–1361.

[15] K. Pramoda, U. Gupta, I. Ahmad, R. Kumara and C. N. R. Rao, *Journal of Materials Chemistry A*, 2016, **4**, 8989–8994.

[16] M. Costas, M. P. Mehn, M. P. Jensen and L. Que, *Chemical Reviews*, 2004, **104**, 939–986.

[17] I. A. Vacchi, J. Raya, A. Bianco and C. Ménard-Moyon, *2D Materials*, 2018, **5**, 035037.

[18] C. Backes, N. C. Berner, X. Chen, P. Lafargue, P. LaPlace, M. Freeley, G. S. Duesberg, J. N. Coleman and A. R. McDonald, *Angewandte Chemie International Edition*, 2016, **54**, 2638–2642.

[19] Z. Xiang, Q. Dai, J.-F. Chen and L. Dai, *Advanced Materials*, 2016, **28**, 6253–6261.

[20] V. Barbera, L. Brambilla, A. Porta, R. Bongiovanni, A. Vitale, G. Torrisia and M. Galimberti, *Journal of Materials Chemistry A*, 2018, **6**, 7749–7761.

[21] J. E. Mates, I. S. Bayer, M. Salerno, P. J. Carrol, Z. Jiang, L. Liu and C. L. Megaridis, *Carbon*, 2015, **87**, 163–174.

[22] L. Dai, *Accounts of Chemical Research*, 2013, **46**, 31–42.

[23] C. Backes, B. M. Szydłowska, A. Harvey, S. Yuan, V. Vega-Mayoral, B. R. Davies, P.-l. Zhao, D. Hanlon, E. J. G. Santos, M. I. Katsnelson, W. J. Blau, C. Gadermaier and J. N. Coleman, *ACS Nano*, 2016, **10**, 1589–1601.

[24] M. Lotya, Y. Hernandez, P. J. King, R. J. Smith, V. Nicolosi, L. S. Karlsson, F. M. Blighe, S. De, Z. Wang, I. T. McGovern, G. S. Duesberg and J. N. Coleman, *Journal of the American Chemical Society*, 2009, **131**, 3611–3620.

[25] R. Narayan and S. O. Kim, *Nano Convergence*, 2015, **2**, 20.

[26] A. Tăbăcaru, B. Furdui, I. O. Ghinea, G. Cârâc and R. M. Dinică, *Inorganica Chimica Acta*, 2017, **455**, 329–349.

[27] Y. Chen, B. Song, X. Tang, L. Lu and J. Xue, *Small*, 2014, **10**, 1536–1543.

[28] Z. Lu, A. Hanif, C. Ning, H. Shao, R. Yin and Z. Li, *Materials & Design*, 2017, **127**, 154–161.

[29] X. Xie, Z. Ao, D. Su, J. Zhang and G. Wang, *Advanced Functional Materials*, 2015, **25**, 1393–1403.

[30] K. Chang and W. Chen, *Chemical Communications*, 2011, **47**, 4252–4254.

[31] C. N. R. Rao, K. Gopalakrishnan and U. Maitra, *ACS Applied Materials & Interfaces*, 2015, **7**, 7809–7832.

[32] F. Bonaccorso, L. Colombo, G. Yu, M. Stoller, V. Tozzini, A. C. Ferrari, R. S. Ruoff and V. Pellegrini, *Science*, 2015, **347**, 6217.

Appendix A

Chapter 3

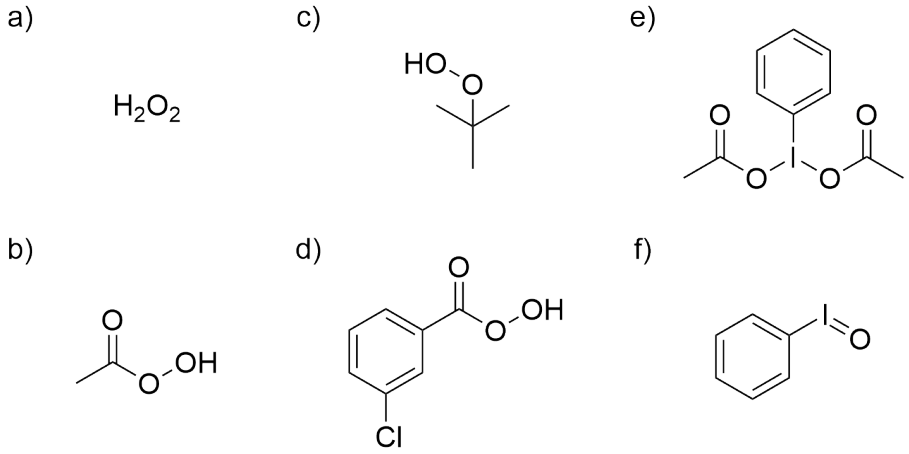

Fig. A.1 The structures of all oxidants used in this study: (a) H_2O_2 (b) peracetic acid (c) ^{t}BuOOH (d) *m*-CPBA (e) DAIB (f) PhIO.

Table A.1 Average I_D:I_G found for graphene from SGN18 and PP10 graphite treated with the oxidants listed.

Oxidants	SGN18	PP10
None	0.25	0.12
H_2O_2	0.26	0.12
^{t}BuOOH	0.26	0.12
Peracetic acid	0.24	0.12
m-CPBA	0.24	0.14
DAIB	0.25	0.11
PhIO	0.25	0.12

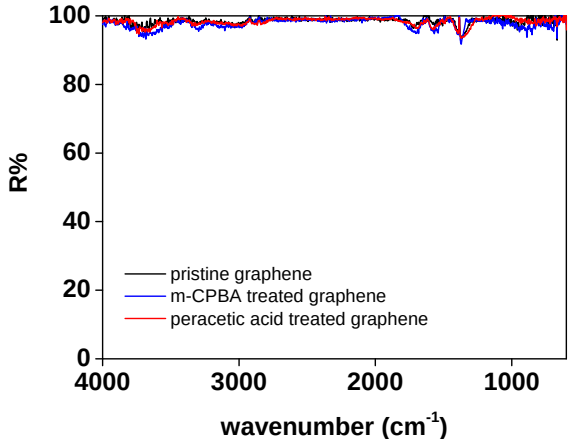

Fig. A.2 DRIFT spectra of PP10 graphene (black) treated with peracetic acid (red) *m*-CPBA (blue).

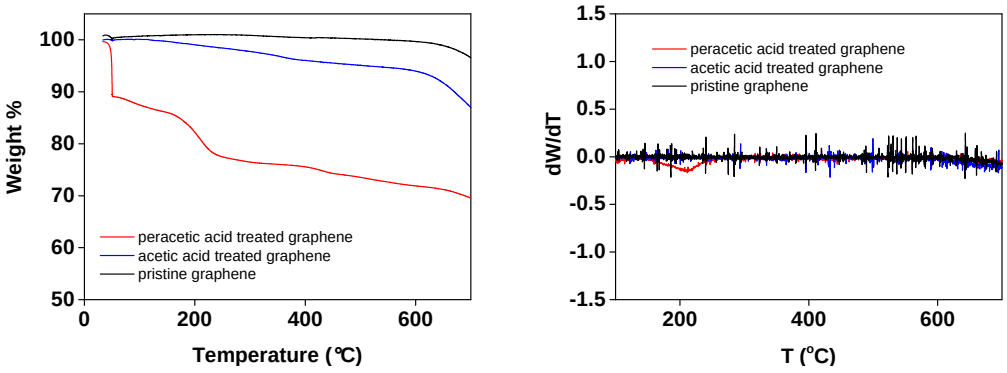

(a) (b)

Fig. A.3 (a) TGA traces and (b) 1st derivative traces of peracetic acid (red) acetic acid (blue) treated graphene and pristine graphene (black).

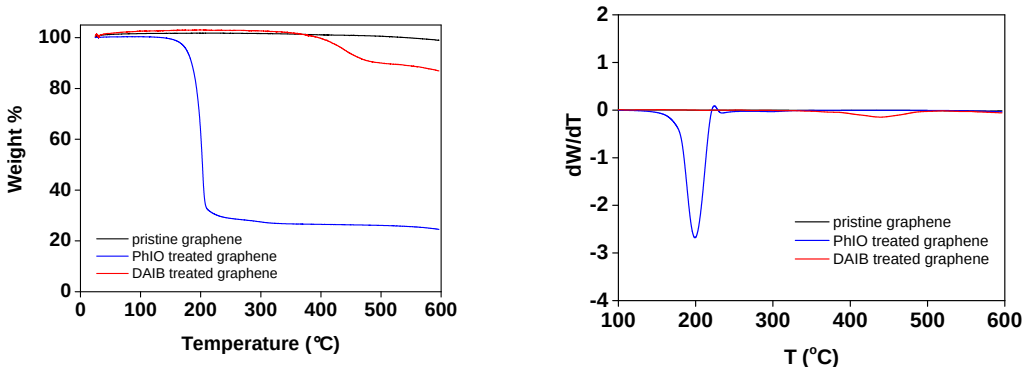

(a) (b)

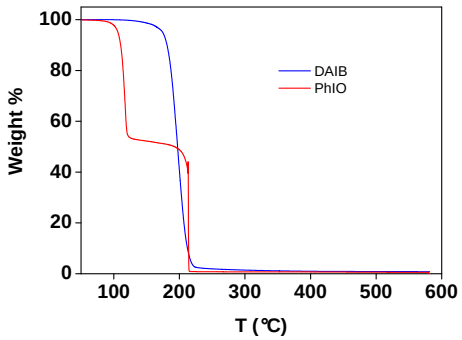

(c)

Fig. A.4 (a) TGA traces of unwashed graphene treated with DAIB (red) and PhIO (blue) and (b) corresponding 1st derivatives. (c) TGA traces of DAIB and PhIO only.

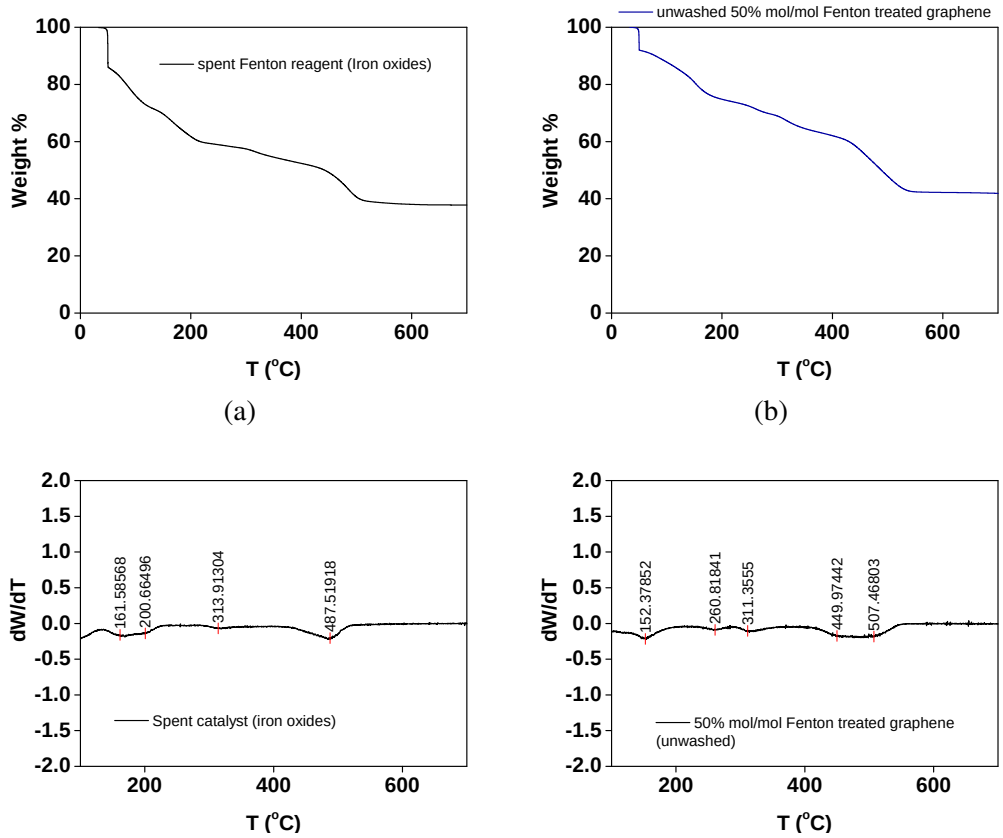

Fig. A.5 (a) TGA traces of the spent Fenton's reagent and (b) unwashed 50% Fenton-treated graphene, showing similar weight losses to the Fenton only trace above. (c) and (d) show corresponding 1st derivative traces.

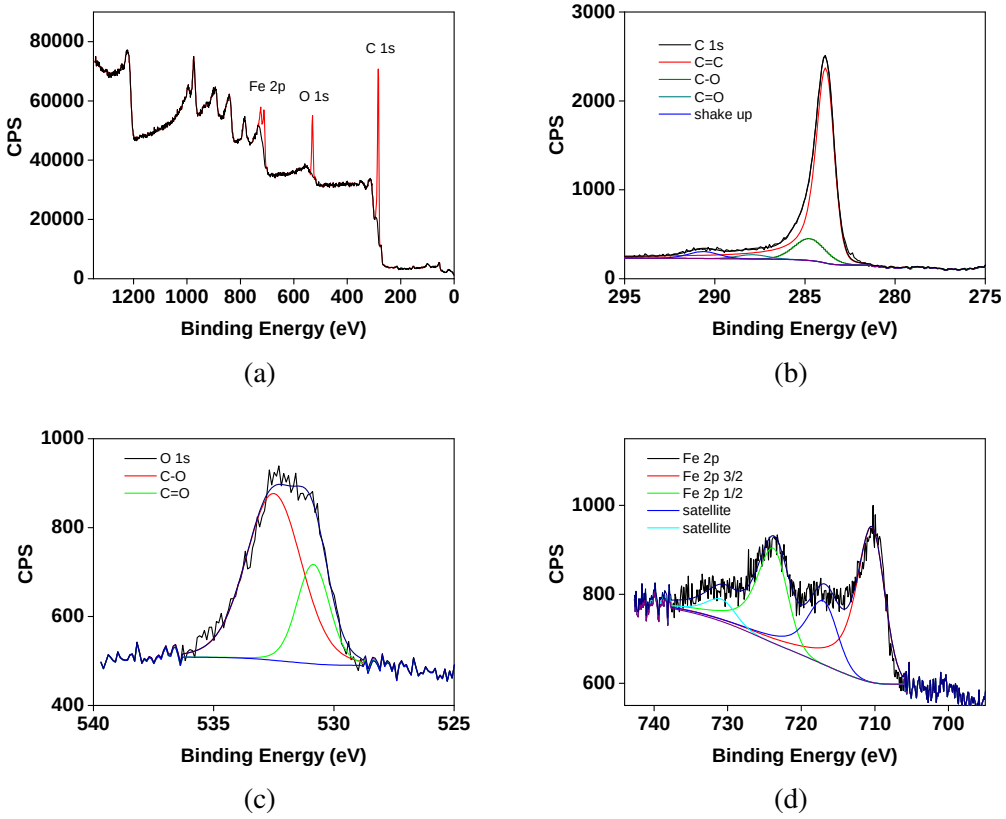

Fig. A.6 (a) Survey spectrum, (b) C 1s core level spectrum, (c) O 1s core level spectrum, (d) Fe 2p core level spectrum of 10% mol/mol Fenton treated graphene.

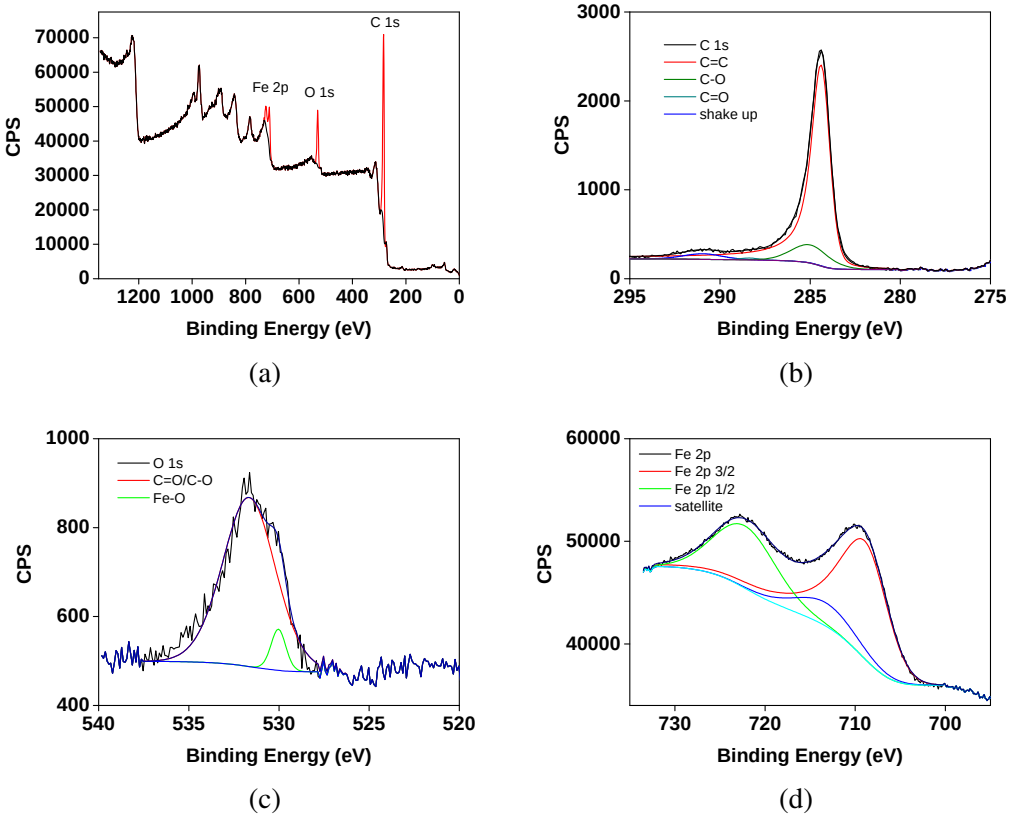

Fig. A.7 (a) Survey spectrum, (b) C 1s core level spectrum, (c) O 1s core level spectrum, (d) Fe 2p core level spectrum of stoichiometric Fenton treated graphene.

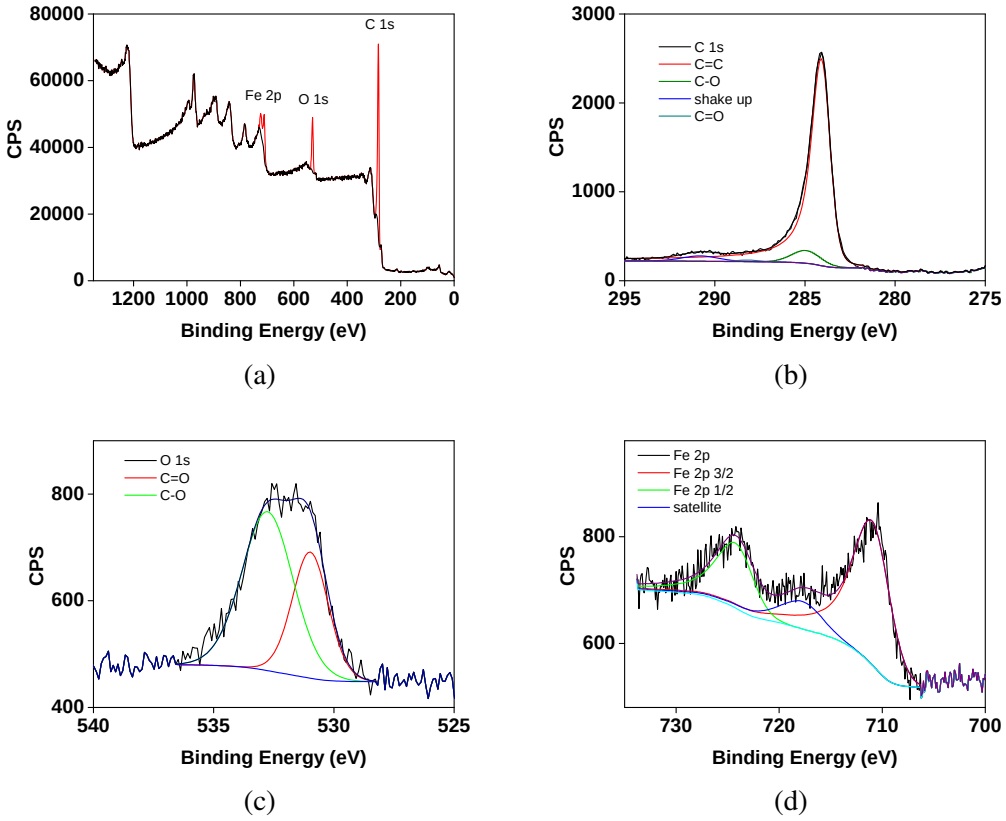

Fig. A.8 (a) Survey spectrum, (b) C 1s core level spectrum, (c) O 1s core level spectrum, (d) Fe 2p core level spectrum of 50% mol/mol Fenton treated graphene.

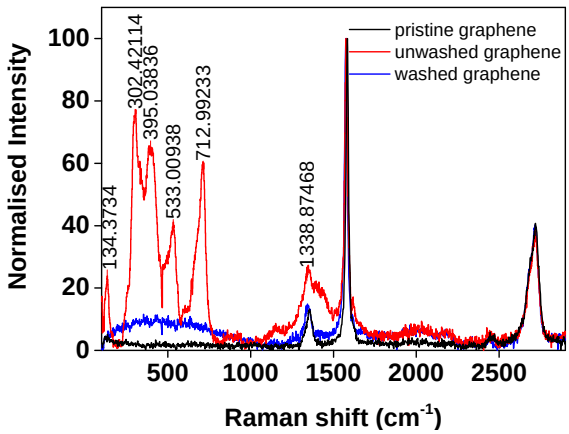

Fig. A.9 Raman spectra of unwashed (red) and washed (blue) 50% mol/mol Fenton treated graphene with pristine graphene (black).

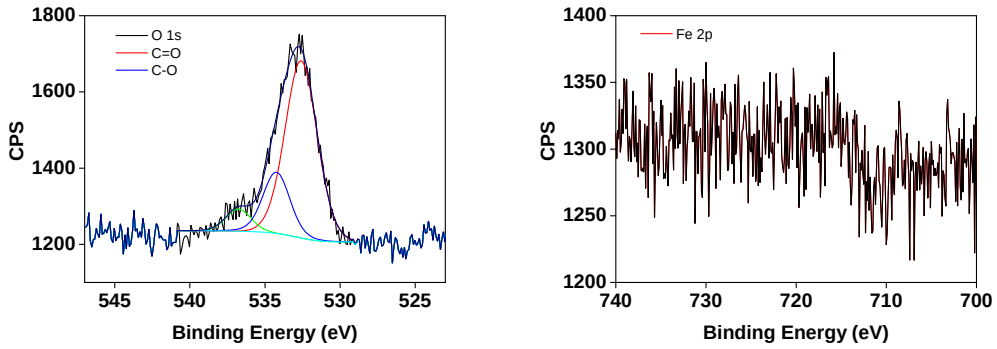

(a) (b)

Fig. A.10 (a) O 1s core level spectrum and (b) Fe 2p core level spectrum of 10% mol/mol [Fe^{V}(BPMEN)(O)(OH)] treated graphene.

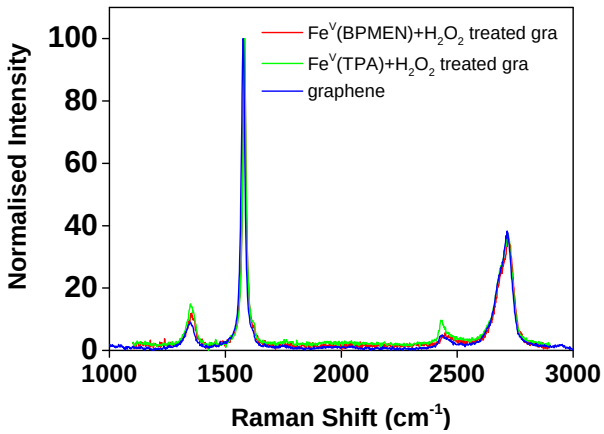

Fig. A.11 Raman spectra of PP10 graphene treated with [Fe^{V}(BPMEN)(O)(OH)] (red) and [Fe^{V}(TPA)(O)(OH)] (green).

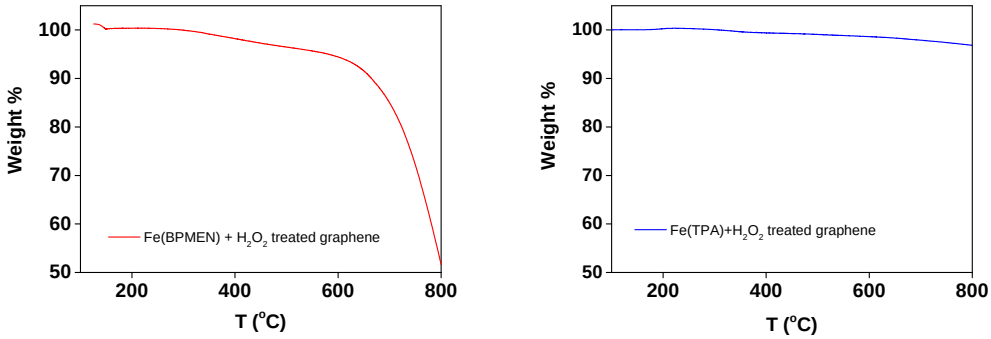

(a) (b)

Fig. A.12 Full range TGA traces of (a) 10% Fe(BPMEN)+H_2O_2 treated graphene and (b) 10% Fe(TPA)+H_2O_2 treated graphene.

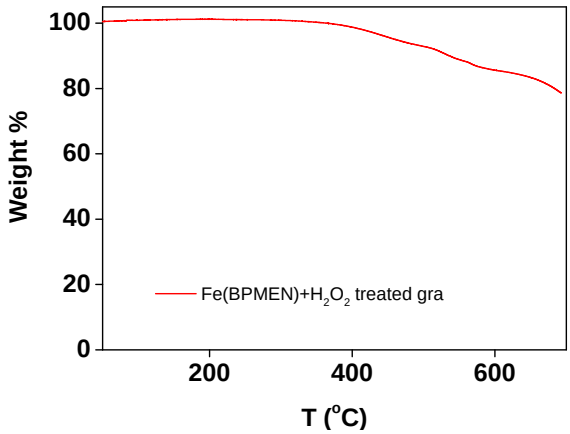

Fig. A.13 TGA trace of 10% mol/mol [Fe^{V}(BPMEN)(O)(OH)] treated graphene.

Appendix B

Chapter 4

B.1 Tables

Table B.1 Average I_D:I_G and 2LA(M):A_{1g} found for ce-1T-MoS_2 and graphene (532 nm).

532 nm	1:5	1:12	1:20	Control
ID:IG	0.2	0.28	0.28	0.29
2LA(M):A1g	0.26	0.41	0.6	0.13

Table B.2 Average I_D:I_G and 2LA(M):A_{1g} found for ce-1T-MoS_2 and graphene (633 nm).

633 nm	1:2	1:10	1:20	Control
ID:IG	0.47	0.44	0.4	0.47
2LA(M):A1g	1.06	0.84	1.44	0.97

Table B.3 Average I_D:I_G and 2LA(M):A_{1g} found for 2H-MoS_2 and graphene (532 nm).

532 nm	5:1	2:1	1:1	1:15	1:25	Control
ID:IG	-	-	-	0.19	0.35	0.2
2LA(M):A1g	0.19	0.11	0.1	0.08	0.06	0.09

Table B.4 Average I_D:$I_G$and 2LA(M):A_{1g} found for 2H-MoS_2 and graphene (633 nm).

633 nm	1:1	1:15	1:25	Control
ID:IG	-	0.24	0.29	0.35
2LA(M):A1g	0.42	0.43	0.6	0.5

B.2 Figures

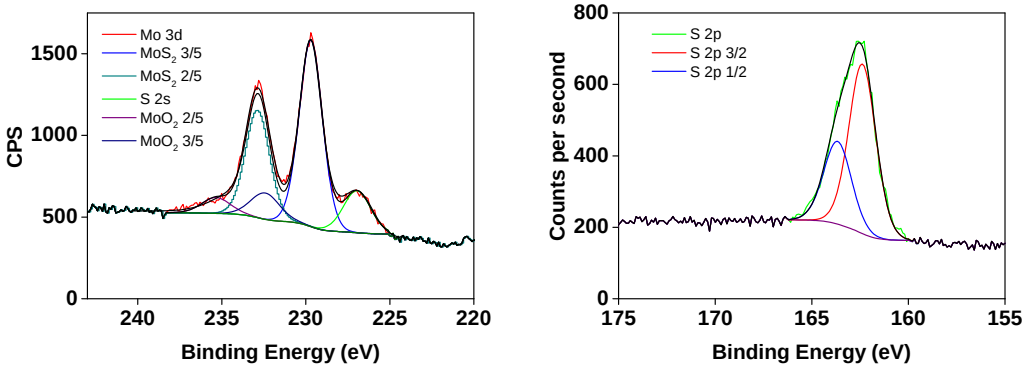

(a) (b)

Fig. B.1 (a) Mo 3d core level and (b) S 2p core level spectra from a 1:5 1T-MoS_2/graphene heterostructure.

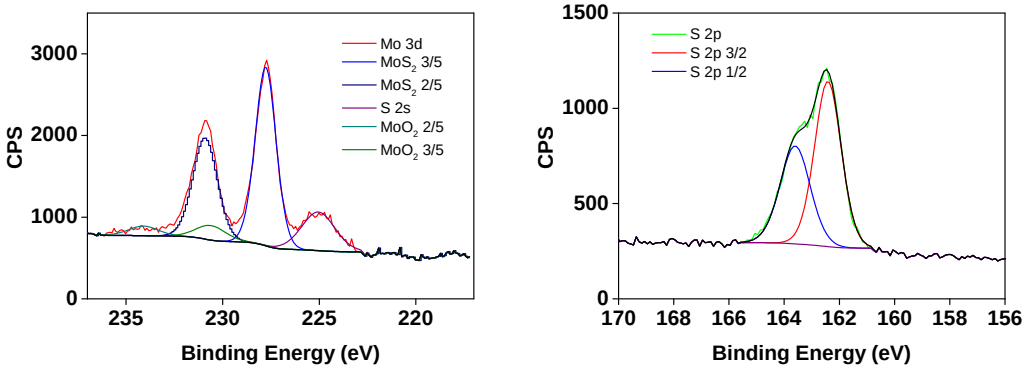

(a) (b)

Fig. B.2 (a) Mo 3d core level and (b) S 2p core level spectra from a 1:25 2H-MoS_2/graphene heterostructure.

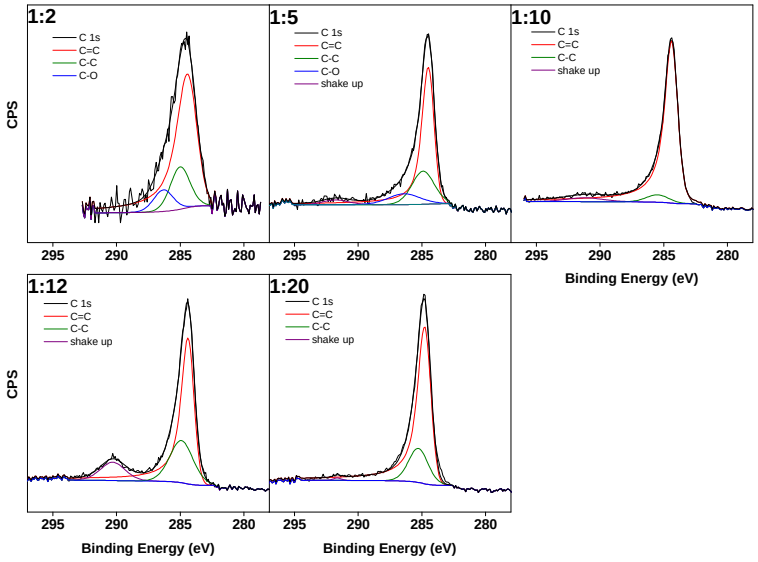

(a)

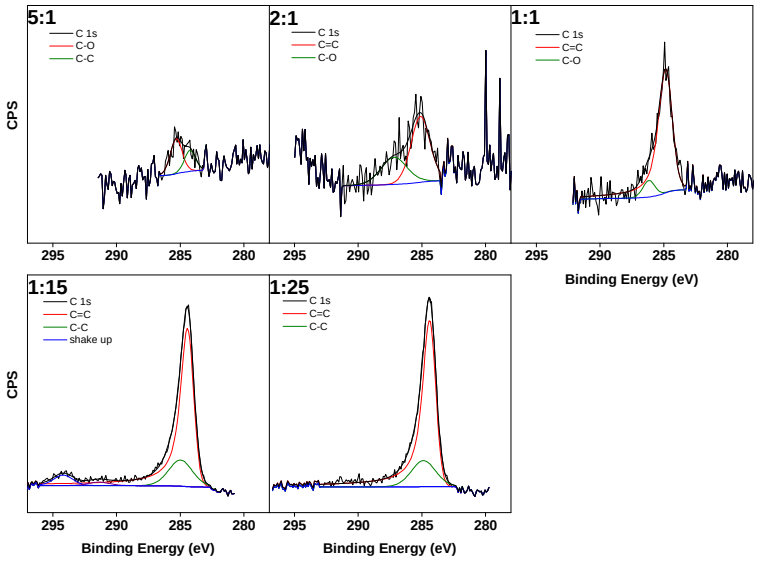

(b)

Fig. B.3 C1s core level spectra for the series of (a) ce-1T-MoS_2/graphene heterostructures and (b) 2H-MoS_2/graphene heterostructure.

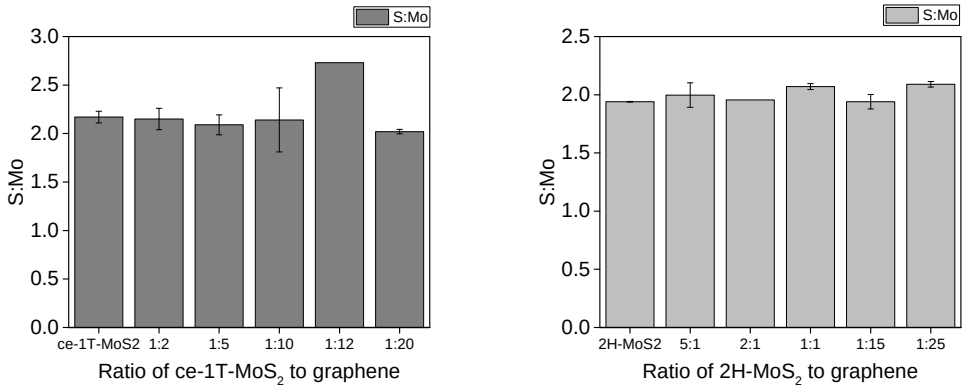

(a) (b)

Fig. B.4 Average sulfur to molybdenum ratio calculated from XPS core level spectra of (a) ce-1T-MoS_2 and heterostructure with graphene and (b) 2H-MoS_2 and heterostructures with graphene.

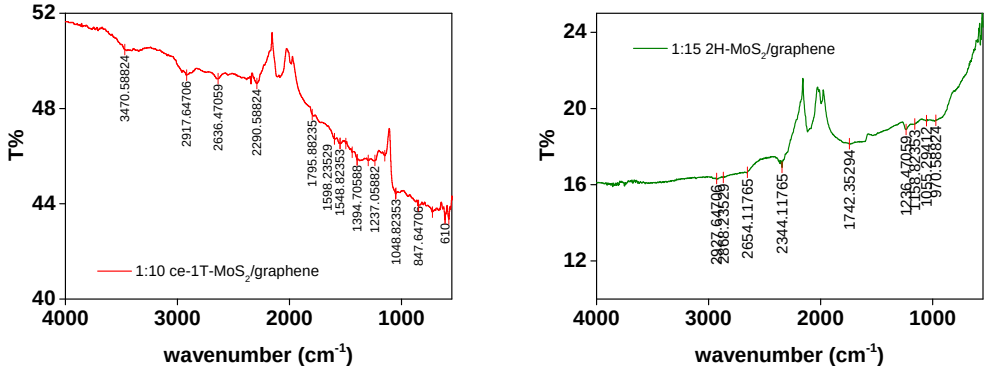

(a) (b)

Fig. B.5 ATR-IR spectra (full range) of (a) a 1:10 ce-1T-MoS_2/graphene heterostructure and (b) a 1:15 2H-MoS_2/graphene heterostructure.

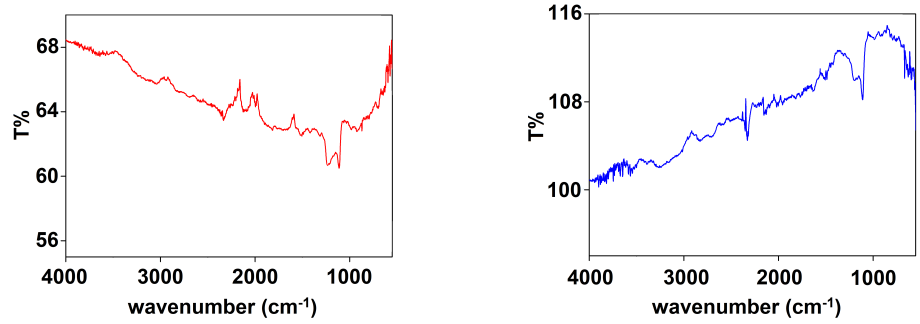

(a) (b)

Fig. B.6 ATR-IR difference spectra showing peaks remaining from the spectra of (a) Graphene subtracted (b) 1T-MoS_2 subtracted from 1:20 ce-1T-MoS_2/graphene.

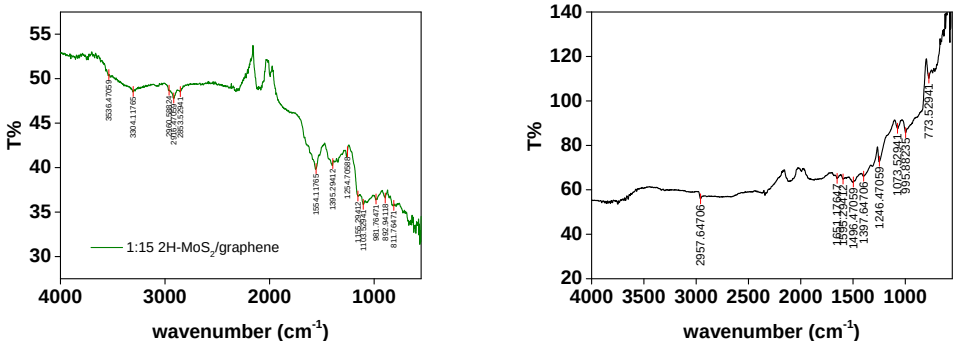

(a) (b)

Fig. B.7 ATR-IR difference spectra showing peaks remaining from the spectra of (a) Graphene subtracted (b) 2H-MoS_2 subtracted from 1:15 2H-MoS_2/graphene

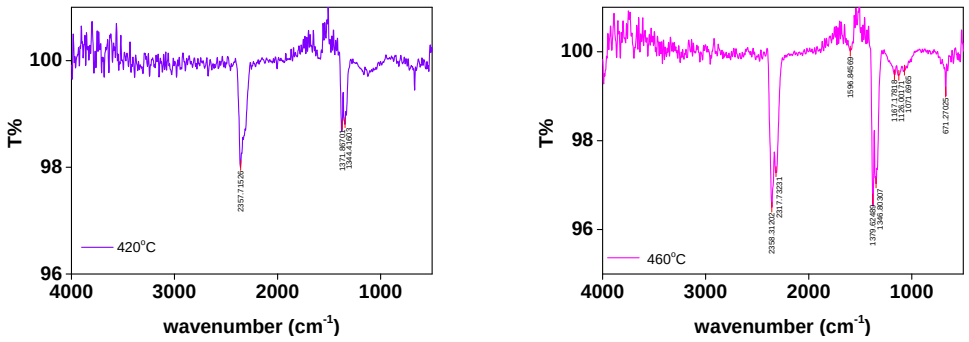

(a) (b)

Fig. B.8 TGA-IR spectrum of (a) 1:5 ce-1T-MoS_2/graphene heterostructure at 420 °C and (b) of 1:15 2H-MoS_2/graphene heterostructure at 460 °C.

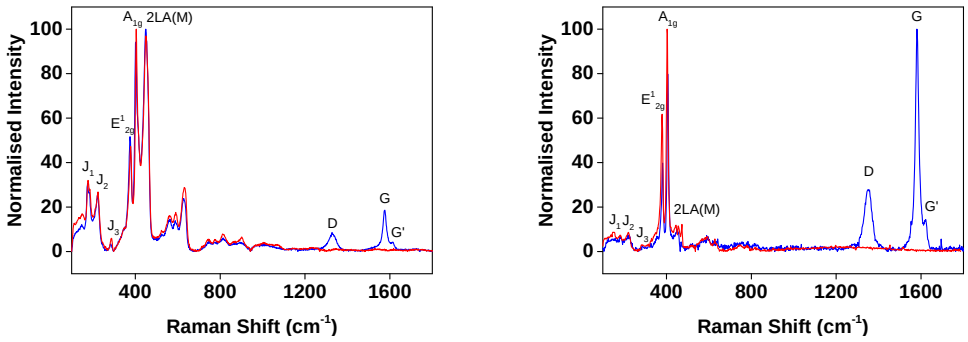

Fig. B.9 (a) Raman spectrum of 1:5 1T-MoS_2/gra (blue line) and MoS_2 control (red line) taken using (a) the 633 nm laser line, (b) the 532 nm laser line.

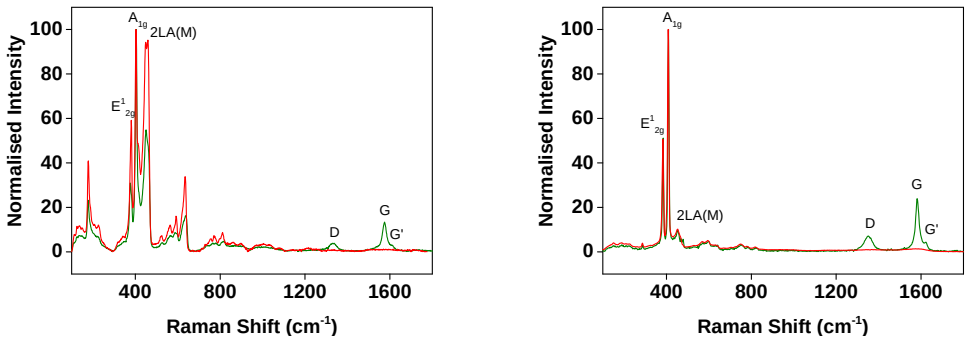

Fig. B.10 (a) Raman spectrum 1:25 2H-MoS_2/gra (green line) with MoS_2 control (red line) taken using (a) the 633 nm laser line, (b) the 532 nm laser line.

Appendix C

Chapter 5

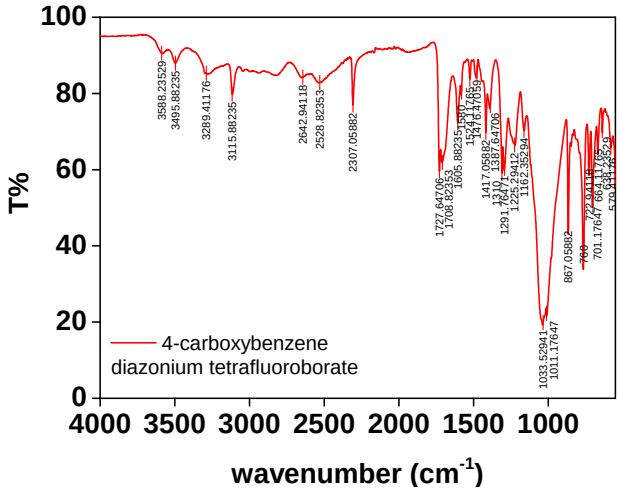

Fig. C.1 ATR-IR spectrum of 4-carboxybenzene diazonium tetrafluoroborate, showing N-N triple bond at 2307 cm^{-1}.

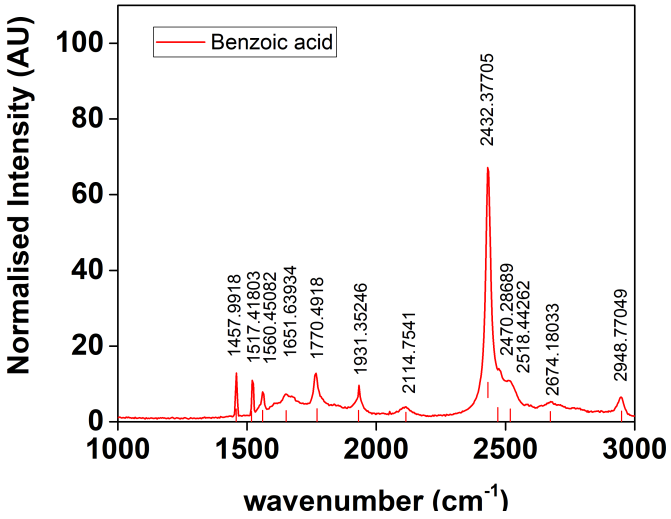

Fig. C.2 Raman spectrum of free benzoic acid.

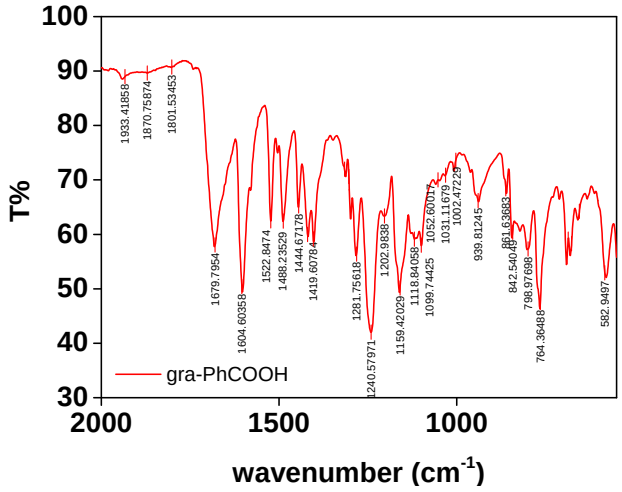

Fig. C.3 Labelled ATR-IR of gra-PhCOOH, 2000–550 cm^{-1}.

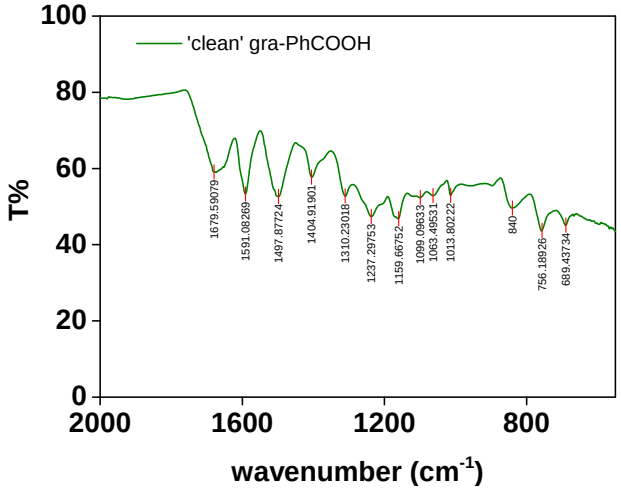

Fig. C.4 Labelled ATR-IR of 'clean' gra-PhCOOH, 2000–550 cm^{-1}.

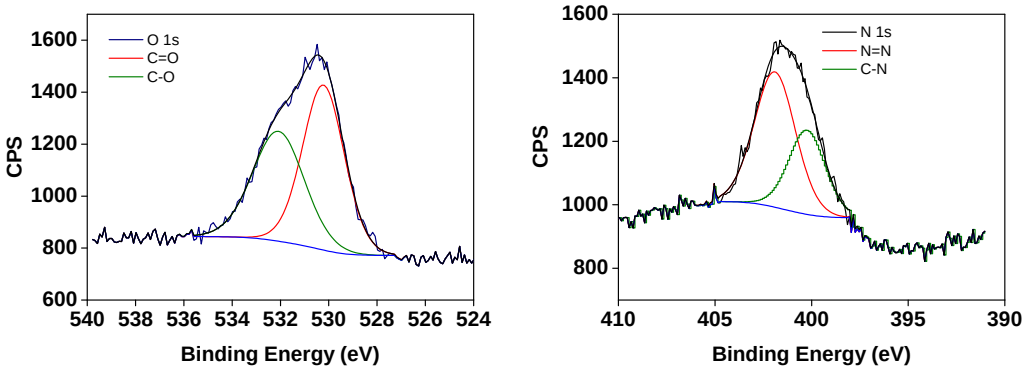

(a) (b)

Fig. C.5 (a) O 1s core level and (b) N 1s core level spectra of gra-PhCOOH.

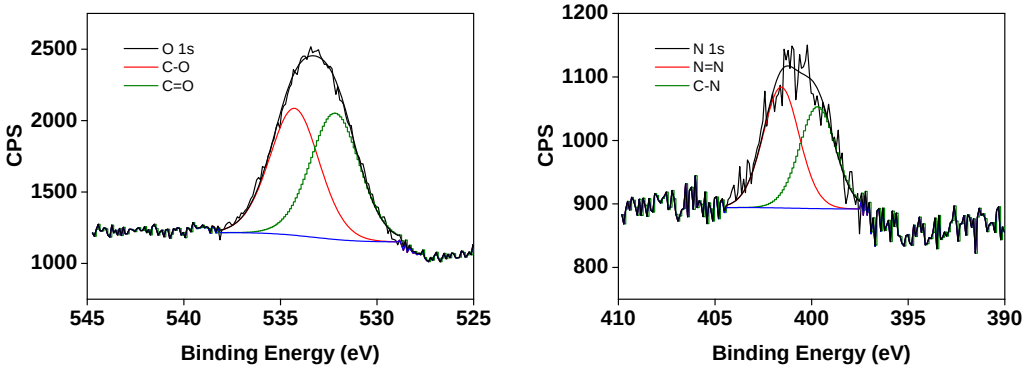

(a) (b)

Fig. C.6 (a) O 1s core level and (b) N 1s core level spectra of 'clean' gra-PhCOOH.

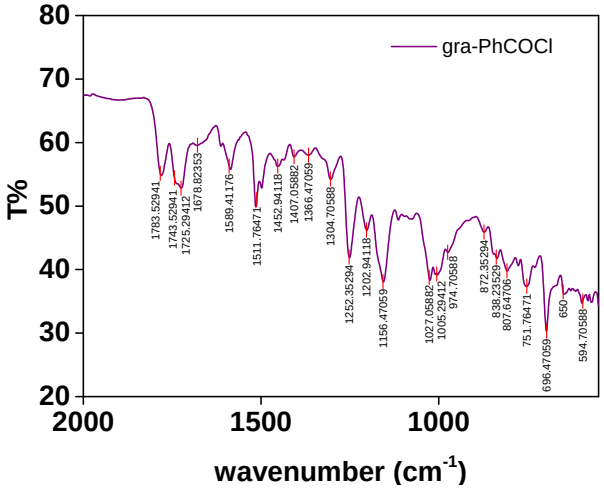

Fig. C.7 Labelled ATR-IR of gra-PhCOCl, 550–2000 cm^{-1}.

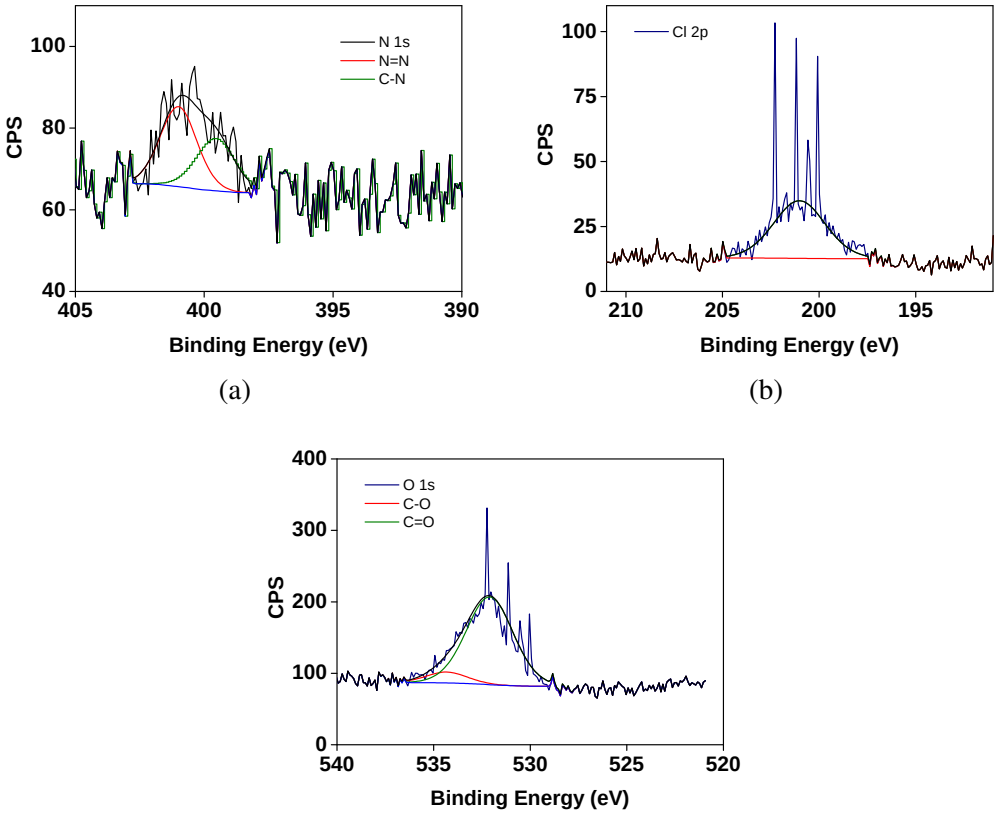

(a) (b)

(c)

Fig. C.8 (a) N 1s core level, (b) Cl 2p core level and (c) O 1s core level spectra of gra-PhCOCl.

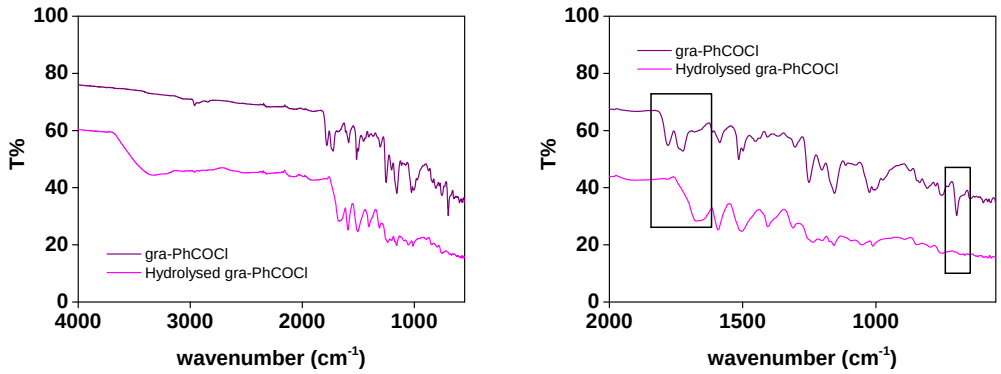

(a) (b)

Fig. C.9 (a) ATR-IR comparison of gra-PhCOCl (purple) and after hydrolysis by refluxing in water (pink). (b) 2000–550 cm^{-1} range with the changes in C=O and C-Cl stretch areas highlighed by black boxes.

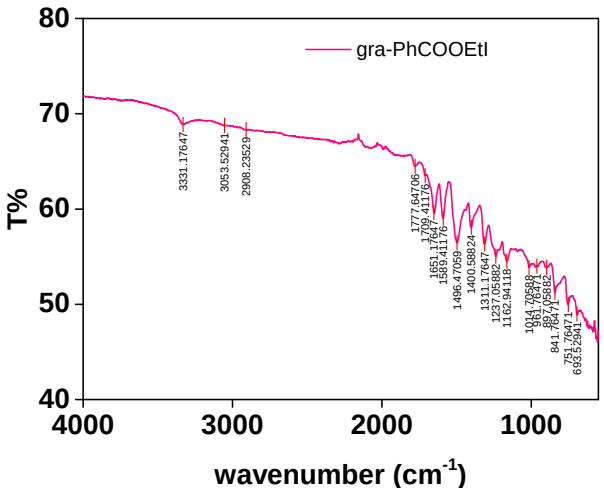

Fig. C.10 ATR-IR spectrum of gra-PhCOOEtI (pink) from gra-PhCOCl and IEtOH.

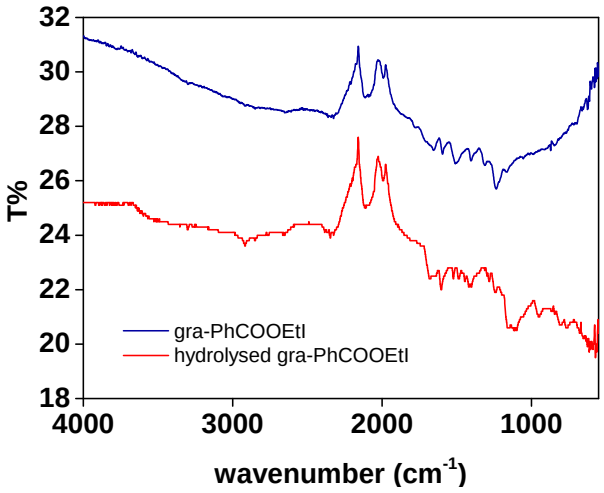

Fig. C.11 ATR-IR comparison of gra-PhCOOEtI (navy) and after hydrolysis by refluxing in dilute HCl (red).

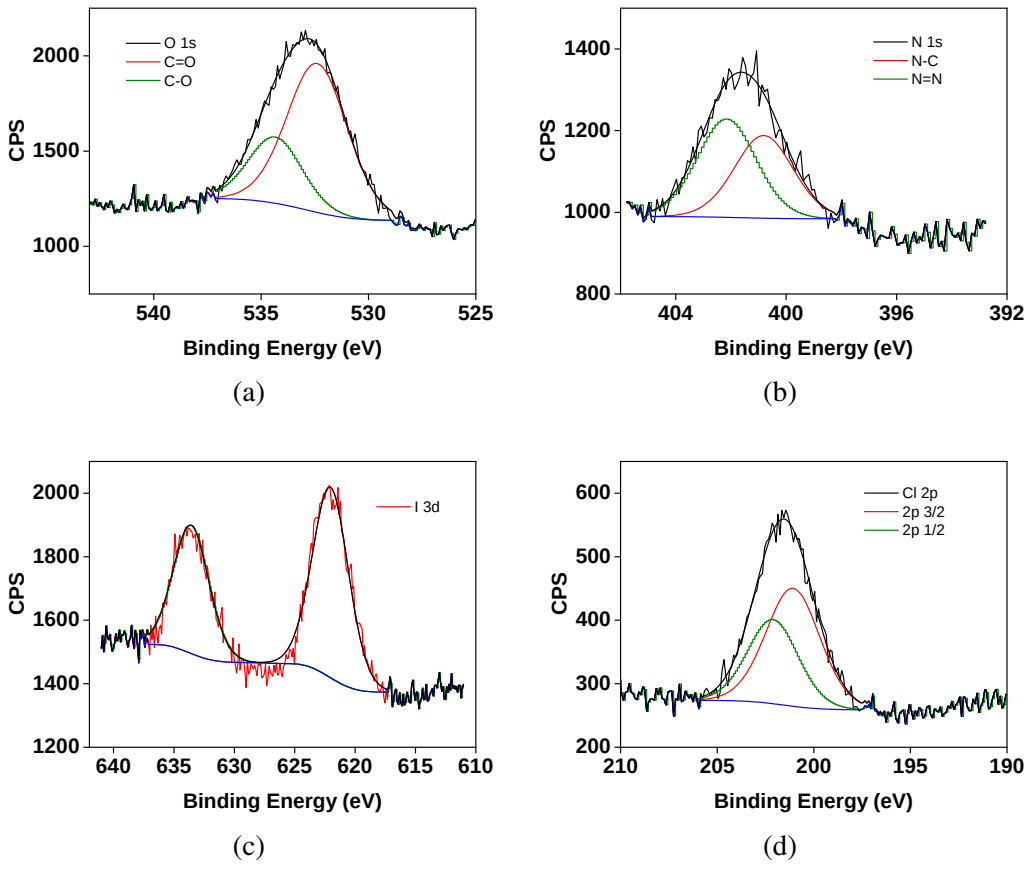

Fig. C.12 (a) O 1s core level, (b) N 1s core level, (c) I 3d core level and (d) Cl 2p core level spectra of gra-PhCOOEtI.

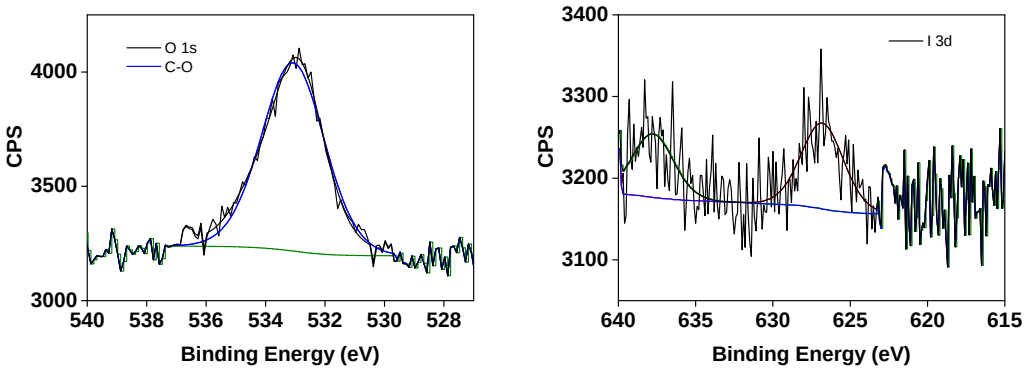

(a) (b)

Fig. C.13 (a) O 1s core level and (b) I 3d core level spectra of MoS_2-EtOH.

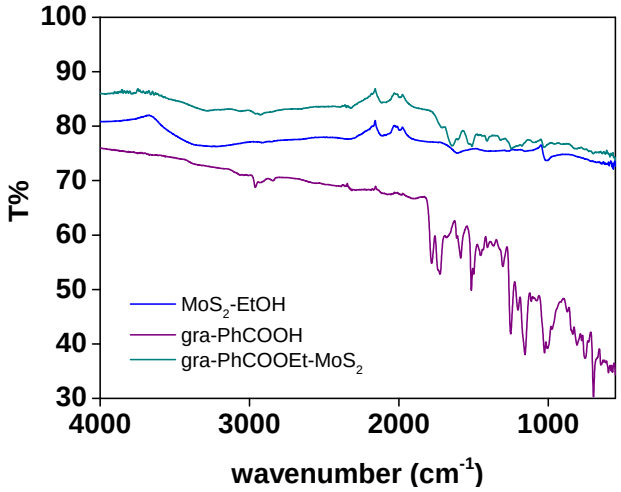

Fig. C.14 ATR-IR comparison of gra-PhCOOEt-MoS_2 (teal), gra-PhCOCl (purple) and MoS_2-EtOH (blue).

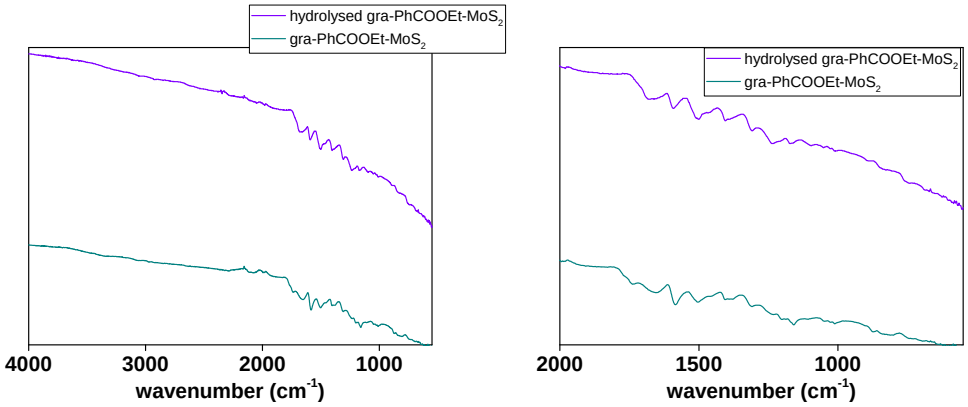

Fig. C.15 (a) ATR-IR of fresh gra-PhCOOEt-MoS_2 (teal) and after refluxing in 0.1 M HCl (violet), full range and (b) 550–2000 cm^{-1}.

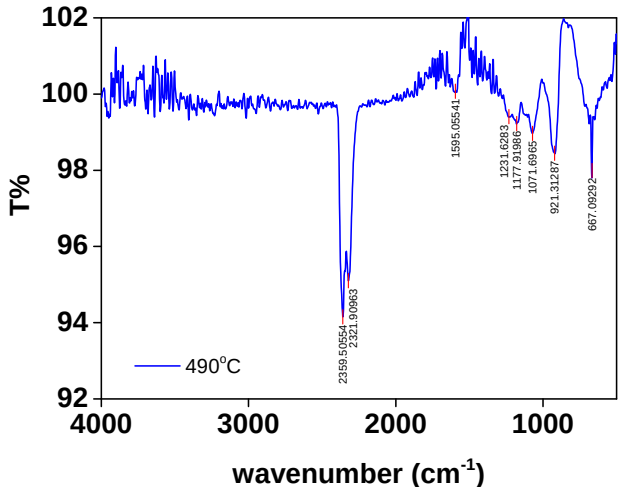

Fig. C.16 TGA-IR spectrum of gra-PhCOOEt-MoS_2 at 490°C, showing CO_2 given off.

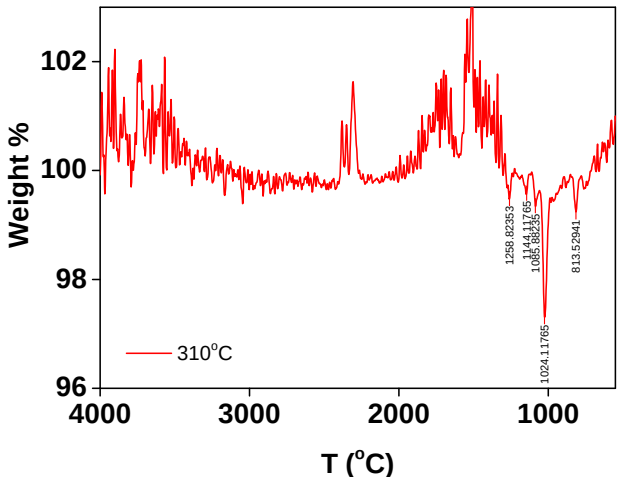

Fig. C.17 IR spectrum (from TGA-IR) of graphene treated with $SOCl_2$ at 310°C, showing peaks.

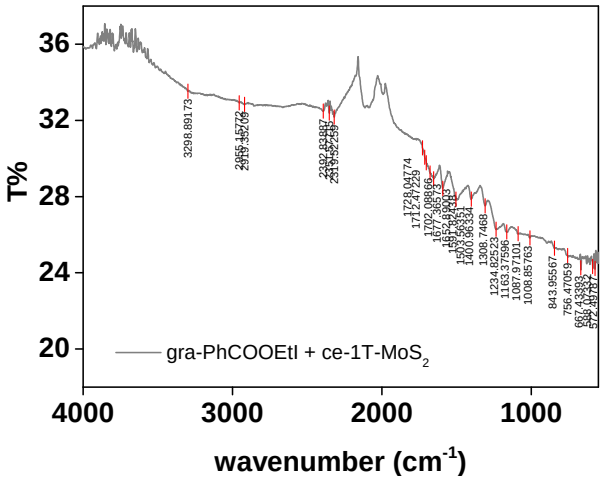

Fig. C.18 ATR-IR of gra-PhCOOEt-MoS_2 from gra-PhCOOEtI and ce-1T-MoS_2.

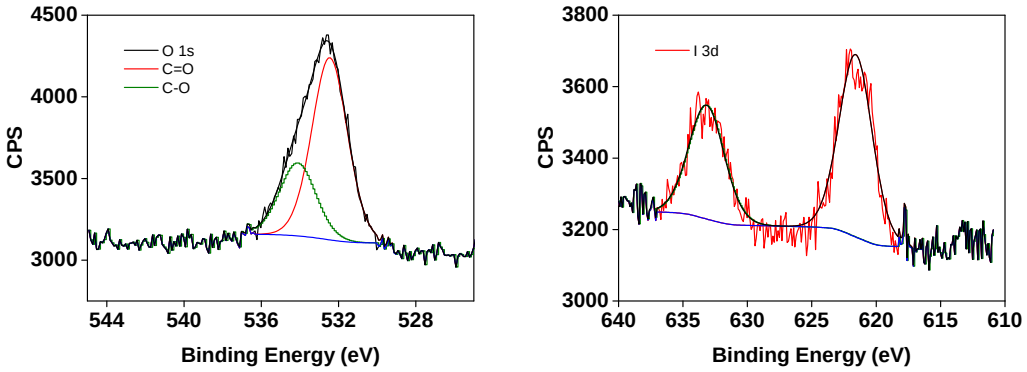

(a) (b)

Fig. C.19 (a) O 1s core level spectrum and (b) I 3d core level spectrum of gra-ester-MoS_2 from gra-PhCOOEtI and ce-1T-MoS_2.